Thin Films of Copper Indium Disulphide and Zinc-based Buffer Layers for Application in Photovoltaic Devices.

A Thesis Submitted in Partial Fulfilment of the Requirements of Northumbria University for the Degree of Doctor of philosophy

by

David Johnston

School of Informatics, Engineering and Technology

Northumbria University

January 2005

Abstract

Thin films of copper indium disulphide and zinc sulphide were fabricated, for use as absorber and window layers respectively for photovoltaic devices. The copper indium disulphide was produced in two stages. In the first stage, a copper indium alloy was produced on molybdenum-coated glass substrates by sputtering from metallic targets. A number of slides were placed together on each platten, giving a total area for deposition of approx. 100 cm^2. A rotating turntable allowed a large number of very thin layers of copper and indium to be deposited alternately, resulting in very good mixing to form the alloy. A range of powers were applied to the copper and indium targets, to produce films of different compositions, including stoichiometric, copper-rich and indium rich material. Rutherford backscattering analysis showed a high degree of compositional uniformity, both over the area of the deposited film, and with depth through the film.

Three different methods were used to convert the copper indium alloy to copper indium disulphide. The first method involved evaporation of sulphur inside a graphite box, in which the substrate (with a copper indium precursor film) was enclosed. The sulphur diffused to fill the enclosed space, thus eliminating the limitations of line-of-sight evaporation. A strip heater was used in the initial experiments. Subsequently, a tube furnace was used to provide a more uniform and stable temperature. This allowed substrates up to 25 mm x 25 mm to be used. Temperatures up to 450°C were used. X-ray diffraction showed essentially complete conversion to copper indium disulphide for films heated to 400°C for 40 minutes. This relatively low temperature allowed soda-lime glass, rather than borosilicate glass, to be used for the substrates. Both uniformity and adhesion to the substrate were good.

The second method also involved heating sulphur in the tube furnace to produce vapour. The size of the substrates used was as above - 25 mm x 25 mm. In this case, the sulphur vapour was transported over the substrates in a flowing argon

stream. This provided an alternative mechanism for overcoming line-of-sight limitations. A similar range of temperatures was used, again allowing soda-lime glass to be used. X-ray diffraction again showed essentially complete conversion to copper indium disulphide for films heated to 400°C for 40 minutes. Adhesion to the substrate was good. Uniformity was good, though less so than for material produced using the graphite box.

A third method involved electrolytic conversion using a sulphur-containing solution. Both water and ethanediol were used as solvents. X-ray diffraction of films produced using water as a solvent showed a high degree of conversion to copper indium disulphide. However, uniformity and adhesion were poor. Films produced with ethanediol as a solvent had improved uniformity and adhesion, but showed only partial conversion to copper indium disulphide. This was improved, to some extent, by a subsequent anneal in vacuum at 400°C for 30 minutes.

Zinc sulphide was produced by chemical bath deposition. Tri-sodium citrate was used as a complementary complexing agent, as a non-hazardous substitute for hydrazine hydrate, which had been used in previous work. The films produced showed high optical transmittance (~ 90 %) over the wavelength range longer than 330 nm. They had good uniformity and adhesion to the substrate. Inclusion of aluminium compounds in the deposition solution, in combination with a post-deposition anneal in vacuum at temperatures up to 400°C, resulted in a significant reduction in the resistivity of the films (~ 1 Ω for a 1 cm^2 device).

Partially-completed devices, consisting of copper indium disulphide and zinc sulphide layers, were sent to Sri Venkateswara University, Tirupati, India, where zinc oxide layers were added, to form complete photovoltaic devices. Voltage-current characteristics showed open circuit voltages of 300 to 400 mV and short circuit current densities of approx. 10 $mAcm^{-2}$. The corresponding fill factor was 0.4.

Acknowledgements

I would like to thank my supervisors, Dr. Robert Miles and Dr. Ian Forbes, for their assistance, both during the practical research and during the writing of this thesis.

I would also like to thank John Coyne and James Scott - technicians within our research group - who gave me much practical advice and assistance during my research.

I also owe thanks to the other members of staff - Prof. Nicola Pearsall, and Dr. Kathleen Hynes - for providing additional support, particularly with regard to the administrative aspects of my research.

In addition, I would like to thank my fellow students - Steven Armstrong, Thomas Bauer, Jayaraman Ramachandran, Paresh Nasikkar and Ogah Ogah - for exchanging ideas, and providing a good communal environment in which to work.

Naturally, I would like to thank my family, particularly my mother, for their continuing support since I started my PhD. Their support gave me the strength to keep going.

Finally, and perhaps most importantly, I would like to thank Li Yazao, who gave me the incentive and the motivation to persevere through the difficulties I experienced, and to complete my PhD.

Contents

List of Figures

Chapter 2

Chapter 2 - continued

Chapter 3

Chapter 4

Chapter 4 - continued

Chapter 5

Chapter 5 - continued

Chapter 5 - continued

Chapter 5 - continued

List of Tables

List of symbols

A	(active) device area	I	current
c	speed of light	I_0	reverse saturation current
d	film thickness	I_L	photo-current
d	lattice spacing	I_m	current at maximum power point
D_n	electron diffusion coefficient	I_{sc}	short circuit current
D_p	hole diffusion coefficient	J	current density
e	electronic charge	k	Boltzmann's constant
E	energy	k	Miller index
E_c	base of conduction band	l	Miller index
E_f	Fermi level	L_n	electron diffusion length
E_g	bandgap energy	L_p	hole diffusion length
δE_{mj}	spacing of majority quasi-Fermi level from band edge in depletion region	m	mass
		n	number density
δE_{mn}	spacing of minority quasi-Fermi level from band edge in depletion region	n	principal quantum number
		n	refractive index
		N_A	acceptor ion density
E_v	top of valence band	N_D	donor ion density
$F(E)$	photon flux	P	power
FF	fill factor	q	electric charge
g_{opt}	generation rate for electron-hole pairs (per unit volume)	R	radius
		R	reflectance
h	Miller index	R	resistance
h	Planck's constant	R_s	series resistance

R_{eh}	pair generation rate
T	temperature
T	transmittance
V	voltage
V_m	voltage at maximum power point
V_{oc}	open circuit voltage
W	depletion layer width
Z	atomic number
α	optical absorption coefficient
ε_0	permittivity of free space
η	efficiency
η	ideality factor
θ	zenith angle
θ_i	angle of incidence
θ_r	angle of reflection
λ	wavelength
ν	frequency
ρ	density
ρ	resistivity
ϕ	activation energy
ϕ	work function
Φ	irradiance
χ	electron affinity

1. Introduction

The solar irradiance reaching the edge of the Earth's atmosphere is 1368 Wm^{-2} [1]. Multiplying by the projected area of the Earth gives a flux over the Earth's surface of approx. 1.7 x 10^{14} GW. This is reduced by atmospheric absorption. (The standard value of solar flux at sea level, for vertical incidence, is 925 Wm^{-2}.) Solar irradiation is limited to daytime, and is dependent on ambient weather conditions. However, the power available remains large, and is widely, but not uniformly, distributed.

Photovoltaic devices are semiconductor devices, which convert radiation directly into electricity. Those which convert solar radiation are referred to as solar cells. The potential for photovoltaic electricity generation is enormous, and could make a significant contribution to an energy supply program based on sustainable sources. As with other forms of sustainable energy production, photovoltaic electricity generation does not deplete limited energy resources (although materials and energy are consumed in fabrication), and does not produce greenhouse gases during operation. This potential has been limited by the high costs of current production methods. Thin film solar cells are being developed by many research groups, in an attempt to reduce these costs, and so increase the competitiveness of solar cells for the generation of electricity.

Due to their method of construction, photovoltaic devices have an advantage at smaller scales of power output (up to hundreds of kW). The basic unit of a photovoltaic generating system is the solar cell. Typically this is a single crystal device, up to 20 cm in diameter. These can be mounted into a module of a square metre or more in size. For large power requirements, a large number of modules can be connected in series and/or parallel. As a result of this modular

construction, the cost of electricity generation (per kWh) is largely independent of generating capacity. In comparison, many alternative generating technologies, e.g., turbine-generators, are more efficient as larger scales.

The advantage of photovoltaic generation at smaller scales has been a factor in determining the sectors within which it has so far been applied. Examples are building-integrated systems, electricity supply (mini-grids) for towns and villages in remote locations, and dedicated power supplies for stand-alone systems – radio transmitters, etc. In order to become cost-effective on a larger scale, where it is in competition with other sources, the generation costs of solar electricity must be reduced by a factor of around five [4]. As the single largest cost is incurred in the production of solar cells, it is in this area that much of the efforts to reduce costs have been concentrated.

A photovoltaic device is a large area semiconductor diode, which generates electric power, when irradiated by light [2]. A number of configurations are used. In flat-panel systems, a large area solar cell collects the incident radiation. In concentrator systems, a large area optical system – consisting of lenses and/or mirrors – focuses radiation onto solar cells of smaller area [3].

As silicon is the primary material for the electronics industry, the processes involved in silicon production form a mature technology. It has been possible to transfer this technology to the production of photovoltaic devices, and silicon solar cells are one of the commonly produced types. These were first developed for satellites, etc, and have since been used in terrestrial applications.

However, silicon solar cells are expensive to produce, for a number of inter-related reasons. As silicon is an indirect band-gap semiconductor, it has a relatively long optical absorption length (~ 100 μm), which sets a lower limit on

the thickness of the cell [2, 3]. In practice, the cell is made using a wafer cut from a cylindrical crystal, and the wafer is typically 0.5 mm thick, to provide mechanical rigidity. In order to achieve reasonable efficiency, the minority carrier diffusion length in the silicon should be long compared to the optical absorption length. Because crystal defects and impurities can act as recombination or scattering centres, the densities of these imperfections produced during manufacture must be minimised. These requirements mean that silicon solar cells must be made of high-purity single-crystal material. Both purification and growth of large crystals are time-consuming processes, which involve high temperatures and handling of reactive gases or other materials. These factors result in production costs, and consequently electricity generation costs, which are considerably higher than those for other sources [4].

Silicon solar cells have been fabricated using amorphous silicon and multi-crystalline silicon, which have reduced fabrication costs, compared to single crystal devices [5]. In both cases, light trapping is used to increase the optical path length, while keeping the film thickness to a minimum.

Devices using amorphous silicon have conversion efficiencies which tend to decrease with time, when exposed to high intensity illumination, due to the Stabler-Wronski effect. In order to compensate for this loss of efficiency, multi-junction cells have been developed [5]. A larger number of narrower junctions collects the photo-generated current more efficiently. In addition, the band gap can be increased by alloying with carbon, or decreased by alloying with germanium. A combination of different band gaps can be selected, which provides improved matching with the photon energy over a broader range of the

solar spectrum. This results in increased conversion efficiency. However, the increased number of layers, and hence process steps, adds to the fabrication costs. Devices based on multi-crystalline silicon can produce good efficiencies [5]. This can be achieved with single junction devices, thus avoiding the complex processing involved in multi-junction fabrication. These can be cast from molten silicon, although there is also development work on thin film devices, where the silicon is deposited, in micro-crystalline form, onto substrates of other materials [5]. This reduces the quantity of silicon required, and has the potential to reduce fabrication costs.

A number of direct band gap materials have been developed for solar cells, in order to improve efficiency. The III-V compounds, notably gallium arsenide, produce the highest efficiencies [3, 5]. This material has been developed for space applications, where its high radiation resistance provides the additional advantage of allowing long cell lifetimes in the space environment (UV radiation, high energy particles, etc). (A related material - indium phosphide - has even higher radiation resistance [5].) Alloys, such as gallium aluminium arsenide, can be produced with higher or lower band gaps. These can be used to form multi-junction cells, which result in even higher efficiencies. Devices made using the III-V compounds are adversely affected by crystal defects and impurities, as for silicon. Therefore, they are produced in single crystal high-purity form. Thus, the fabrication costs are high. Gallium arsenide based cells are considerably more expensive than those based on silicon. However, the high performance can results in savings in other costs (e.g. lower launch costs due to lower panel size), which can more than offset the higher fabrication costs. As a result, gallium arsenide

cells are more economical in space, and for a number of terrestrial applications, where performance requirements outweigh fabrication costs.

Gallium arsenide cells are also used in concentrator systems. The smaller area of the cells, compared to the equivalent flat panel, reduces the semiconductor material requirement, and contributes a reduction in cost. If this more than offsets the added cost of the concentrator, and the sun-tracking system, which is also required, there is a net cost reduction for the whole system.

In addition to thin film devices, based on various forms of silicon, a number of devices based on direct band-gap thin film compound semiconductors have been developed. The thin film solar cells are fabricated by depositing layers of semiconductor materials onto a relatively low-cost substrate such as glass [5]. Because of the direct band gap, these materials have a short optical absorption length (~ 1 μm), which has a number of effects relating to cost. Firstly the film thickness need only be of the order of a few μm, which greatly reduces the quantities of materials used. Secondly, the requirement for a long minority carrier diffusion length can be relaxed to some extent, which means that polycrystalline materials can be used, and the acceptable levels of impurities can be higher. Both of these factors allow a number of processing and production techniques to be used, which have been developed for a range of thin film applications [5]. These have potentially lower costs than the production methods used for single-crystal silicon.

By successively depositing different materials, heterojunction devices can be formed [2,5]. The uppermost layer of such a device is generally made of a wide band-gap material, which allows most of the spectrum to penetrate to the junction, where it can generate a current. For this reason, the top layer is known as a

window layer. The lower layer is made of a material which is chosen for its ability to absorb the solar spectrum and convert it efficiently into electricity. This layer is thus called the absorber layer. By using a suitable combination of materials for these two layers, it is possible in principle to fabricate devices with higher conversion efficiencies than for homojunction cells, such as those made of silicon.

The use of two different materials to form the heterojunction results in a large range of possible combinations, which can be used to form photovoltaic devices [5]. Two types of material used for absorber layers are the II-VI compounds, notably cadmium telluride, and the chalcopyrite semiconductors (I-III-VI_2), of which copper indium diselenide is an example. With both of these types of absorber layer, a window layer consisting of one or more II-VI materials is commonly used – zinc selenide and cadmium sulphide being examples. In some devices, an additional layer, known as a buffer layer, is added between the absorber and window layers. This is generally a II-VI semiconductor. The electrical losses due to crystal defects and impurities in these materials are generally less than for silicon and gallium arsenide. This allows useful efficiencies to be achieved with devices based on polycrystalline material.

Although there has been much development of cadmium telluride based solar cells, which has resulted in efficiencies up to 16.5 %, there is concern over the environmental and health hazards associated with cadmium compounds [6]. The chalcopyrite semiconductors avoid this particular hazard. Zinc compounds are being developed for use as window layers [6, 7]. These materials generally have wide bandgaps (3.7 eV for ZnS), and are thus transmissive over much of the solar spectrum, leading to potentially high efficiencies. In addition, they provide an

alternative to cadmium sulphide. In combination with a chalcopyrite absorber layer, the resulting photovoltaic devices are completely cadmium-free.

Much of the early development of chalcopyrite semiconductors focused on copper indium diselenide. Although the band gap of this material is 1.04 eV, which is considerably less than the optimum for the solar spectrum, photovoltaic devices have been produced with efficiencies up to 18.8 % [6]. In order to increase the band gap to a value closer to the optimum, the alloy copper indium gallium diselenide has been developed. Although a sufficient fraction of gallium can result in an optimum (or larger) band gap, such materials have high electrical resistances, and hence result in devices with low efficiencies. In practice, this limits the band gap of usable materials to 1.2 eV. Cells of this type have produced efficiencies up to 19.3 % [7].

Another chalcopyrite material, which has also been investigated for solar cells, is copper indium disulphide, which has a bandgap of 1.5 eV. As this is close to the optimum value for use with the solar spectrum, it has the potential for high efficiency (approx. 25 % for a minority carrier concentration of 10^{11} cm^{-3}) [2, 3]. Although this potential has not yet been fulfilled, efficiencies of 12.5 % have been achieved [8, 9]. As a ternary compound, the fabrication processes tend to be less complex, compared with those for quaternary alloys, such as copper indium gallium diselenide. This has the potential to reduce fabrication costs.

Copper indium disulphide has been deposited by a number of widely-used thin film deposition techniques. These include a number of vacuum-based techniques, such as thermal evaporation and sputtering. A number of non-vacuum techniques, such as electrodeposition, have also been developed. These have the advantages

of reduced capital cost, and generally reduced energy budgets, when compared to vacuum-based techniques.

In this work, copper indium disulphide and zinc sulphide have been investigated for application as the absorber and buffer layers respectively in photovoltaic devices. The production of copper indium disulphide involved two stages. In the first stage, a copper-indium alloy was deposited by sputtering. In many types of photovoltaic device fabrication, lateral variations in composition limit the area of the devices, which can be produced. Sputtering is used in a wide range of applications, to produce large area thin films of uniform composition, and may therefore have the potential to overcome these variations, which would allow devices of larger area to be produced.

Three alternative methods were investigated for the second stage – conversion to copper indium disulphide. The first two methods involved evaporation of sulphur. There are a number of factors, which limit the applicability of this method. Firstly, high substrate temperatures are often required, which necessitates the use of borosilicate glass [8]. Secondly, the evaporated sulphur tends to diffuse more strongly along the line of sight, leading to uneven deposition on large-area surfaces. Both of the evaporation techniques used in this work - enclosure of the substrate in a graphite box, and transfer of sulphur vapour in a flowing argon stream - addressed these issues. The use of lower substrate temperatures was investigated, allowing soda-lime glass to be used, with a potential cost saving, when applied on larger scales. The indirect diffusion of sulphur in each method overcomes the line-of-sight limitations, potentially allowing larger area devices to be fabricated.

The third method involved electrolytic conversion of the copper-indium alloy to copper indium disulphide. This is a non-vacuum technique, and in combination

with similar techniques for deposition of the remaining layers of the device, it offers the potential for developing a completely non-vacuum production sequence, with a consequent reduction in capital cost of equipment.

A commonly used material for window layers is cadmium sulphide, which has been produced by a number of techniques, including chemical bath deposition. This technique has previously been used for a range of materials [9, 10]. Therefore it can be used to produce a number of similar materials, which can directly substitute for cadmium sulphide, thus avoiding the health and environmental hazards associated with that material. These include a range of zinc compounds. However, it has been found that, when depositing zinc-based compounds, certain hazardous materials are required in the solution [6, 7]. In this work, an environmentally benign material has been substituted to perform the same function, and thus reduce the environmental and health hazards associated with the process.

Devices were also fabricated at Sri Venkateswara University, Tirupati, India, based on partially fabricated devices from Northumbria University.

This thesis presents:

1. A summary of the background theory of photovoltaic devices, with a focus on topics relevant to thin film devices.
2. A review of research, which has been done, on chalcopyrite-based cells, and copper indium disulphide cells in particular, focusing on the work most closely related to that presented in this thesis.
3. A description of the deposition techniques and analytical methods used during the experimental work in this research.
4. A presentation of the results of the experimental work, together with discussion of those results.
5. Conclusions derived from the results, and recommendations for future work.

2 Background Theory

2.1 Solar radiation

The total power output of the Sun is 4 x 10^{26} W, mostly in the form of electromagnetic radiation [1, 2]. The spectral distribution of this radiation is approximately that of a black body at 5800 K. The actual spectrum differs somewhat from this, due to emission from regions at different temperatures, line emission and absorption, etc.

As the Earth's atmosphere further modifies the incident radiation, solar cells in different locations (e.g. Earth's surface and space) are exposed to different spectral distributions. Therefore a number of standard spectra are defined, based on the depth of atmosphere penetrated [3, 4]. The spectrum just above the Earth's atmosphere is defined as AM0 (air mass zero). At the mean distance of the Earth from the Sun (1.5 x 10^8 km), the solar irradiance is 1368 Wm^{-2} [1]. This is known as the solar constant. The spectral distribution is essentially that emitted by the solar surface, scaled according to the inverse square law. After passage through the atmosphere, this is reduced in overall intensity due to absorption by ozone, water vapour, aerosols, etc. As absorption by ozone is particularly strong in the ultra-violet region of the spectrum, the average wavelength of the AM1 spectrum is slightly longer than for AM0.

Because the depth of atmosphere penetrated by solar radiation scales as $1/(\cos\theta)$, where θ is the angle from the zenith, additional spectra can be defined for different solar elevations [3, 4]. The spectral distribution at the Earth's surface when the Sun is directly overhead is denoted AM1. The AM2 spectrum is that incident at the Earth's surface when the Sun is at 60° from the zenith ($\cos\theta = 0.5$). The AM0 and AM1 spectra are shown in Fig. 2.1.

As well as absorbing radiation, some constituents of the atmosphere - notably aerosols - can scatter light. This does not reduce the total radiation reaching the Earth's surface, but does reduce the direct component. On this basis, solar spectra can be further differentiated. The global spectrum (eg; AM1.5G) includes light incident from all directions, and thus includes light scattered by aerosols, clouds, etc. The direct spectrum (eg; AM1.5D) includes only light directly from the Sun. The AM1D spectrum has a power density of 925 Wm^{-2}. For research in solar photovoltaics, the AM1.5 spectrum (adjusted to a total power density of 1 kWm^{-2}) is taken as typical of average conditions over the Earth's surface. As some of the scattering mechanisms (e.g. Rayleigh scattering) are wavelength dependent, the spectral distributions, as well as the total intensities, of the direct and global spectra will generally be different.

Flat panel solar cells can use both direct and scattered radiation, and thus the global spectrum is appropriate for evaluation of cell performance [4]. Cells incorporating concentrators can only use direct sunlight, and thus the direct spectrum must be used. Local climatic conditions will influence which type of solar collector system is used, and hence which spectrum is appropriate. For instance, in Northern Europe, there is a high frequency of cloud cover, and hence the diffuse component of the solar irradiance is relatively large. This would limit the usefulness of concentrators, and therefore flat panels are widely used. In desert areas, direct sunlight is available most of the time, and concentrators become a practical option.

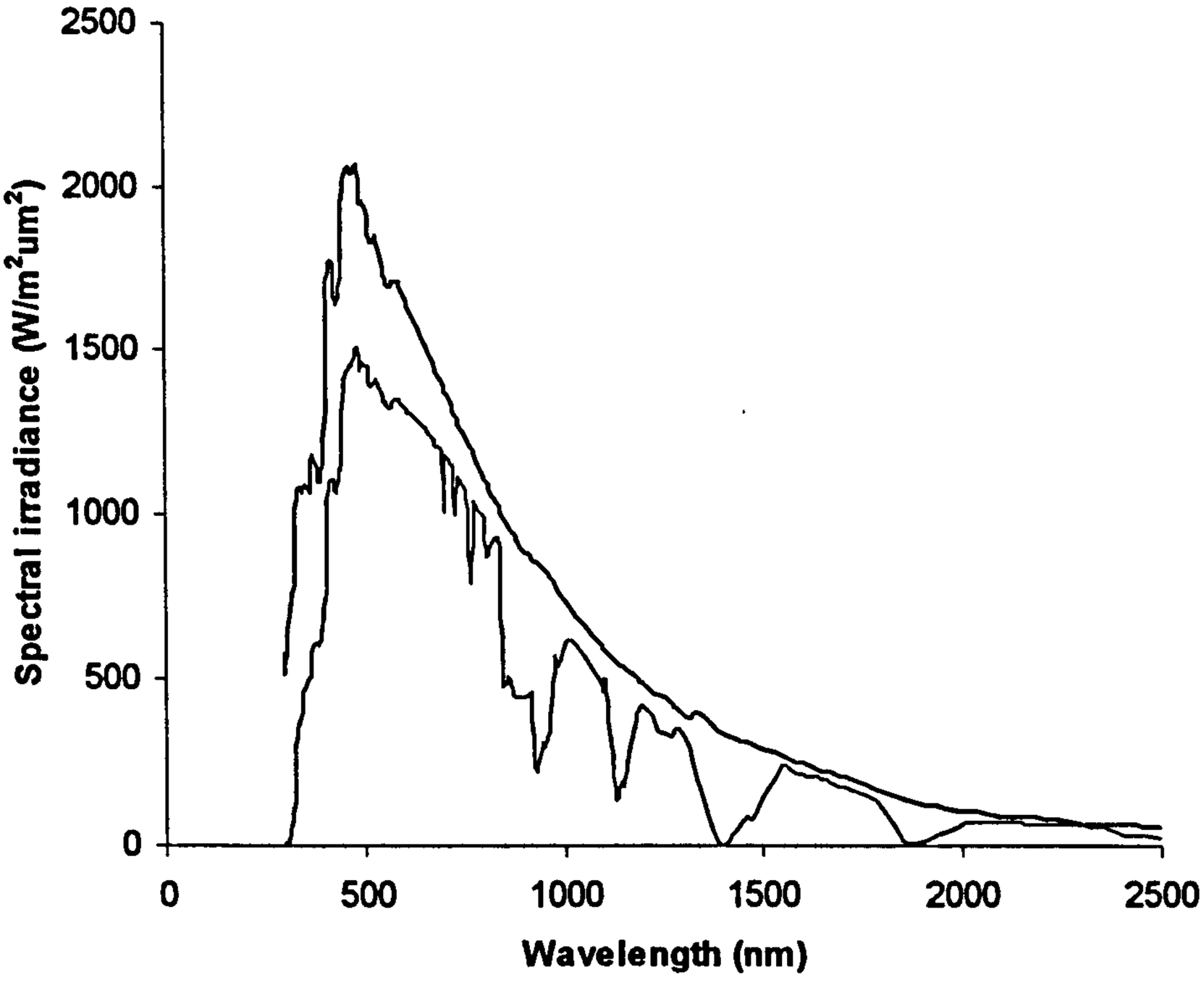

Figure 2.1. Standard solar spectra: Black – AM0 (outside Earth's atmosphere), Blue – AM1 (Earth's surface - vertical incidence)

2.2 Characteristics of solar cells

2.2.1 The homojunction solar cell

A photovoltaic cell is a large-area p-n junction, which generates electric power, when exposed to radiation [4, 5, 6]. An incident photon excites an electron from the valence band to the conduction band, creating an electron-hole pair. Electrons in the p-type region, and holes in the n-type region, constitute minority carriers, and in the regions remote from the junction, they quickly recombine with the ambient majority carriers. However, the electron-hole pairs, which form within the depletion region, or within a diffusion length of the edge of the depletion region, are separated by the electric field in this region. They thus result in a drift current in the device, flowing in the opposite direction to diffusion current, which constitutes essentially all of the forward current in the normal operation of a diode. This photo-generated current thus flows from negative to positive within the cell, and will therefore flow from positive to negative in an external circuit, delivering power to a load device.

A device in which the p-type and n-type regions are produced by doping of the same material is referred to as a homojunction. Silicon solar cells are of this type. The current-voltage characteristic for an ideal device is

$$I = I_0\left[\exp\left(\frac{qV}{\eta.kT}\right)-1\right] \qquad (2.1)$$

The factor η is called the ideality factor [5, 6]. If diffusion current is the dominant mechanism, η has a value of 1. Where recombination within the depletion region is the source of current, η has a value of 2. For practical devices, an intermediate value is applicable.

The photo-generated current adds to the normal diode current, as shown below.

$$I = I_0\left[\exp\left(\frac{qV}{\eta kT}\right)-1\right]-I_L \tag{2.2}$$

The photo-current I_L is defined by

$$I_L = g_{opt}qA\left(L_n + L_p + W\right) \tag{2.3}$$

g_{opt} = generation rate for electron-hole pairs (per unit volume)

A = (active) device area

L_p = hole diffusion length

L_n = electron diffusion length

W = depletion layer width

The value of g_{opt} is proportional to the flux of photons which have energy greater than the band gap of the material, and can thus excite electrons to the conduction band.

The current I_0 is the reverse bias saturation current, defined by

$$I_0 = A\left[\frac{qD_p}{L_pN_D}+\frac{qD_n}{L_nN_A}\right].\left[\exp\left(-\frac{E_g}{kT}\right)\right] \tag{2.4}$$

D_p = hole diffusion coefficient

D_n = electron diffusion coefficient

N_D = donor ion density

N_A = acceptor ion density

E_g = bandgap energy

The currents within the diode are shown in Figure 2.2, and the connection to an external circuit in Figure 2.3. Current-voltage (*I-V*) characteristics under illumination are shown in Figure 2.4.

The short circuit current is the device current when the output voltage is zero, and is equal (in magnitude) to the photo-generated current for an ideal diode.

$$I_{SC} = -I_L \tag{2.5}$$

It is thus proportional to the flux of photons in the incident spectrum, which have energy higher than the bandgap of the material.

The open circuit voltage is the voltage for which the output current is zero. This occurs when the diffusion current flowing in one direction is equal in magnitude to the photo-generated current flowing in the opposite direction. Its value can be calculated as shown below.

$$I_0\left[\exp\left(\frac{qV}{\eta kT}\right)-1\right] \approx I_0\left[\exp\left(\frac{qV}{\eta kT}\right)\right] = I_L \tag{2.6}$$

$$V = V_{OC} \equiv \frac{\eta kT}{q}\ln\left(\frac{I_L}{I_0}\right) \tag{2.7}$$

From this equation, it can be seen that V_{oc} increases logarithmically with I_{sc}, and hence with the incident irradiance. This difference in scaling between I_{sc} and V_{oc} is reflected in the output currents and voltages of operating devices, and this must be considered when connecting to load circuit.

Both the short circuit current and open circuit voltage are important parameters in the performance of solar cells, and are thus contributory factors to the conversion efficiency.

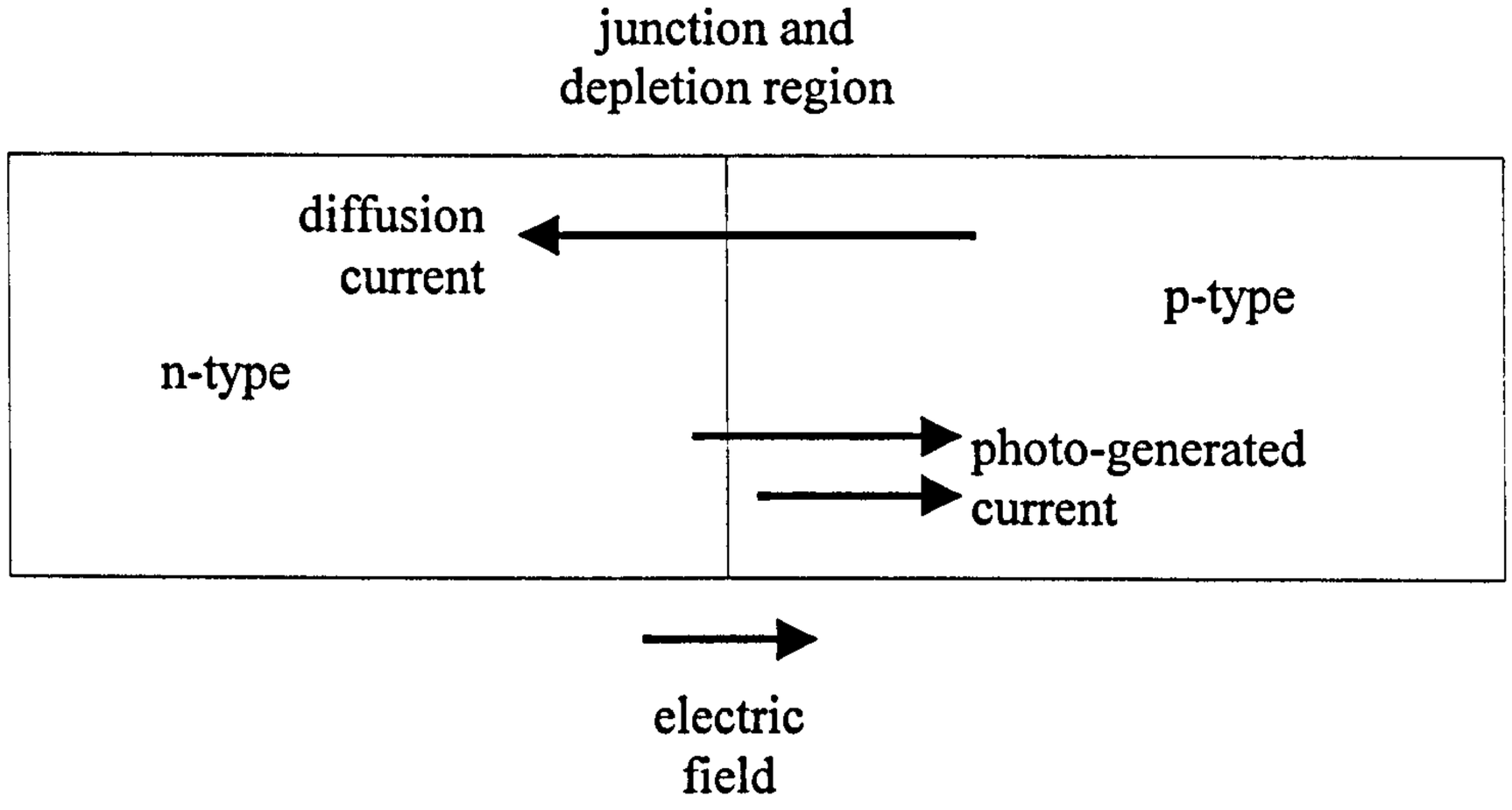

Figure 2.2. Photo-generated (drift) current and forward (diffusion) current within a photovoltaic device. Each of the currents shown consists of hole flow in the direction of the arrow, and electron flow in the opposite direction.

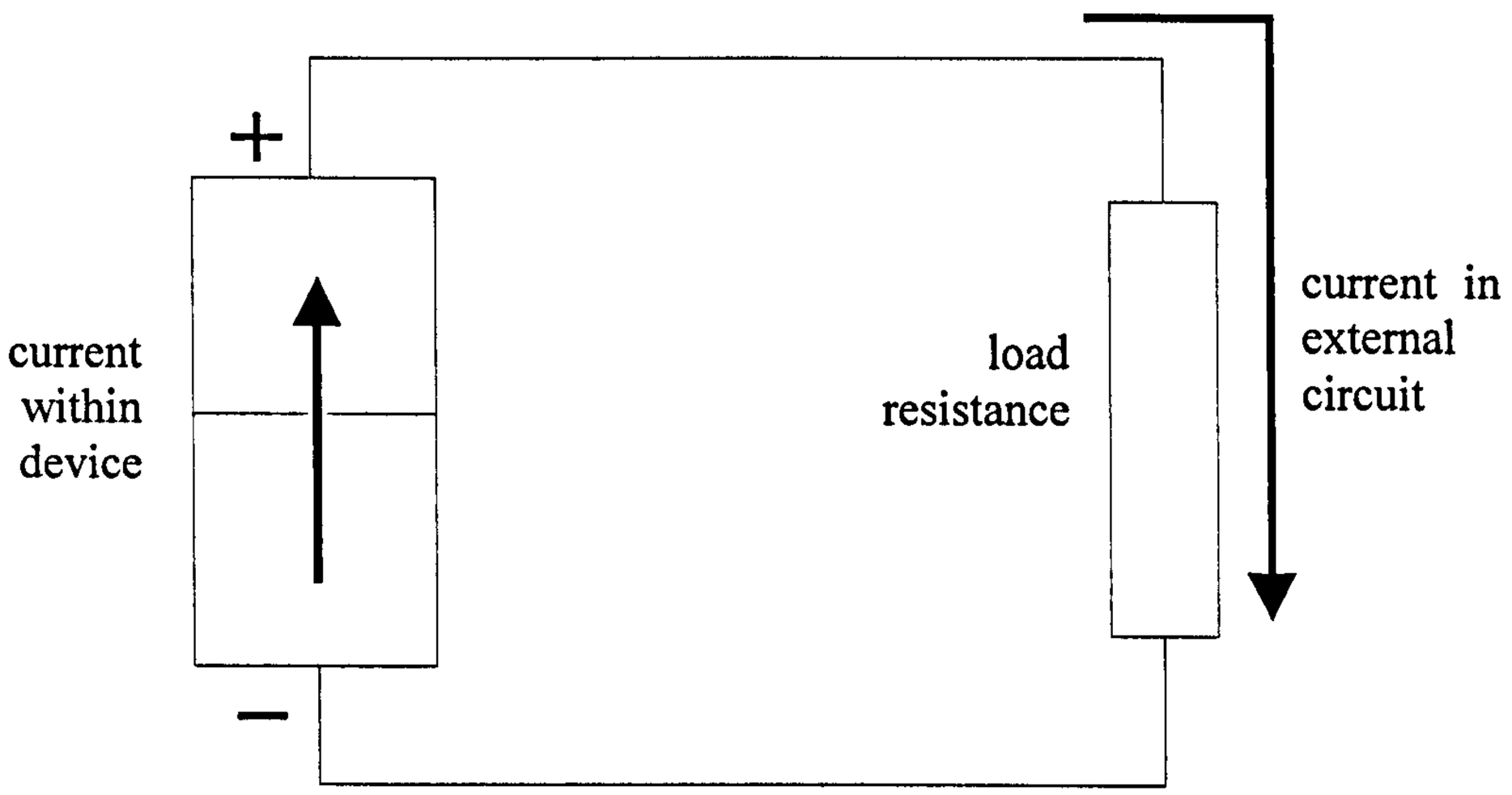

Figure 2.3. Internal current from negative to positive within the photovoltaic cell, producing a current from positive to negative in the external circuit, thus delivering power to the load.

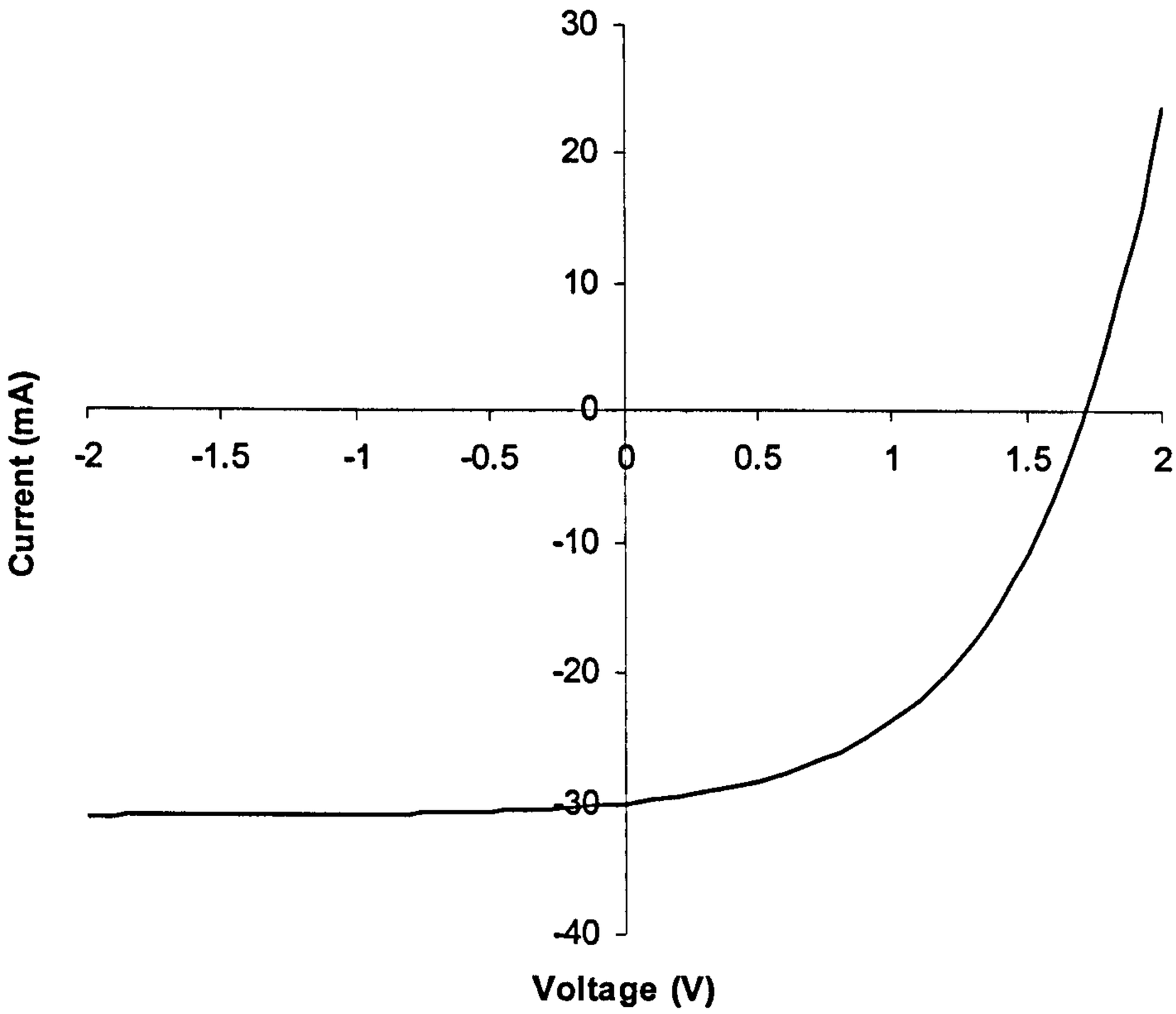

Figure 2.4. *I-V* characteristic for an ideal solar cell under illumination.

2.2.2 Heterojunction solar cells

A device formed from the junction of two different materials is known as a heterojunction [7, 8, 9]. By using materials of different band gaps, there is more flexibility in the properties of the junction. Heterojunction devices are used in the electronics industry, particularly for high-speed devices [9]. They are also used in a variety of types of solar cell, where they confer a number of advantages specific to this application [4,10]. These are considered in more detail in the following sections, where the structure of a solar cell, and the function of each of its components, are described.

Each material has its own set of energy levels, with generally different band gaps and work functions. For the purpose of analysis, the junction can be considered as being formed by bringing layers of the two materials into contact. Initially, the vacuum levels are equal. Due to the differences in work function, etc, the other energy levels differ from one material to the other, as shown in Figure 2.5a. The energy difference between the Fermi level and the bottom of the conduction band is different for each material, and results in different electron concentrations in the conduction band. (In Figure 2.5a, it is higher for material 1.) This results in a diffusion current (from material 1 to material 2, in this case). For the energy levels shown, there will also be a hole diffusion current from material 2 to material 1. These currents produce a space charge on either side of the junction, which results in an electric field, and hence a voltage, across the junction (Fig. 2.5b). Equilibrium is established when the drift current due to this field equals the diffusion current, at which point the Fermi levels are equal on both sides of the junction. This results in a relative displacement of the energy levels. (This is an example of the Anderson band-diagram, in the limit of the abrupt junction.)

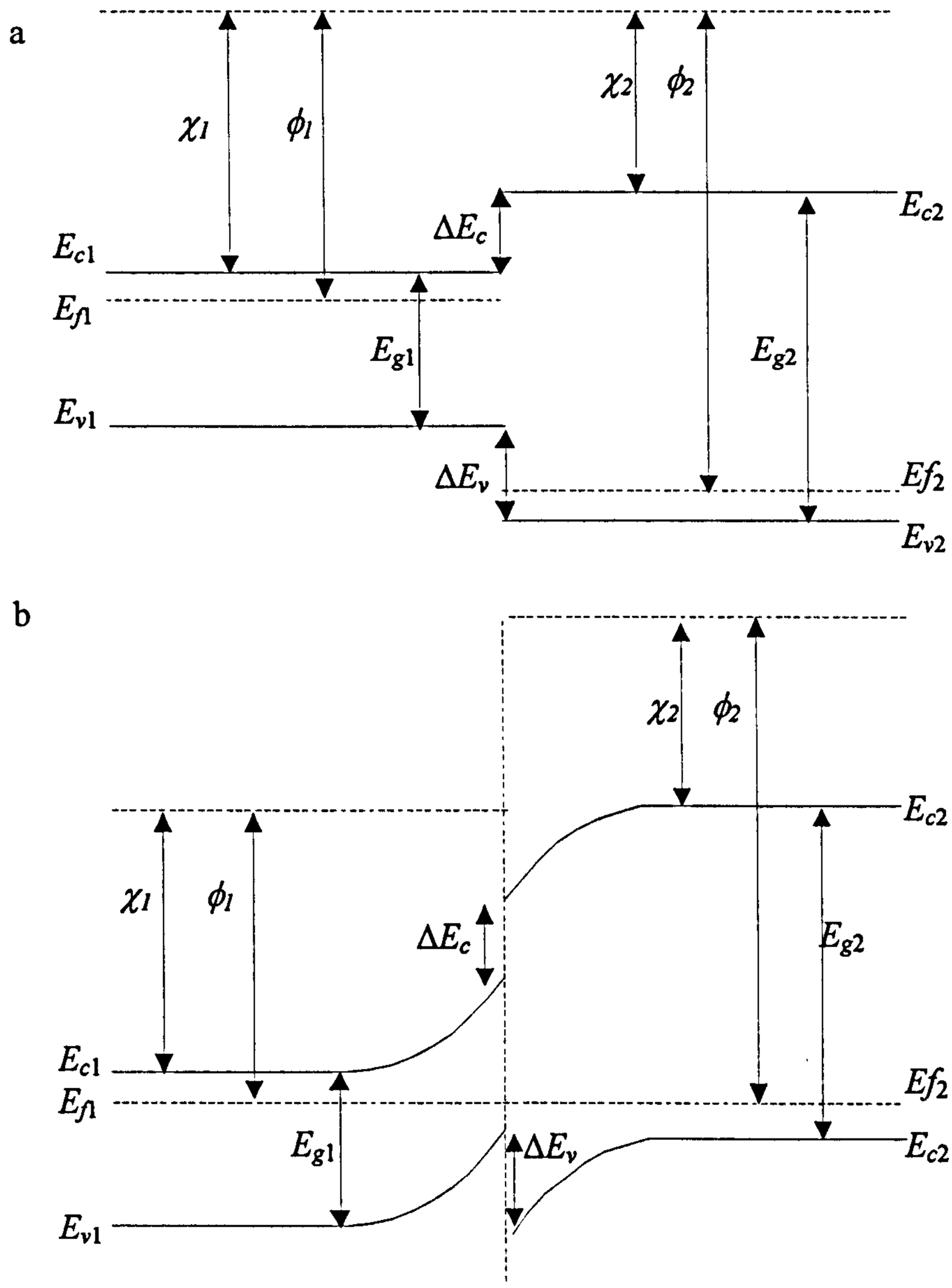

Figure 2.5 Energy levels in a typical heterojunction. For each material -

χ = electron affinity ϕ = work function

E_c = base of conduction band E_v = top of valence band

E_f = Fermi level

The voltage is continuous across the junction, and therefore, so is the displacement of the energy levels from their initial values. Thus, any discontinuities initially present at the junction are preserved in the displaced levels. If the difference in the tops of the valence bands (ΔE_v) is in the opposite sense to the initial difference in Fermi levels (ΔE_f), there will be a spike in the valence band (as shown in Figure 2.5), and similarly for the conduction band. Such a spike acts as a barrier to electrical conduction - a small current can flow due to quantum tunnelling. To maximise conduction, combinations of materials are chosen, with energy levels (work functions) such that spikes are avoided.

A number of models have been constructed to describe the electrical behaviour of heterojunctions. The Anderson Model is based on diffusion currents and extends much of the theory of homojunctions to the case for two different materials, each with its own set of electrical properties [11]. A number of other processes were added to this in later models. The Pearlman-Feucht model includes the effects of thermionic emission of electrons over an energy level spike [12]. The effects of quantum tunnelling through a spike is described in the model by Rediker, Stopek and Ward [13]. Riben and Feucht, and Donnelly and Milnes have developed models that incorporate the possibility of tunnelling to recombination centres at the interface [14, 15]. These various mechanisms have been synthesised into a single model. The current density is given by

$$J = J_{00} \exp\left(-\frac{\phi}{kT}\right)\left[\exp\left(\frac{qV}{\eta kT}\right)-1\right] \qquad (2.8)$$

The current J_{00} and the activation energy ϕ are constants, which incorporate the various mechanisms described above. The term η is the ideality factor, and is analogous to that for a homojunction.

2.3 Structure of a photovoltaic device

The functional core of a photovoltaic device is the p-n junction between two semiconductor regions. In order to produce an operational device, additional layers must be added, to deliver electrical energy from the junction to an external circuit, while still allowing radiation to be transmitted to the junction. A model of a photovoltaic device is shown in Figure 2.6, including components which are common to many types of devices [4].

In order to reach the junction, light must be transmitted through the overlying semiconductor. (In a heterojunction, this is a distinct material layer.) Because many semiconductors have high refractive indices, a large fraction of the light may be reflected from the front surface. An anti-reflection layer may be deposited on this surface to reduce such losses [4, 16, 17].

Electrical contacts are made to the junction, so that it forms a diode, which can be connected to an external circuit. As the back contact is below the junction, light is not required to pass through it, and a layer of metal or semiconductor can be used [18, 19].

However, the front contact must allow light to pass, and reach the junction, as well as providing electrical connection. A grid of narrow metal contacts (called fingers) is placed on top of the semiconductor [4, 20, 21]. Current generated at the junction is conducted through the overlying semiconductor layer to the nearest metal finger, and then to the external circuit.

In each stage of the flow of energy, a fraction is transmitted to the next stage - contributing to efficiency - and the remainder is lost. These stages are

1. Optical transmittance
2. Optical to electrical conversion
3. Electrical performance

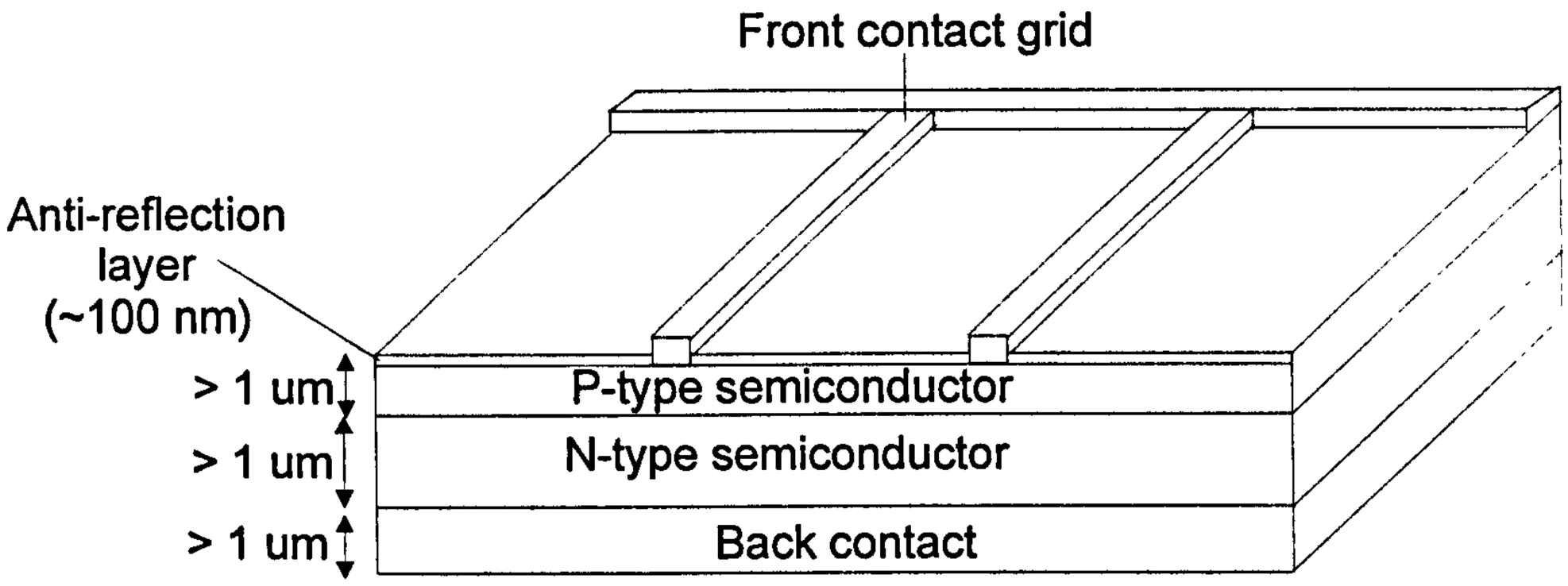

Figure 2.6 Structure of a generalised solar cell. In this example, the upper semiconductor layer is p-type. Cells can also be fabricated with the n-type layer uppermost.

2.4 Optical performance and losses

Radiation may be prevented from reaching the junction, because of a number of mechanisms

- Reflection from the front surface
- Obstruction by the metal front contact grid
- Absorption within the region of semiconductor above the junction

A number of design choices, including material selection, can reduce these losses, and hence improve optical performance.

2.4.1 Anti-reflection coatings

Light is reflected at the boundary between two optical media of different refractive indices, due to Fresnel reflection [22]. For light incident normally on the surface, this is

$$R = \left(\frac{n_1 - n_2}{n_1 + n_2} \right)^2 \tag{2.9}$$

n_1 = refractive index of semiconductor

n_2 = refractive index of air = 1

For silicon, the refractive index is 3.7, giving a reflectance of 33.5 % [23]. For light incident at an oblique angle, the reflectance is even higher, reducing optical efficiency still further.

An anti-reflection coating is a thin film of material with a refractive index intermediate between that of the semiconductor and that of the air. If the film thickness is a quarter of the wavelength of the incident light, the optical path difference for light reflected at the air/film interface and the film/semiconductor interface is half a wavelength. This results in destructive interference between the two reflected components, which greatly reduces the reflectance.

Because destructive interference depends on the ratio of optical path difference to wavelength, it has two limitations.

- It is wavelength dependent. For light at a wavelength other than the design wavelength, the optical path difference is not half a wavelength. In general, destructive interference is not total, and the reflectance remains high. For broadband radiation, such as the solar spectrum, reflectance will be reduced or eliminated for some wavelengths but not others. The film thickness is generally chosen to give minimum reflectance at the peak of the solar spectrum (~ 500 nm).
- It is angle dependent. The optical path length in the film is $2d/\cos\theta$. As the relative position of the Sun changes during the day, the reflectance will change. Although this means that destructive interference, and hence reduced reflectance, will now occur at another wavelength, for large angles this will generally be at a wavelength where the solar spectral irradiance is much lower.

Despite these limitations, anti-reflection coatings produce a useful increase in optical performance, and are widely used in solar cells [4, 16, 17].

2.4.2 Obstruction of light by the contact grid

The contact grid occupies a fraction of the area of the device, and obstructs the same fraction of the incident light. Increasing the finger spacing or decreasing the finger thickness reduces the fractional area of the grid. However, as will be shown later, this increases the electrical resistance, and hence the electrical component of the efficiency.

A number of surface topologies have been investigated, to overcome this limitation [4, 20, 21]. For instance, contact fingers with triangular cross sections have sloping sides, which reflect incident light onto other parts of the junction.

2.4.3 Window layers and optical absorption

A photon which has an energy greater than the band gap of the semiconductor will generate an electron-hole pair. In a homojunction, a photon which has sufficient energy to be absorbed in the depletion region can also be absorbed in the overlying semiconductor material. If this occurs more than a recombination length from the depletion region, the minority carrier will recombine with ambient majority carriers, and will not contribute to the device current. However, the photon has been absorbed and cannot therefore reach the junction.

In a heterojunction, the band gaps of the two semiconductors can be selected independently. Each can be chosen to optimise the function of the layer, which it forms. One of the functions of the layer overlying the junction is to transmit light to the junction. Photons with energies less than the band gap cannot generate electron-hole pairs, and are not readily absorbed.

For a photon with an energy equal to the band gap, the wavelength is

$$\lambda = \frac{hc}{E_g} \tag{2.10}$$

Evaluation of the constants gives

$$\lambda\,(\mu\text{m}) = 1.24/E_g\,(\text{eV}) \tag{2.11}$$

Photons with larger energies (shorter wavelengths) are largely absorbed, whereas photons with lower energies (longer wavelengths) are mostly transmitted. For this reason, the wavelength ($1.24/E_g$) is called the cut-off wavelength. A graph of spectral transmittance is shown in Figure 2.7.

In a heterojunction device, the top semiconductor layer is selected to have a wide band gap, to be transmissive over as large a wavelength range as possible. Because of its high transmittance, this layer is called the window layer.

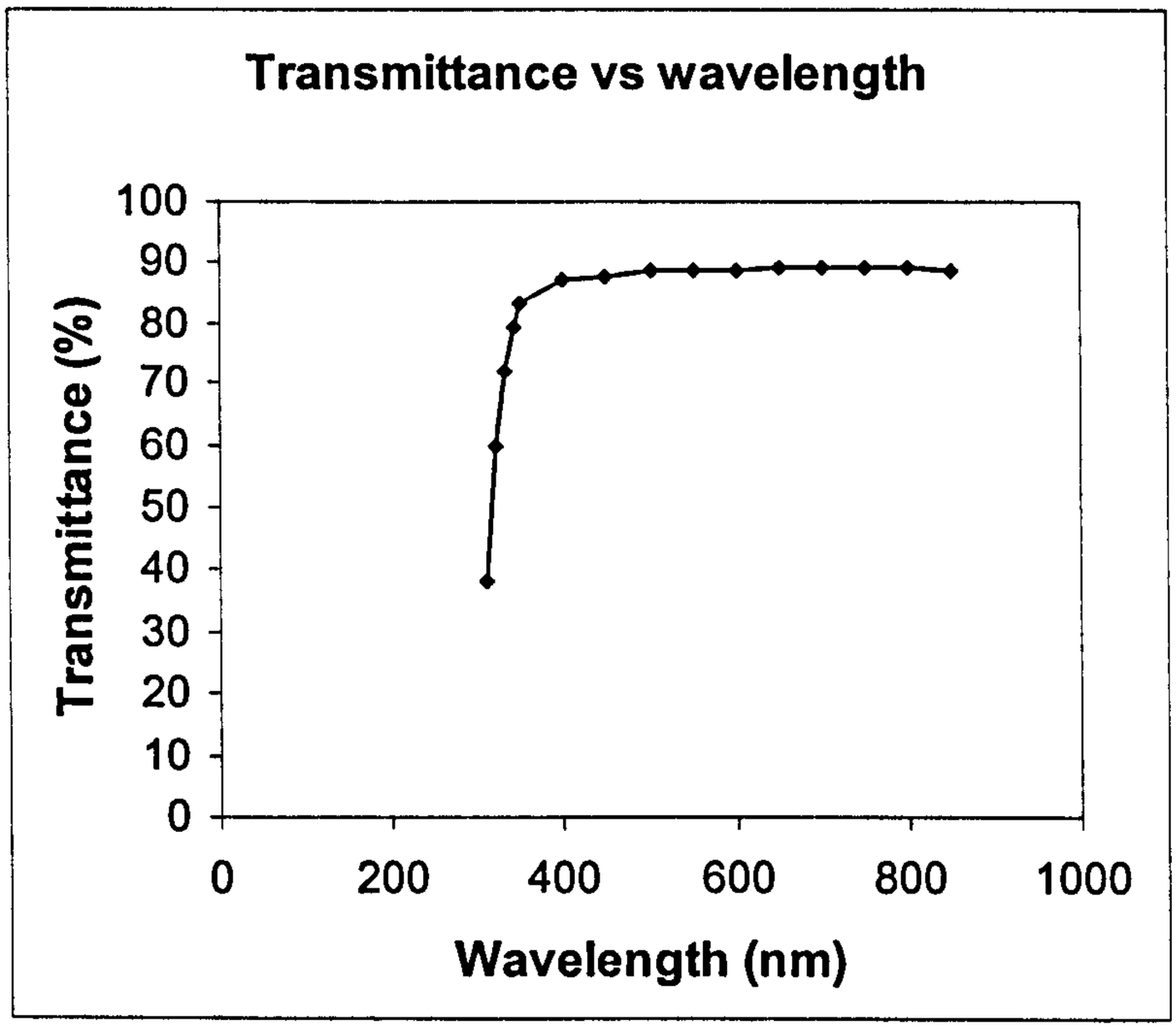

Figure 2.7 Spectral transmittance of a semiconductor with a direct energy band-gap of 3.7 eV (e.g. zinc sulphide), giving a cut-off wavelength of 330 nm.

Typical window layer materials include zinc sulphide (ZnS, E_g = 3.7 eV, λ_{co} = 330 nm), and cadmium sulphide (CdS, E_g = 2.42 eV, λ_{co} = 512 nm) [4, 10, 24, 25]. The cut-off wavelength of ZnS is in the ultra-violet part of the spectrum, and this material is transmissive over substantially all of the solar spectrum. For this reason, this and similar materials, have been developed for use as window layers.

The solar radiation reaching the junction is given by [4].

$$\Phi_J = \int_0^\infty \Phi(\lambda).T(\lambda).d\lambda \tag{2.12}$$

This can be given as a fraction of the incident spectrum, and thus forms a component of the optical efficiency.

$$\text{Fraction transmitted} = \frac{\int_0^\infty \Phi(\lambda).T(\lambda).d\lambda}{\int_0^\infty \Phi(\lambda).d\lambda} = \frac{\int_0^\infty \Phi(\lambda).T(\lambda).d\lambda}{\Phi_{AMn}} \tag{2.13}$$

2.4.4 Total optical efficiency

Combining losses due to Fresnel reflection from the front surface, obstruction by the front contact grid, and absorption in the window layer allows the overall optical efficiency to be calculated.

$$\eta_{opt} \equiv \frac{P_{J,opt}}{P_{incid}} = (1-R)(1-f_G)\frac{\int_0^\infty \Phi(\lambda).T(\lambda).d\lambda}{\Phi_{AMn}} \tag{2.14}$$

f_G = fractional area of grid

This is the fraction of the incident optical energy reaching the junction. The fraction of this, which can be converted to electrical energy, is considered in the next section.

2.5 Optical to electrical conversion

Photons which reach the junction, and the depletion region, generate electron-hole pairs, which can potentially deliver electrical power to an external circuit. However, only a fraction of the photon energy is converted to the energy of the electron-hole pair, and this depends on the photon energy relative to the band gap. Thus selection of material, and hence band gap, is important in maximising efficiency [4].

Photons with an energy less than the band gap do not generate electron-hole pairs. Therefore, the generation rate is determined by the flux of photons with an energy higher than this. The rate of generation of electron-hole pairs is related to the incident spectrum and the band gap, as shown below.

$$R_{eh} \propto \int_{E_g}^{\infty} F(E)dE \qquad (2.15)$$

$F(E)$ = photon flux (number) at energy E

Neglecting losses due to recombination, which will be considered later, the photo-generated current is given by

$$I_{gen} = qR_{eh} \qquad (2.16)$$

If the band-gap energy is low, compared to the average photon energy in the incident spectrum, most photons will generate electron-hole pairs, and the current will be high.

If a photon with an energy higher than the band gap is absorbed, the electron is excited to a level well above the base of the conduction band. However, it then relaxes to this base level, as shown in Figure 2.8. The electrical energy, neglecting other losses, is E_g, the remainder ($h\nu$ - E_g) being lost to the semiconductor lattice as heat.

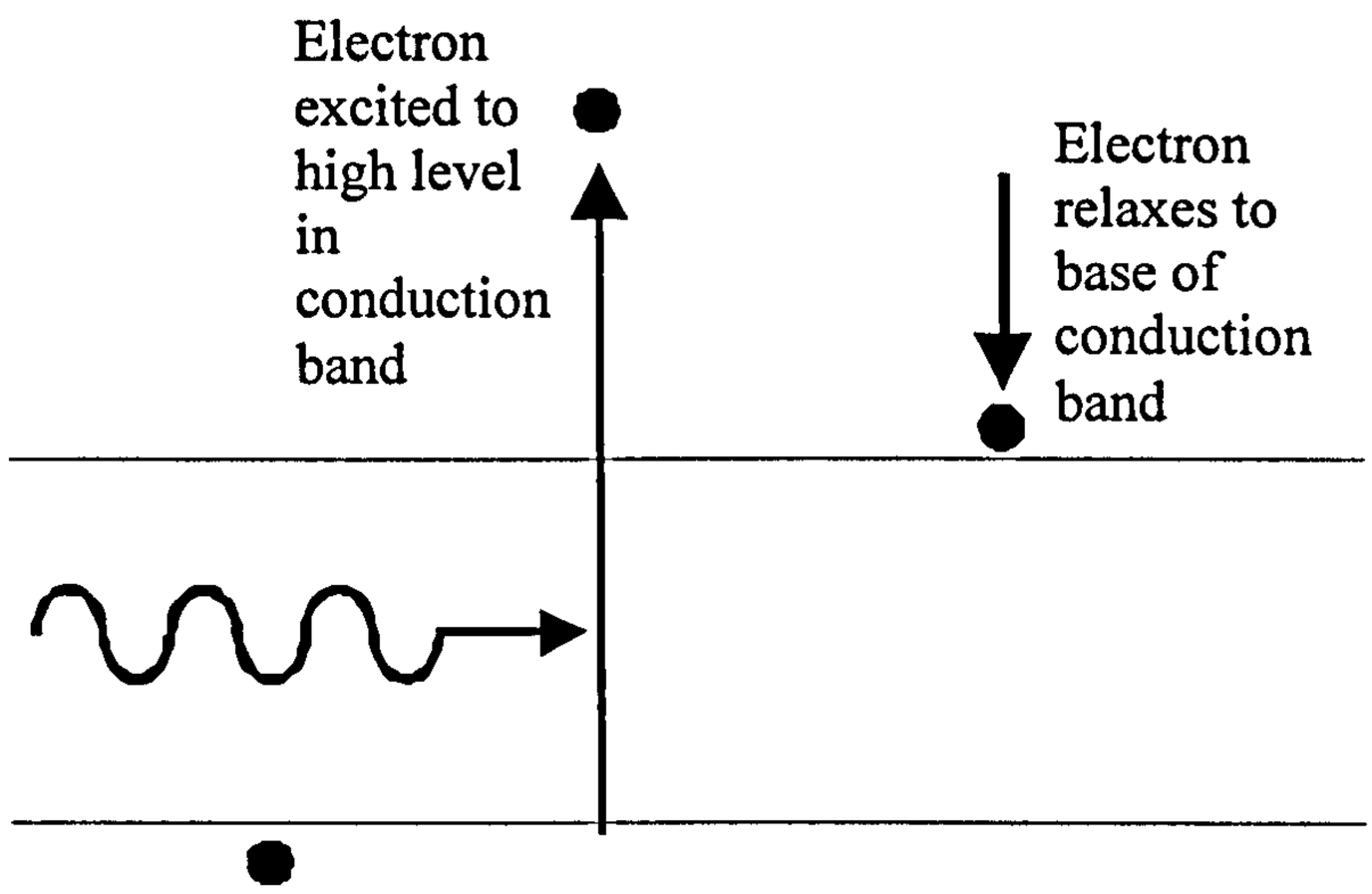

Figure 2.8 Absorption of a photon to create an electron-hole pair, and subsequent relaxation to the base of the conduction band

The voltage, which could potentially be developed, is

$$V_g = E_g / e \tag{2.17}$$

(Losses, which are considered later, reduce the output voltage below this level.)

Combined with the photo-generated current, this gives an electrical power of

$$P = I_{gen} V_g \tag{2.18}$$

The ultimate efficiency, η_{UE}, is defined as the ratio of this power to the optical power absorbed at the junction [26].

$$\eta_{UE} = \frac{I_{gen} V_g}{P_{J,opt}} = \frac{\left[e \int_{E_g}^{\infty} F(E).dE \right] . \left[\frac{E_g}{e} \right]}{P_{J,opt}} \tag{2.19}$$

The value of this factor depends on the band gap, and hence the material selected. If the band gap is low, the photo-generated current is large, but the voltage is small, leading to low electrical power and efficiency. Conversely, if the band gap is high, the open circuit voltage will be high, but the current will be low, again resulting in low output power. For some intermediate value of band-gap energy, the product $P = I_{gen} V_g$ will be a maximum. For the solar spectrum, the optimum energy is approx. 1.4 eV, as shown in Figure 2.9 [4, 5, 6]. This maximises the level of photogenerated power, and hence conversion efficiency, for a given spectrum. This is then used either to select a material with a band-gap approximately equal to this value, or to adjust the composition of an alloy to have the optimum band-gap energy exactly.

In a heterojunction device, photon absorption occurs in the lower semiconductor layer - in or near the depletion region. As the function of this layer is to absorb photons, it is called the absorber layer. The band gap of this material can be selected independently of that of the window layer.

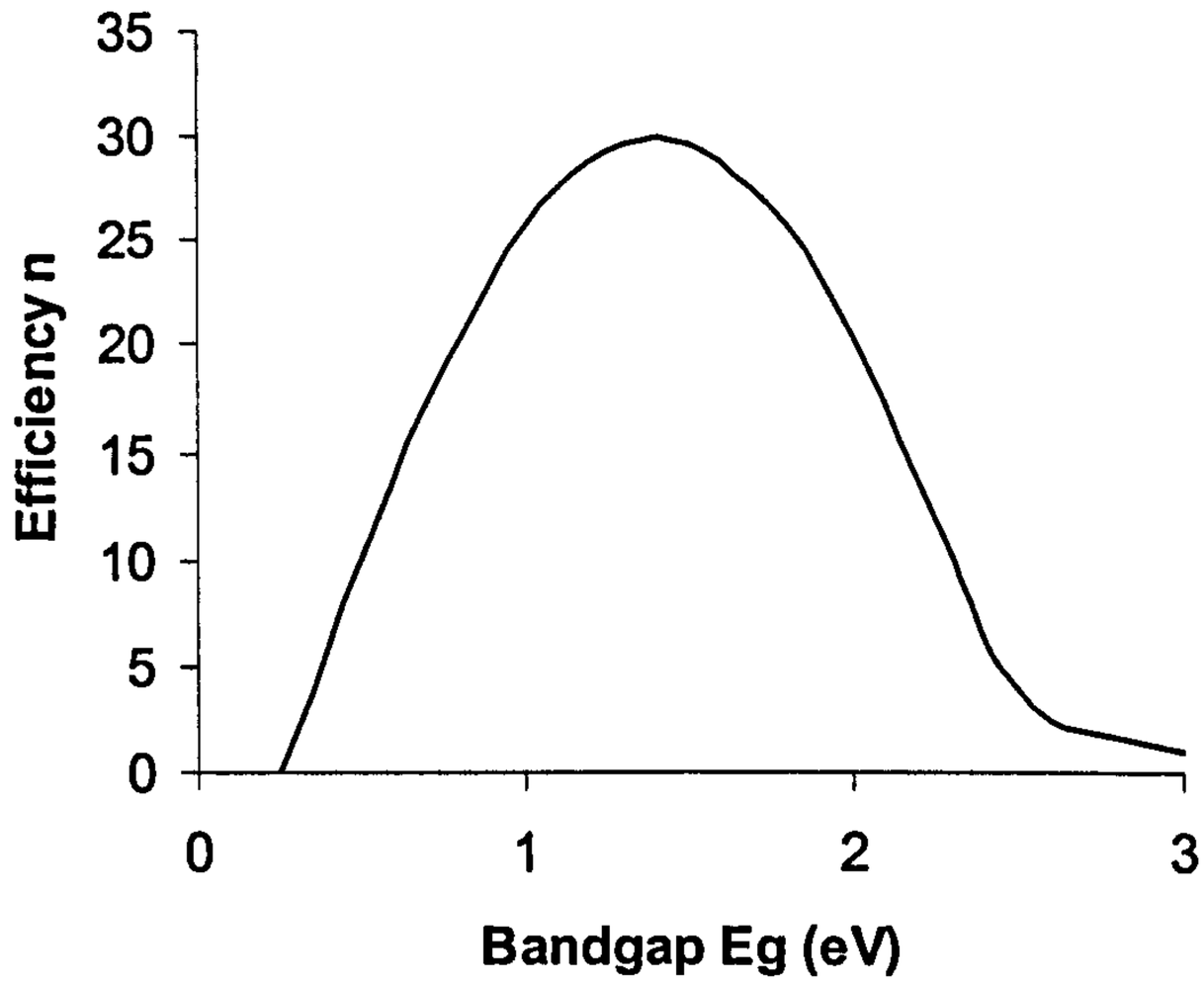

Figure 2.9 Ultimate efficiency vs. band gap, showing a maximum for the solar spectrum at $E_g \approx 1.4$ eV.

The effects of wavelength-dependent absorption in the window layer and wavelength-dependent conversion in the absorber layer can be combined in the spectral quantum efficiency. This is the ratio of electron-hole pair generation to photon (number) flux, at a given wavelength (or energy). The processes occurring in each wavelength region are shown in Figure 2.10. The resulting spectral quantum efficiency is shown in Figure 2.11.

At short wavelengths - $\lambda < hc/E_{g(\text{window})}$ - photons are absorbed in the window layer. In practice, a small fraction of the light in this region is transmitted, and the transmittance does not reduce to zero precisely at the cut-off wavelength. In the intermediate region - $hc/E_{g(\text{window})} < \lambda < hc/E_{g(\text{absorber})}$ - photons generate electron-hole pairs. Due to electrical losses (to be considered in the next section), not all the photo-generated electrons are available at the output, and the quantum efficiency in this region is slightly less than unity.

The previous discussion on the optimum band gap for the absorber layer was based on this layer in isolation. The band gap of the window layer may have a modifying effect. If the band gap of this layer is only slightly higher than the optimum for the absorber layer, only a narrow region of the spectrum generates electrical energy. The ultimate efficiency is then calculated by integrating over the spectrum between the two band gap energies

$$\eta_{UE} = \frac{I_{gen} V_g}{P_{J,opt}} = \frac{\left[e \int_{E_g(absorber)}^{E_g(window)} F(E).dE \right] \left[\frac{E_g}{e} \right]}{P_{J,opt}} \qquad (2.20)$$

It may be necessary to reduce the band gap of the absorber layer (by selecting a different material, or adjusting the composition of an alloy), so that photo-generation occurs over a wider wavelength region. This would increase efficiency, despite the lower voltage obtainable. (For window layer materials such as ZnO or ZnS, the band gap is so high that this effect is negligible.)

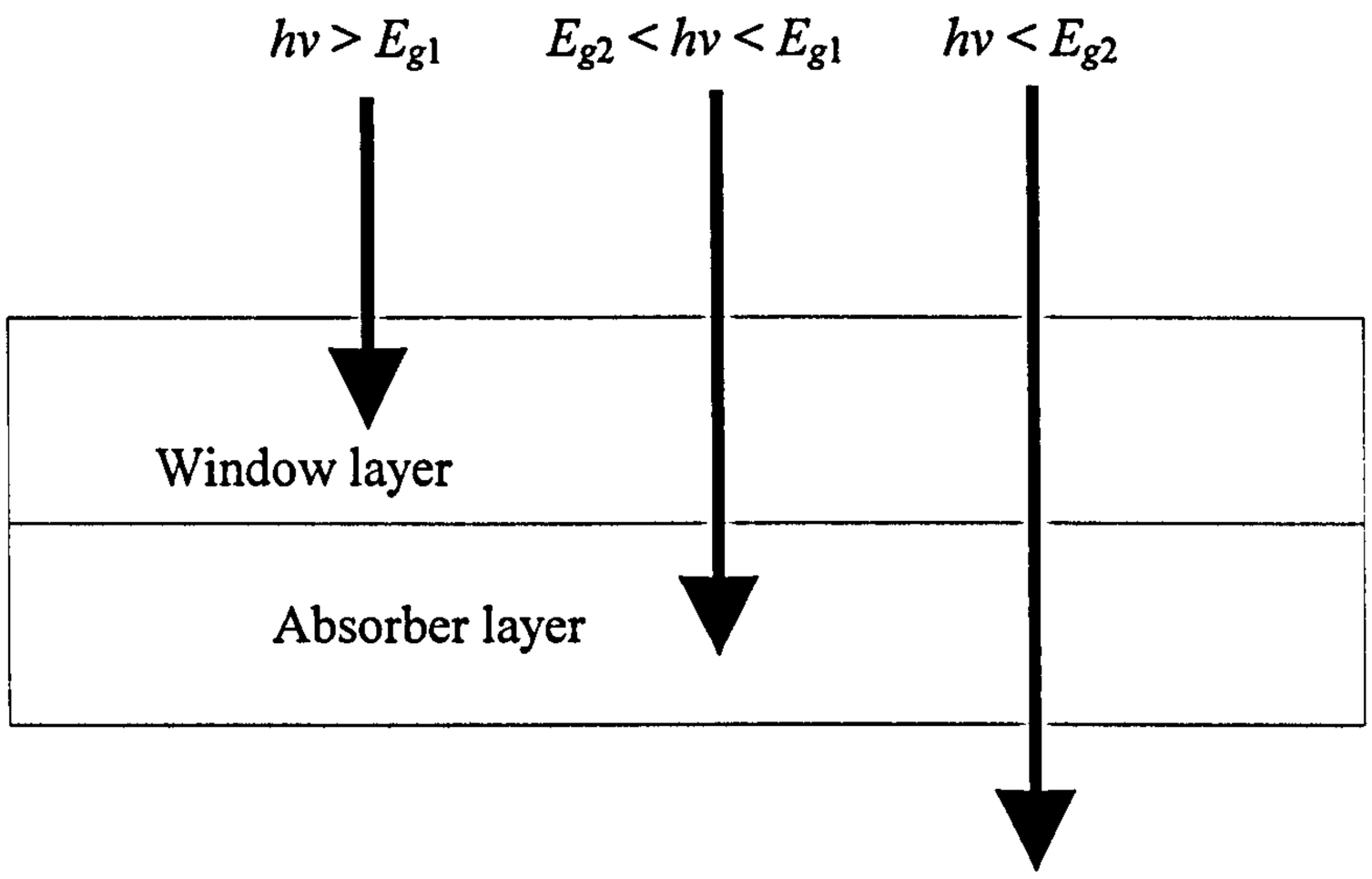

Figure 2.10 Absorption of photons in the different regions of a heterojunction.

(E_{g1} = energy band gap of window layer; E_{g2} = energy band gap of absorber layer)

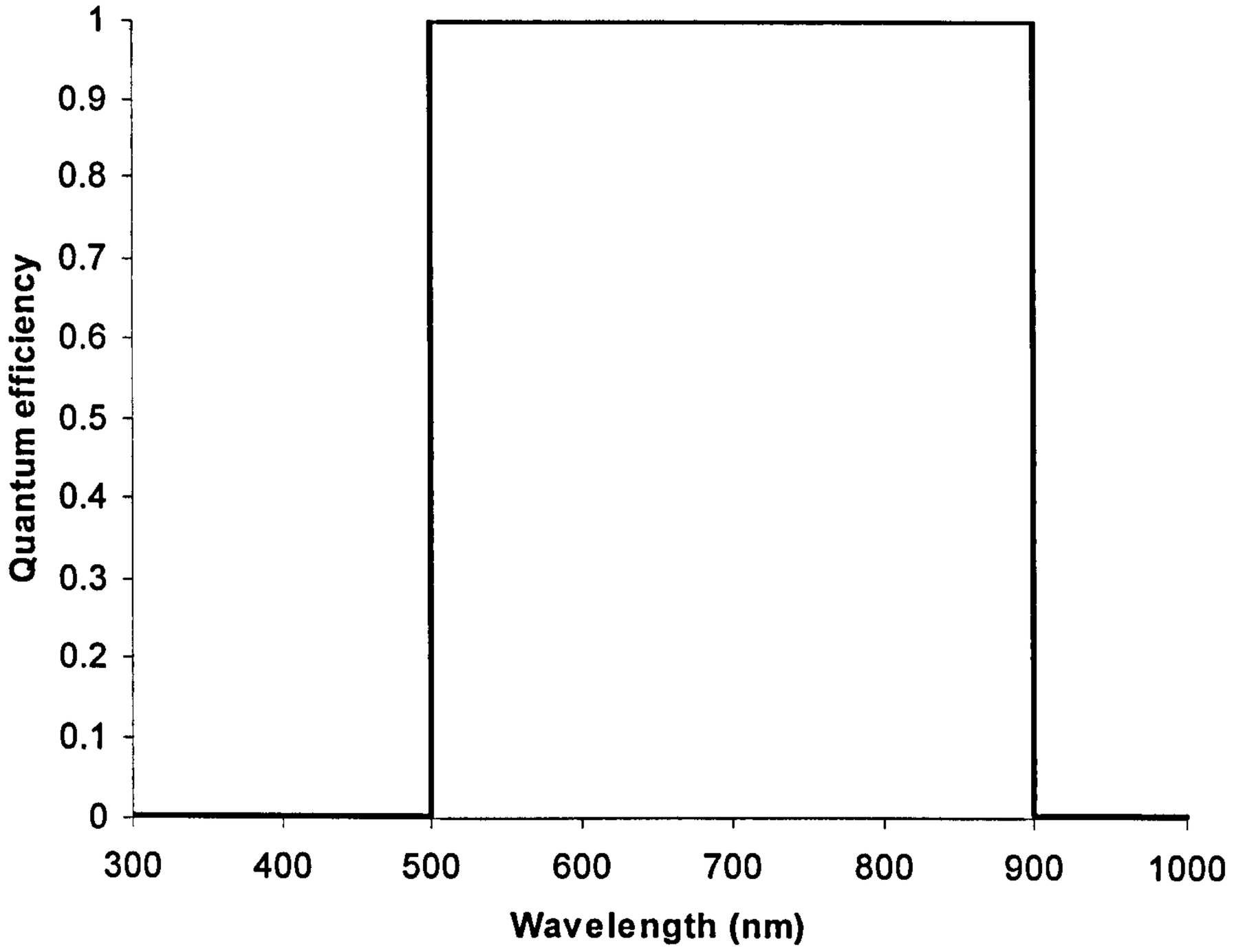

Figure 2.11. Spectral quantum efficiencies of an ideal heterojunction solar cells, showing cut-off at the band-gap energies of the window layer (E_g = 2.48 eV) and absorber layer (E_g = 1.38 eV).

2.6 Electrical Performance

A number of loss mechanisms reduce the actual electrical power below that which is potentially available from electron-hole pair generation. These include

- Current loss due to recombination
- Voltage loss due to shifts in Fermi levels
- Operation at voltage and current less than V_{oc} and I_{sc}.
- Resistance in the semiconductor materials, and the interfaces between them

Each of these is now considered

2.6.1 Recombination

When an electron-hole pair is generated in a p-type region, the electron is a minority carrier, and may recombine with a hole, which is a majority carrier in this region. Similarly, in an n-type region, a photo-generated hole may recombine with an ambient electron. Lattice defects and impurities can act as centres for recombination, thus increasing the rate.

In the depletion region, the reduced charge carrier densities reduce the rate of recombination. Outside this region, the charge density remains high, and recombination readily occurs. However, if an electron-hole pair is generated just outside the depletion region, the minority carrier may diffuse into the depletion region. (It is then carried across the junction by the field due to the space charge. As it is now a majority carrier, recombination is much less probable, and the charge contributes to the output current.)

In order to reduce recombination, photons should be absorbed as close to the depletion region as possible, and the distance they can travel before recombining should be less than this.

optical absorption length < recombination length

Figure 2.12 shows the relative effects of recombination, for the case where the optical path length is longer than the recombination length, and for the case where it is shorter.

Scattering of charge carriers folds the path over which they travel, so that the resultant distance travelled is much less than the actual path length. This reduces the recombination length. Lattice defects and impurities can act as scattering centres, resulting in a reduction of recombination length, in addition to their direct effect as recombination centres.

Recombination is responsible for the spectral quantum efficiency being less than unity, in the intermediate wavelength range, as noted in the previous section. In practice, spectral quantum efficiencies of more than 0.9 have been achieved [10].

For indirect band gap semiconductors, such as silicon, the optical charge generation rate is low, giving a low optical absorption coefficient for the material. This results in a long optical path length. In order to produce a recombination length, which is longer than this, lattice defects and impurities must be kept to a minimum. For this reason, silicon solar cells are often made from high purity single crystals. An alternative method is to produce light trapping in the material. Scattering of photons results in folding of the optical path, so that absorption occurs nearer the depletion region, thus reducing the distance over which recombination occurs.

Many of the compound semiconductors used in solar cells are direct band gap materials [4, 10]. The higher optical absorption coefficients result in a shorter optical absorption length. In a heterojunction device, the absorber layer material can be selected to have a high optical absorption coefficient, in addition to having an optimum band gap.

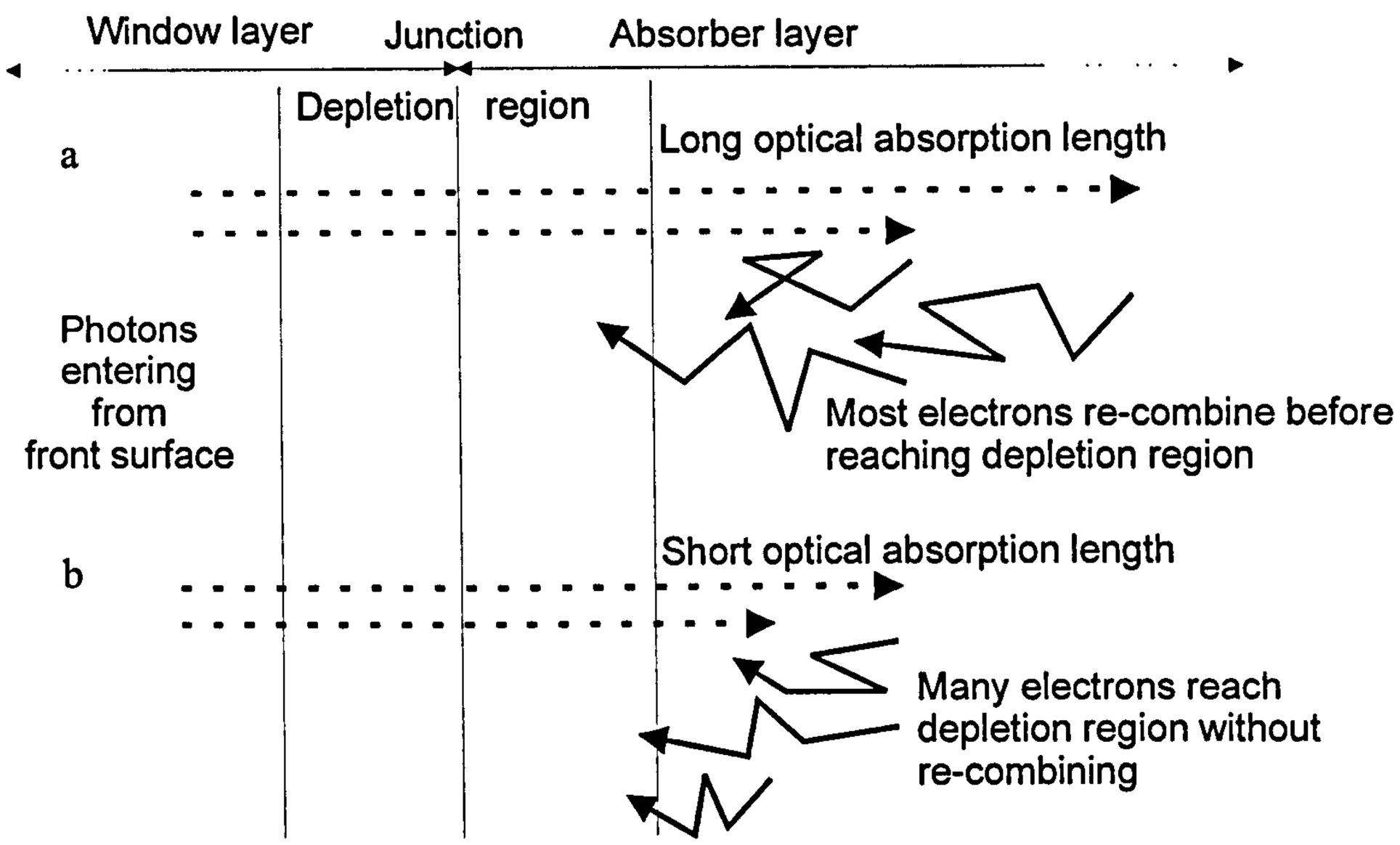

Figure 2.12 Optical absorption and recombination of charge carriers. a. Optical path length is longer than recombination length. b. Optical path length is shorter than recombination length.

The current remaining after these losses is available at the output as the short circuit current. This can be related to the photo-generated current, giving the collection efficiency.

$$\eta_{QE} \equiv \frac{I_{sc}}{I_{gen}} = \frac{I_{sc}}{e\int_{E_g}^{\infty} F(E).dE} \tag{2.21}$$

Collection efficiencies of more than 0.9 have been achieved, corresponding to similar values for spectral quantum efficiencies [27].

2.6.2 Voltage losses

Ideally, the open circuit voltage is given by the band gap.

$$V_{oc} = V_g = \frac{E_g}{e} \tag{2.22}$$

In practice, shifts in the quasi-Fermi levels reduce the energy of the excited electrons. This has a corresponding effect on the open circuit voltage [4].

$$V_{oc} = \frac{E_g - \delta E_{mj} - \delta E_{mn}}{e} \tag{2.23}$$

δE_{mj} = spacing of majority quasi-Fermi level from band edge in depletion region

δE_{mn} = spacing of minority quasi-Fermi level from band edge in depletion region

The magnitude of the shifts is proportional to the minority carrier density, as shown in Figure 2.13a, and therefore depends on factors such as doping density and level of illumination.

It is useful to give V_{oc} as a fraction of V_g. This is known as the voltage factor, and is a component in the overall efficiency [26].

$$\eta_{oc} \equiv \frac{V_{oc}}{V_g} = \frac{E_g - \delta E_{mj} - \delta E_{mn}}{E_g} = 1 - \frac{\delta E_{mj} + \delta E_{mn}}{E_g} \tag{2.24}$$

This is shown in Figure 2.13b. It can be seen that voltage loss is more significant for small band gaps.

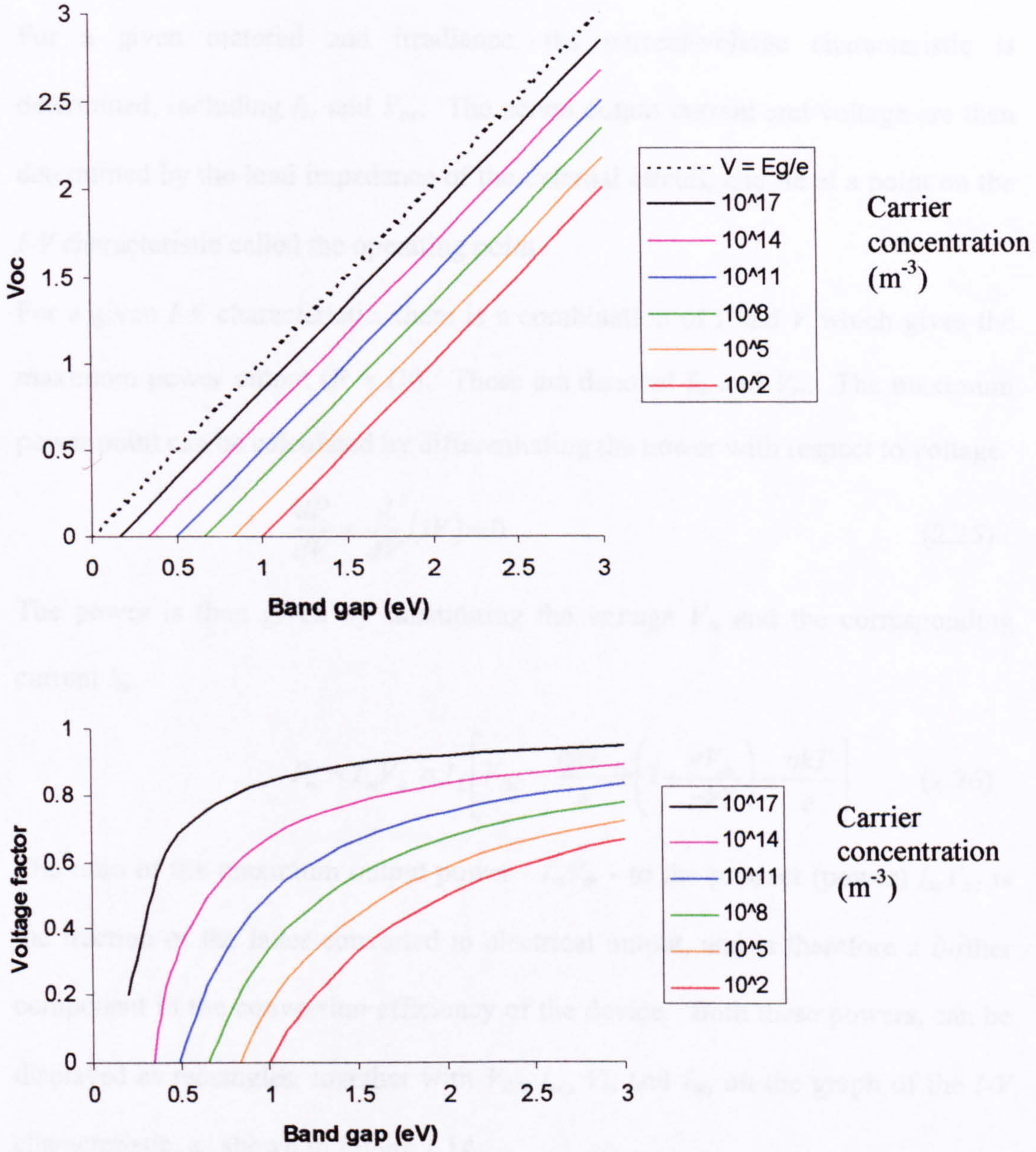

Figure 2.13 a. Open circuit voltage as a function of band gap. b. Voltage factor as a function of bandgap [4].

2.6.3 Operating point and fill factor

For a given material and irradiance, the current-voltage characteristic is determined, including I_{sc} and V_{oc}. The actual output current and voltage are then determined by the load impedance of the external circuit, and lie at a point on the *I-V* characteristic called the operating point.

For a given *I-V* characteristic, there is a combination of I and V which gives the maximum power output ($P = IV$). These are denoted I_m and V_m. The maximum power point can be calculated by differentiating the power with respect to voltage.

$$\frac{dP}{dV} = \frac{d}{dV}(IV) = 0 \tag{2.25}$$

The power is then given by substituting the voltage V_m and the corresponding current I_m.

$$P_m = I_m V_m \cong I_L\left[V_{OC} - \frac{\eta kT}{e}\ln\left(1+\frac{eV_m}{\eta kT}\right) - \frac{\eta kT}{e}\right] \tag{2.26}$$

The ratio of the maximum output power - $I_m V_m$ - to the product (power) $I_{sc}V_{oc}$ is the fraction of the latter converted to electrical output, and is therefore a further component in the conversion efficiency of the device. Both these powers, can be displayed as rectangles, together with V_{oc}, I_{sc}, V_m and I_m, on the graph of the *I-V* characteristic, as shown in Figure 2.14.

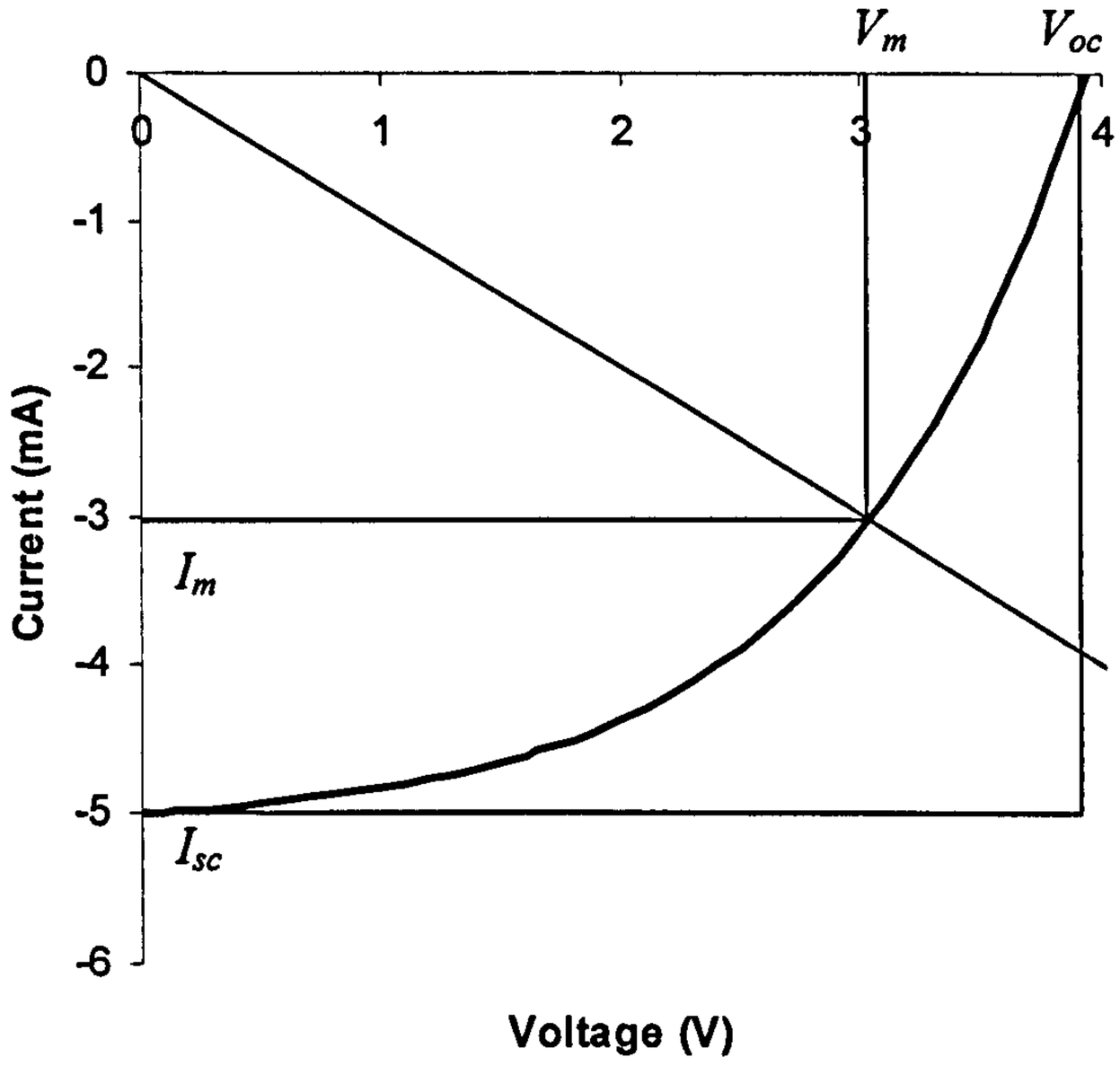

Figure 2.14. *I-V* characteristic showing I_{sc}, V_{oc}, I_m and V_m. The areas of the corresponding rectangles represent $I_{sc}V_{oc}$ and the electrical output power - I_mV_m. The load line due to the external circuit is shown by the sloped line through the origin.

The ratio of the areas of these rectangles is equal to the corresponding factor in the conversion efficiency, and is known as the fill factor (*FF*) [4, 5, 6].

$$\text{Output electrical power} = P_{\text{out}} = I_m V_m \tag{2.27}$$

$$\text{Fill factor} = FF = \frac{P_{out}}{I_{sc} V_{oc}} = \frac{I_m V_m}{I_{sc} V_{oc}} \tag{2.28}$$

The ratio V/I is the resistance of the external circuit. Therefore, operation at maximum efficiency requires that the load device has a suitable resistance. This is indicated on Figure 2.14 by the load line for $R = V_m/I_m$. As I_{sc} scales linearly with incident optical power, and V_{oc} scales logarithmically, the values of I_m and V_m will not scale in the same proportion. Thus the optimum load resistance will vary with incident light intensity. A load resistance selected for optimum efficiency at one level of irradiance will not, in general, be operating at maximum efficiency at another irradiance. In order to overcome this, specialised power supplies, known as power conditioning units, are used to match the output impedance of the cell (or array of cells) to the input impedance of the load circuit, over a range of incident irradiance [4, 23].

2.6.4 Electrical resistance in cells

Scattering of charge carriers by impurities and lattice defects contributes to the electrical resistivity of the bulk semiconductor regions, which connect the junction to the external circuit. In addition, resistance in the interfaces between regions of the diode (p- and n- regions, semiconductor-metal contacts, connections to the external circuit, etc) also contribute to the electrical resistance of the device. The resulting resistance - known as series resistance - creates a voltage drop, which reduces the output voltage.

The current-voltage characteristic, including series resistance, is

$$I = I_0\left[\exp\left(\frac{e(V - IR_s)}{kT}\right) - 1\right] - I_L \qquad (2.29)$$

The effect of series resistance on the *I-V* characteristic is shown in Figure 2.15. This results in a reduction in fill factor, which reduces conversion efficiency. In order to minimise the loss in efficiency, one of the objectives of fabrication techniques is to reduce series resistance to the lowest practical level. A series resistance below 0.1 Ω for a 1 cm^2 device is considered a requirement for operational devices [4].

Current flows horizontally in the window layer to the connection to the external circuit. In order to reduce series resistance, this path length should be minimised. However, this would require closer spacing of the grid contacts, which would decrease the optical efficiency. There is thus a trade-off between these two requirements.

Some of the current generated by the junction can flow directly from the n-type region to the p-type region (or vice versa) – an effect known as leakage. (Tunnelling may also contribute to this process.) This reduces the current which is available to flow in the external circuit, and effectively acts as a short-circuit within the cell. This reduction in current produces a corresponding reduction in the output current, further reducing the output power. The current loss can be modelled by a parallel resistance - also known as shunt resistance - which is internally connected across the output terminals of the cell. As for the series resistance, this alters the *I-V* characteristic and fill factor, as shown in Figure 2.16. In order to reduce the current loss to an acceptable level, the shunt resistance should be as large as possible, and values greater than 1 MΩ for a 1 cm^2 device are generally considered to be required [4]. An equivalent circuit, showing both series and shunt resistances, is given in Figure 2.17.

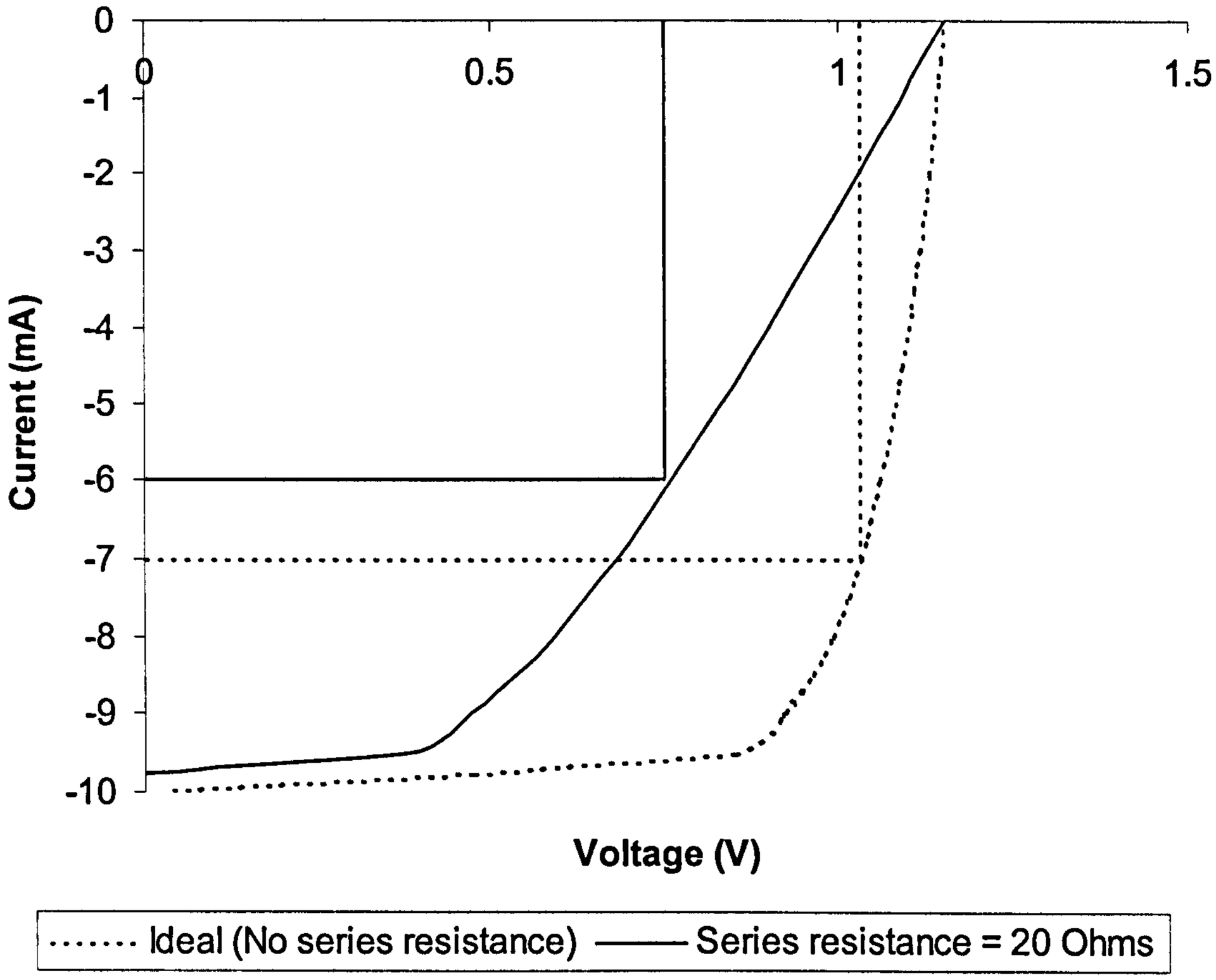

Figure 2.15 *I-V* characteristic for a solar cell with series resistance, showing reduction in I_{sc} and fill factor.

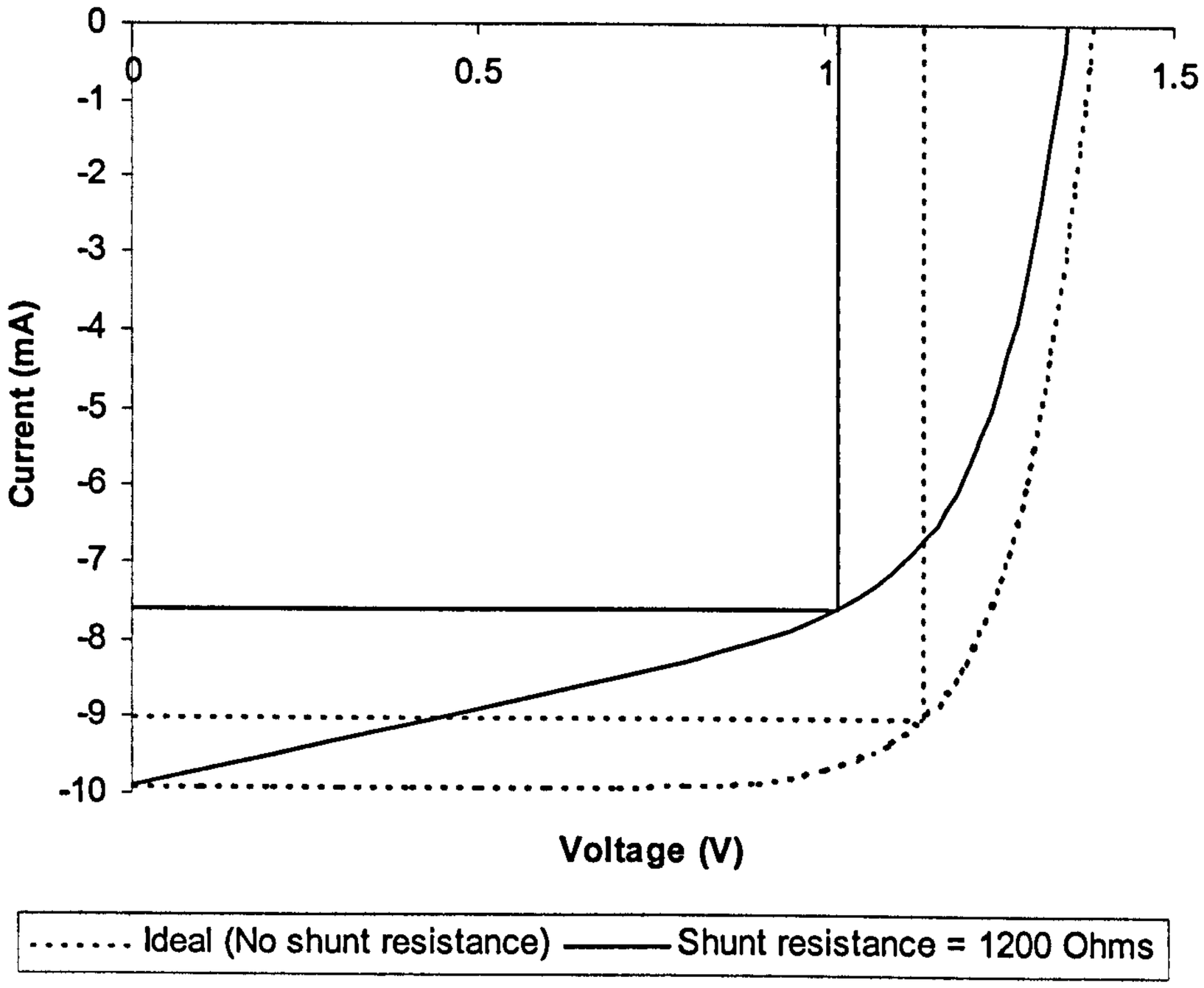

Figure 2.16. *I-V* characteristic for a solar cell with shunt resistance, showing reduction in V_{oc} and fill factor.

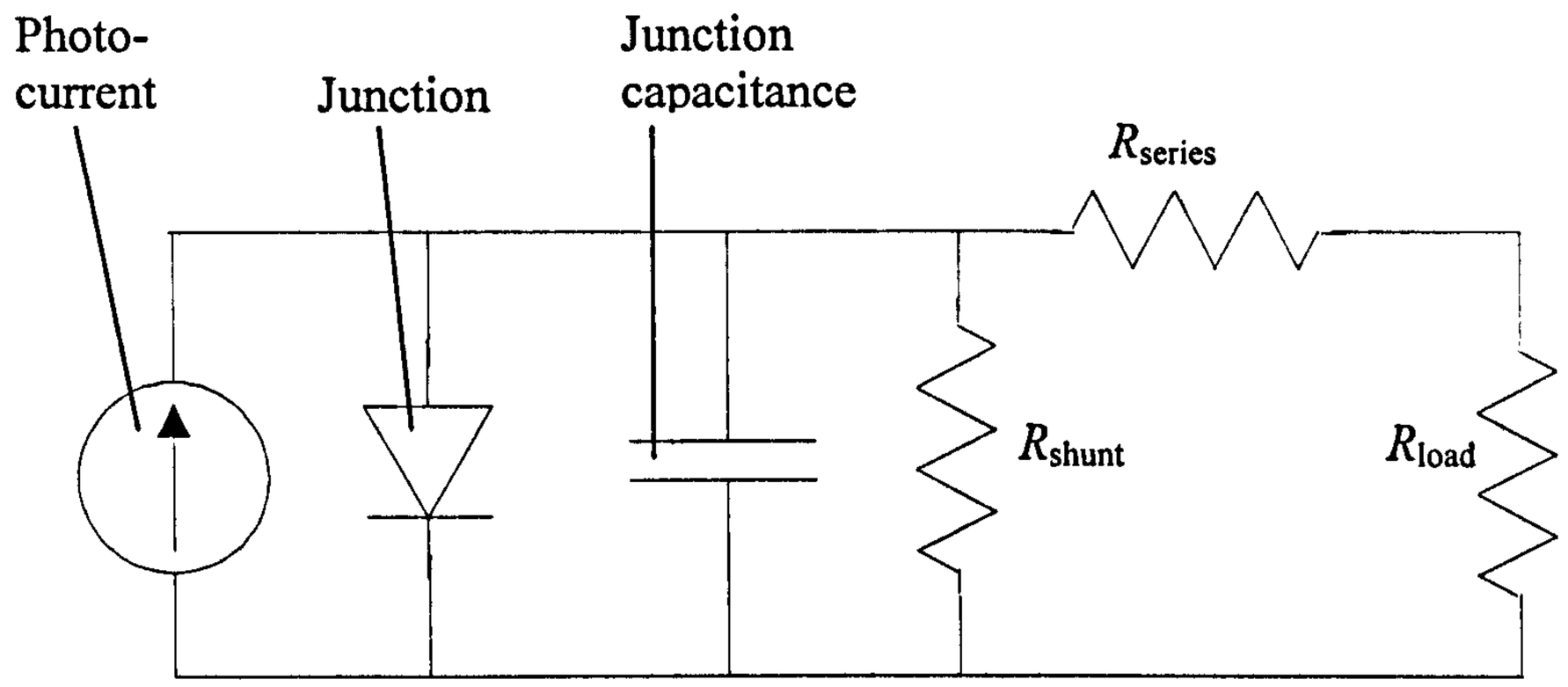

Figure 2.17 Equivalent circuit of a photovoltaic cell, showing series and shunt resistances.

2.7 Overall efficiency of solar cells

The electrical power that can be produced by the cell reduced by all the loss mechanisms described in the previous sections. The overall efficiency - ratio of output electrical power to incident optical power - is defined in terms of the efficiencies associated with each of these losses.

$$\eta = \eta_{opt}\eta_{UE}\eta_{QE}\eta_{OC}FF \tag{2.30}$$

Some of these factors are simple ratios, and it is useful to express them explicitly.

$$\eta = \eta_{opt}\eta_{UE}\frac{I_{sc}}{I_{gen}}\frac{V_{oc}}{V_g}\frac{I_m V_m}{I_{sc}V_{oc}} \tag{2.31}$$

This is the efficiency of an individual cell. In a photovoltaic system, a number of cells are mounted on a panel. The cells do not occupy the entire area of the panel, and thus the active area is reduced. This reduces the efficiency, measured in terms of the optical power incident on the entire area of the panel.

The cells in the array are connected in series and/or parallel to produce the required output voltage and current. Because of variations during the manufacturing process, not all of the cells have equal performance. In many cases, the cells with the lowest performance (output current or voltage) limit the performance of other cells, with which they are connected. This limits the efficiency of the whole array.

The array is connected to electronic power supplies, which provide the correct output for the load requirements. For AC loads, an inverter is required. There are losses associated with these power supplies.

As a result of these additional losses, the efficiency of a complete photovoltaic system is less than that of the cells, on which they are based.

2.8 Requirements of heterojunction cells

Because a heterojunction is formed from two different materials, there is greater freedom to choose these materials, to meet the functional requirements of a photovoltaic device. Having identified the energy transfers in a photovoltaic device, in the previous sections, and the associated losses and efficiencies, it is possible to define the required properties of each layer in a heterojunction device, and of the interface between them.

2.8.1 Absorber layer requirements

1. The band gap should be matched to the solar spectrum, to convert the maximum fraction of the photon energy into electrical energy. The solar spectrum approximates a black body at 5800 K, with a peak at 500 nm. The optimum band gap for this spectrum is 1.4 eV. Band gaps in the region 1 to 1.7 eV produce useful efficiencies [4].
2. The optical absorption coefficient should be high, in order that most of the radiation in the usable wavelength range is absorbed close to the depletion region. As well as contributing to higher current collection, and hence higher efficiency, this allows the absorber layer to be made thinner, with a consequent reduction in fabrication costs.
3. The recombination length should be long. As seen in Section 2.7.1, this should be longer than the optical absorption length. Sources of both recombination and scattering should be minimised. This includes crystal defects and impurities. Grain boundaries contain high densities of crystal defects and greatly reduce the recombination length in certain materials.

4. The bulk resistivity of the layer should be low, in order to minimise series resistance. As scattering tends to increase resistivity, crystal defects and impurities should be minimised.

2.8.2 Window layer requirements

1. The band gap should be as wide as possible, so that the layer is transmissive over most of the solar spectrum. Materials such as ZnO and ZnS are used. These have band gaps of 3.4 and 3.7 eV [10]. In order to further increase transmittance, the window layer should be as thin as possible.
2. The window layer should have a low electrical resistance. High band gap materials have low intrinsic carrier concentrations, and therefore have high resistivities. This can be overcome, to some extent, by doping with a suitable material. Zinc based window layer materials can be doped with group III elements (Al, Ga, In) [28, 29, 30, 31]. As for the absorber layer, a low density of scattering centres - crystal defects and impurities - reduces resistivity. As the current path in the window layer is largely lateral, a thicker layer results in lower series resistance. Comparison with point 1 shows that there are trade-offs, in terms of band gap and layer thickness, in meeting the optical and electrical requirements.

2.8.3 Interface requirements

The photovoltaic device includes a number of interfaces between layers of different materials.

- Front metal contact (grid) - window layer
- Window layer - absorber layer
- Absorber layer - back metal contact

The interface between the window layer and the absorber layer forms the p-n junction. If there is a mismatch between the lattice spacings of the two materials, there will be a large number of crystal defects at the junction. These will act as centres for recombination and scattering, reducing the performance of the cell. Where one of the materials is an alloy, the lattice spacing can be adjusted (within limits) to give good matching with the other material [4, 10, 32]. It is also important to match the electron affinities of the two materials, to avoid spikes in the valence or conduction band, which would limit the flows of charge carriers. The other two junctions should have matching electron affinities, so that they result in Ohmic contacts. These have low resistance, and thus minimise the loss in efficiency associated with these components of the device.

2.9 Polycrystalline thin film solar cells based on II-VI and I-III-VI_2 compounds

There are a number of compound materials, which are used in heterojunctions, for which the losses incurred due to crystal defects are not as severe as is the case for silicon or gallium arsenide [4, 10]. Examples are cadmium telluride (CdTe) and copper indium diselenide ($CuInSe_2$) [33, 34, 35, 36]. These have the potential to be used in polycrystalline form, with a consequent reduction of the demands on the fabrication processes. These materials are direct band-gap semiconductors, which therefore have high optical absorption coefficients. As a result, the depth of the layer required to effectively absorb the light is small (a few μm), and the thicknesses of the individual layers of the device can be of the same order. Combining this factor with the suitability of the materials for use in polycrystalline form allows thin film deposition techniques to be used. Thus thin films of semiconductor materials can be deposited onto an inexpensive substrate,

such as glass. The less demanding fabrication processes, together with the lower volume of materials required, can potentially reduce the cost of solar cell production, thus making photovoltaic generation more economically viable.

Thin film solar cells can be fabricated in either of two configurations. In superstrate configuration devices, the semiconductor films are deposited onto rear surface (as used in operation) of the superstrate, as shown in Figure 2.18. Because the light must pass through the superstrate, it must be transparent. Glass is the most commonly used such material. Other properties, such as relatively low cost and environmental stability, make glass a suitable material. In substrate configuration devices, the films are deposited onto the front surface of the base material, as shown in Figure 2.19. As the light does not pass through the substrate, it can be made of a non-transparent material, such as a metal or a ceramic [37].

The window layer performs a number of functions. As well as forming a junction with the absorber layer, and transmitting light to that junction, it provides an electrical path to the metal contact(s), and thus to the external circuit. In some devices, these functions are performed by two separate layers. The front contact layer provides a lateral conductive path to the metal connectors, and must combine optical transmittance with high electrical conductivity. A number of metal oxides combine these properties, and this layer is usually referred to as the transparent conducting oxide (TCO) layer [4, 10, 38]. The buffer layer forms the junction with the absorber layer, and prevents diffusion of material between this layer and the TCO layer. (Interdiffusion of these layers may reduce electrical output [39, 40].) One such combination is a zinc oxide (ZnO) TCO layer and a zinc compound (ZnS, $Zn(OH)_2$, etc) buffer layer [41]. Alternatively, the window layer may consist of a single material combining the functions of forming a heterojunction with the absorber layer, and providing electrical contact to the external circuit.

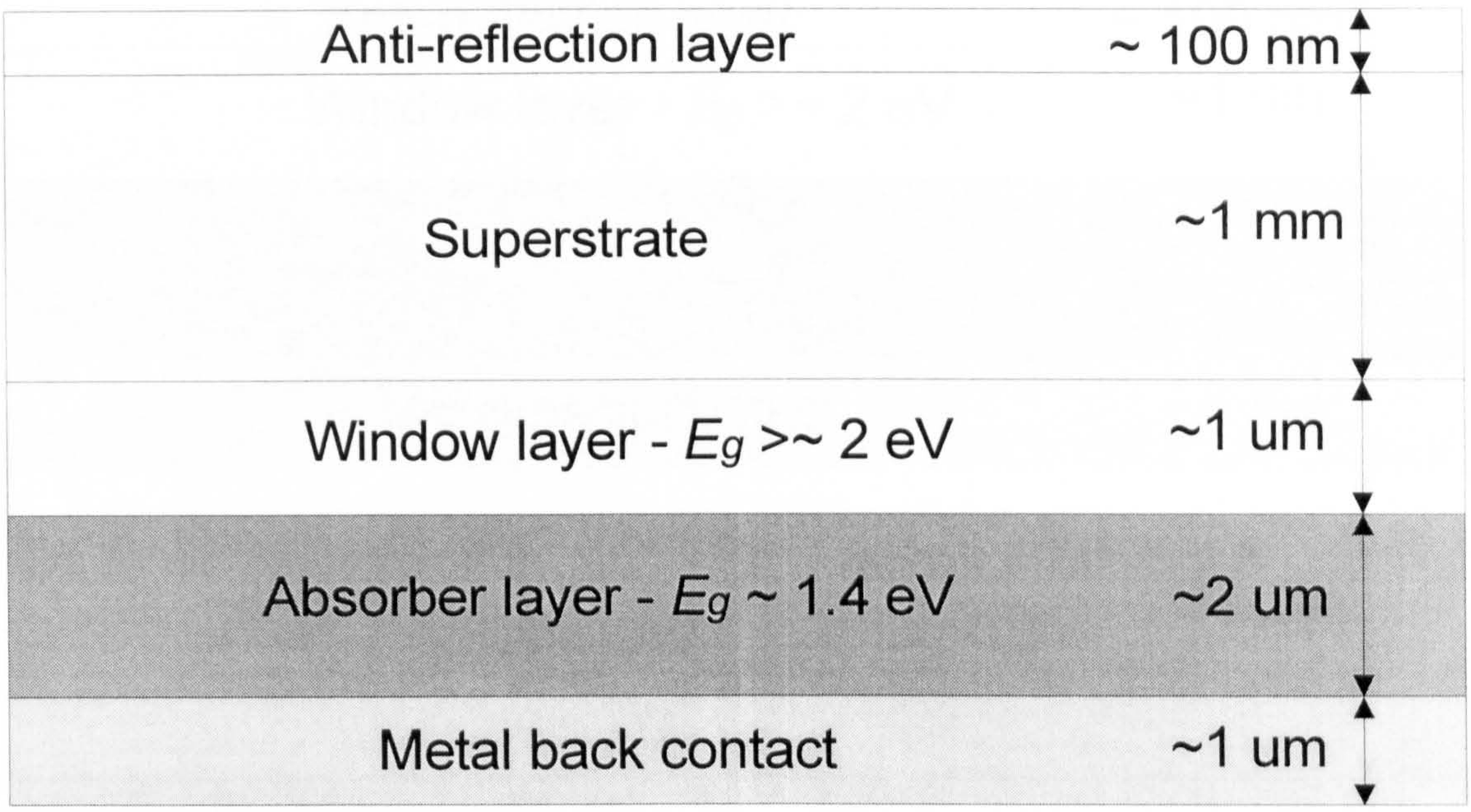

Figure 2.18. Superstrate configuration photovoltaic device

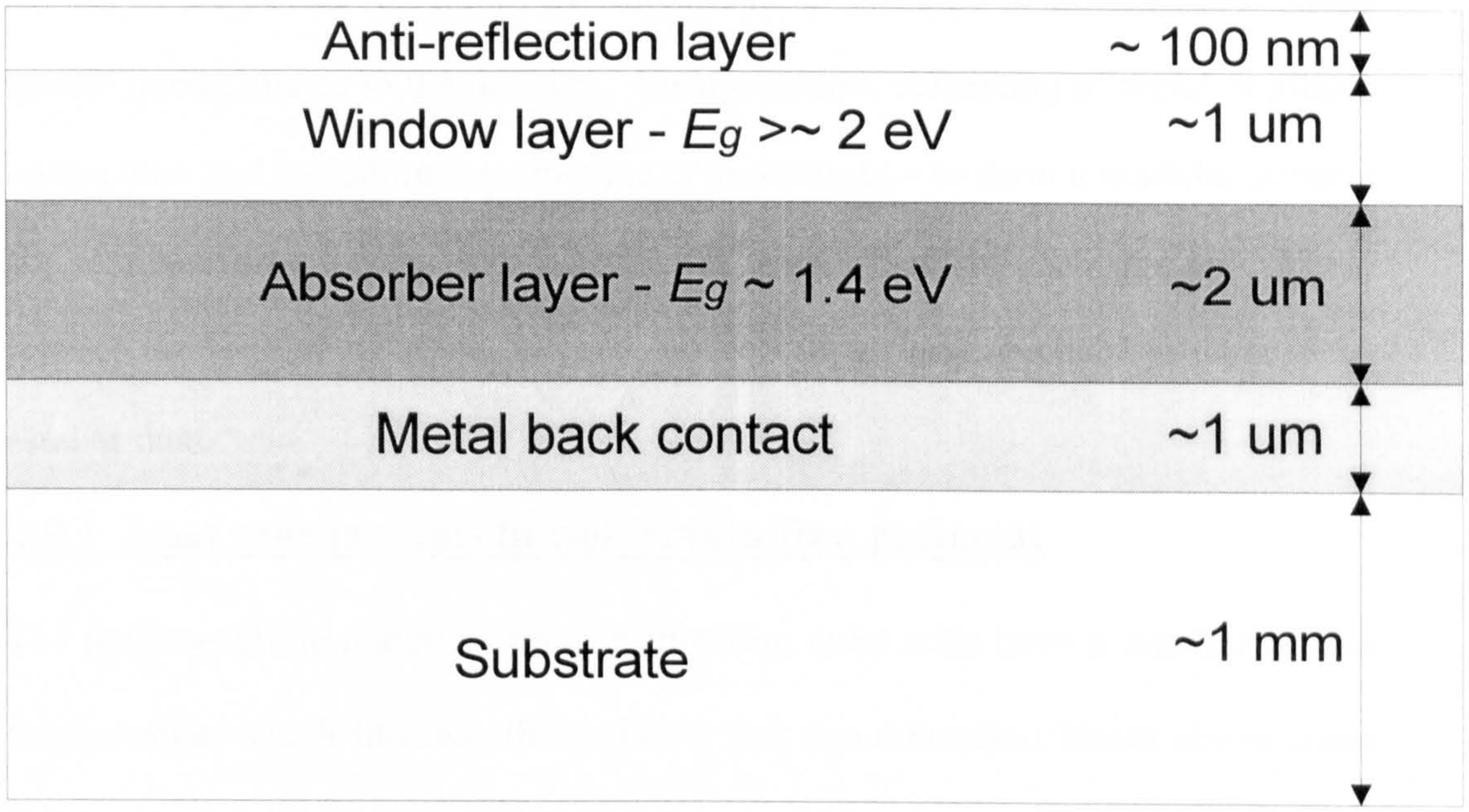

Figure 2.19. Substrate configuration photovoltaic device

A back contact, below the absorber layer, provides electrical connection to an external circuit. This is made of, or includes, a layer of a metal which forms a low resistance (Ohmic) contact to the absorber layer [42, 43].

In addition to the layers, which generate the photocurrent, and connect it to an external circuit, a number of other components are incorporated in thin film solar cells. As with other types of solar cell, an anti-reflection coating is deposited on the top of the device (on top of the superstrate in this type of device), to increase optical transmittance to the junction. Encapsulation, consisting of metal or plastic layers, etc - and including the substrate or superstrate – to form a module, protects the semiconductor layers from detrimental elements in the environment. These include ultra-violet radiation, oxygen, water vapour, and mechanical damage by sand or dust.

2.9.1 Loss mechanisms in polycrystalline material

The polycrystalline materials used in thin film solar cells have a number of loss mechanisms, which increase the resistive and recombination losses above those for single crystal devices [44, 45].

In a single crystal, the atoms are arranged in a regularly spaced lattice. In a polycrystalline material, each crystal (grain) consists of a periodic lattice, which in general has a different orientation to those in adjacent crystals. Consequently, there is a mismatch of lattice sites at the grain boundaries, which act as an area defect in the crystal lattice. These defect sites at the grain boundaries represent a departure from the periodicity of the lattice, which has a number of effects on the electrical properties. The mismatch between adjacent crystals is shown in Figure 2.20.

The scattering of the conduction electrons is increased, reducing their mean free path, and consequently increasing the resistivity of the material. The grain

boundaries generally have much higher resistivity than the internal regions of the grains, where the crystal lattice is more regular.

The potential energy of a given atom is determined by the spacing of neighbouring atoms. Thus the atoms at a grain boundary have a range of potential energies, which differ slightly from those of atoms in a regular lattice. Atoms at higher or lower energies can form localised energy levels, which can act as recombination centres for electrons in the conduction band, or holes in the valence band. This reduces the current which can be delivered to the external circuit.

Grain boundaries act as sites for impurity atoms. If a crystal lattice contains impurity atoms of a different size from the host atom, it moves neighbouring atoms from their normal equilibrium positions. This produces a strain in the lattice in the locality of the impurity, resulting in a slight increase in the potential energy of the lattice. This tends to limit the extent to which certain impurities can be added to a given host crystal. In the grain boundary, the regularity of the grain boundary is reduced, with different points having different local lattice spacings. Thus an impurity atom can be added without straining the lattice to the same extent. As a result, much higher levels of impurities can be incorporated at the grain boundaries. In general, these impurities act as additional sources of scattering and recombination, both of which reduce the electrical output of the cell still further. However, it has been found experimentally, that certain impurities incorporated into the grain boundaries of polycrystalline semiconductors improve their electrical characteristics [46].

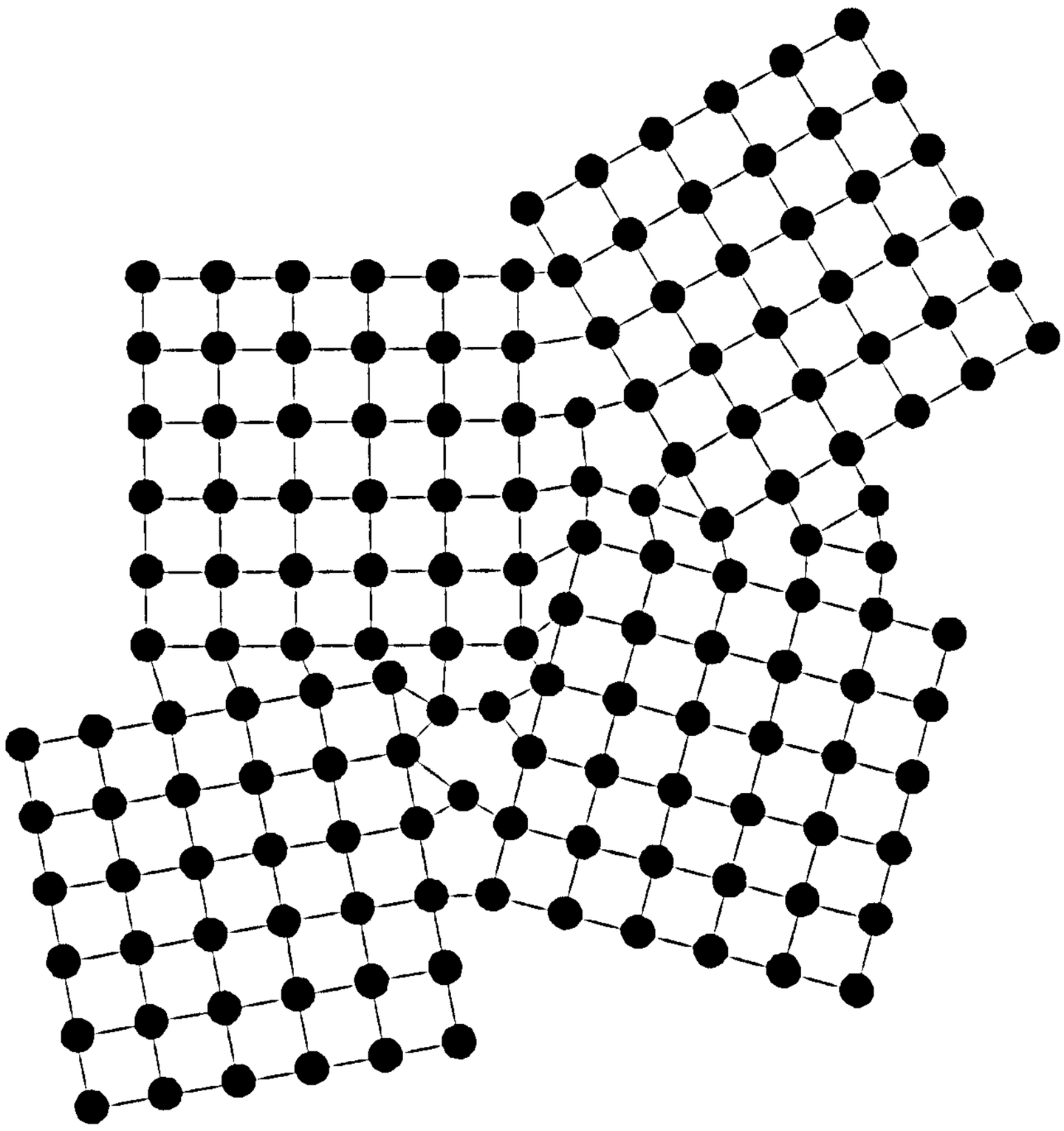

Figure 2.20 Lattice mismatch at the boundaries between adjacent crystals.

A number of characteristics of polycrystalline materials add to the shunt resistance of the cell. The high levels of impurities, which can exist at grain boundaries, may include conductive materials, which provide a current path through the layer. As the layers of a thin film solar cell are deposited sequentially, it is possible that material forming an upper layer diffuses into the grain boundaries of the film onto which it is being deposited, as shown in Figure 2.21. Such material may provide a current path between the overlying and underlying layers, short-circuiting the junction. This reduces the output current, and is equivalent to a shunt resistance connected internally to the cell.

As the material is made of small crystals of the order of 1μm, polycrystalline films have a surface roughness of the same order. If the film thickness is comparable to this, there may be regions where the thickness reduces to zero. Such a region is known as a pinhole, and is shown in Figure 2.22. At a pinhole, the overlying and underlying layers come into direct contact. If the junction is formed between the intermediate layer and one of the adjacent layers, the pinhole may provide a current path which short-circuits this junction. This acts as current loss mechanism, and is an additional component of a shunt resistance connected internally across the cell.

The effect that grain boundaries and impurities have on the opto-electrical performance of the cell depends not only on the combination of materials used, but also on the methods used for their deposition and any post-deposition processing, which may be applied. Current research in the field of thin film solar cells is aimed at developing fabrication methods, which reduce the adverse effects of polycrystallinity, so that the cells might approach closer to their maximum potential efficiency.

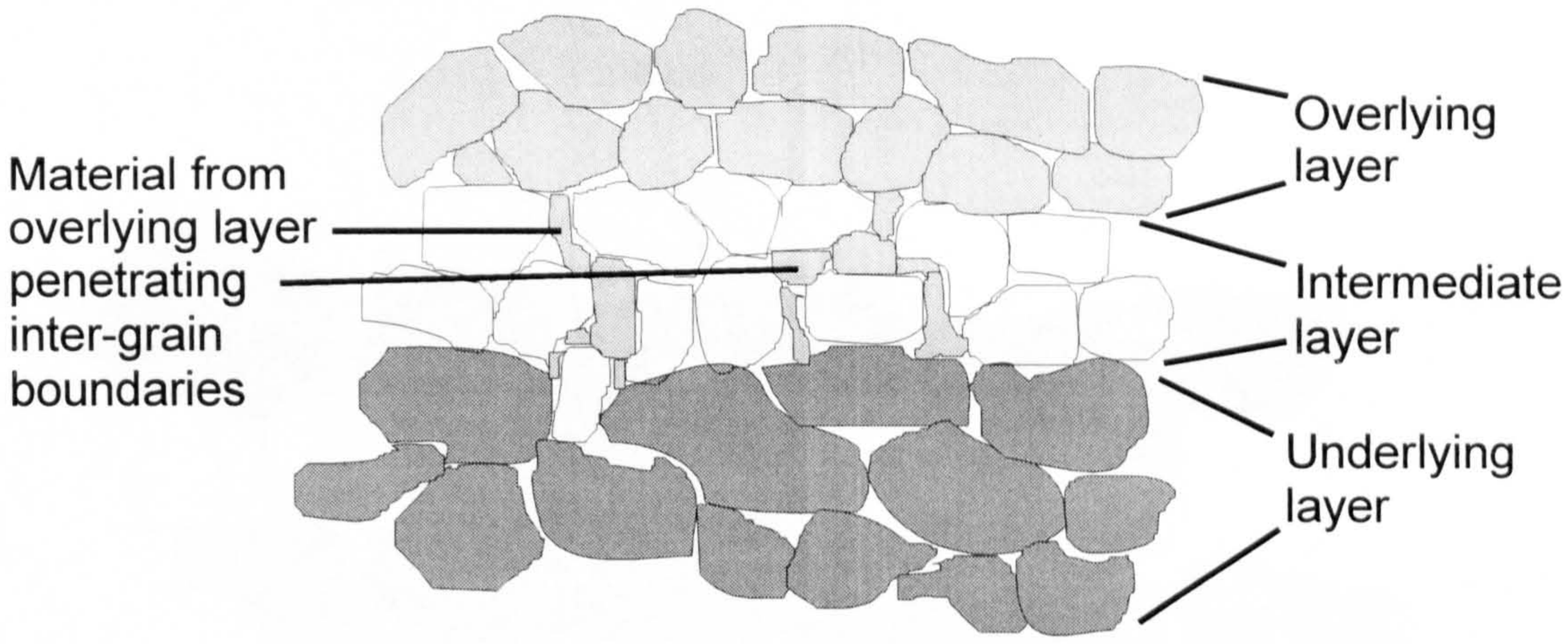

Figure 2.21 Polycrystalline layers, showing diffusion of upper layer material along grain boundaries in the intermediate layer, which allows a direct electrical contact between the upper and lower layers.

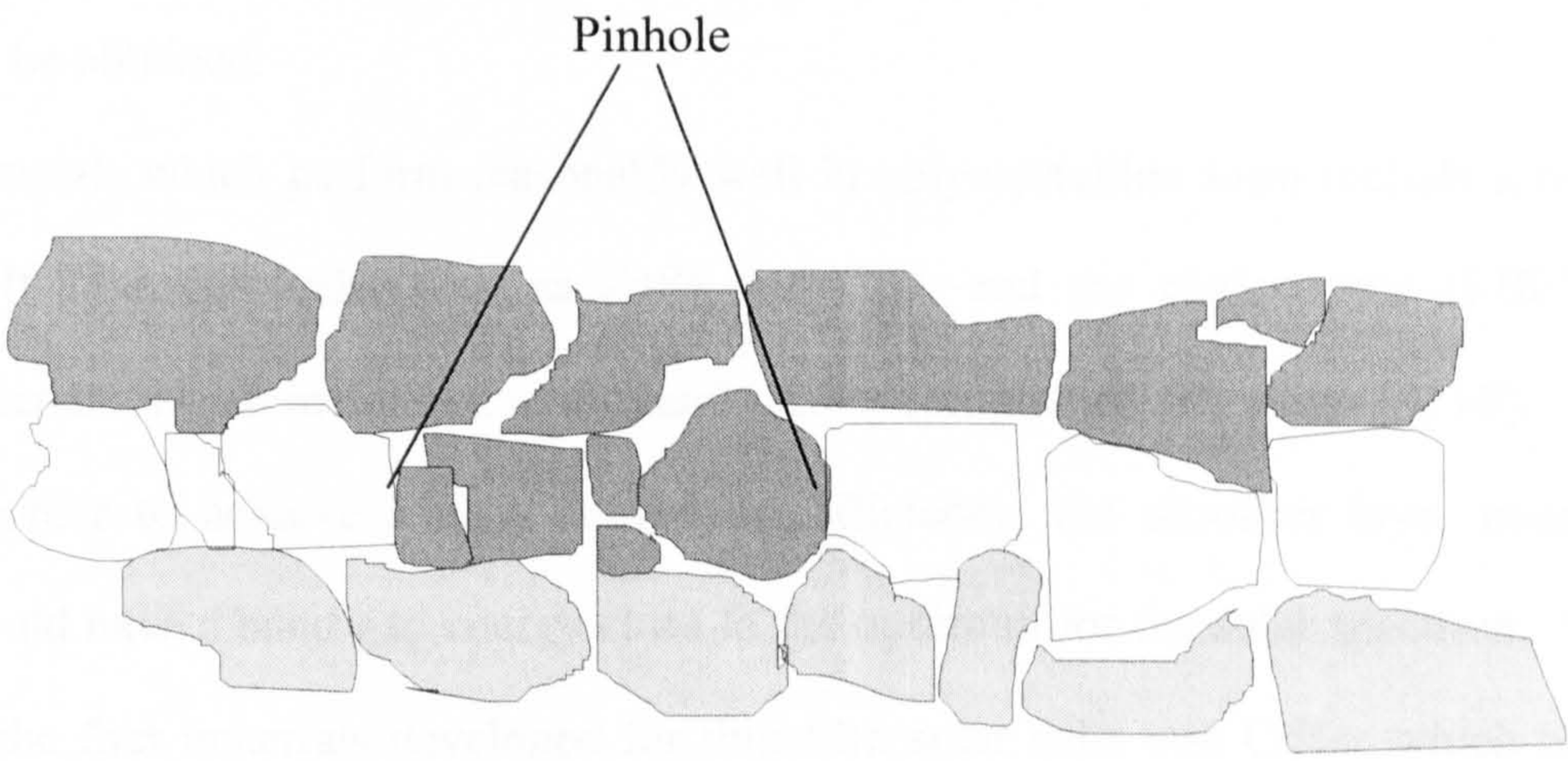

Figure 2.22. Polycrystalline layers, showing a pinhole in the intermediate layer, which allows a direct contact between the upper and lower layers.

2.9.2 Materials used for thin film solar cells

Materials for use in thin film solar cells are selected, according to a number of criteria. One of these is that the electrical losses, due to their polycrystalline structure, should be minimal. For silicon, these loss mechanisms result in a substantial reduction in conversion efficiency. (Despite this, a number of technological advances have allowed polycrystalline and amorphous thin film silicon cells to be developed [4, 10, 47, 48].) For some materials, such as CdTe, the losses due to grain boundaries, etc, are not as severe, and useful efficiencies can be obtained.

Materials which perform reasonably well in polycrystalline form include a range of II-VI compounds, such as ZnSe and CdS, and the chalcopyrite (I-III-VI_2) materials, which includes $CuInSe_2$ and similar compounds and alloys [4, 10].

In order to achieve a high conversion efficiency, the absorber layer material should have a band-gap energy close to the optimum for the solar spectrum. One of the first materials developed for thin film solar cells was CdTe, which has a band-gap energy of 1.44 eV [10, 49]. More recent research has been done on $CuInSe_2$, which has a band-gap energy of 1.05 eV [10, 35]. This material has a very high optical absorption coefficient, but the band-gap energy is significantly lower than the optimum value. A related chalcopyrite material, copper indium disulphide ($CuInS_2$), has been developed, which has a band-gap energy of 1.45 eV [10, 50]. As this is closer to the optimum band-gap, it has the potential to produce high conversion efficiencies. Similarly, copper indium gallium diselenide ($Cu(In,Ga)Se_2$) has a higher band gap than $CuInSe_2$, and is being developed as an absorber layer [10, 51, 52].

The material selected for the window layer should have a band-gap energy larger than that of the absorber layer. Window layers are commonly made of II-VI

compounds. Not all of these semiconductors can be fabricated in both n-type and p-type. The window material used with a particular absorber material must be such that they can form a complementary pair of n-type and p-type materials, thus forming a p-n junction at their interface. This further limits the choice of possible combinations of II-VI compounds materials, which can be used as a window layer and absorber layer materials. A number of the chalcopyrite materials can be formed as either n-type or p-type, with the conductivity type being controlled by altering the ratio of the I and III elements. Thus there is no restriction on the conductivity type of the absorber layer, and any material with a suitable band-gap energy may be selected.

Much of the early development work in thin film solar cells focused on devices with CdTe absorber layers. Cells based on this material have reached conversion efficiencies of 16.8 % [53]. Modules constructed with CdTe cells have reached commercial production. However, concerns over the health and environmental effects of cadmium have been a factor in the development of alternative cadmium free materials. The chalcopyrite materials, such as $CuInSe_2$ and $Cu(In,Ga)Se_2$, which have also been developed as photovoltaic materials, are cadmium-free, and thus avoid this hazard. They have demonstrated similar efficiencies to cells based on CdTe [54, 55].

2.9.3 Fabrication processes for thin film solar cells

Many of the deposition techniques, which are used in the fabrication of solar cells, are common to the thin film industry in general [56, 57].

For many of these processes, a major requirement is to produce uniformity of a number of properties over a large area.

These properties include

- Film thickness. As the films are of the order of 1μm thick or less, variations on this scale can seriously affect device performance. In extreme cases, pinholes (small gaps penetrating the film) can create short circuits.
- Composition. The required compound must be formed, with minimal amounts of other compounds - produced by partial formation or side reactions.
- Conductivity. This is related to composition, and includes conductivity type and magnitude.

In addition, adhesion to the substrate or to underlying films is required over the area of the device.

In research into thin film device fabrication, small-area devices may be produced, which can demonstrate high conversion efficiencies. If larger area devices are produced, these may be non-uniform, in which case high efficiencies can be produced for limited parts of the devices (e.g., by limiting the region, which is irradiated, and for which current is collected). The non-uniformity means that other parts of the device may have lower efficiency, or show no photovoltaic activity. This reduces the overall efficiency of the device. One of the objectives of continuing research in photovoltaics is to replicate the efficiency, demonstrated on small-scale devices, for the larger devices (up to typically 1 m^2) which would be produced industrially [51, 58].

3 Thin film solar cells based on chalcopyrite semiconductors

Thin film photovoltaic devices have been developed based on a range of chalcopyrite semiconductors as the absorber layer, including copper indium diselenide ($CuInSe_2$), copper indium gallium diselenide ($Cu(In,Ga)Se_2$) and copper indium disulphide ($CuInS_2$) [1]. As these are cadmium free, they offer an environmentally-benign alternative to the cadmium telluride (CdTe) based solar cells, which constitute another major type of thin-film device. Cells based on chalcopyrite materials are fabricated with a number of window layers, including cadmium sulphide (CdS), zinc selenide (ZnSe) and zinc oxide (ZnO). Where zinc oxide is used as the window layer, some researchers have observed that interaction with the chalcopyrite absorber layer reduces the open circuit voltage [2]. Therefore, zinc oxide may be used in a two-component window layer, with the zinc oxide acting as a TCO layer, and zinc sulphide (ZnS), CdS or ZnSe as a buffer layer. Molybdenum (Mo) forms an Ohmic (low resistance) contact with many p-type (Cu-rich) chalcopyrite semiconductors, and is used as the back contact in many chalcopyrite-based devices [3]. The structure of a typical chalcopyrite-based solar cell is shown in Figure 3.1

As $CuInSe_2$ and $CuInS_2$ can be fabricated as both n-type and p-type materials, by controlling the Cu:In ratio, it is possible to grade from one conductivity type to the other within the chalcopyrite layer [4]. Thus the p-n junction can be formed within this layer, below the interface with the window layer. Such a structure is called a buried homojunction, and is shown in Figure 3.2. In this case, the window layer acts simply to provide an electrical current path to the external circuit.

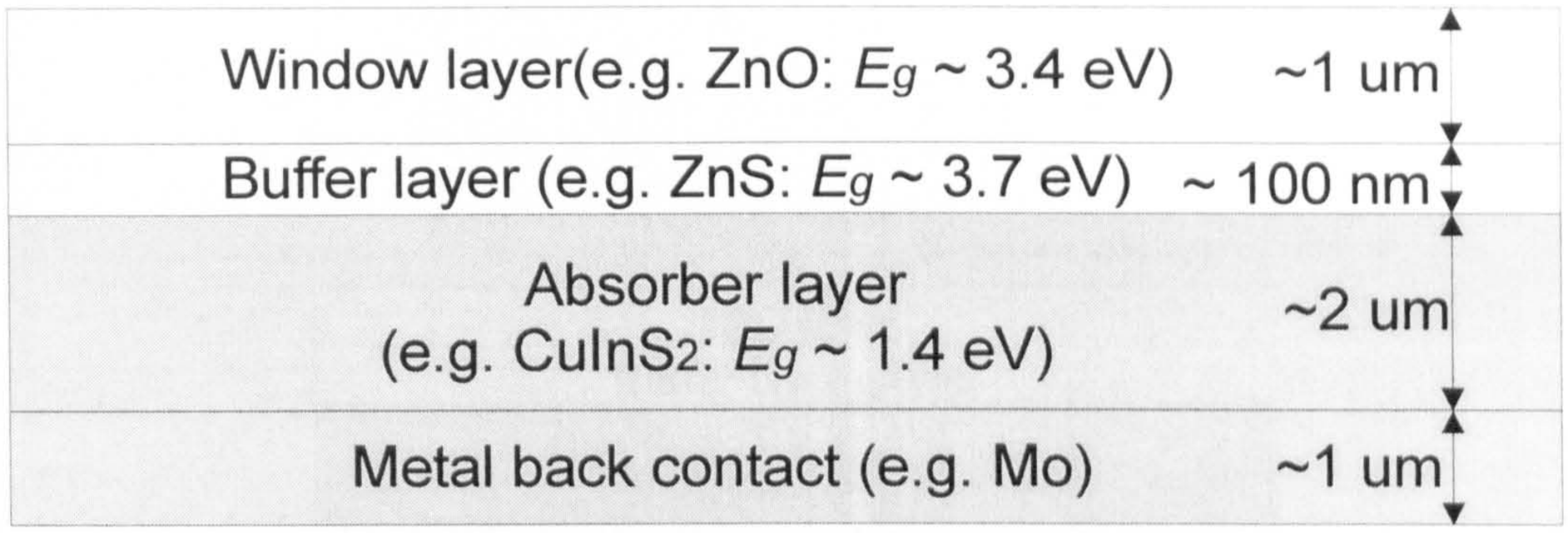

Figure 3.1 Structure of a chalcopyrite-based solar cell. This example has a two-component window. Some window materials, e.g., ZnSe, combine both functions in one layer.

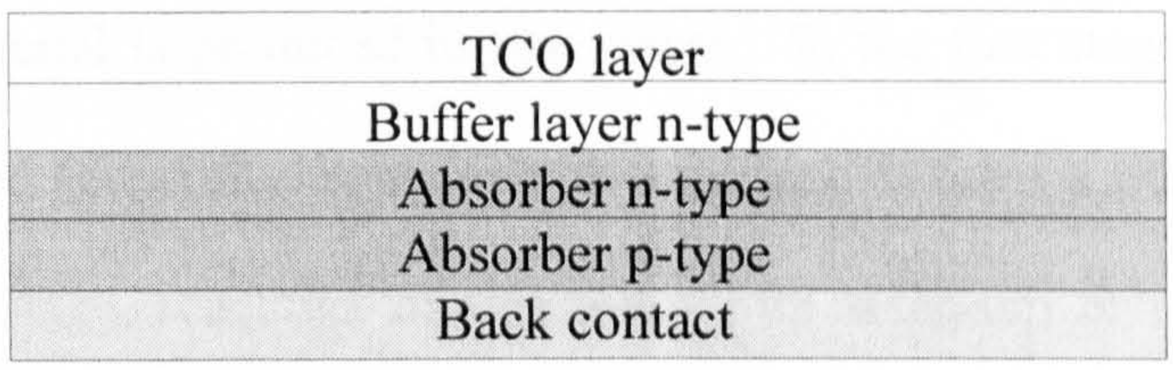

Figure 3.2 Buried homojunction. The p-n junction is within the absorber layer.

As $CuInSe_2$ and $CuInS_2$ are ternary, rather than binary compounds, control of the composition during fabrication is more complicated. This affects the choice of deposition process used, and the way in which it is applied. The source materials, and their method of application, can be grouped into three broad categories, independently of the particular deposition method used.

1. The three elements can be deposited simultaneously, such that they react on the substrate to form chalcopyrite compounds, e.g., $CuInSe_2$ or $CuInS_2$ [5, 6, 7].
2. The binary compounds (e.g. Cu_2Se and In_2Se_3) can be deposited simultaneously from separate sources. These then react on the substrate to form $CuInSe_2$.[8]
3. The material is produced in two stages. In the first stage, Cu and In are deposited (generally from separate sources), to form a CuIn alloy. In the second stage, reactions of this alloy with selenium or sulphur, or their compounds, results in the formation of $CuInSe_2$ or $CuInS_2$. (The deposition techniques used in the two stages may be different.) [9, 10]

A number of other chalcopyrite compounds have been developed for use as absorber layers, such as copper gallium diselenide ($CuGaSe_2$) and copper gallium disulphide ($CuGaS_2$), and a range of alloys of the basic compounds – copper indium sulphur selenide ($CuInS_{2x}Se_{2-2x}$), etc [11, 12, 13]. As the alloys are quaternary or pentenary materials, the greater number of elements involved may require more stages in the fabrication process.

If films with graded composition are required, a sequence of stages may be used, involving one or more of the configurations stated above. Although doping may be produced by adding dopants of other materials, it is more common to control

the conductivity type of $CuInS_2$ by controlling the Cu:In ratio [4]. Excess Cu produces p-type material (although too great an excess may lead to the formation of Cu_2S grains, which adversely affect cell performance). Similarly, excess In produces n-type material. The formation of an Ohmic contact with the Mo back contact requires a p-type region, which can be produced by making the material Cu-rich. If a buried homojunction is formed within the chalcopyrite film, the top region is made n-type by depositing In-rich material. In a superstrate device, the deposition process thus proceeds from In-rich to Cu-rich, while the reverse occurs in substrate devices.

3.1 Copper indium diselenide-based solar cells

Copper indium diselenide is one of the most developed of the chalcopyrite semiconductors. Although the band gap energy of 1.05 eV is significantly less than the optimum value, high conversion efficiencies (18 %) have been achieved [1]. A number of techniques have been used to deposit this material. One of these – thermal evaporation – is described below.

Due to problems, such as thermal decomposition, only some compounds are suitable for direct evaporation [14]. Both Cu_2Se and In_2Se_3 are such compounds. Thus thermal evaporation of $CuInSe_2$ can be performed by co-evaporation of the elements or by co-evaporation of the selenides [8, 15]. Both of these approaches are used for deposition of $CuInSe_2$, although elemental co-evaporation is the more common.

To avoid adverse reactions with the crucible, the materials of the crucibles are matched to the source materials evaporated from them. A molybdenum crucible is used for Cu, and graphite crucibles are used for In and Se [14]. Source

temperatures are typically 1000°C for Cu, 1050°C for In, and 280°C for Se. The substrate temperature depends on the material used. For borosilicate glass, relatively high temperatures can be used, and values of 500°C or higher are typical [8]. If soda-lime glass is used, temperatures of 300-350°C are more commonly used [2]. In the case of superstrate devices, the temperature during deposition may be limited by the need to avoid damage to previously deposited films.

One method of fabricating $CuInSe_2$ involves co-evaporation of the elements [2, 16]. Alternatively, the metals can be evaporated, and then post-deposition reactive annealing can be performed in an atmosphere of Se-vapour [9]. The process is terminated when the correct composition is achieved.

Although much research has been done on simultaneous evaporation and deposition of the elements, an alternative approach is to deposit each element in turn to produce a stacked elemental layer [7]. The temperature for deposition and subsequent annealing is typically 500°C, which results in sufficient mixing and reaction of the elements to produce the ternary compound.

Formation of $CuInSe_2$ from the binary compounds has been performed by evaporating each material in turn [8]. It has been found that relatively thick layers of In_2Se_3 and Cu_2Se can be produced and mixed to form $CuInSe_2$.

It has been found that the incorporation of sodium into $CuInSe_2$ films improves their electrical properties. The Na ions tend to become incorporated into grain boundaries, reducing the extent to which they cause charge carrier recombination. For films produced by thermal evaporation, Na_2S is co-evaporated with the primary source materials [6]. Typically, the quantity of Na_2S added is equivalent to 5 % of the $CuInSe_2$ film. This research shows that, for substrate temperatures above 350°C, the incorporation of sodium also improves grain growth.

In order to assess the effects of grain boundaries in polycrystalline films, these have been compared to films grown epitaxially on crystalline substrates. In a number of studies, $CuInSe_2$ films have been grown onto crystalline GaAs by molecular beam epitaxy. [15, 17]. By using various thermal treatments, specific types of defects can be produced. These can then be investigated in isolation, and their effects combined in modelling polycrystalline films, where numerous types of defect are present simultaneously.

Investigation of the films produced by the methods described above include analysis of a range of properties, which have an effect on the conversion efficiency of photovoltaic devices based on this material. In a ternary compound, such as $CuInS_2$, a number of additional materials are generally present in the film. The presence of these can be determined by XRD. These materials are the result of incomplete reaction, and include both elements and binary compounds. The degree to which the reactions proceed to completion – formation of $CuInS_2$ – has been shown to depend on the substrate temperature [18]. For temperatures below 200°C, the binary compounds $CuSe_2$ and In_2Se_3 form. For temperatures between 200°C and 400°C, a number of additional reactions occur, including partial decomposition and transformation of $CuSe_2$ to Cu_2Se. For temperatures above 400°C, the binary compounds react to form $CuInSe_2$.

Conversion efficiencies of over 17 % for $CuInSe_2$-based devices have been recorded by NREL, and a number of other research groups have recorded efficiencies of more than 15 % [19]. However, these measurements are generally made for small area devices, and factors, such as series resistance in the TCO layer, will become more significant, when fabrication is extended to larger area devices.

3.2 Other chalcopyrite materials and solar cells

A number of chalcopyrite semiconductors have been developed, which used gallium (Ga) in complete or partial substitution for indium. These materials have higher band-gap energies than their indium-based equivalents.

One such high band gap material which is being developed is $CuGaSe_2$ [20, 11]. This material has a band gap energy of 1.73 eV. By alloying with $CuInSe_2$, materials with intermediate band gaps can be formed [21, 22, 23, 24, 25]. A material with a very high band gap (2.43 eV) is $CuGaS_2$ [12]. Alloying can produce the quaternary $Cu(In,Ga)S_2$ [26, 27]. In all such alloys, there is one degree of freedom in the composition. This allows the band gap energy to be determined by the deposition conditions. However, once the composition is chosen, the lattice constant is determined. Although polycrystalline materials allow a wide tolerance for lattice matching with adjacent layers, good matching tends to improve performance. One pentenary material that is being developed is $Cu(In,Ga)(S,Se)_2$ [28]. This material has two degrees of freedom and thus allows the band gap energy and lattice constant to be chosen independently (within certain limits).

In addition to Ga, aluminium (Al) can be substituted for In to produce higher band gap materials $CuAlSe_2$ and $Cu(In,Al)Se_2$ [29]. Of the chalcopyrites alloys being developed as alternatives to $CuInSe_2$, much of the research has focused on fabrication of $Cu(In,Ga)Se_2$.

As $Cu(In,Ga)Se_2$ is an alloy, it allows photovoltaic cells to be produced with a band gap energy anywhere in the range 1.05 to 1.7 eV [1]. In a device with series resistance, the output voltage will drop below V_{OC} by an amount proportional to the output current.

A material with a higher bang gap energy will have a higher V_{OC} and a lower output current, and consequently a lower voltage drop, for a given output current. This will result in a smaller decrease in conversion efficiency from its ideal (zero series resistance) value. As a consequence, the optimum band gap energy for solar cells with series resistance is generally slightly higher than the ideal value of 1.45 eV for those with no resistance, and $Cu(In,Ga)Se_2$ films with the composition required to produce this band gap energy are being developed [23]. Efficiencies of up to 13.8 % have been achieved. In order to further increase band gap energy, this research has extended to fabrication of $Cu(In,Ga)(S,Se)_2$ [28].

The greater complexity of the quaternary material is reflected in the greater complexity of some of the fabrication methods. Both evaporation and sputtering of all the elements, or the metallic elements, have been developed for this material. Co-evaporation of the elements has been developed, although this requires simultaneous control of four deposition rates [29, 25]. However, methods involving multi-stage deposition have also been widely developed. Precursors made up of stacked layers of the metals are converted to $Cu(In,Ga)Se_2$ using a selenium compound such as H_2Se [30].

The use of a multi-stage process allows grading of the composition [4]. For the production of substrate devices, an initial layer of Cu-rich material can be deposited, forming an Ohmic junction with the Mo back contact. Subsequent deposition of In, Ga and Se produces an n-type region at the surface, resulting in a buried homojunction. For the fabrication of superstrate devices, the grading process is applied in the reverse order.

As with $CuInSe_2$ the incorporation of sodium into the grain boundaries has a beneficial effect [4, 22]. This is generally accomplished by evaporating Na_2Se as

a source material. For sputtered films, a separate target of Na_2Se has been used [31].

Given the complex composition of the material, which may include grading, measurement of the composition is important. Secondary ion mass spectrometry (SIMS) is particularly useful in analysing the composition of thin films, and determining the way this varies with depth through the film. The wide dynamic range in the measurements allows the fractions of major and minor components (including impurities such as Na) to be determined.

Current-voltage (*I-V*) measurements of Mo-Cu(In,Ga)Se_2-CdS-ZnO solar cells have shown efficiencies up to 11% [32].

Continuing development of the chalcopyrite semiconductors is focusing on a number of aspects. Control of composition during fabrication is a major issue, given that the fabricated material consists of from three to five elements. Specific aspects include grading the ratios of particular pairs of elements through the film, control of conductivity type, and reduction of the fractions of other materials (Cu_2Se, etc). Some of the losses in electrical performance are attributed to the effects of grain boundaries (scattering, recombination). Efforts are being made to improve the crystal quality, in an attempt to reduce these effects. The effects of the interface with adjacent layers are also being investigated. This includes the p-n junction with the window layer, which is the subject of section 3.5.

Photovoltaic devices based on Cu(In,Ga)Se_2 have achieved conversion efficiencies of 18.8 % [33]. This has been measured for devices with Cu(In,Ga)Se_2 produced by physical vapour deposition. Similar measurements by the same research group have recorded efficencies of 15.4 % for devices based on electrodeposited Cu(In,Ga)Se_2. This latter process has potential for large area device fabrication, and thus has the potential to reproduce the results achieved at the larger scale of production devices.

Analysis, such as scanning electron microscopy, shows uniform films with good quality grain structure [34]. This tends to reduce the losses typical of polycrystalline materials, and as a result, the performance can approach more closely the ideal level, as determined from the band gap.

The band gap of $Cu(In_{1-x}Ga_x)Se_2$ tends to increase with the gallium fraction (x), and thus the conversion efficiency has a maximum for some value of x. A number of fabrication techniques, notably sputtering, allow accurate and reliable control of the elemental composition of the deposited material. Studies of $Cu(In,Ga)Se_2$ produced by sputtering of Cu, In and Ga, followed by selenisation in Se vapour, have shown total area efficiencies having a maximum of 9 % for films with an elemental ratio for Cu:In:Ga:Se of 24.25:22.21:4.40:49.14 [35]. This is equivalent to a value of x of 0.17. This is consistent with the lower voltage drop, due to series resistance, for materials with higher band gaps, and the prediction that the optimum band gap for materials with non-zero series resistance is slightly higher than that for ideal devices, with no series resistance.

In a similar manner, the properties of $CuIn(S_xSe_{1-x})_2$ can be observed, and correlated with composition – in terms of the sulphur fraction x. The addition of sulphur increases the band gap energy from 1 eV for $CuInSe_2$ towards the optimum for the solar spectrum of approx. 1.45 eV. An efficiency of 8.1 % has been achieved for a sulphur fraction of 0.6, corresponding to a band gap of approx. 1.3 eV [13].

The crystal structure, as determined by SEM, has been observed to vary with sulphur content [36]. Films with a lower sulphur content tend to consist of larger crystals, with a higher packing density. This is consistent with higher electrical performance. Conversely, the higher potential efficiency, due to increased band gap, resulting from sulphur incorporation, is to some extent offset by the lower crystal quality of such films.

3.3 Characteristics of copper indium disulphide films and solar cells

Copper indium disulphide is being developed by research groups in a number of countries, in order to fulfil the potentially high conversion efficiency made possible by a band gap, which is closely matched to the solar spectrum. Some of these groups are shown in Table 3.1.

Copper indium disulphide has been produced using a range of techniques. These include direct deposition of the elements, two stage formation, etc, as for $CuInSe_2$ and other chalcopyrites.

A variety of electrodeposition methods have been used for production of $CuInS_2$. This is a low-temperature non-vacuum technique, which offers the possibility of low energy budgets and low capital investment in equipment. It also has the potential for development into a large area deposition technique. Both one-stage and two-stage electrodeposition have been investigated.

In one-stage deposition, all the elements are deposited simultaneously from source materials in the electrolyte [37]. Control of the elemental composition is achieved by altering the concentrations of the source materials in solution, and the applied voltage. Other factors, such as temperature and pH, have an influence on composition. As for ternary compounds generally, an important consideration is maximising the production of $CuInS_2$, while minimising the production of binary compounds, other ternary compounds, metals and metal alloys, etc.

In the two-stage process, a Cu/In alloy is deposited electrolytically, and this is then sulphidised in sulphur vapour [38]. Although this method is more complex, it allows the Cu:In ratio to be controlled during electrodeposition, and the sulphur content can then be controlled independently during the sulphidisation stage.

Country	University or Research Centre	Researchers (not exhaustive)	Research Activities
Germany	Hahn Meitner Institute, Berlin	R. Klenk S. Bakehe	$CuInS_2$, $Cu(In,Ga)Se_2$ by PVD, MOCVD, CVD, etc.
India	Sri Venkateswara University, Tirupati	K.T.R. Reddy	$CuInS_2$-based cells ZnO by spray pyrolysis.
Japan	Shinshu University (Dept. Electrical + Electronic Engineering) Nagano	K. Ito T. Ohashi	$CuInS_2$, $CuIn(S,Se)_2$ by thermal evaporation.
United Kingdom	Northumbria University	R.W. Miles I. Forbes	$CuInS_2$ by sputtering and sulphidisation. Chemical bath deposition of ZnS.
	Cranfield University	D.W. Lane K. Rodgers	$CuInS_2$ by spray pyrolysis.
United States	NASA Glenn Research Center	M. H. Jin K.K. Banger	$CuInS_2$ by spray pyrolysis. Chemical bath deposition of ZnS.

Table 3.1. Representative sample of the research groups working on copper indium disulphide.

Spray pyrolysis has been used to produce $CuInS_2$ [39]. Typical source materials are $CuCl_2$, $InCl_3$ and $CS(NH_2)_2$ for Cu, In and S respectively. Substrate temperatures of 650°C have been used, which would require the use of borosilicate glass. However, development of the technique to the point where lower temperatures could be used would allow the use of soda-lime glass. This would make the technique more economically favourable.

Production of $CuInS_2$ by thermal evaporation has been performed using a two-stage process [40]. In the first stage, Cu and In are evaporated to form a stacked elemental layer. In the second stage, this precursor is exposed to sulphur vapour, and converted to $CuInS_2$. Annealing during sulphidisation mixes the Cu and In layers in the precursor, so that uniform composition results. Annealing temperatures are typically 350 to 500°C. The higher temperature is at the limit of use of soda lime glass, and the lower temperatures would allow large-area soda lime substrates to be used, without excessive thermal stresses.

A similar two-stage process has been used, in which sputtering is used for the formation of the Cu/In precursors [41]. The second stage involves evaporation of sulphur, and reaction to form $CuInS_2$. The sputtering process produces a larger number of thinner layers of Cu and In, which improves mixing, prior to sulphidisation in the second stage. Sputtering has been used industrially for deposition of a wide range of materials, and can produce large area films with good uniformity, and good adhesion to the substrate. These qualities are advantageous for the fabrication of solar cells. Sputtering can deposit material onto substrates held at room temperature, and sulphidisation can be performed within the temperature range of soda lime glass, thus reducing fabrication costs.

Although $CuInS_2$ has a band-gap energy, which is close to the optimum for the solar spectrum, and therefore should result in high-efficiency solar cells, in practice, cells based on $CuInS_2$ generally have lower efficiencies than those based on $CuInSe_2$ [1]. A number of studies have been performed to identify the loss mechanisms [42 , 43]. Some of these include comparison with similar mechanisms in $CuInSe_2$ [42]. A number of specific mechanisms, including high levels of scattering and recombination, and formation of other compounds, have been identified. These are attributable to the relatively low quality of $CuInS_2$ crystals which have been produced so far [42].

Studies of the microstructure of the films, using scanning electron microscopy (SEM) and related techniques, show typical crystal sizes of approx. 1μm, forming a reasonably compact structure, although there are many inter-grain spaces [44]. The crystals are typically rounded, although under certain deposition conditions, more elongated crystals have been produced [42].

Energy dispersive X-ray analysis (EDAX) is used to determine the elemental composition of the film – specifically the fractions of Cu, In and S [43]. The Cu:In ratio determines the conductivity type, and the proportion of sulphur indicates whether this element has been incorporated to the required degree. (This is particularly important in two-stage processes, where the sulphur has to diffuse through the precursor film.) Correlation of the composition data with the input parameters of the deposition process(es) can be used to optimise those parameters. It has been found that a wide range of Cu:In ratios can be achieved [44]. In particular, very Cu-rich material can be produced, for certain deposition techniques [22]. Other analytical methods are required to determine whether these elements are present as $CuInS_2$ or as other compounds.

X-ray diffraction (XRD) has been used to identify the compounds present in the films for different Cu:In ratios [44]. For films with a Cu:In ratio at or close to stoichiometry (1:1), the XRD shows $CuInS_2$ as the dominant phase, with a prominent (1 1 2) peak. Results for In-rich films show the presence of indium sulphide (In_2S_3), with the prominent peaks being (1 0 4) and (1 1 0). Alternatively, copper sulphide compounds, e.g., $Cu_{2-x}S$, have been observed in Cu-rich films [44]. In some studies of fabrication of $CuInS_2$ via CuIn precursors, XRD peaks for copper-indium alloys, notably $Cu_{11}In_9$, have been observed. By etching the surface, to successively remove layers of material, and taking an XRD at each stage, it has been determined that the unconverted metal alloy is at the back of the $CuInS_2$ layer, adjacent to the back contact. This is attributed to insufficient diffusion of sulphur through the film.

In order to improve the efficiency of $CuInS_2$-based solar cells, a variation of the basic device is to fabricate each layer of the device by successively depositing films of different resistivities [45]. This is known as a four-layer structure. The regions of the window and absorber layers adjacent to the junction have low charge carrier concentrations, leading to high resistivity. The low charge carrier concentration increases the depletion layer width, allowing photo-currents to be generated over a greater volume. The regions further away from the junction have higher charge carrier concentrations, and thus lower resistivities. These layers to provide a current path to the external circuit, with lower resultant series resistance for devices fabricated in this manner. A typical four-layer structure is shown in Figure 3.3.

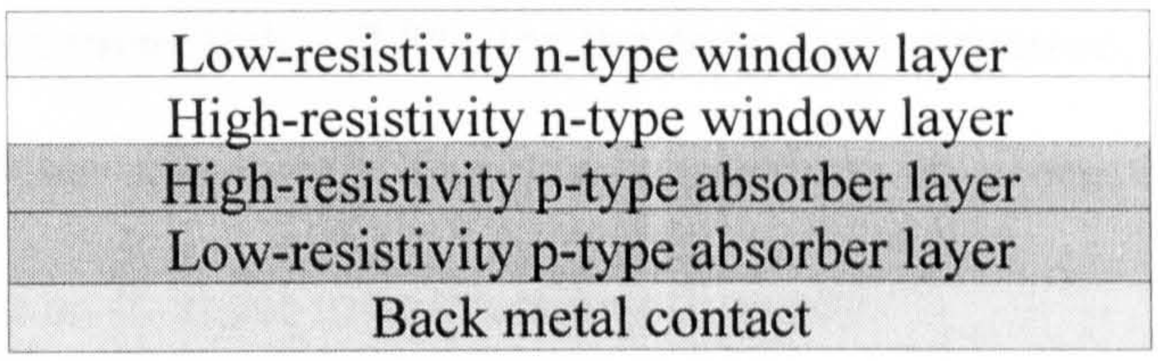

Figure 3.3. Schematic structure of a four layer thin film solar cell.

Previous work has included analysis of a four-layer devices consisting of a $CuInS_2$ absorber layer and a CdS window layer, and comparison with a device with an equivalent two-layer structure [45]. The conductivity of the CdS layer was controlled by doping with indium (In), and that of the $CuInS_2$ by controlling the ratio of elements.

The analysis shows improvements in the electrical output parameters – V_{oc}, I_{sc}, and fill factor, with a consequent improvement in conversion efficiency. The results are shown in Table 3.2 [45]. As the table shows, the conversion efficieny is increased from 5.66 % to 8.25 %. It was also found that there was a slight decrease in lattice mismatch – 2.8% for the four-layer structure, compared to 3.2 % for the two-layer structure. This may contribute to a decrease in electrical losses, and hence an increase in conversion efficiency.

In summary, the grain structure of $CuInS_2$ films has been suggested as leading to scattering and recombination losses. Furthermore, other materials – $Cu_{2-x}S$, In_2S_3, $CuIn_3S_5$ – are present within the absorber layer, in addition to residual unconverted copper indium alloys. Research continues to improve the structural and compositional properties of $CuInS_2$ thin films, in order to approach the potentially high conversion efficiency, which could result from its having a band-gap energy which is close to the optimum for a solar spectrum.

In addition to this, research is being performed to develop other chalcopyrite semiconductors, which have band-gap energies in the required range (and, in some cases, can be adjusted by varying the composition).

Parameter	2-layer device	4-layer device
V_{OC} (V)	0.461	0.58
I_{SC} (A)	0.0269	0.0306
Efficiency (%)	5.66	8.25
Fill factor	0.685	0.697

Table 3.2 Comparison of electrical output of two-layer and four-layer $CuInS_2/CdS$ solar cells [45].

3.4 Window and buffer layers

A number of materials have been developed for use as window and buffer layers in thin film solar cells, with absorber layers of cadmium telluride (CdTe) and copper indium disulphide ($CuInS_2$) and related chalcopyrite semiconductors. These materials are mostly II-VI compounds, such as cadmium sulphide (CdS) and zinc selenide (ZnSe), although there are a few exceptions, such as indium hydroxide ($In(OH)_3$). As CdTe is also a II-VI compound, many of the techniques used to fabricate this material are used in the fabrication of window layers. As CdS had previously been developed for other applications, such as light sensors, it has been possible to transfer the technology to the production of photovoltaic materials. This material was applied to fabrication of solar cells at an early stage in the development of thin film devices.

A number of zinc compounds have been investigated, as alternative window layer materials. These have generally been used in conjunction with chalcopyrite absorber layers, to produce completely cadmium-free solar cells. These zinc compounds have higher band-gap energies than CdS, and hence shorter cut-off wavelengths. As a result, they transmit a larger fraction of the solar spectrum, and therefore solar cells using zinc compounds as window layers have the potential for higher efficiency. A number of window layer materials are listed in Table 3.3, showing their band-gap energies and cut-off wavelengths. It can be seen that zinc oxide (ZnO) and zinc sulphide (ZnS) have very large band-gap energies, giving cut-off wavelengths in the ultra-violet part of the spectrum. Thus they are transmissive over substantially all of the solar spectrum, and the potential for high conversion efficiency is particularly high for these materials.

Material	Bandgap (eV)	Cut-off wavelength (nm)
CdS	2.42	510
ZnSe	2.65	470
ZnS	3.70	330
ZnO	3.40	365

Table 3.3. Commonly used window layer materials, showing their band-gap energies and cut-off wavelengths.

Although ZnO is sometimes used as a single window layer in chalcopyrite-based solar cells, it has been found that interactions with the absorber layer result in low open circuit voltages [46]. If a thin (~ 100 nm) buffer layer is deposited between deposition of the ZnO and the absorber layer, it prevents such interactions, including inter-diffusion between these layers, as well as sputtering damage during subsequent deposition stages. This results in higher open circuit voltages. Materials used for this purpose include ZnS, CdS and zinc hydroxide ($Zn(OH)_2$). Although ZnO and ZnS have good optical properties, their high band-gap energies result in low intrinsic carrier concentrations, and hence high resistivities. (This can be overcome by doping with group III metals, such as gallium (Ga) or aluminium (Al) [47, 48, 49].) In order to increase conductivity, ZnS can be combined with ZnSe to form the alloy ZnS_xSe_{1-x}. This has an intermediate band-gap energy, which increases with the sulphur fraction (x). As the band-gap increases, the wavelength range for high optical transmittance increases, but the conductivity decreases. A compromise must therefore be reached between these two properties, in order to optimise efficiency.

A number of the thin film deposition technologies, which have been developed for other applications, can be adapted to the production of II-VI compounds for photovoltaic applications. Applicable processes include thermal evaporation, sputtering, spray pyrolysis, electrodeposition and chemical bath deposition (CBD). Some of these are described in the next sections.

3.4.1 Thermal evaporation of II-VI compounds

Thermal evaporation is a technique which is widely used to deposit thin films of materials onto substrates, for a range of applications [14]. The evaporation and subsequent deposition of single elements, such as metals, presents little difficulty (unless the melting and boiling points are high). However, when compounds are heated, in order to evaporate them, they may partially decompose into their constituent elements. These elements will, in general, have vapour pressures which differ in ratio from the elemental composition of the source material. This difference will be manifest in the composition of the deposited film. In such cases, more complex techniques, such as separately evaporating the elements (co-evaporation), should be used. It has been found that most of the II-VI compounds used in photovoltaics can be evaporated directly [14]. This allows a single source to be used, resulting in less complex fabrication technology. The base pressure required for thermal evaporation is of the order of 10^{-5} mbar, and a standard rotary-diffusion pump vacuum system is generally used.

Source temperatures of 700°C are required to evaporate CdS and CdTe. The temperature of the substrate is determined by a number of factors. Formation of a continuous film requires that islands formed around nucleation centres merge into each other. This necessitates a certain degree of mobility in the deposited atoms. The mobility increases with temperature, thus setting a lower limit. However, some of the deposited material re-evaporates, particularly at high temperatures. As a result of these factors, there is a range of temperatures (upwards of 200°C), which results in optimal deposition. The substrate temperature is also limited by the thermo-mechanical properties of the substrate. In order to minimise cost, it is preferable to use low-cost substrate materials, one of which is glass. Ordinary

(soda-lime) glass tends to deform at temperatures much above 400°C. Although borosilicate glass, such as the Corning range, can be used at higher temperatures, this material is more expensive. Thus, economic factors generally limit the substrate temperature to less than 400°C.

A problem which occurs in thermal evaporation is spattering - the ejection of relatively large pieces of solid material from the source. This material can impact on the substrate with sufficient energy to damage the partially formed film, resulting in pinholes and other forms of localised defects. This is a particular problem in the deposition of buffers layers, as these are extremely thin, and impact damage can easily penetrate the layer to form a pinhole. In some cases, barriers may be placed between the source and substrate, to avoid line-of-sight transport. This stops spattered material, but allows evaporated material to flow round the barrier. However, the efficiency of vapour transport may be reduced, and a design compromise is necessary to meet these requirements.

Post-deposition heat treatment can improve the properties of deposited films, leading to higher device efficiencies. One such treatment is heating to temperatures above 400°C in the presence of cadmium chloride ($CdCl_2$) (in the case of cadmium compounds) and/or O_2. For zinc compounds, zinc chloride ($ZnCl_2$) is used in place of $CdCl_2$. This enhances grain growth, thus reducing the effects of lattice defects at grain boundaries.

Cells with CdTe absorber layers and CdS window layers produced by close-spaced vapour transport (CSVT - a variant of thermal evaporation) have efficiencies up to 15.8 % [1]. Similar performances have been achieved by cells with CdS window layers produced by a number of different processes, including conventional thermal evaporation.

Thermal evaporation is one of a number of methods used for deposition of ZnO. It has been found that, although the resistivity of this material is high, it can be reduced by doping with other elements [47]. Group III metals, substituting for Zn, produce n-type doping. The metals Ga and Al can be incorporated into the base material up to concentrations of a few per cent. For concentrations up to ~ 1%, these metals substitute for Zn, resulting in high doping densities, high charge carrier concentrations, and hence reduced resistivities. For higher concentrations, the doping metals form separate grains of Ga_2O_3 or Al_2O_3, intermixed with the ZnO grains. This tends to slightly increase resistivity. Thus the resistivity is at a minimum for ~ 1% concentration of dopant. The optical transmittance tends to decrease with dopant concentration [48]. Therefore, a compromise must be made between the optical and electrical performance of the material.

3.4.2 Chemical bath deposition of II-VI compounds

Chemical bath deposition (CBD) is used to produce thin films of a wide range of materials, including II-VI compounds, for a number of applications [50]. As a non-vacuum low-temperature technique, it offers low equipment costs and low energy budgets. In the development of photovoltaics, and in other applications, it has demonstrated the ability to be applied to deposition of large area films. These factors potentially allow the production of low cost, large area thin film solar cells, which should contribute to lowering the costs of solar cell fabrication. It has the further advantage over electrodeposition, that it can be used to deposit films directly onto non-conductive substrates (or superstrates). This makes it applicable to solar cells using glass superstrates.

Chemical bath deposition has been used for deposition of a number of materials for photovoltaic applications. One of these is CdTe, for use as absorber layers. A larger number of materials have been deposited, by this technique, for use as window layers. This includes CdS, ZnSe and ZnS [50].

The chemical reactions involved have a number of common features, which are independent of the particular material being deposited, and hence of the source materials being used. A source material is used for each of the elements (one metal and one non-metal) in the deposited film. The source material for the metal is a soluble salt. For Cd, compounds such as cadmium sulphate ($CdSO_4$) and cadmium nitrate ($CdNO_3$) are used. Suitable soluble compounds of the non-metallic element are not always available (depending on which non-metallic element is being used), so soluble ions of this element are produced by reaction with another material present in the solution. Ammonium or metal hydroxides (NH_4OH, NaOH, KOH, etc) provide hydroxyl ions (OH^-), which break down a range of suitable source materials. Thus alkaline conditions are used for CBD of a wide range of materials.

The reactions are broadly similar for a number of different materials. Those for the deposition of CdSe are shown, as an example

$$CdSO_4 \rightarrow Cd^{2+} + SO_4^{2-} \qquad (3.1)$$

The non-metallic ions are generally provided by the breakdown of a suitable compound in the presence of hydroxide ions – thus requiring an alkaline solution.

Selenourea ($CSe(NH_2)_2$) is a common source for selenide (Se^{2+}) ions.

$$CSe(NH_2)_2 + OH^- \rightarrow SeH^- + CH_2N_2 + H_2O \qquad (3.2)$$

$$SeH^- + OH^- \leftrightarrow Se^{2-} + H_2O \qquad (3.3)$$

For the production of sulphides, thiourea ($CS(NH_2)_2$) may be used.

Because the solubility product of the ions is extremely low, most of them combine in solution to form a precipitate of the compound.

$$Cd^{2+} + Se^{2-} \rightarrow CdSe \qquad (3.4)$$

This precipitate settles onto the surface of the substrate, forming a layer with poor adhesion and uniformity, and with low optical transmittance. This is known as homogeneous deposition (or precipitation), and is shown in Figure 3.4.

In order to prevent this, additional materials are added to the solution, which form complex ions with the metal ions. The solubility product of this complex ion with the non-metallic ion is much higher, allowing more ions to remain in solution. The most widely used such material is NH_3, which is used for deposition of a number of materials.

$$Cd^{2+} + 4NH_3 \rightarrow (Cd(NH_3)_4)^{2+} \qquad (3.5)$$

The NH_3 exists in equilibrium with NH_4OH, which provides the OH^- ions to break down the source material for the non-metallic ion.

$$NH_3 + H_2O \leftrightarrow NH_4^+ + OH^- \qquad (3.6)$$

For this reason, NH_4OH is used in the CBD of a wide range of II-VI materials. The higher solubility of the complex ions allows them sufficient time to migrate to the substrate surface. If the ion reaches an active site on the surface (such as an active ion or a crystal defect), it can decompose and react with the non-metallic ion.

$$Cd(NH_3)_4^{2+} + Se^{2-} \rightarrow CdSe + 4NH_3 \qquad (3.7)$$

These molecules remain attached to the active site, and act as nucleation centres for further deposition. Circles of film grow from each such centre, until they merge with each other, forming a continuous film. This is known as the heterogeneous process, and is shown in Figures 3.5 and 3.6.

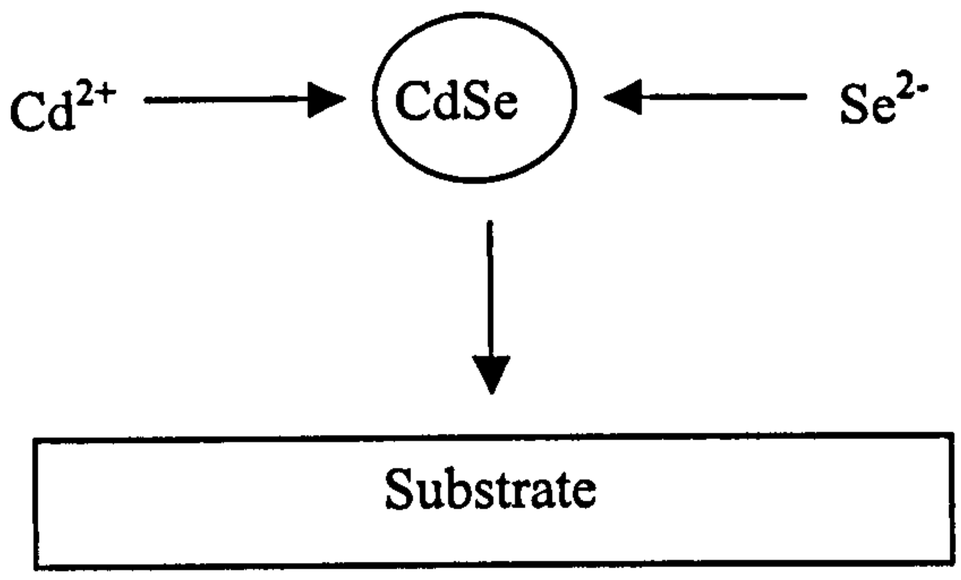

Figure 3.4. Homogeneous deposition of CdSe, showing grain formation in solution, and subsequent precipitation to the substrate surface.

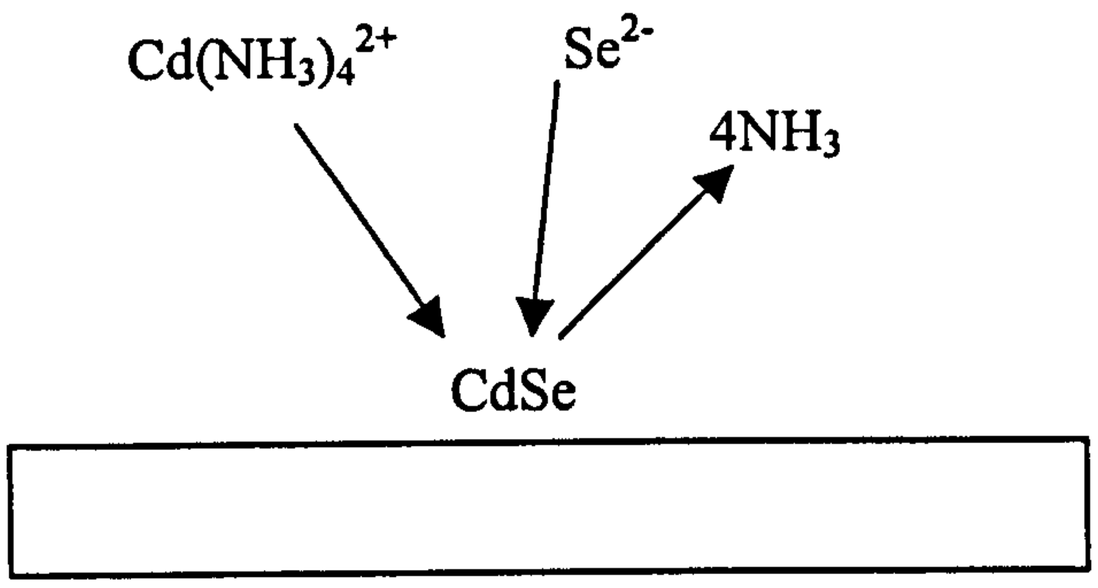

Figure 3.5. Heterogeneous deposition, showing formation of complex ions, their migration to the substrate surface, and their reaction to form CdSe.

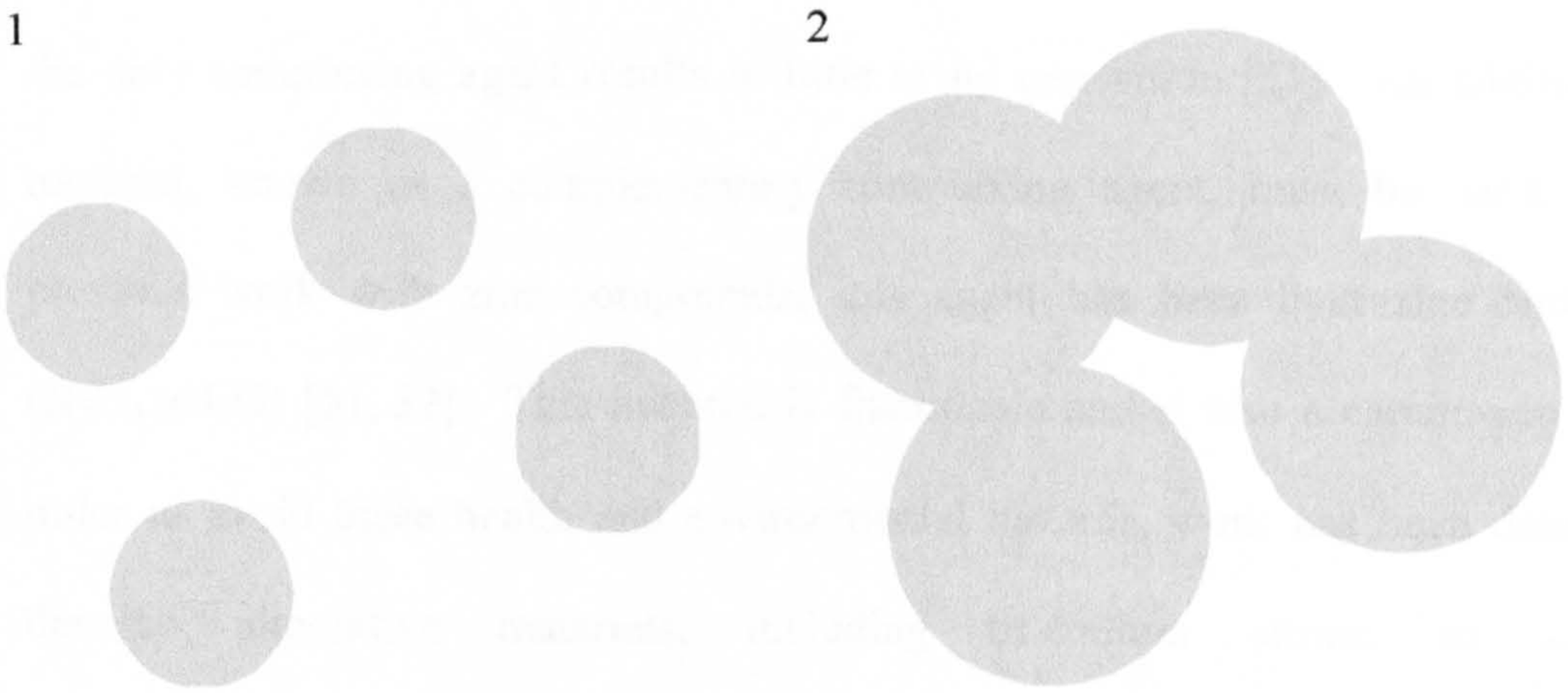

Figure 3.6. Growth of thin films by heterogeneous deposition. Growth starts at a number of nucleation centres, which then grow into islands. These merge until the substrate is completely covered. Subsequently, the film grows in thickness.

The resulting film generally has good adherence and uniformity, and is highly transmissive over the wavelength range longer than the cut-off wavelength. Control of the solution conditions, including the concentrations of the source materials and other components, is used to produce heterogeneous deposition, in preference to homogeneous deposition.

When depositing CdS or CdSe, ammonia provides sufficient complex ions to produce heterogeneous deposition. When depositing ZnS, the use of ammonia as the only complexing agent results in little or no deposition [51]. An additional material, known as a complementary complexing agent, must be used. In previous work with zinc compounds, this agent has been hydrazine hydrate ($N_2H_4.nH_2O$) [51, 52]. This material is flammable and is also a carcinogen. In order to avoid these health and environmental hazards, work has been done to develop alternative materials, including tri-sodium citrate, as safer, complementary complexing agent for CBD of ZnS [53].

3.4.3 Physical and compositional properties of films produced by chemical bath deposition

These properties include film thickness, fraction of elements – determined by energy dispersive X-ray analysis (EDAX), and crystal phases and sizes – determined by X-ray diffraction (XRD). Assessment of film quality (uniformity, etc) can be made by scanning electron microscopy (SEM). Measurements of optical transmittance give the band-gap energy. Differences from the value for single crystals of the material can indicate details of crystal structure.

Measurements of film thickness can be used to determine rate of growth, and to identify the range of conditions (concentrations, temperature) required for

successful growth. It has been found that, for each material used in the solution, there is a limited range over which films are produced. This varies with the particular material being deposited. Similarly, a limited range of temperatures result in successful deposition. Although this varies to some extent with material, temperatures in the range 60 to 80°C are generally used.

One of the most significant features of CBD is that film thickness does not increase beyond a certain period of time after immersion of the substrate in the solution. This varies with material and solution conditions, but typical times for cessation of film growth of 30 minutes to a few hours have been observed. This is generally attributed to depletion of the solution. Reactions proceed as soon as the materials are added to the solution (including the reactions for both heterogeneous and homogeneous reactions). After a period of time, all of the source materials have reacted, and no further growth is possible (unless additional materials are added during the process). A typical graph of film thickness vs time is reproduced in Figure 3.7 [51].

X-ray diffraction can be used to identify the compound or compounds present in the film, as well as their crystal phases. In addition, the width of the peaks gives an indication of typical crystal sizes within the film. Many of the II-VI compounds deposited for photovoltaic applications have been observed in both the face-centred cubic (zincblende) structure, and the hexagonal (wurzite) structure.

Measurements of the width of XRD peaks shows higher and sharper peaks for thicker films [50]. This would suggest that there is a correlation between crystal size and film thickness, with thicker films tending to have larger grains. For films with thicknesses of ~100 nm, the XRDs show that the material is almost amorphous.

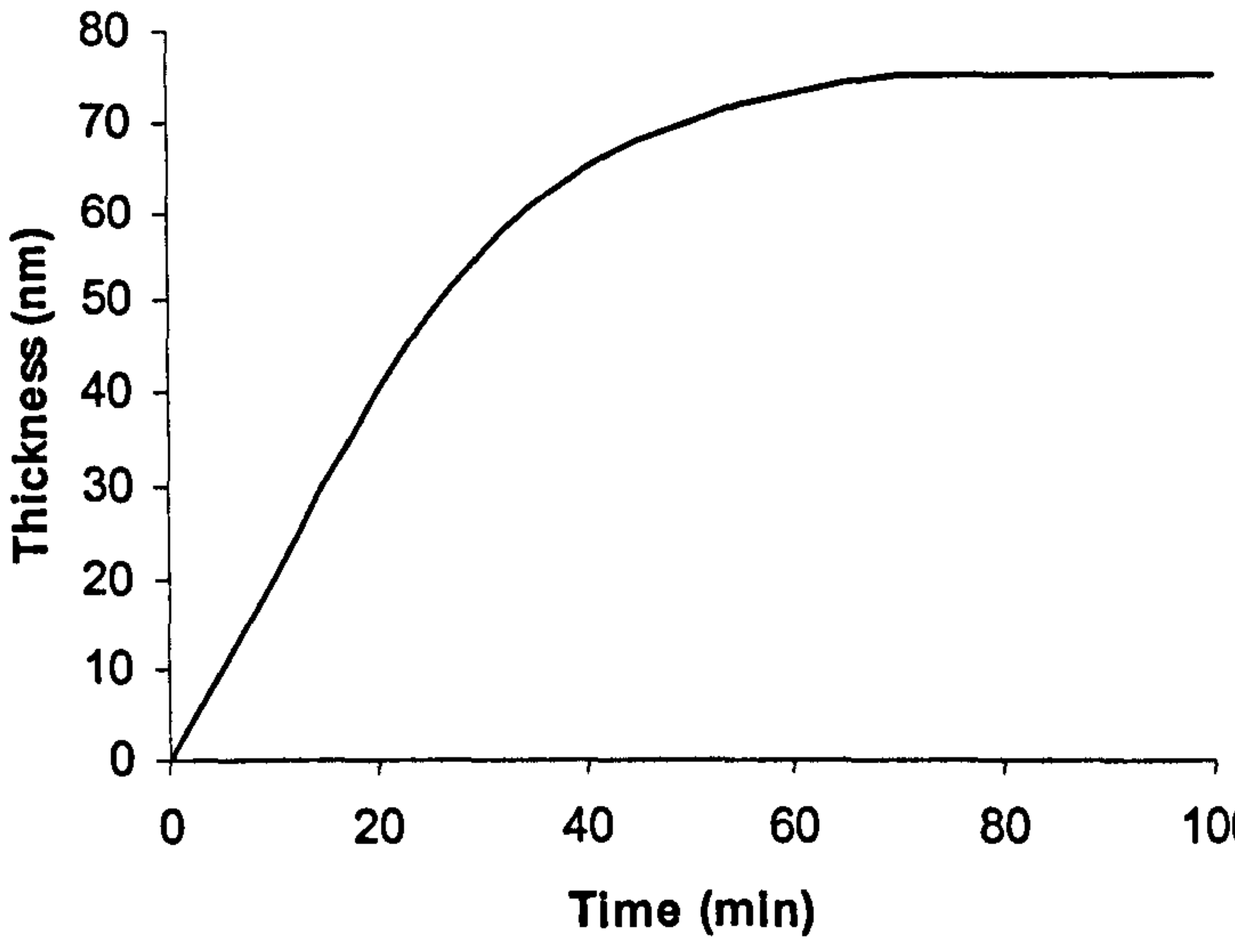

Figure 3.7 Film thickness vs time for ZnS (Reproduced from [51].)

Measurements of optical transmittance can be used to determine the cut-off wavelength. By converting this data to a graph of $(\alpha hv)^2$ vs hv, a more accurate value of the band gap energy can be derived. This gives values which are generally slightly higher than for the equivalent bulk material (large crystal).

One explanation for this is given in terms of quantum confinement [50]. The confinement of electrons within small crystals results in a series of closely-spaced discrete energy levels, rather than continuous energy bands. This results in the lowest conduction level being slightly higher than the base of the conduction band (for a large crystal), and similarly the highest valence level is slightly lower. These effects increase the bandgap slightly, compared to that for a large crystal, and this increases as crystal size decreases.

It has been observed that the increase in bandgap is larger for thinner films. The XRD results show that thinner films have smaller crystals, so that the observed trend in bandgap increase would be consistent with quantum confinement.

Typical grain sizes of 5 nm have been derived from optical measurements of II-VI compounds [50]. As for the XRD observations, there is a correlation between grain size and film thickness.

3.4.4 Optical and electrical properties of films produced by chemical bath deposition

Window layers of CdS have reasonable electrical conductivity, and good optical transmittance (80 – 90 %) at wavelengths longer than the cut-off has been observed [54]. However, the band gap energy of 2.42 eV results in a cut-off wavelength of approx. 510 nm. As the solar spectrum peaks at approximately this

wavelength, this results in absorption of much of the short-wavelength component of the solar spectrum.

In order to overcome this, a number of materials with higher band gap energies have been developed. (An additional motive for developing these materials is to provide alternatives to cadmium compounds, with their associated toxic hazards.) Binary compounds of zinc have been studied for such applications. These include ZnSe (band gap energy: 2.69 eV) and ZnS (3.7 eV) Both these materials can be deposited by CBD [51, 52].

ZnSe has a slightly higher band gap energy than CdS, and thus transmits over a wider wavelength range. Transmittances of 90% have been observed in the wavelength region longer than the cut-off. It has a fairly high electrical conductivity, and can thus provide sufficient lateral conduction to act as a (single) window layer.

The very high band gap energy of ZnS results in high optical transmittance over substantially all of the solar spectrum. Measurements of transmittance vs wavelength show a cut-off wavelength of approx. 350 nm, and transmittance at longer wavelengths in excess of 80% [51]. A typical graph of transmittance vs wavelength is reproduced in Figure 3.8. However, this high band gap energy also reduces the charge carrier concentration, leading to low electrical conductivity. Therefore, ZnS is generally used as a buffer layer, between the absorber layer and a front contact layer made of a more conductive material, such as (doped) ZnO. This material also has a high band gap energy (3.4 eV), giving a cut-off wavelength of 350-400 nm, and is thus transmissive over much of the solar spectrum.

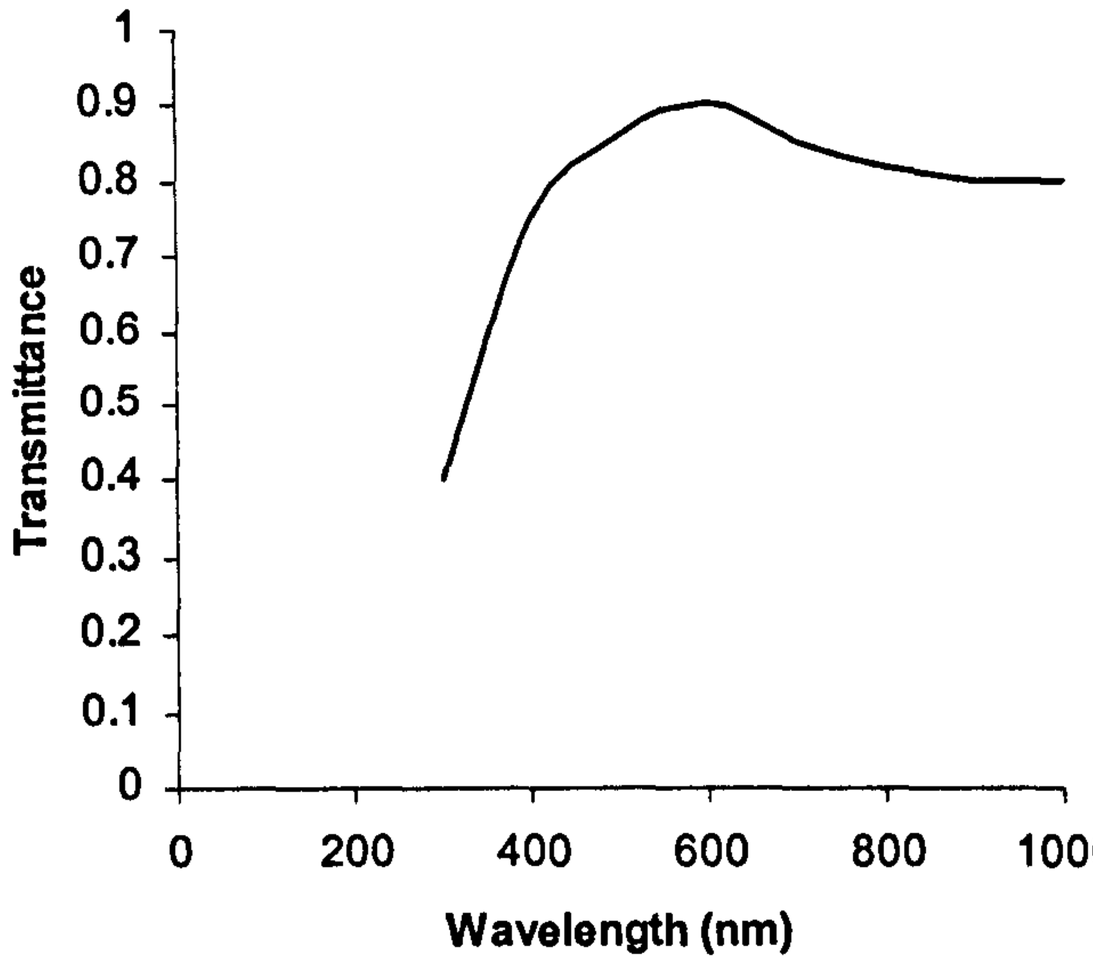

Figure 3.8. Transmittance vs wavelength for ZnS deposited by CBD. (Reproduced from [51].)

Transmittances at longer wavelengths of 80 to 90% have been observed for ZnO films, produced by a range of deposition methods. Thus a ZnO-ZnS window layer can allow perhaps as much as 80% of the relevant solar spectrum to be transmitted to the p-n junction.

Much work continues on deposition of window layers based on II-VI compounds and alloys, using both thermal evaporation and CBD. Modification of the chemical bath deposition process, involving less toxic materials will improve the environmental aspects of the production of solar cells. One objective is to develop improved combinations of optical transmittance and electrical conductivity. In particular, significant reduction of the high resistivity of ZnS would combine with good optical transmittance to provide a suitable material for buffer layers , for use with $CuInS_2$ and other chalcopyrite absorber layers.

4 Experimental Procedure

4.1 Sputtering of copper indium alloy

Sputtering was used both for the deposition of the Mo back contact and the Cu/In alloy. The sputtering was performed in a Nordiko 2000 r.f. magnetron sputtering machine, which is shown in the photograph in Fig 4.1, and schematically in Fig. 4.2. This machine can operate two targets simultaneously, each powered by an r.f. generator, and has a turntable on which up to three platens can be mounted. Substrates for sputter-deposition are placed on these platens. As the turntable rotates, each platen passes alternately under each target.

The substrates for deposition were microscope slides (76 x 26 mm). Seven slides could be mounted on each platten, giving a total of 21 for each deposition run. The slides were identified with a two-part numerical index (e.g. 2/14), written onto the reverse side of the slide with a diamond scriber. The first part of the index indicated the sputtering run, and hence the sputtering conditions. The second part indicated which platten each slide was placed on, and which part of the platten. Thus a given slide was always placed on the same platten and the same position, for sputtering of both the Mo and the Cu/In alloy. In subsequent analysis, the position of the slide on the platten could be re-established from its index. This allowed the properties of the films to be measured as a function of position over the whole set of slides on a single platten. In this way, the set could be regarded as effectively a single substrate, of approx. 10 x 10 cm, onto which a large area thin film was deposited, and over which the film properties could be measured.

In the preliminary stage, Mo back contacts were sputtered onto glass substrates Prior to sputtering, the slides were cleaned in distilled water, isopropanol and dry nitrogen.

Figure 4.1. Nordiko 2000 r.f. magnetron sputter deposition system

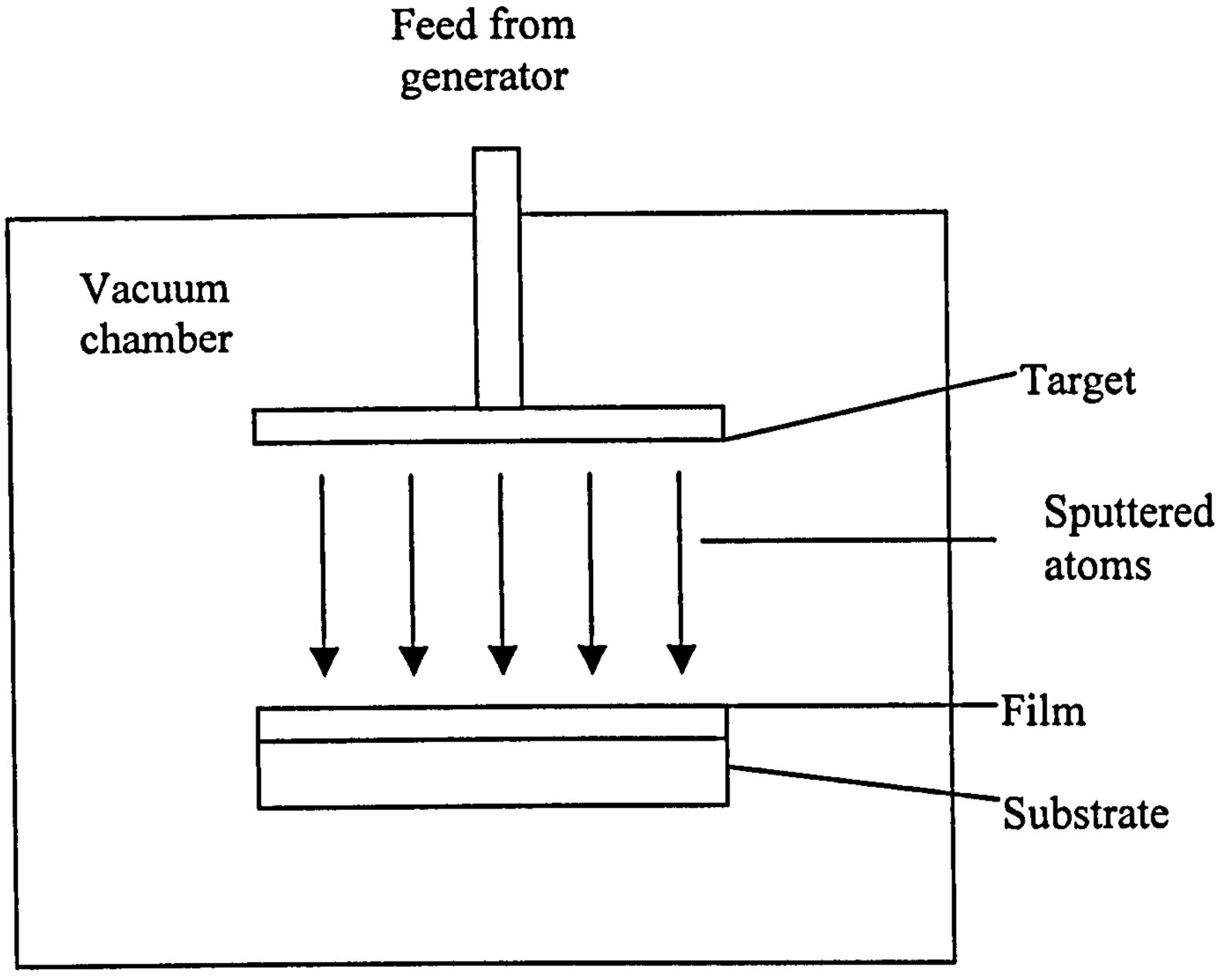

Figure 4.2 Simplified diagram of a sputtering system.

After placing onto the plattens, and loading into the sputtering machine, a sputter etch was used to remove any residual contamination from the substrates. A pre-sputter removed any contamination from the surface of the Mo target.

Previous work using this sputtering machine has found that the best uniformity of thickness over the area of the platten was achieved by using the maximum separation (100 mm) between target and substrate [1]. This was used for sputtering of both Mo and Cu/In. For sputtering of Mo, a target power of 200 W was used. The deposition time was four hours and the turntable was rotated continuously at 1 rpm.

Targets of Cu and In were then installed in the sputtering machine. These had purities of 99.998 % and 99.999 % respectively. The Mo-coated substrates were cleaned with distilled water, isopropanol and dry nitrogen. They were then loaded into the sputtering machine, and a sputter-etch and pre-sputter were performed, using the same conditions as prior to Mo sputtering.

The turntable rotation speed of 1 rpm, over a deposition period of 24 hours, resulted in approx. 1440 cycles of alternating deposition of Cu and In. In the absence of mixing, this would produce alternating layers of these metals, each less than 1 nm thick. However, the collisions of incoming sputtered atoms with atoms already deposited displace the latter by a distance of typically a few nm. As a result, complete mixing of the layers should result, as deposition occurs, without the need for further processing (e.g., annealing). The degree of uniformity was investigated by subsequent analysis.

In order to form stoichiometric $CuInS_2$ films, it is necessary to control the composition of the Cu/In pre-cursors, from which they are fabricated. This is controlled by the relative deposition rates of the two materials. The deposition

rates in turn are determined by the r.f. power applied to each target [2, 3]. By applying different target powers on each sputter deposition, each set of films should have a different composition. Measurement of the composition of the film can then be used to select the target power settings which give the required composition.

Analysis of the sputtered films consisted of various measurements of the composition, and its variation both with area and depth. Measurement of elemental composition was made using Energy Dispersive X-ray Analysis (EDAX) at Northumbria University, and Rutherford back scattering (RBS) at Cranfield University. X-ray diffraction (XRD) was used to identify the compounds into which the elements had formed, and the particular crystal phases present. Scanning electron microscopy (SEM) was used to examine the small-scale structure and uniformity of the layers, in conjunction with a visual inspection to assess the large-scale uniformity, as well as adhesion to the substrate. These analytical techniques are described in sections 4.6 to 4.10, in terms of their basic principles, and their application to the materials produced in this work.

4.2 Conversion to copper indium disulphide using high pressure elemental sulphidisation

In this conversion method, the substrates with Cu/In precursor layers were placed in a graphite box, which was heated within an evacuated chamber. This is a continuation of work previously performed at Northumbria University [4, 5]. A strip heater in a conventional cylindrical vacuum chamber was used in the first set of experiments. For subsequent conversions, a tube furnace was used. By enclosing the substrate/precursor in a small volume, together with the sulphur to be evaporated, the vapour pressure of the sulphur inside the box is somewhat

greater than that in the larger chamber. This increases the density of the sulphur vapour, potentially increasing the rate of incorporation into the precursor films, and hence their conversion to $CuInS_2$.

For heating by strip heater, a graphite box with lid (40 x 30 x 30 mm, inc. lid) was fabricated, with an internal space sufficient to hold a substrate measuring 26 x 26 mm (approx. 1/3 of a microscope slide). The box, with enclosed substrate/precursor, was mounted directly on the stainless steel strip heater. The vacuum chamber was then evacuated to less than 10^{-1} mbar using a rotary pump, and the valve to the vacuum pump closed. The strip heater was then heated by the current passing through it. This current was controlled via a variac auto-transformer, and a fixed-ratio step-down isolating transformer, which provided the low voltage and high current required for the relatively low resistance heating element. A schematic diagram of the experimental apparatus is shown in Figure 4.3.

A series of experiments were performed, in which different temperatures were applied, and for different times.

Although the graphite box provided improvements in uniformity and stability over heating of a substrate placed directly onto the strip heater, there were still spatial and temporal fluctuations in the temperature. In order to overcome these, a tube furnace was used for the remaining conversion experiments.

A Carbolite CFW 1 furnace was used. This furnace has four spiral ceramic heating elements, spaced equally around the central (tube) axis, and parallel to it. The tube furnace is shown in Figure 4.4 and schematically in Figure 4.5. An outer vitreous silica tube was mounted permanently in the furnace, and an inner quartz tube could be inserted inside this, along the same axis. (A number of quartz tubes were available, and these could be changed between experiments using different materials, to avoid cross contamination.)

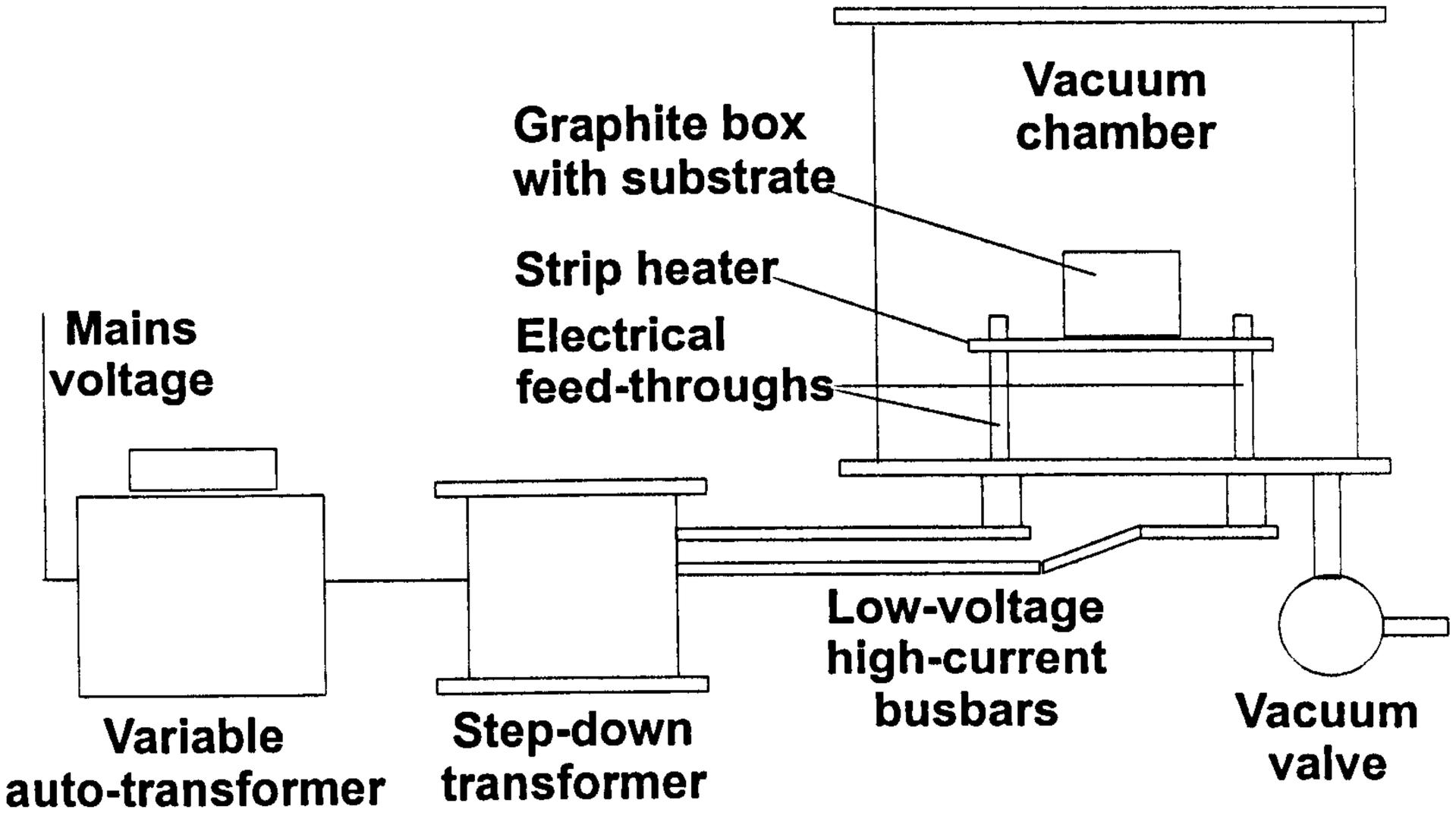

Figure 4.3. Schematic diagram of the experimental apparatus for sulphidisation in a graphite box, using a strip heater.

The disposition of the heating elements, augmented by the indirect heating via the vitreous silica outer tube, resulted in a highly spatially uniform temperature distribution. The large thermal mass, including the insulation outside the heating elements, produced a much more stable temperature. (Both the spatial uniformity and temporal stability of the temperature were confirmed by preliminary measurements.) The bore of the quartz tubes was nominally 40 mm. In order to fit within this dimension, a new cylindrical graphite box was fabricated, with a diameter of 35 mm. This had a rectangular internal space sufficient to hold a microscope slide (76 x 26 mm). The lid was formed from the same graphite as the cylinder. The graphite box was mounted on the end of a steel rod, which in turn was joined to the end cap for the tube. The length of the rod was such that the box would be at the centre of the tube furnace. A glass tube (10 cm) with one end sealed, was inserted into the other end of the graphite box. Sulphur placed at the sealed end of the tube would be approx. 15 cm from the centre of the furnace, and would therefore be at a somewhat lower temperature.

At the beginning of each experiment, the graphite box containing the substrate/precursor was inserted into the tube furnace. The tube was evacuated to a pressure of less than 10^{-1} mbar using a rotary vacuum pump. The heating elements were then switched on and the furnace heated to the required temperature. In order to further increase temperature stability, a PID controller was used. The furnace was left at the required temperature for a specified period, after which the heating elements were switched off. A fan was used to blow air between the outer vitreous silica tube and the inner quartz tube, providing forced convective cooling to reduce the cooling time.

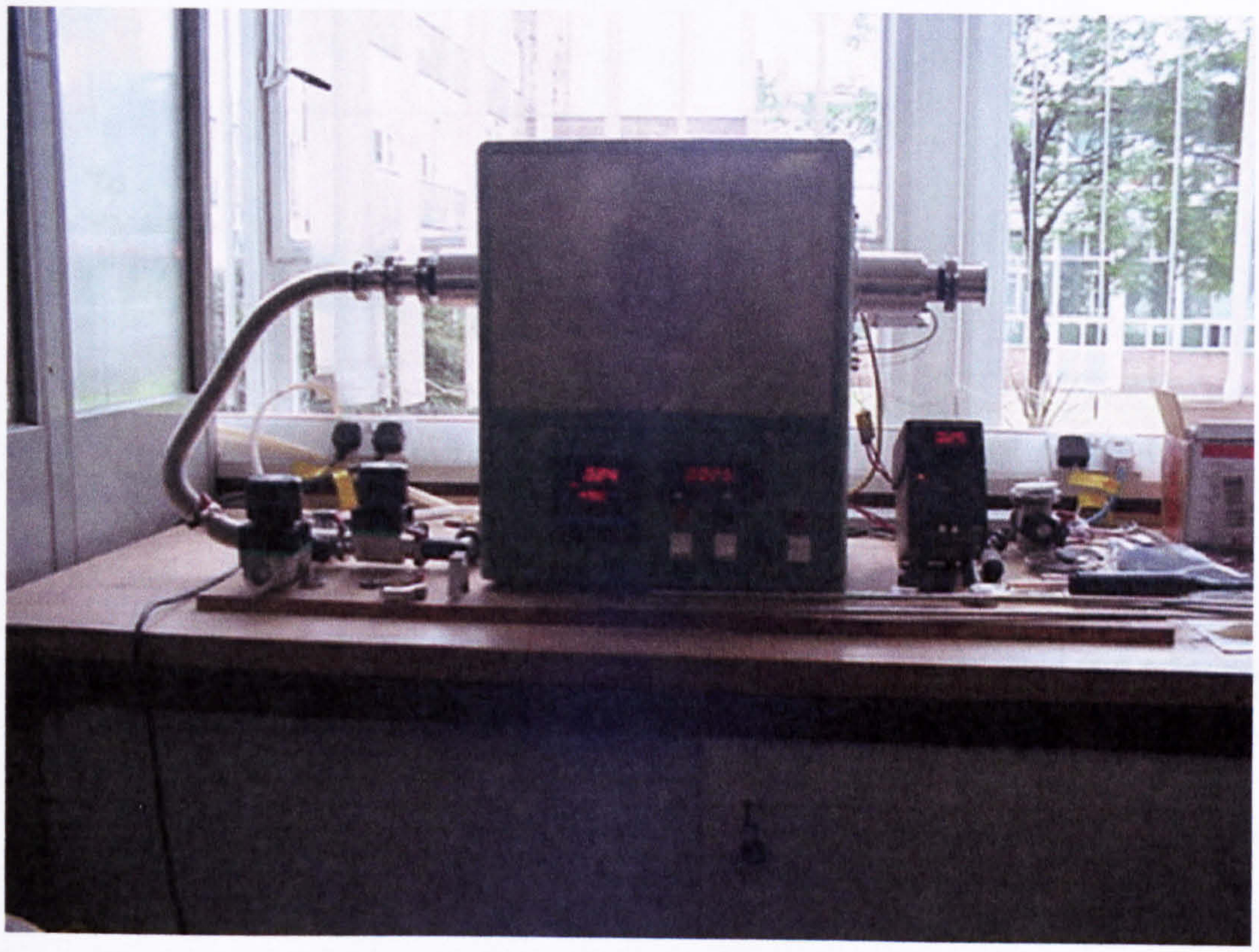

Figure 4.4. Carbolite CFW 1 tube furnace, showing mounting system for quartz tubes.

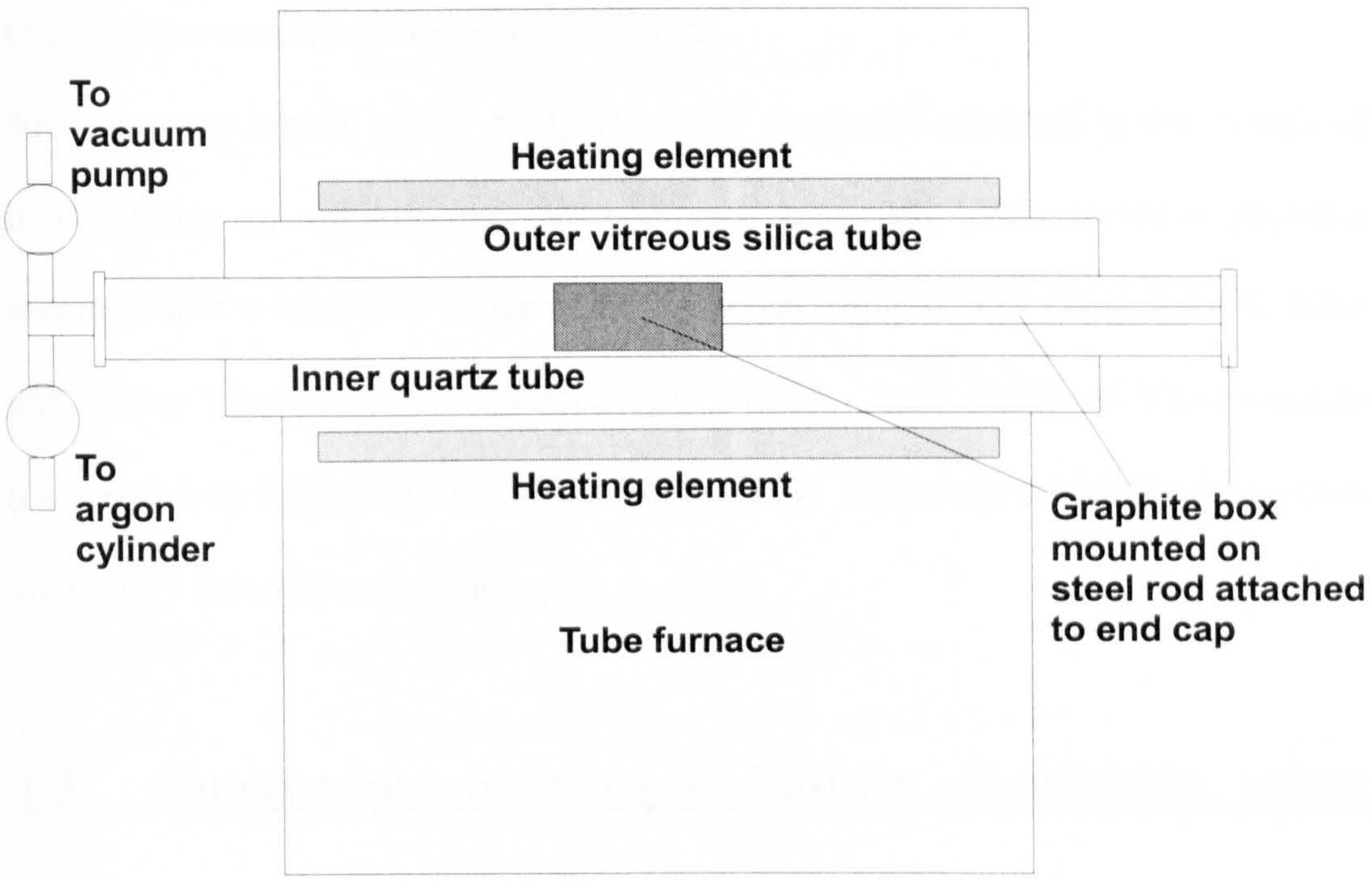

Figure 4.5. Schematic diagram of tube furnace showing heating elements, tubes, and graphite box, etc.

When the furnace had returned to approx. room temperature, argon was used to exhaust the sulphur vapour from the tube, without it having to pass through the vacuum pump. (Argon was used as a carrier gas for sulphur vapour transport, to be described in section 4.3, and was used in this section of the work to exhaust sulphur vapour after each experiment.) The graphite box could then be withdrawn from the furnace, and the substrates removed for subsequent analysis of the films, to assess the extent of conversion to $CuInS_2$.

An important aspect of the analysis of the converted material is the extent of incorporation of sulphur into the precursor material. This includes physical incorporation - measured in terms of elemental composition using EDAX, RBS and X-ray photo-electron spectroscopy (XPS) - and chemical incorporation (conversion to sulphides), identified using XRD. These are described in sections 4.6 to 4.11 on analytical techniques.

4.3 Conversion to copper indium disulphide using elemental sulphur in argon carrier gas

In this variation of elemental sulphidisation, sulphur was thermally evaporated into a flowing argon stream, which carried the sulphur over the substrate/precursors. Some of this sulphur was incorporated into the precursor layers, leading to the formation of sulphides of the metals. This method combines some of the advantages of elemental sulphidisation in vacuum, and sulphidisation using hydrogen sulphide [6, 7, 8]. Hydrogen sulphide, being a gas, can be transported over relatively large distances, potentially giving even coverage over large areas. As it is not limited to direct (line-of-sight) travel, it can flow around complex channels. In larger scale production, this could allow a large number of substrates to be stacked in the chamber, for conversion of Cu/In to $CuInS_2$.

However, hydrogen sulphide presents a toxic hazard, and it is therefore preferable to use an alternative material. Elemental sulphur vapour does not present the same toxic hazard, but evaporation is, to a certain extent, directional, leading to non-uniform deposition over large areas. By evaporating the sulphur into an argon stream, it is possible to gain the advantages of gaseous flow, without the toxic hazards of hydrogen sulphide.

The tube furnace, described in the previous section, was used for this part of the experimental work. As mentioned previously, this provided a uniform and stable temperature for the conversion process. A metal boat containing the sulphur and a metal plate, on which the substrate/precursor was placed, were mounted on a stainless steel rod, attached to the end cap for the tube. These were positioned, such that the substrate was at the centre of the furnace, and the sulphur was approx. 15 cm upstream, relative to the argon flow. The arrangement of these components is shown in Figure 4.6.

With these components in place in the tube, the valve to the rotary vacuum pump was opened, and the tube was evacuated to less than 10^{-1} mbar. The vacuum valve was then closed. Argon from a standard industrial gas cylinder passed through a regulator, limiting the pressure to 1 bar, and the flow rate to 1 Ls^{-1}. A valve was then opened to admit the argon into the quartz tube. A relief valve at the opposite end of the tube allowed the argon to be exhausted, without sulphur passing through the vacuum pump, possibly causing damage. The system of valves and gas and vacuum connections is shown in Figure 4.6.

The heaters were then switched on, and the furnace was heated up to the selected temperature. The argon was allowed to continue flowing, after the heaters were switched off, in order to reduce the time required for cooling of the furnace.

Analysis of the converted material was essentially the same as for high pressure sulphidisation, and used the same items of measurement equipment for each type of analysis.

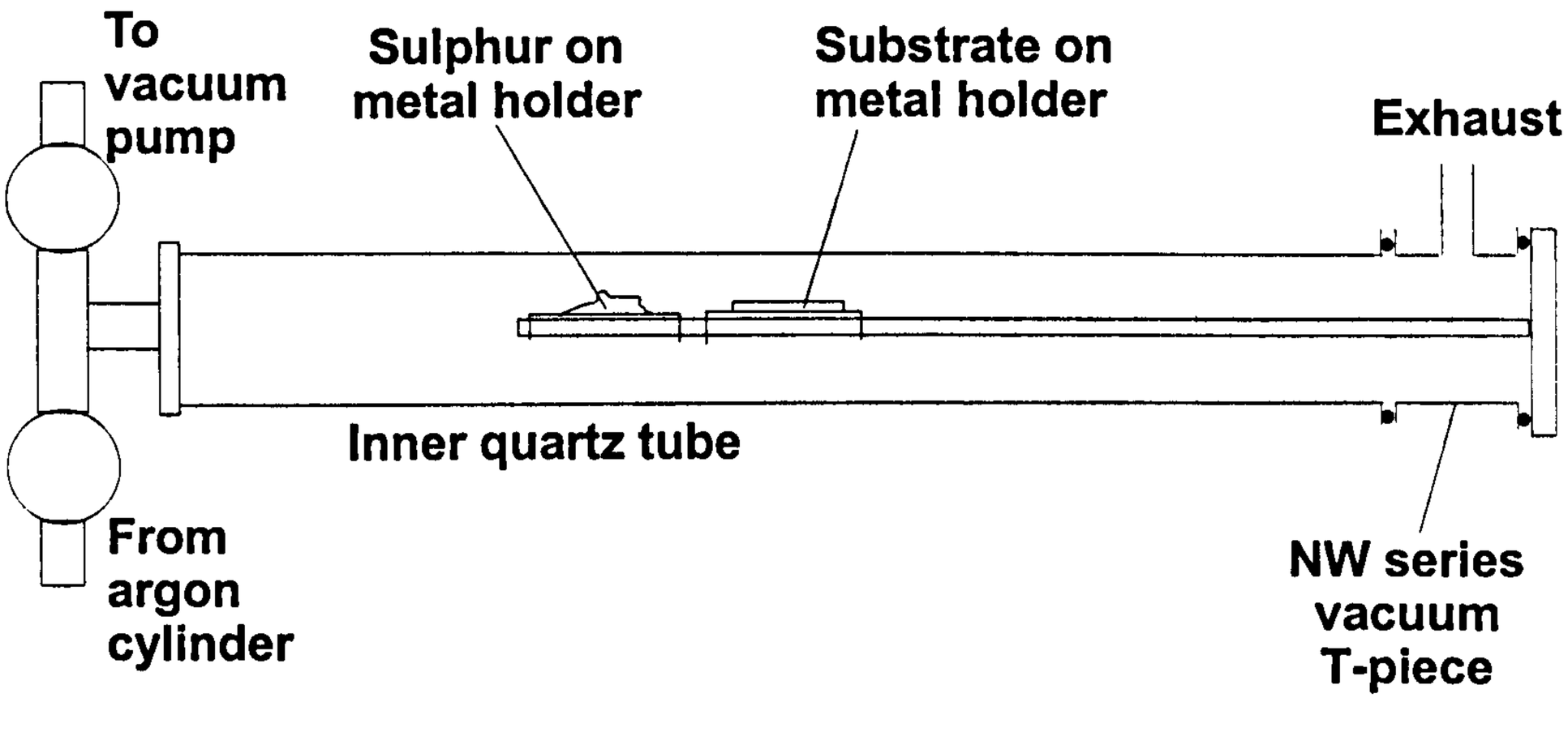

Figure 4.6. Schematic diagram of internal components and gas and vacuum connections for sulphidisation in argon carrier gas.

4.4 Conversion to copper indium disulphide by anodic sulphidisation

This section of the experimental work was a continuation of work performed previously at Northumbria University [9]. In this process, a Cu/In precursor was connected electrically to the positive output terminal of a Keithley Instruments constant current power supply, and immersed in a solution containing sodium sulphide (Na_2S). A platinum electrode was connected to the negative output terminal of the current source. Thus the precursor/substrate and the platinum electrode acted as the anode and cathode respectively of the electrolytic cell containing the Na_2S solution. The experimental apparatus is shown in Figure 4.7. The Na_2S in the solution is in equilibrium with Na^+ and S^{2-} ions. Application of a current through the electrodes and the solution causes S^{2-} ions to migrate to the anode, where they react with the metals to form sulphides. For example –

$$2Cu + S^{2-} \rightarrow Cu_2S + 2e^- \qquad (4.1)$$

Similar reactions occur for the formation of other sulphides.

A number of different solutions were used in the experiments. This included two different solvents – water, and ethanediol, which had been used in the previous experiments. The first series of experiments used water as a solvent. (This was used with and without alkaline additives.) However, this led to poor uniformity (to be described in Chapter 5), and ethanediol was used in all subsequent trials.

As ethanediol molecules have reduced dipole moments, compared to water molecules, it was uncertain whether this solvent would produce sufficient dissociation of Na_2S into Na^+ and S^{2-} ions. Therefore, alkaline materials were added. (Acidic conditions were avoided, as this would have resulted in the evolution of hydrogen sulphide.) The sulphidised films produced under these

conditions had improved uniformity and adhesion, compared to those for aqueous solutions, but not sufficient to be considered usable. Subsequent solutions consisted simply of Na_2S in ethanediol, and produced further improvements in film quality.

Conversions were performed over a range of temperatures and current densities. For each series of conversions, at a given current, the current was applied for a range of times.

Analysis for the material converted by anodic sulphidisation included the same measurements as for the two techniques involving elemental sulphidisation. EDAX was used to determine the elemental composition, and is described in section 4.9.

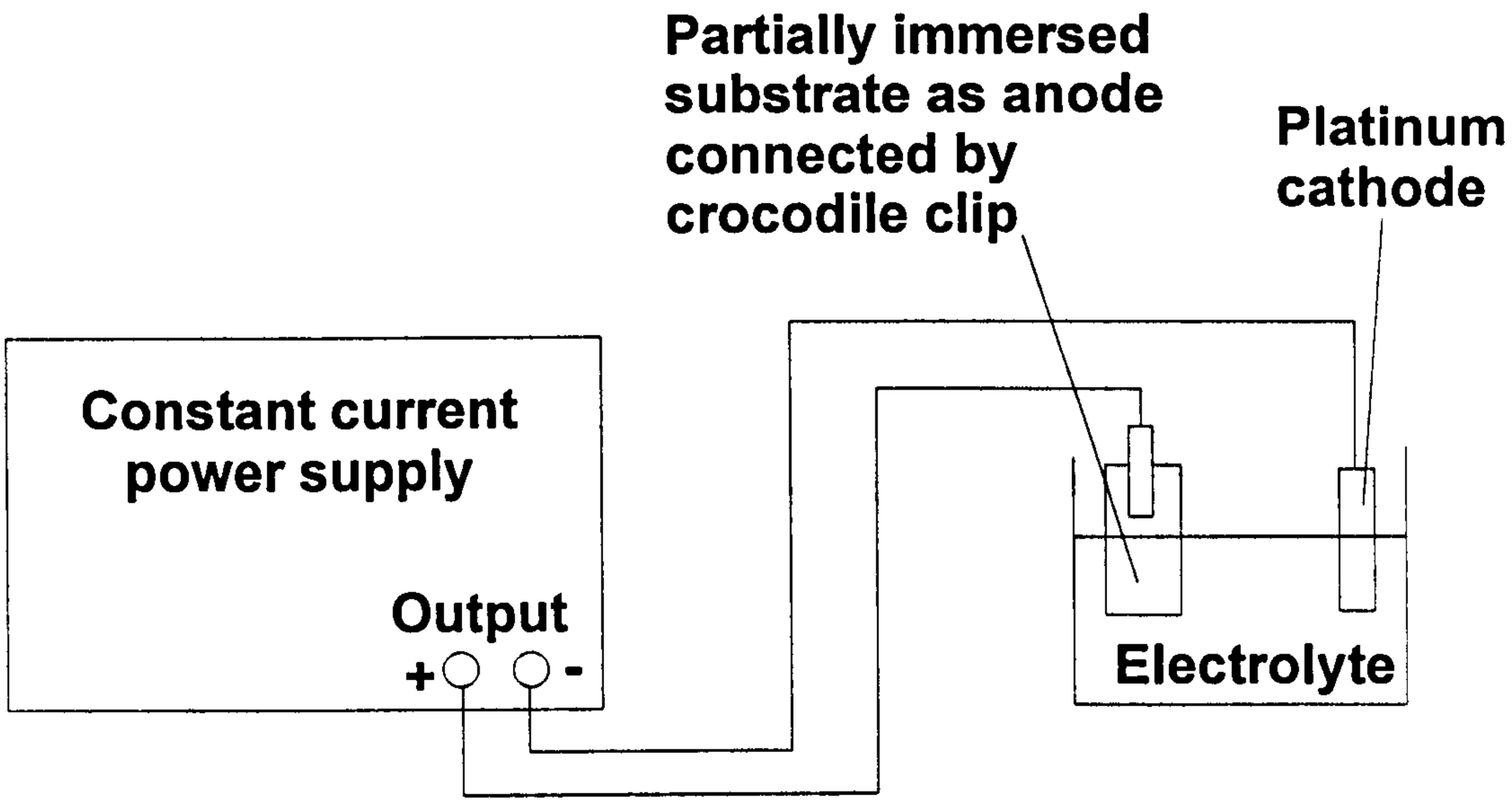

Figure 4.7. Schematic diagram of electrical circuit for anodic sulphidisation.

4.5 Chemical bath deposition of zinc sulphide

The work described in this section aims to deposit thin films of zinc sulphide (ZnS) by chemical bath deposition, for use as buffer layers in photovoltaic devices. The layers produced are intended to be incorporated into ZnO/ZnS/$CuInS_2$ devices. An advantage of this material is that it has a wider energy bandgap than other buffer layer or window layer materials, which results in it transmitting over substantially all of the solar spectrum. This could potentially increase the conversion efficiency of solar cells incorporating this material.

Previous work on the deposition of ZnS (and also zinc selenide - ZnSe) has used hydrazine hydrate in the chemical bath as a complementary complexing agent [10, 11]. However, hydrazine hydrate is flammable, and is a toxic material in several respects, including being carcinogenic. Thus, although the end product (ZnS) is non-toxic, hazardous materials are present during the manufacturing stage. In the present work, tri-sodium citrate was used as a substitute for the hydrazine hydrate, reducing the hazards associated with the processing.

Chemical bath deposition is used to deposit thin films of a wide range of materials [12, 13]. The deposition mechanism is largely the same for all such materials. A soluble salt of the required metal is dissolved in an aqueous solution, to release cations. The non-metallic element is provided by a suitable source compound, which decomposes in the presence of hydroxide ions, releasing the anions. The anions and cations then react to form the compound. The source materials used in this work were zinc sulphate ($ZnSO_4$) and thiourea ($CS(NH_2)_2$).

$$ZnSO_4 \rightarrow Zn^{2+} + SO_4^{2-} \qquad (4.2)$$

The decomposition of the thiourea is given by –

$$CS(NH_2)_2 + OH^- \rightarrow SH^- + CH_2N_2 + H_2O \qquad (4.3)$$

$$SH^- + OH^- \leftrightarrow S^{2-} + H_2O \quad (4.4)$$

The ions then react to form ZnS.

$$Zn^{2+} + S^{2-} \leftrightarrow ZnS \quad (4.5)$$

Due to its low solubility, the ZnS produced in the solution by this direct reaction precipitates onto exposed surfaces (homogeneous process). Films produced in this way have a rough topology, resulting in low optical transmittance.

To minimise this process, a complexing agent is used to form complex ions with the metal ions. The most widely used such agent is ammonia (NH_3). This exists in equilibrium with ammonium hydroxide (NH_4OH), which also provides the hydroxide ions for decomposition of thiourea.

$$NH_4^+ + OH^- \leftrightarrow NH_3 + H_2O \quad (4.6)$$

$$Zn^{2+} + 4NH_3 \leftrightarrow Zn(NH_3)_4^{2+} \quad (4.7)$$

These complex ions and the sulphide ions migrate to the substrate surface, where they react to form ZnS (heterogeneous process).

$$Zn(NH_3)_4^{2+} + S^{2-} \rightarrow ZnS + 4NH_3 \quad (4.8)$$

Active sites on the substrate surface act as nucleation centres, which are important in initiating deposition. Layers formed by the heterogeneous process have good uniformity and are highly transmissive. Although some materials, such as CdS, can be produced with NH_3 as the only complexing agent, previous work has shown that a complementary complexing agent is required for deposition of zinc compounds [10, 11]. Without such an agent, deposition is minimal, or does not occur at all. The agent previously used has been hydrazine hydrate. In this work, tri-sodium citrate has been found to perform a similar function.

The apparatus used for chemical bath deposition is shown in Figure 4.8. In order to minimise precipitation of material from homogeneous reactions, the slides were mounted near-vertically.

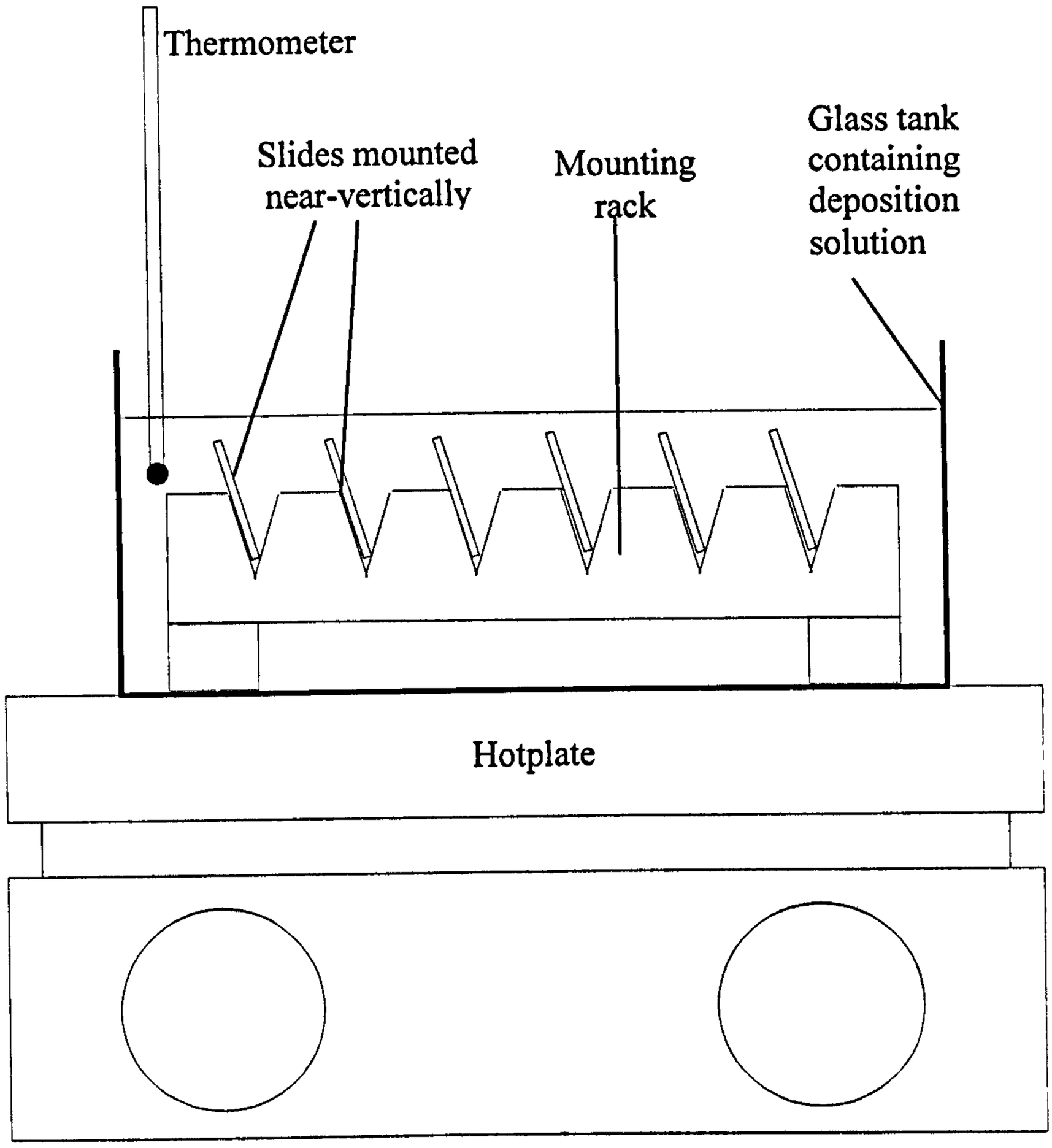

Figure 4.8 Apparatus for chemical bath deposition of zinc sulphide. A rack was used to mount the slides in a near-vertical position, in order to minimise deposition of material produced by homogeneous reactions.

Zinc sulphide has a large band gap, which results in a low charge carrier density, and hence high resistivity. In order to reduce the electrical resistance, a further set of samples was produced, with aluminium sulphate ($Al_2(SO_4)_3$) added to the chemical bath solution. Some of the aluminium was then incorporated into the films. This then partially substituted for zinc, resulting in n-type doping, although formation of separate grains of Al_2S_3 may also have occurred. Films were deposited for aluminium concentrations in solution of 0.25, 0.5 and 1%. (This is not necessarily the percentage incorporated into the film, although both will tend to increase together.) Indium contacts were then deposited, and silver paint and copper wires added. Electrical resistance measurements were made with a multimeter.

Analysis of the ZnS films was categorised as identification and evaluation. Firstly, as the films were produced by a technique, which was a new development of previous methods, it was necessary to confirm that the material deposited was ZnS. A combination of EDAX, XRD and band gap measurement from optical spectroscopy was used. Secondly, the qualities relating to the functions performed by a buffer layer were assessed. These functions are

1. It acts as a buffer against diffusion of material between the underlying absorber layer and the overlying transparent conducting oxide (TCO) layer.
2. Together with the TCO layer, it transmits radiation to the p-n junction.
3. Together with the TCO layer, it forms an electrical path to an external circuit.

Measurements of optical transmittance and electrical resistivity were used to evaluate the quality of the films in relation to the second and third of these functions. Optical absorption measurements can be used to determine film thickness, and hence evaluate its effectiveness in buffering diffusion.

4.6 Optical spectro-photometry

A number of analytical techniques were used in this work, and are described in this and the following sections.

In a spectro-photometer, light from a broadband source, such as a tungsten halogen lamp, passes through a narrow slit onto a diffraction grating (or a prism), which spreads the light out into a spectrum [14]. By moving the position of a second slit, the wavelength of the light passing through it can be selected. This single-wavelength light then passes through the sample being analysed, and onto a photodetector. In order to determine the fraction of light transmitted by the sample, a second wavelength scan is made, with the sample removed, so that the light passes directly to the photodetector. This acts as a baseline. The transmittance at each wavelength is obtained by dividing the signal for the sample by that for the baseline, both at the given wavelength. By repeating this for all wavelengths, a graph of transmittance vs. wavelength can be produced. (Alternative configurations can be used to measure the reflectance of a surface as a function of wavelength.) A schematic diagram of a spectrophotometer is shown in Figure 4.9. A Pye Unicam SP6-500 Spectrophotometer, for which the wavelength is scanned manually, and a Hitachi Spectrophotometer, which is interfaced to a computer, and scans the wavelength range automatically, were both used in this work. A photograph of the Hitachi U-4000 Spectrophotometer is shown in Figure 4.10.

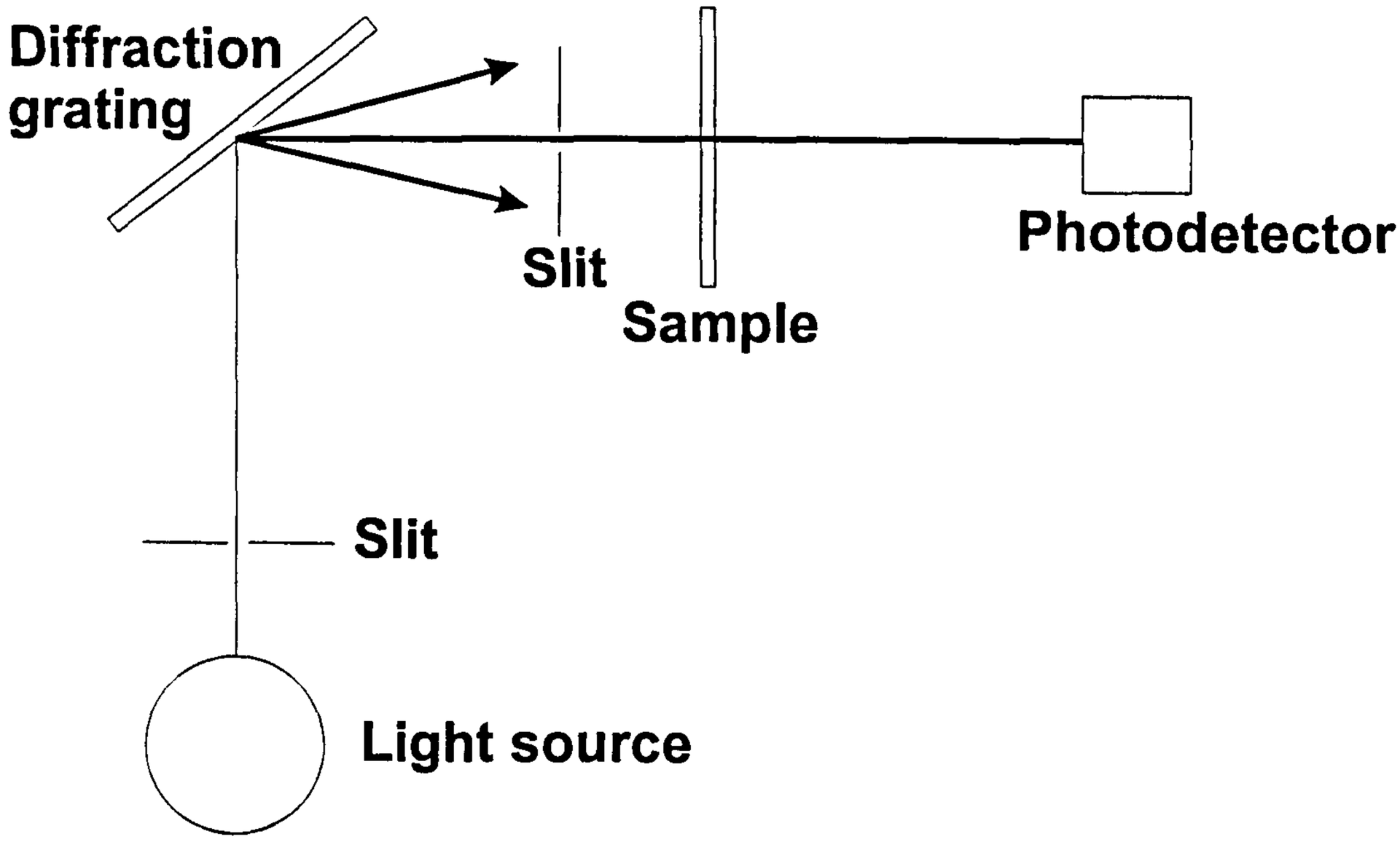

Figure 4.9 Schematic diagram of the optical components of a spectro-photometer.

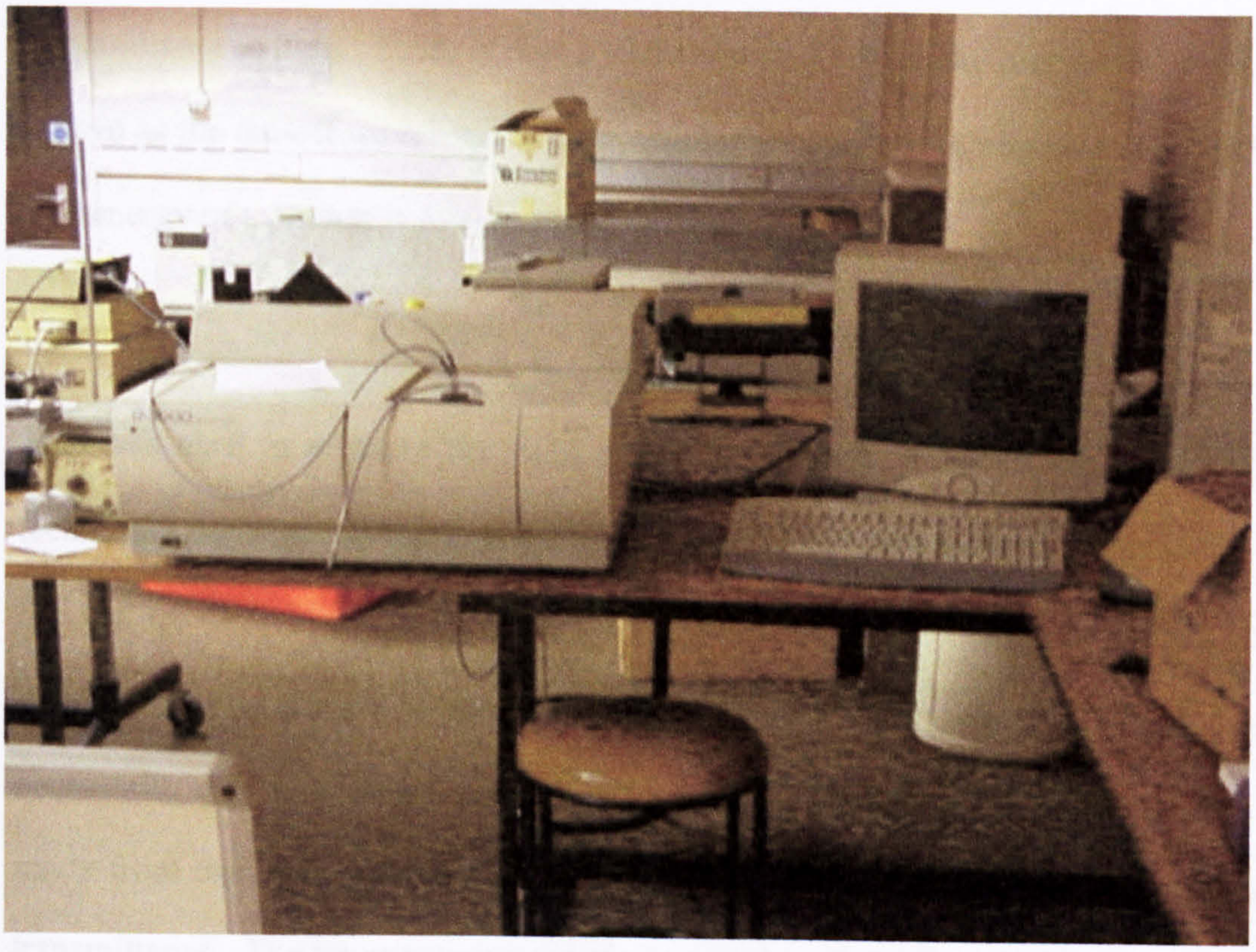

Figure 4.10. Photograph of the Hitachi U-4000 Spectrophotometer

A number of material properties can be assessed from spectroscopic measurements. In a semiconductor, photons with energy larger than the band gap excite electrons to the conduction band, and are absorbed in the process. As a result, the optical transmittance is low for such photons. Conversely, photons with lower energy than the band gap are not absorbed, and their optical transmittance is high. There is thus a transition in the transmittance a wavelength, known as the cut-off wavelength, from which the band gap can be calculated [15]. The energy of a photon is related to the wavelength by

$$E = h\nu = \frac{hc}{\lambda} = \frac{1240}{\lambda(\text{nm})} \text{ for } E \text{ in eV} \qquad (4.9)$$

This was used to measure the band gap of the $CuInS_2$ prepared by the various techniques described in sections 4.2 to 4.4, and the ZnS prepared by chemical bath deposition.

The cut-off wavelength is not always sharply defined, and therefore does not necessarily give an accurate value of the band gap. A more accurate value can be made from the optical absorption coefficient, which is derived from the spectral transmittance. The transmittance at a given wavelength is given by

$$T = \exp(-\alpha.d) \qquad (4.10)$$

α = optical absorption coefficient $\quad$ d = film thickness

Conversely, the optical absorption coefficient can be calculated from the observed transmittance.

$$\alpha = \frac{1}{d}\ln\left(\frac{1}{T}\right) \qquad (4.11)$$

The optical absorption coefficient is calculated for each wavelength. It is useful to plot this as a function of photon energy. For a direct band gap semiconductor, the value of α is given by [16]

$$\alpha \propto \frac{1}{h\nu}\left(h\nu - E_g\right)^{1/2} \tag{4.12}$$

$$\therefore \qquad (\alpha h\nu)^2 \propto h\nu - E_g \tag{4.13}$$

Thus a plot of $(\alpha h\nu)^2$ vs $h\nu$ intercepts the $h\nu$ axis at E_g, allowing this parameter to be evaluated. This was used to calculate band gaps for the $CuInS_2$ and the ZnS prepared in this project, and in each case was used as one source of confirmation of the identity of the material concerned.

For window layers, for which high optical transmittance is an important function, optical spectrophotometry gives additional information. Many window layer materials, particularly ZnS, have high band gaps, and therefore short cut-off wavelengths [17]. They are thus transmissive over much of the optical waveband, and therefore much of the solar spectrum. Measurement of the transmittance in this region gives a measure of the fraction of the solar spectrum reaching the junction with the absorber layer. This forms one factor in the conversion efficiency of solar cells.

Measurements of the optical absorption coefficient near the cut-off wavelength can be used to calculate the thickness of the film [3]. This is given by

$$d = \frac{1}{\alpha}\ln\left(\frac{1}{T}\right) \tag{4.14}$$

The value of α is a function of wavelength. If the transmittance is measured at a number of wavelengths (near the cut-off), and the known value of α is used in each case, ideally the calculated thickness should be the same for all wavelengths. The variation in calculated values is an indication of the uncertainty of the film thickness.

4.7 X-ray diffraction

X-ray diffraction results from the scattering of X-rays from the periodic array of atoms in a crystalline lattice [18]. The angular variation of the diffraction pattern produced by a crystal is characteristic of the lattice spacing and the wavelength of the incident X-rays. If a sample of crystalline material is illuminated by X-rays, the diffraction pattern can be observed. From the angles of the diffraction peaks, and the wavelength of the incident X-rays, the lattice spacing can be determined. From the lattice spacing along a number of directions within the crystal, the three-dimensional crystal structure can be determined.

The principles of X-ray diffraction are explained with reference to Figure 4.11. This shows a plane normal to the surface. The atoms in the lattice can be grouped into different sets of planes, each set with its own orientation. The intersection of each of these sets the planes with the plane of the diagram is a set of parallel lines. The scattered intensity is strongest in the direction for which constructive interference occurs, i.e., where the X-rays scattered from all the atoms are in phase, or differ in phase by a whole number of cycles. For X-rays scattered from atoms within a given plane, there is no phase difference when the angle at which X-rays are scattered from the plane equals the angle at which they are incident on the plane. This is similar to specular reflection, and defines the first condition.

$$\theta_r = \theta_i \tag{4.15}$$

For X-rays scattered from different planes, the difference in path lengths must equal a whole number of wavelengths. For adjacent planes this gives

$$n\lambda = 2d\sin\theta \tag{4.16}$$

These two conditions are called the Bragg conditions, and determine the direction in which X-rays are scattered.

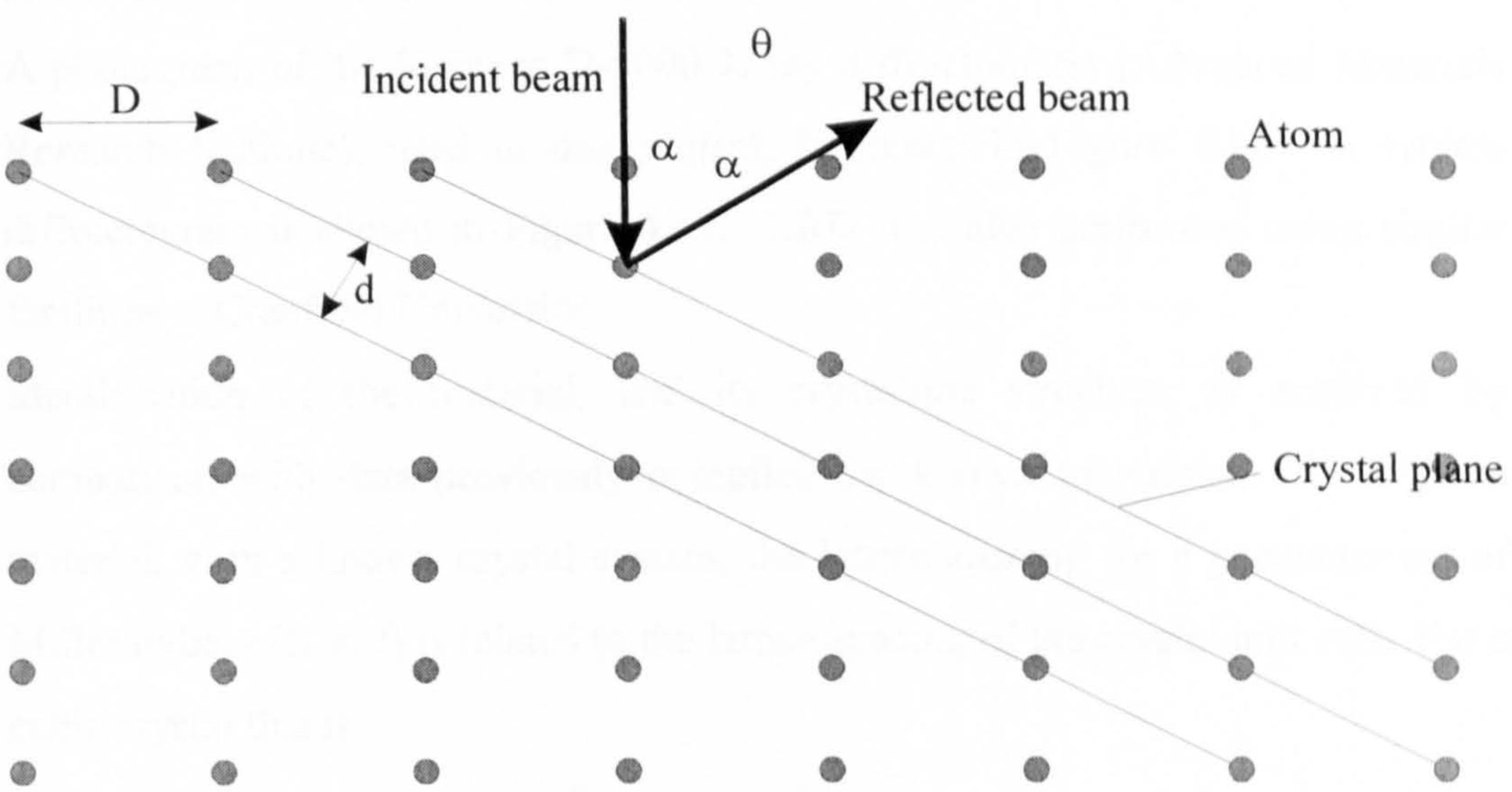

Figure 4.11. Scattering of X-rays from a crystalline lattice.

A polycrystalline material consists of a large number of crystals, each at a different orientation. For this type of material, the sample is kept fixed, and the X-ray source and detector are moved such that they maintain equal angles to the material (film) surface, as shown in Figure 4.11. When the angle of incidence is such that the second Bragg condition is met for those crystals with lattice planes parallel to the film surface, strong reflection will result. By moving the X-ray source and detector from 0 to 90°, the full range of lattice spacings is scanned. This then gives the full set of lattice spacings for the sample, from which the crystal structure can be determined.

A photograph of the Siemens D-5000 X-ray diffractometer (Advanced Materials Research Institute), used in this project, is shown in Figure 4.12. A typical diffractogram is shown in Figure 4.13. XRD was also performed using similar facilities at Cranfield University.

Identification of the material, and its crystalline structure, is achieved by comparison with data previously compiled for known materials. For a given material, with a known crystal system, the lattice spacing for a particular set of Miller indices (h, k, l) is related to the lattice spacing of the crystal unit cell. For a cubic crystal this is

$$d_{hkl} = a/\left[h^2 + k^2 + l^2\right]^{1/2} \tag{4.17}$$

In many modern computer-based systems, the reflections are presented as a set of lines (stick patterns) superimposed onto the diffractogram. For example, in Figure 4.13, patterns are included for ZnO and $Zn(OH)_2$. There is a good match between the diffractogram and the pattern for ZnO, which would lead to this being identified as probably being the material present. (The (100) peak has a spacing of 2.79 Å, which corresponds to the same spacing for the unit cell in this direction.) The match for $Zn(OH)_2$ is less good (approximate match for one peak), suggesting that this material is not present in large quantities. In certain fabrication processes, it may be possible for a number of materials to be produced (ZnO and $Zn(OH)_2$ in the case of chemical bath deposition). XRD can thus be used to determine which of these materials has actually been produced.

Figure 4.12 Siemens D-5000 X-ray diffractometer (Advanced Materials Research Institute)

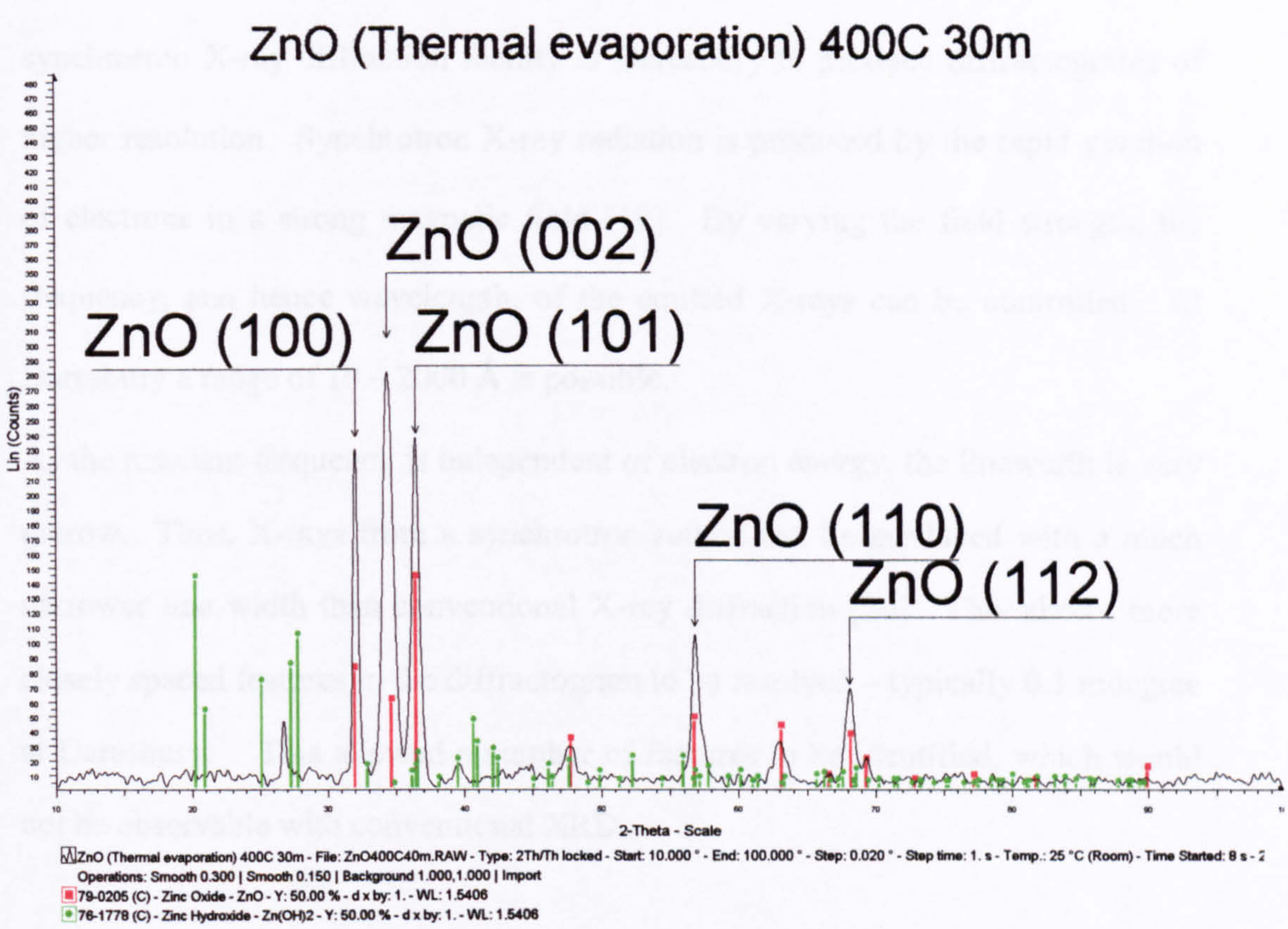

Figure 4.13 Diffractogram of zinc oxide, with calibration patterns for ZnO (red) and $Zn(OH)_2$ (green).

In a conventional X-ray diffractometer, the X-rays are generated by high energy electrons striking a metal target (copper in the machine at AMRI - K_α: $\lambda = 1.5406$ Å). The line-width of the emitted radiation means that a peak due to a given lattice spacing in a crystal has a relatively large angular width. As a result, two peaks corresponding to slightly different lattice spacings may not be resolved.

During this project, a number of co-workers and collaborators used the synchrotron X-ray diffraction facility at Daresbury to produce diffractograms of higher resolution. Synchrotron X-ray radiation is produced by the rapid gyration of electrons in a strong magnetic field [19]. By varying the field strength, the frequency, and hence wavelength, of the emitted X-rays can be controlled. At Daresbury a range of 10 – 2000 Å is possible.

As the resonant frequency is independent of electron energy, the linewidth is very narrow. Thus, X-rays from a synchrotron source can be produced with a much narrower line width than conventional X-ray diffraction [20]. This allows more closely spaced features in the diffractogram to be resolved – typically 0.1 mdegree at Daresbury. This allowed a number of features to be identified, which would not be observable with conventional XRD .

4.8 Scanning electron microscopy

Electron microscopy uses scattering of an electron beam to form images of the microscopic structure of a sample of material [21]. At high incident energies, the electrons have much smaller wavelengths than light, and therefore electron microscopy can resolve smaller details than is possible for conventional optics. (Typically features of a few nanometres can be resolved.) The electron optics focus the beam onto a small spot on the surface of the sample, and also focus the

backscattered electrons onto a detector, thus giving a measure of the reflection from that point.

In scanning electron microscopy (SEM), the electron optical system scans the beam across the surface in a line. By scanning along a number of parallel lines, an image of the surface can be built up. The Hitachi S-4000 scanning electron microscope (Advanced Materials Research Institute), which was used in this project, is shown in Figure 4.14.

SEM can be used to observe the small-scale structure of a range of materials. In the case of polycrystalline materials, individual crystals can be seen, and their typical shapes, sizes and preferred orientations (if any) determined [22]. The overall uniformity of the surface can be evaluated, by viewing at a range of magnifications. In the case of thin films, depressions in the film can be noted, as potential sites for pinholes [23].

By cutting through the film, and then placing the sample at a large angle to the electron beam, with the beam incident on the edge of the film, it is possible, in some cases, to obtain a visual estimate of the film thickness. It is also possible to examine the material for the presence of voids, and other defects, below the surface.

Scanning electron microscopy was used to evaluate different properties of each of the materials produced. For the sputtered Cu/In precursors, uniformity of surface topography and thickness were assessed. For the various processes for fabrication of $CuInS_2$, the typical grain sizes and inter-grain spaces were observed, as well as checking for the presence of voids, which could potentially form pinholes. For the ZnS, produced by chemical bath deposition, surface uniformity and absence of pinholes were important features to be determined.

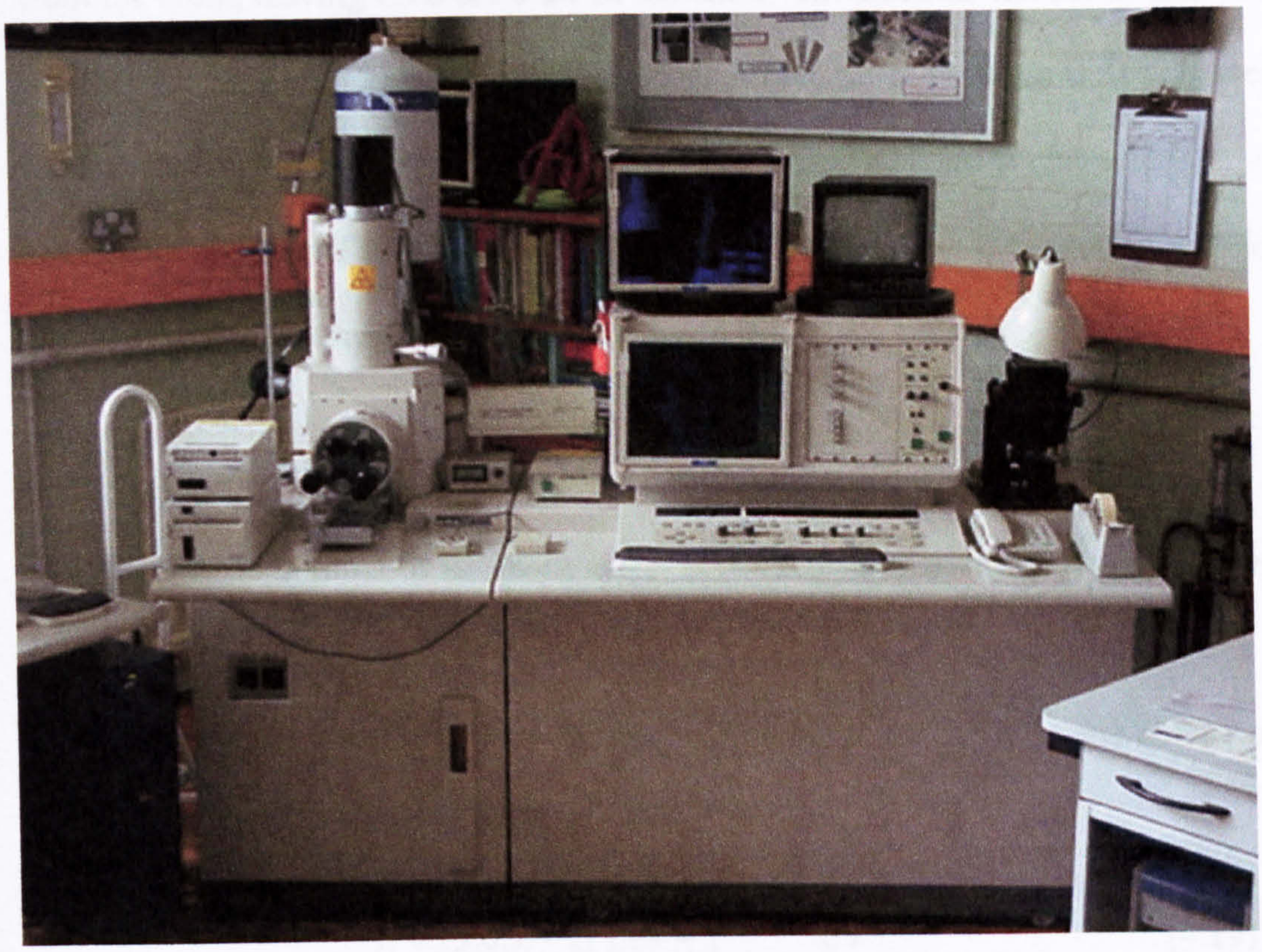

Figure 4.14. Hitachi S-4000 scanning electron microscope (Advanced Materials Research Institute)

4.9 Energy dispersive X-ray analysis

This is used to identify the elements present in a material sample, and to determine the fractional composition of each element [24]. The principles are explained with reference to Figure 4.15. When high energy (~ keV) electrons penetrate the surface of a sample, some of them transfer energy to electrons in the lower energy shells of the atoms in the material. These electrons are then ejected from the atom, leaving a vacant state in the shell. An electron can move into this shell from a higher energy shell, with the energy difference between the two states being emitted as X-rays. The wavelength of the X-rays emitted is characteristic of the atomic number of the atom, and the shells between which the electron moves. The energy of a given state of an atom is given by

$$E = -13.6\frac{Z^2}{n^2} \qquad \text{eV} \tag{4.18}$$

(Z is the atomic number of the atom and n is the principal quantum number of the electron shell.)

For an electron moving from the l-shell ($n = 2$) to the k-shell ($n = 1$), the energy of the emitted X-ray is approximately

$$E = 13.6(Z-1)^2\left(1-\frac{1}{4}\right) \qquad \text{eV} \tag{4.19}$$

As there are transitions between a range of electron shells, each type of atom can emit at a number of wavelengths. The wavelengths of the emitted X-rays can be used to identify the elements present in the sample. The intensities of the peaks in the spectrum can be used to determine the fraction of each element present. A typical EDAX spectrum is shown in Figure 4.16. In many cases, a scanning electron microscope can also perform EDAX. In this project, a Linc eXL energy analyser, attached to the Hitachi S-4000 scanning electron microscope, was used.

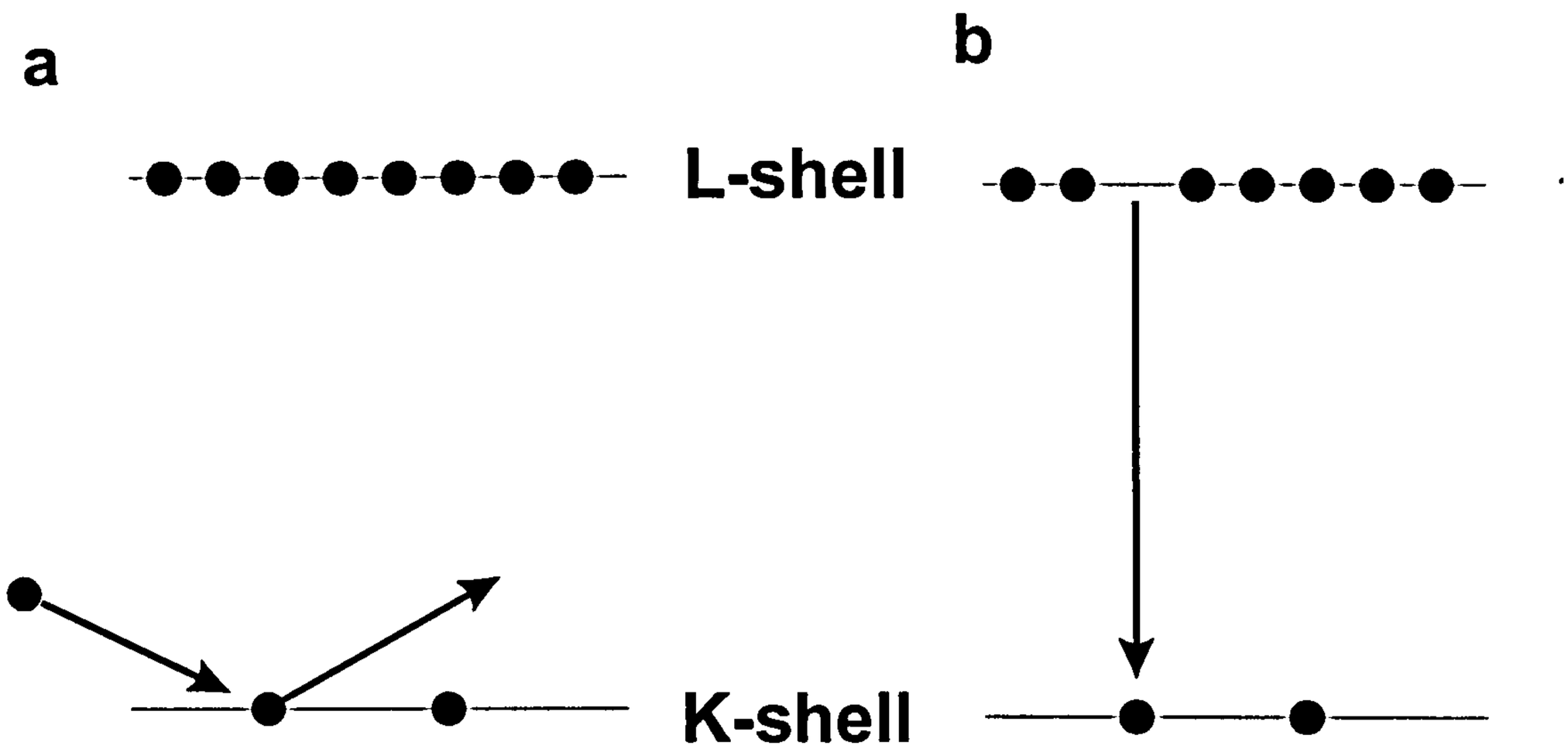

Figure 4.15. X-ray emission in EDAX. a. Incident electron ejects an electron from a lower energy (K) shell. b. Electron moves to the vacant site from a higher energy (L) shell.

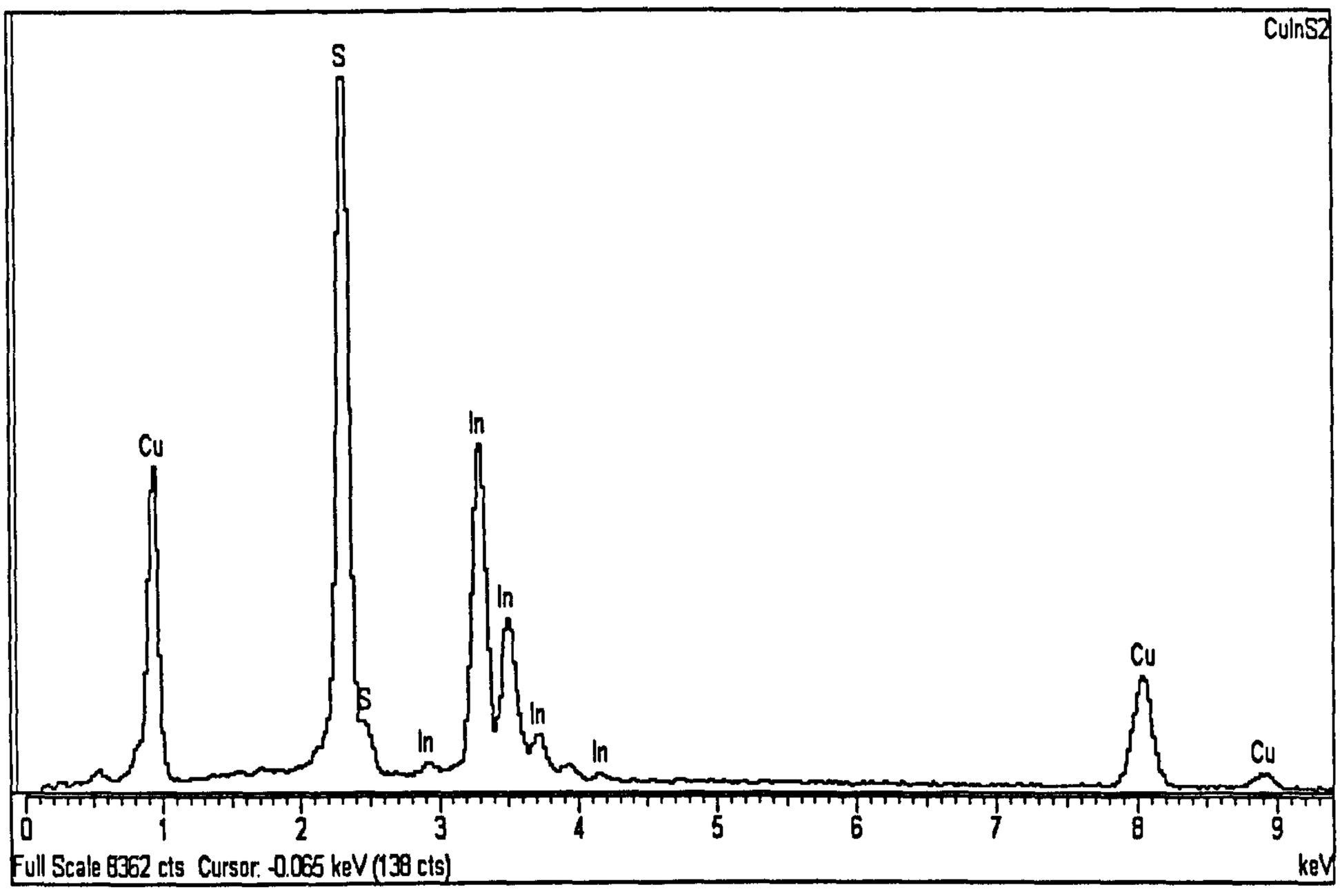

Figure 4.16. EDAX spectrum of copper indium disulphide.

Due to limited penetration of the electron beam, EDAX measurements tend to be limited to within a certain depth of the surface. The region, from which signals are returned, is an approximately spherical region, just below the point of incidence of the electron beam on the surface of the sample. This is called the volume of primary excitation, and is shown in Figure 4.17. The radius of this sphere is related to the energy of the incident electrons and the density of the material.

$$R = \frac{4120}{\rho} E^{(1.265-0.0954E)} \tag{4.20}$$

(R is in nm, ρ is in g cm^{-3} and E is in keV.)

The depth of penetration may be of the order of 1 μm, which is less than the few μm typical of the $CuInS_2$ films produced. As a result of this limited penetration, the composition measured is that of the sub-surface layer, and not necessarily that of the whole film. For films thinner than 1 μm, the electron beam may penetrate to underlying layers. If these layers include similar elements to the layer being investigated, it may be difficult to distinguish the location of the elements being observed.

In this work, EDAX was used to determine the elemental composition of the sputtered Cu/In films, in order to determine the target power settings required for stoichiometry. For the various methods of sulphidisation, the sulphur content was measured, to determine the extent to which it had been incorporated. In addition, the Cu and In fractions were measured, to ascertain whether preferential loss had occurred. For the ZnS films, the fractions of Zn and S were measured, to check whether the stoichiometric ratio had been obtained.

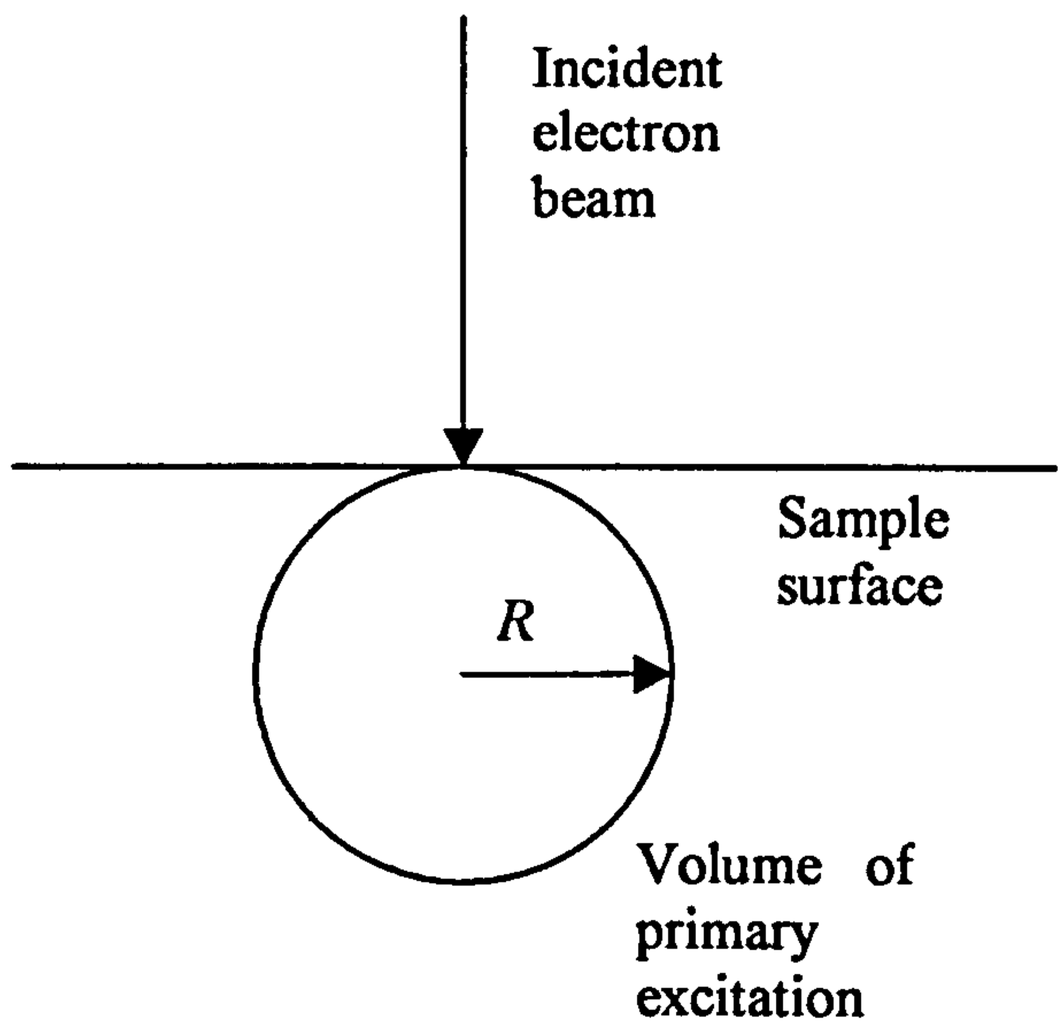

Figure 4.17. Volume of primary excitation, showing penetration below the surface

4.10 Rutherford back scattering

Rutherford back scattering (RBS) is large angle deflection of a light nucleus (typically He^{2+}) from a larger nucleus [25]. In Rutherford scattering, most collisions involve small deflection angles, with a much smaller number having the large angles, characteristic of back scattering. The small angle deflections gradually reduce the energy of the incident nuclei, as do interactions with atomic electrons in the material of the target. The number of collisions before large angle deflection occurs increases with the depth of the material penetrated. Thus the energy loss of the back scattered ions, relative to the energies of the incident ions, is a measure of the depth at which back scattering occurred. The strength of the back scattered signal at a given energy is indicative of the quantity of material at the corresponding depth. An example is shown in Figure 4.18.

The maximum energy of a deflected ion increases with the nuclear charge (atomic number) of the target ion, from which it is deflected. (This is the energy for particles back scattered from the surface, with no loss due to penetration into the material.) For heavy elements, e.g., tungsten, the maximum energy is almost equal to the incident energy of the particles, whereas for light elements, e.g., oxygen, the maximum energy is typically 15 % of the incident energy. For each element, there is a sharp increase (with decreasing energy) in the strength of the back scattered signal. The energy at which this occurs indicates the atomic number of the element.

As the particles lose energy - due to low-angle scattering - the cross-section for large-angle scattering increases. This results in an increase (with decreasing energy) in the intensity of the spectrum, for a given concentration of the element. Allowing for this effect, the intensity as a function of energy can be used to

calculate the concentration of the element as a function of depth. Depth resolution of 10 to 20 nm is possible.

The back scattered intensity varies as the square of the atomic number. This affects the lower limit on the concentration of a given element, which can be detected. For light elements, the limit is $n \sim 10^{11}$, while for heavy elements, $n \sim 10^{15}$.

Computer software can be used to convert the backscattered signal into measurements of composition. The energies, at which abrupt changes in intensity occur, can be used to identify the elements present. The spectrum is then resolved into components for each element. The factors stated above - dependence on Z^2 and back scattered energy - are then used to convert the intensity into concentration for each element. This can be given either as a function of depth through the film, or as a variation across the area of the film.

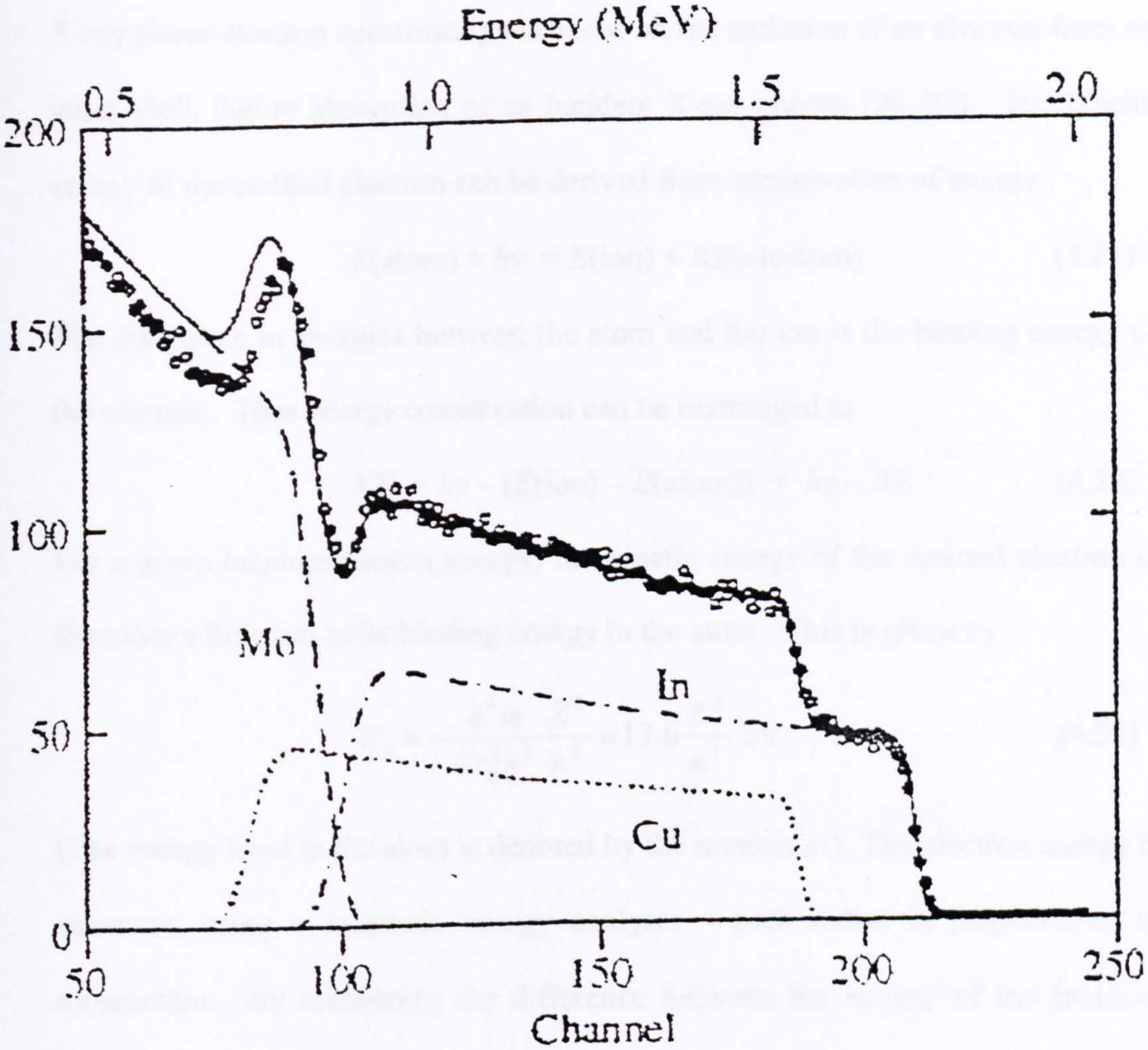

Figure 4.18. Rutherford backscattering graph, showing sharp increase in signal for each element, corresponding to back-scattering at the maximum energy. The signal is resolved into components for each element, and the continuously-varying signal from each discontinuity indicates the variation in quantity of the element with depth.

4.11 X-ray Photo-electron Spectroscopy

X-ray photo-electron spectroscopy is based on the emission of an electron from an inner shell, due to absorption of an incident X-ray photon [26, 27]. The kinetic energy of the emitted electron can be derived from conservation of energy.

$$E(\text{atom}) + h\nu = E(\text{ion}) + KE(\text{electron}) \qquad (4.21)$$

The difference in energies between the atom and the ion is the binding energy of the electron. Thus energy conservation can be rearranged as

$$KE = h\nu - (E(\text{ion}) - E(\text{atom})) = h\nu - BE \qquad (4.22)$$

For a given incident photon energy, the kinetic energy of the emitted electron is therefore a function of its binding energy in the atom. This is given by

$$E_n = -\frac{e^4 m}{8\varepsilon_0^2 h^2}\frac{Z^2}{n^2} = 13.6\frac{Z^2}{n^2}\ \text{eV} \qquad (4.23)$$

(The energy level in the atom is denoted by the number n.) The electron energy is measured using a magnetic energy analyser – path radius is proportional to momentum. By measuring the difference between the energy of the incident photon and that of the emitted electron, the atomic number of the element can be calculated. By scanning over a range of electron energies, the elements present in a material can thus be identified. (The energies of the inner shells are modified slightly by chemical bonding of the atom to neighbouring atoms, which involves rearrangement of the valence electrons. This allows particular chemical combinations to be identified.)

XPS identifies the elements at the surface of the material. Sputter-etching can be used to gradually remove material, exposing the underlying layers. As this process continuous, XPS can be used to derive a depth profile of the variation in composition through the film [28].

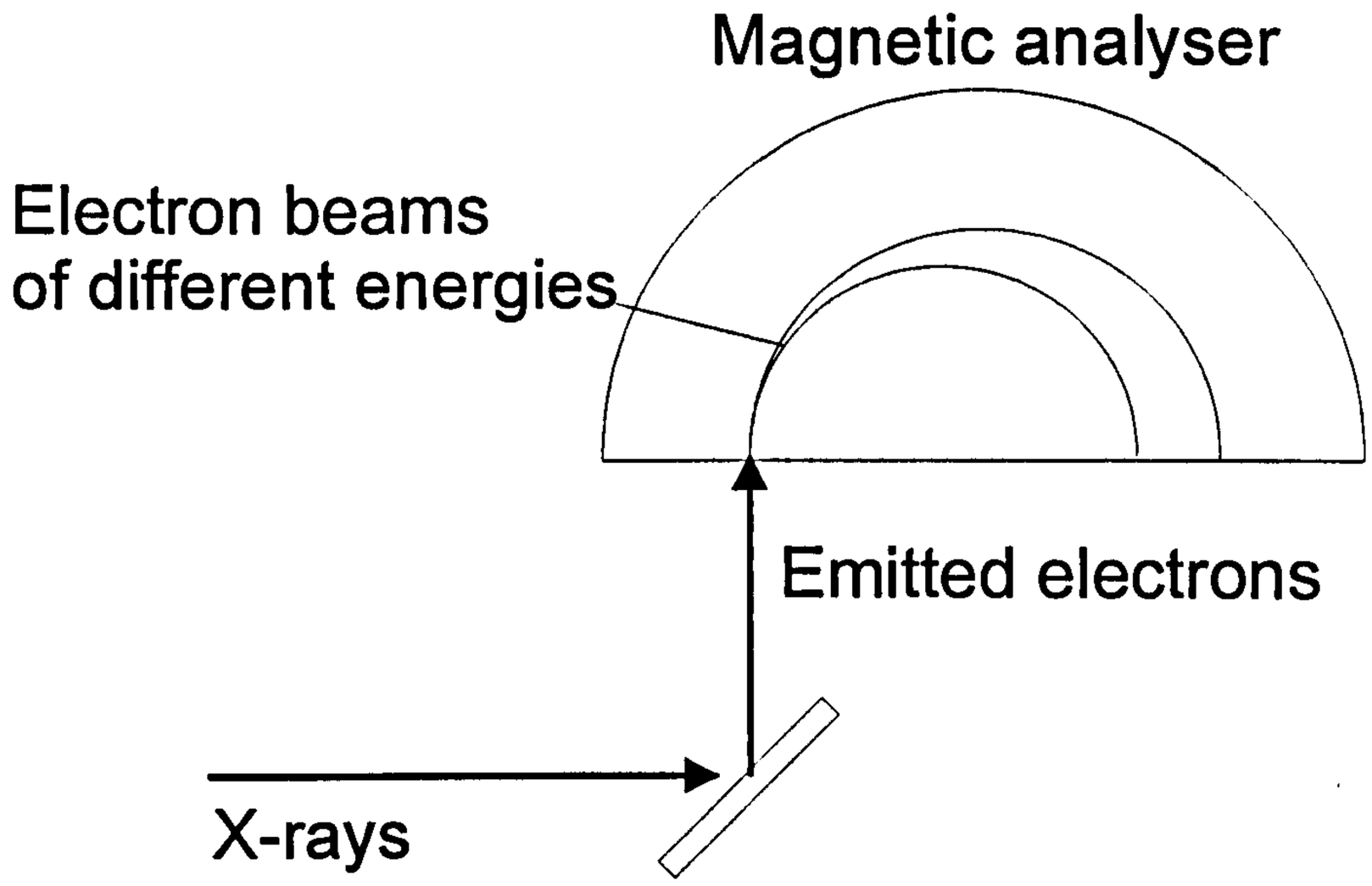

Figure 4.19. X-ray photoelectron spectroscopy. Incident X-ray photons eject electrons from atoms in the sample. In the magnetic field of the analyser, the path radius is proportional to electron momentum, and hence increases with energy. By scanning across the beam, the intensity can be determined as a function of energy.

4.12 Measurement of Electrical Resistivity

One of the standard methods for measuring electrical resistivity of thin films is the Van der Pauw method [29]. In this technique, four electrical contacts are placed in a square array on the surface of the film, as shown in Figure 4.20. A voltage is applied between contacts 3 and 4, and the current between contacts 1 and 2 is measured. This gives a value

$$R_{12,34} \equiv \frac{V_{34}}{I_{12}} \tag{4.24}$$

Similarly, a voltage is applied between contacts 4 and 1, and the current measured between contacts 2 and 3.

$$R_{23,41} \equiv \frac{V_{41}}{I_{23}} \tag{4.25}$$

The resistivity is then given by

$$\rho = \frac{\pi d}{\ln 2}\left(R_{12,34} + R_{23,41}\right)\frac{F}{2} \tag{4.26}$$

where d is the film thickness, and F is a correction factor for the dimensions of the sample and the placement of the contacts.

This method was used to measure the resistivity of the ZnS films. As these films were very thin and highly resistive, no current could be measured. An alternative method was used, in which the ZnS was deposited onto tin dioxide (SnO_2) coated glass. A layer of indium was deposited onto the ZnS to form an Ohmic contact. Electrical contacts were then connected to the SnO_2 coating and the indium layer, so that current flowed through the ZnS, along its smallest dimension. Measuring the current for a range of voltages gave the resistance of the film. From its thickness and effective cross section (the area of the contact with the indium), the resistivity was calculated.

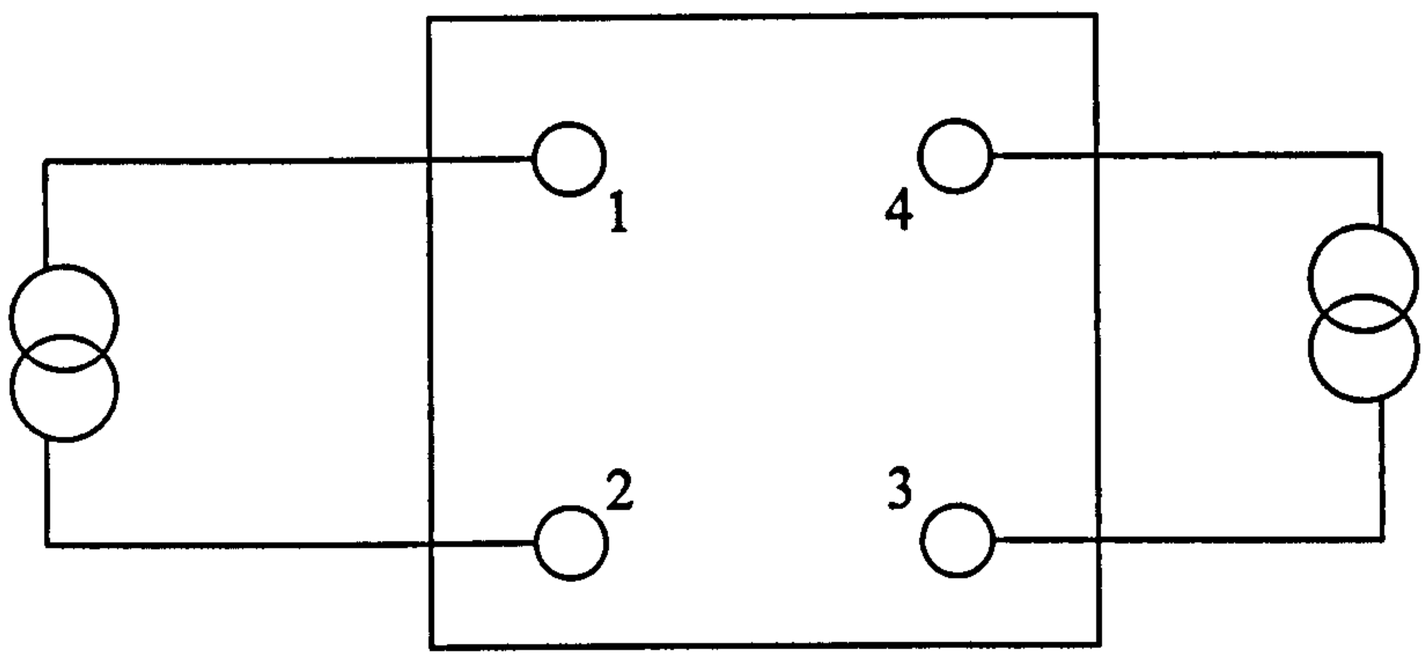

Figure 4.20 Arrangement of electrical connections in the Van der Pauw method.

This set of connections give the value of $R_{12,34}$

4.13 Measurement of current-voltage characteristics

A range of voltages (of both polarities) is applied to the device, and the current is measured for each voltage. The results are plotted as a graph, known as the current-voltage, or *I-V* characteristic [30]. This is performed in darkness and under standard illumination (AM1.5 solar spectrum - 1000 Wm^{-2}), or other specified conditions. A typical *I-V* characteristic is shown in Figure 4.21.

The output power is the product of the current and voltage. For a given device, and a given level of illumination, there is a particular combination of current and voltage that gives the maximum power. This is represented on the *I-V* graph by a rectangle. The ratio of this to the product of open-circuit voltage (V_{oc}) and short-circuit current (I_{sc}) - also represented by a rectangle - is known as the fill factor.

$$FF \equiv \frac{V_m I_m}{V_{oc} I_{sc}} \tag{4.27}$$

As the product $V_{oc}I_{sc}$ increases with incident optical power, and V_mI_m is the electrical power output, the fill factor is a measure of one factor in the conversion efficiency of the device.

Samples of $CuInS_2$, converted by elemental sulphidisation in a graphite box, were sent to Sri Venkateswara University, India, for incorporation into substrate-configuration thin film photovoltaic devices. Some of these samples included ZnS films, chemically deposited at Northumbria University, prior to sending to India. The final layer of the devices was a Ga-doped ZnO transparent conducting oxide layer. This was deposited by spray pyrolysis at Sri Venkateswara University. Current-voltage characteristics were derived for both of these types of devices.

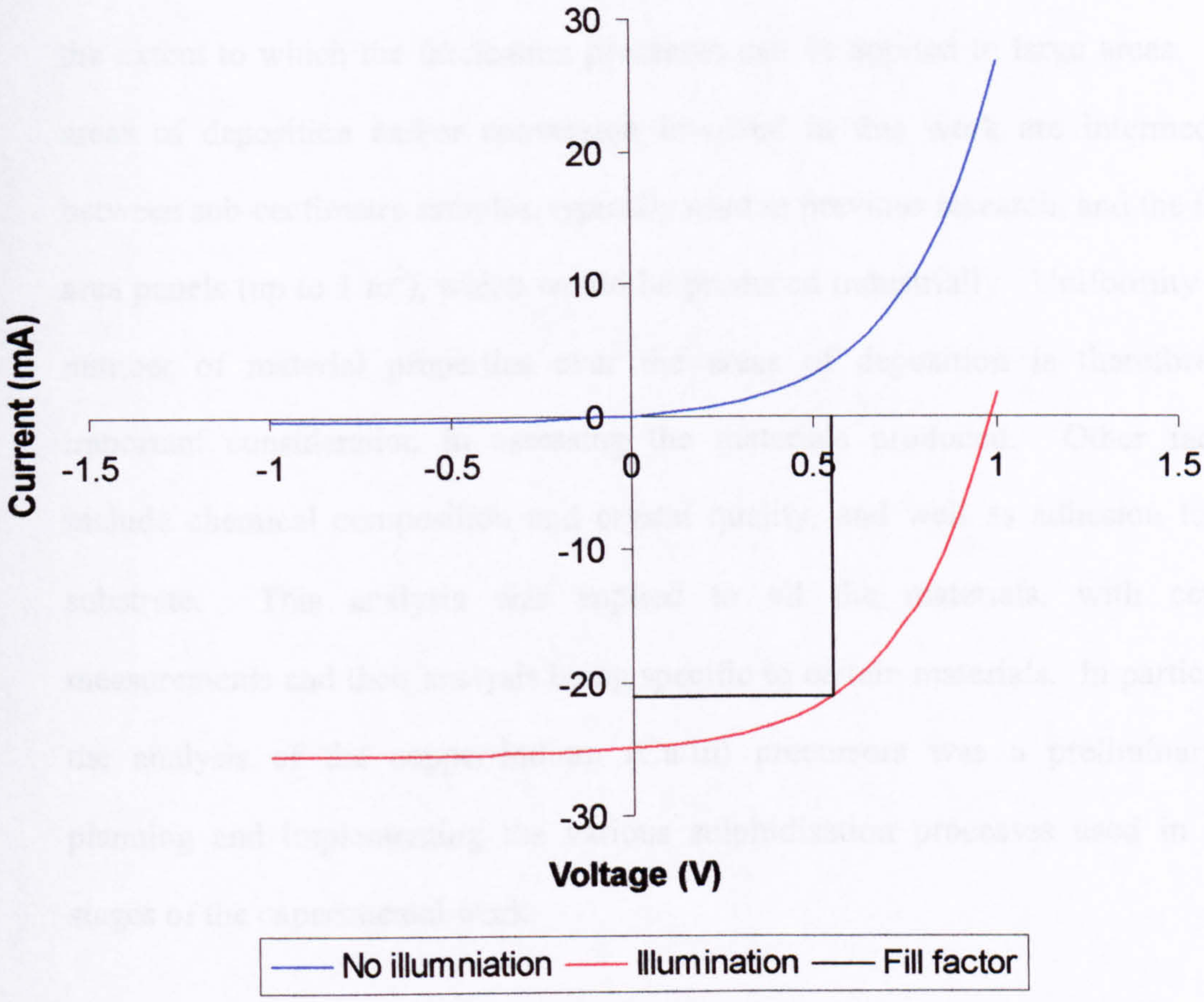

Figure 4.21. Current-voltage characteristics for unilluminated and illuminated devices. The fill factor is shown for the maximum power point.

5. Results and analysis of experiments

The objectives of the experimental procedures, described in the previous chapter, and the analysis of the results derived from these experiments, is to assess the suitability of the materials for use in photovoltaic devices. One important factor is the extent to which the fabrication processes can be applied to large areas. The areas of deposition and/or conversion involved in this work are intermediate between sub-centimetre samples, typically used in previous research, and the large area panels (up to 1 m^2), which would be produced industrially. Uniformity of a number of material properties over the areas of deposition is therefore an important consideration in assessing the materials produced. Other factors include chemical composition and crystal quality, and well as adhesion to the substrate. This analysis was applied to all the materials, with certain measurements and their analysis being specific to certain materials. In particular, the analysis of the copper-indium (Cu/In) precursors was a preliminary to planning and implementing the various sulphidisation processes used in later stages of the experimental work.

5.1 Copper indium precursors

Previous work, performed by another student, at Northumbria Photovoltaic Applications Centre (NPAC) had established that the film thickness produced by sputtering was uniform over most of the area over which material was deposited [1]. The current work developed from this to include uniformity of composition, both over the area and with depth through the film. Rutherford back-scattering data, provided by collaborating researchers at Cranfield University, yielded information on both of these factors. These results are shown in Figures 5.1 and 5.2 [2].

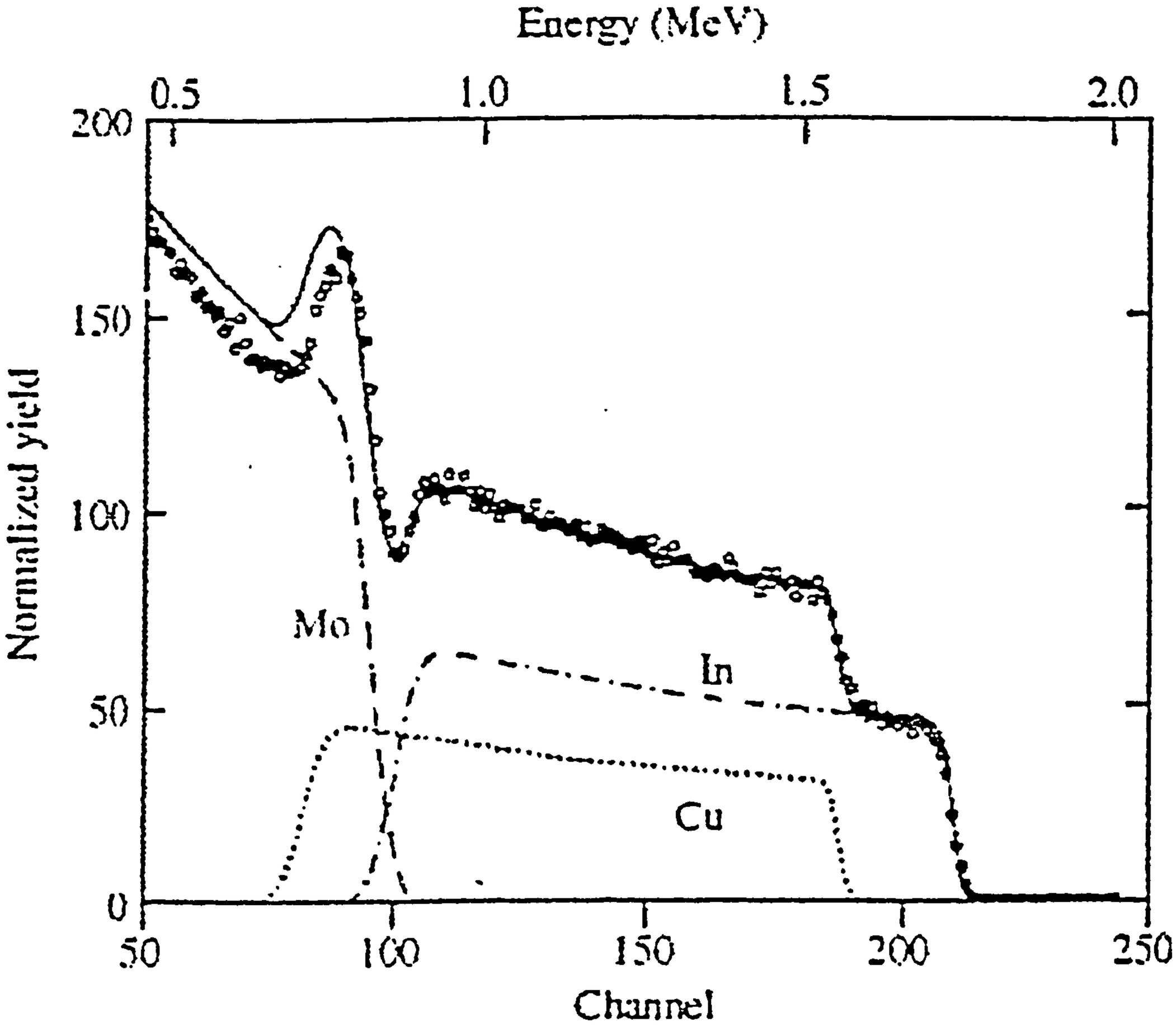

Figure 5.1 Rutherford back-scattering data for Cu/In layers sputter-deposited onto Mo-coated glass. The data are show a layer of copper and indium, distinct from the underlying molybdenum layer. (Data provided by the Centre for Materials Science and Engineering, Cranfield University.)

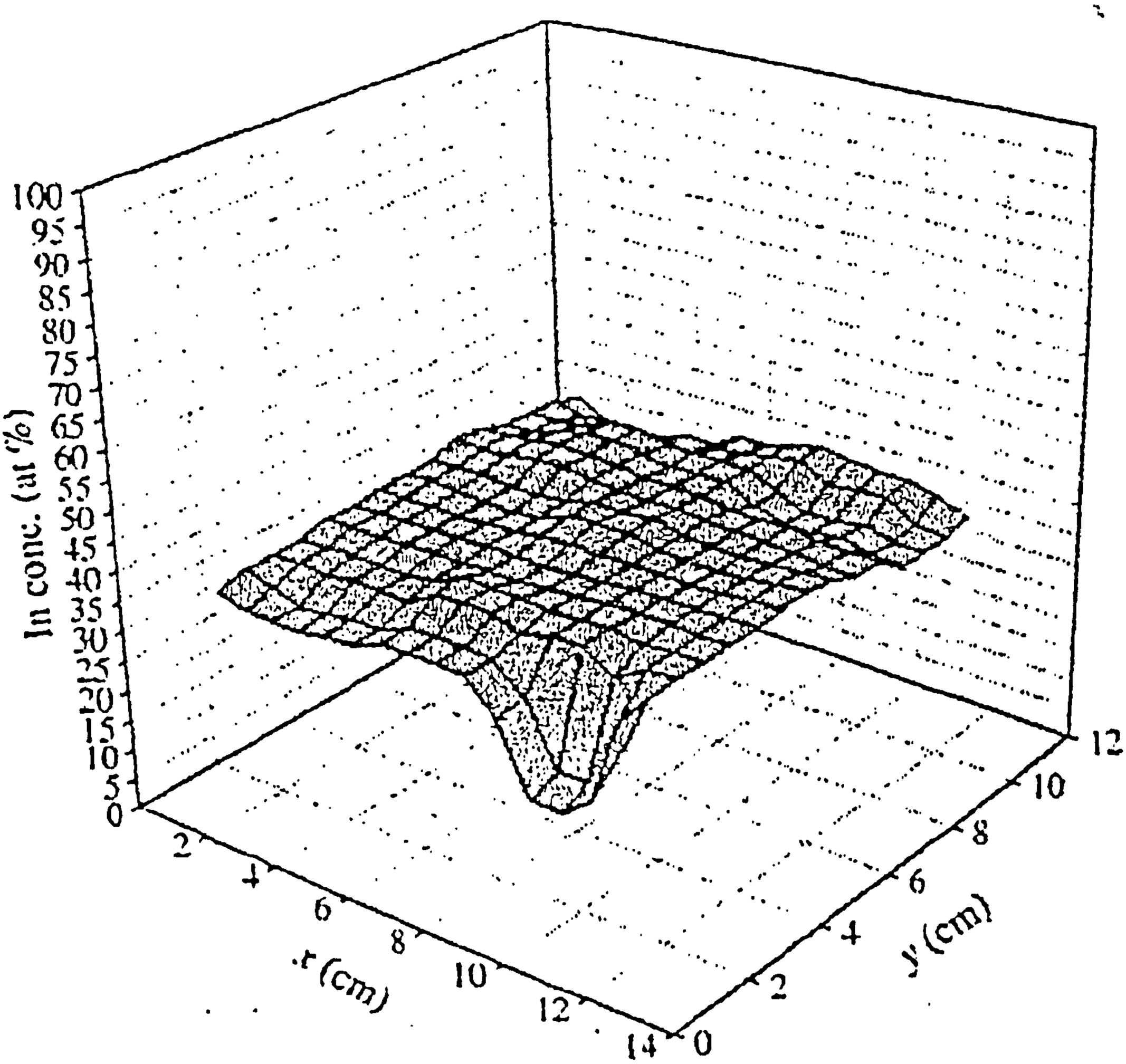

Figure 5.2 Variation in indium concentration in Cu/In precursors layers with position over the deposition area (as atomic percentage of total CuIn). (RBS data provided by the Centre for Materials Science and Engineering, Cranfield University.)

The sputtering conditions were as given in Table 5.1.

The energy of the incident He^+ ions is increasingly dissipated with greater penetration into the layer before large angle scattering occurs. Thus, decreasing energy in the back-scattered beam corresponds to greater depth within the film. In Figure 5.1, depth into the film is therefore measured from right to left. The data, as analysed by the RUMP software package, shows Cu/In films with a high degree of uniformity. A sharp demarcation between the Cu/In precursor and the underlying Mo layer is also evident.

The RBS data showed a high degree of compositional uniformity in the range 30 - 35 % indium over the area measured – approx. 120 cm^2 – as shown in Figure 5.2. (A variation at one corner may be due to this location being at the limits of the deposition area, and with the rate of In deposition falling off preferentially.) The data relating to elemental composition, provided by RBS, was complemented by EDAX measurements, which gave 33 % for this sample. These were used to determine the variation in composition with r.f. power applied to the indium target during sputtering. This allowed the power setting required to achieve stoichiometry (or any other specified composition), and was used in the selection of suitable precursors for subsequent conversion to $CuInS_2$. The results are shown in Figure 5.3 and Table 5.2.

Conditions constant for all depositions	
Copper sputtering power	32 W
Sputter time	24 hours
Rotation rate	1 RPM
Conditions for each deposition	
Sample number	Indium power
4	33 W
5	34 W
6	35 W
7	36 W
8	37 W
9	38 W
10	39 W
11	41 W

Table 5.1. Sputtering conditions for deposition of copper-indium alloys.

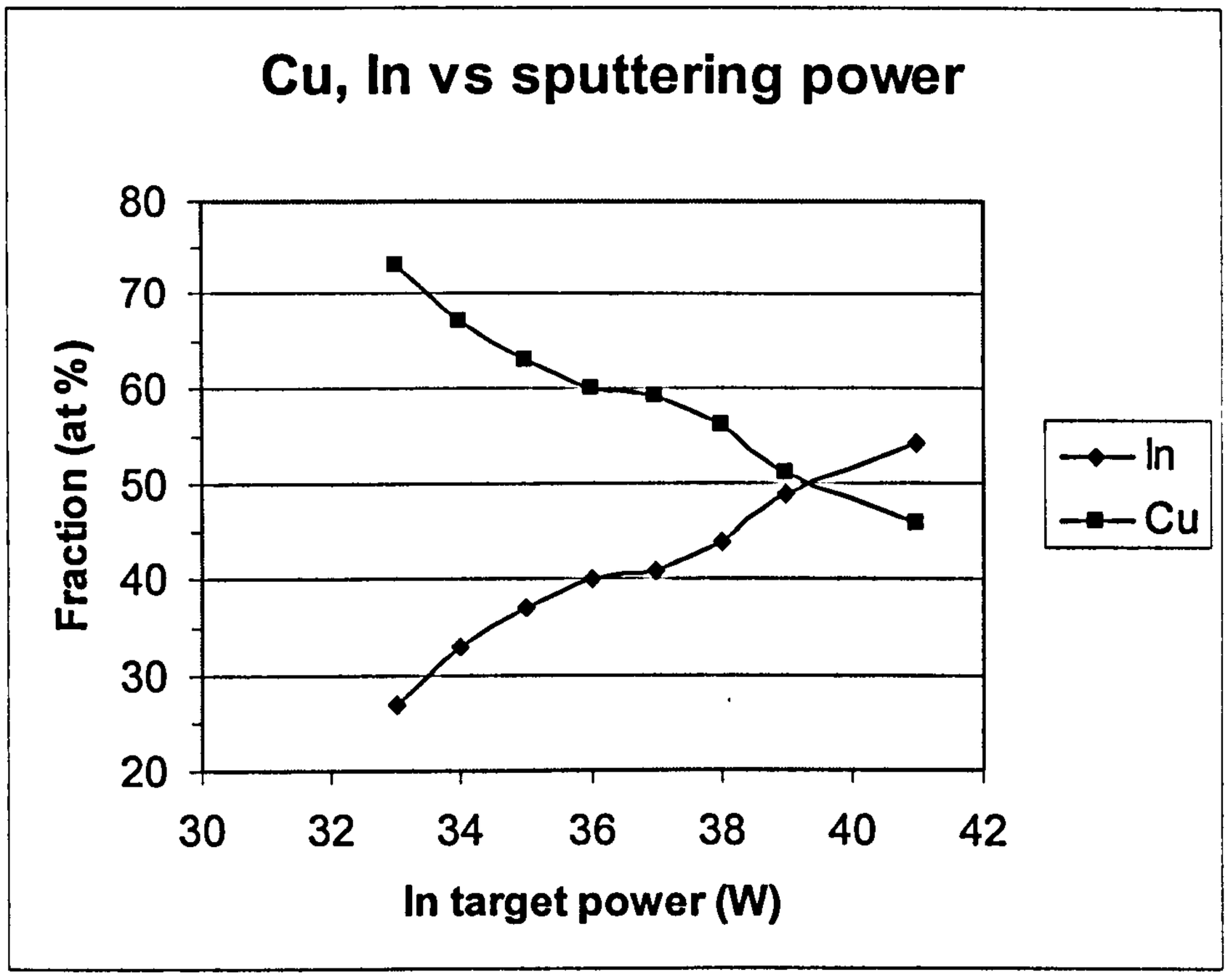

Figure 5.3. Atomic percentages of copper and indium in Cu/In precursor layers, for a range of power settings on the indium target. (Power on the copper target was 32 W for all depositions.) Measurements were produced by EDAX.

Power applied to indium target (W)	Indium fraction (at %)	Copper fraction (at %)
33	27	73
34	33	67
35	37	63
36	40	60
37	41	59
38	44	56
39	49	51
41	54	46

Table 5.2. Atomic percentages of copper and indium in Cu/In precursor layers, for a range of power settings on the indium target. (Power on the copper target was 32 W for all depositions.) Measurements were produced by EDAX. (Data provided by Advanced Materials Research Institute, Northumbria University.)

The data on physical composition, provided by RBS and EDAX, was complemented by XRD, which indicated the chemical compounds present, and the crystal phases in which they occurred. A diffractogram for a Cu/In precursor layer is shown in Figure 5.4. This shows the copper indium to be present in the form of $Cu_{11}In_9$, with no peaks observed for the metals Cu and In. Thus the metals have completely combined chemically. No peaks due to alloys of Mo with Cu and/or In were observed.

Scanning electron microscopy was used to assess a number of the microscopic properties of the films. The images were almost featureless, as shown in Figure 5.5. This indicates a generally smooth topography, with no inhomogeneities visible at a resolution of a few μm, such as voids or liquid droplets. The latter have previously been observed, due to separation of indium during annealing [3]. The edge-on SEM (Fig.5.6) shows the uniformity of thickness, and also the dense packing of the material, with few internal spaces. This should be conducive to formation of similarly dense structures in the final material.

5.1.1 Discussion

The depth profile produced by RBS shows that the Cu and In concentrations have a high degree of uniformity over the depth of the layer, indicating that extensive mixing has occurred during the sputter deposition. This may be attributable to the large number of thin layers deposited, compared with the smaller number of relatively thick layers, produced in previous work. The depth profile also shows a relatively sharp delineation between the Mo and Cu/In layers, and thus that little mixing has occurred between these two layers.

The RBS measurements of elemental composition over the area of approx. 120 cm^2, also indicates a high degree of uniformity. Thus, the results of measurements on the Cu/In precursors show a high degree of uniformity, both over the area of deposition, and with depth through the film.

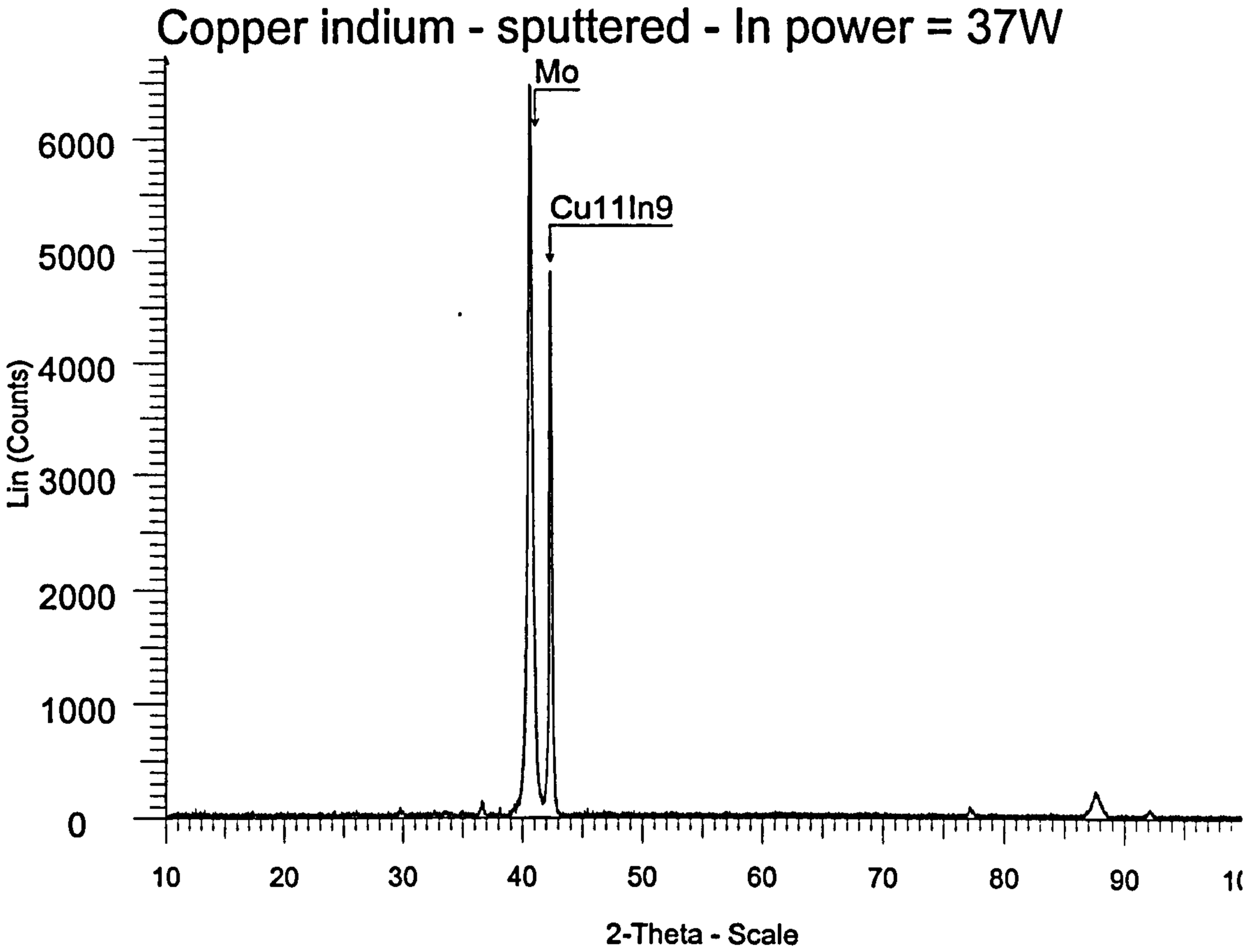

Figure 5.4. X-ray diffractogram of Cu/In precursors, showing formation of Cu_2In, with no material remaining in elemental form.

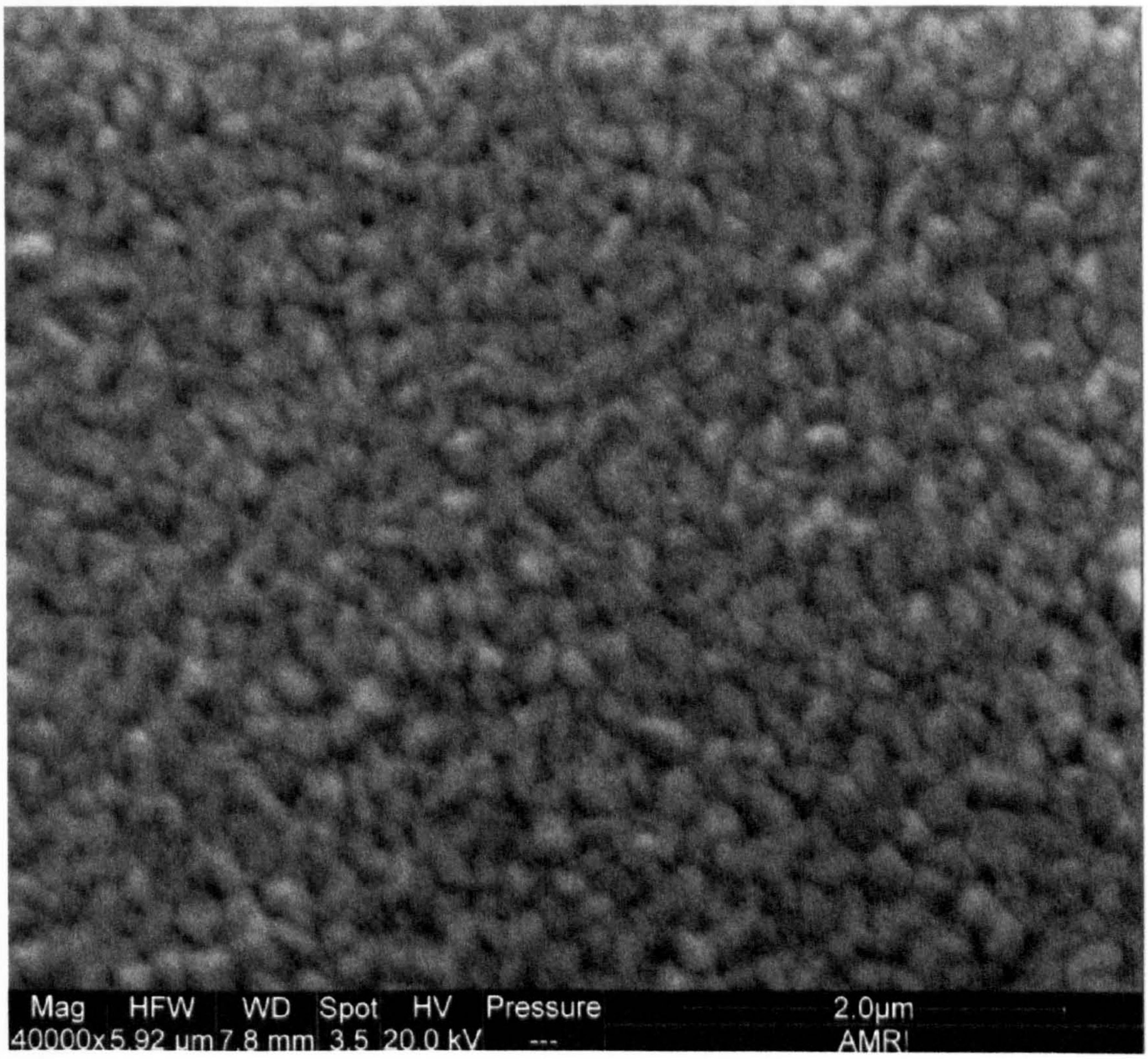

Figure 5.5 SEM of Cu/In precursor layer, showing a uniform surface topography, consisting of crystals of typically 0.2 µm.

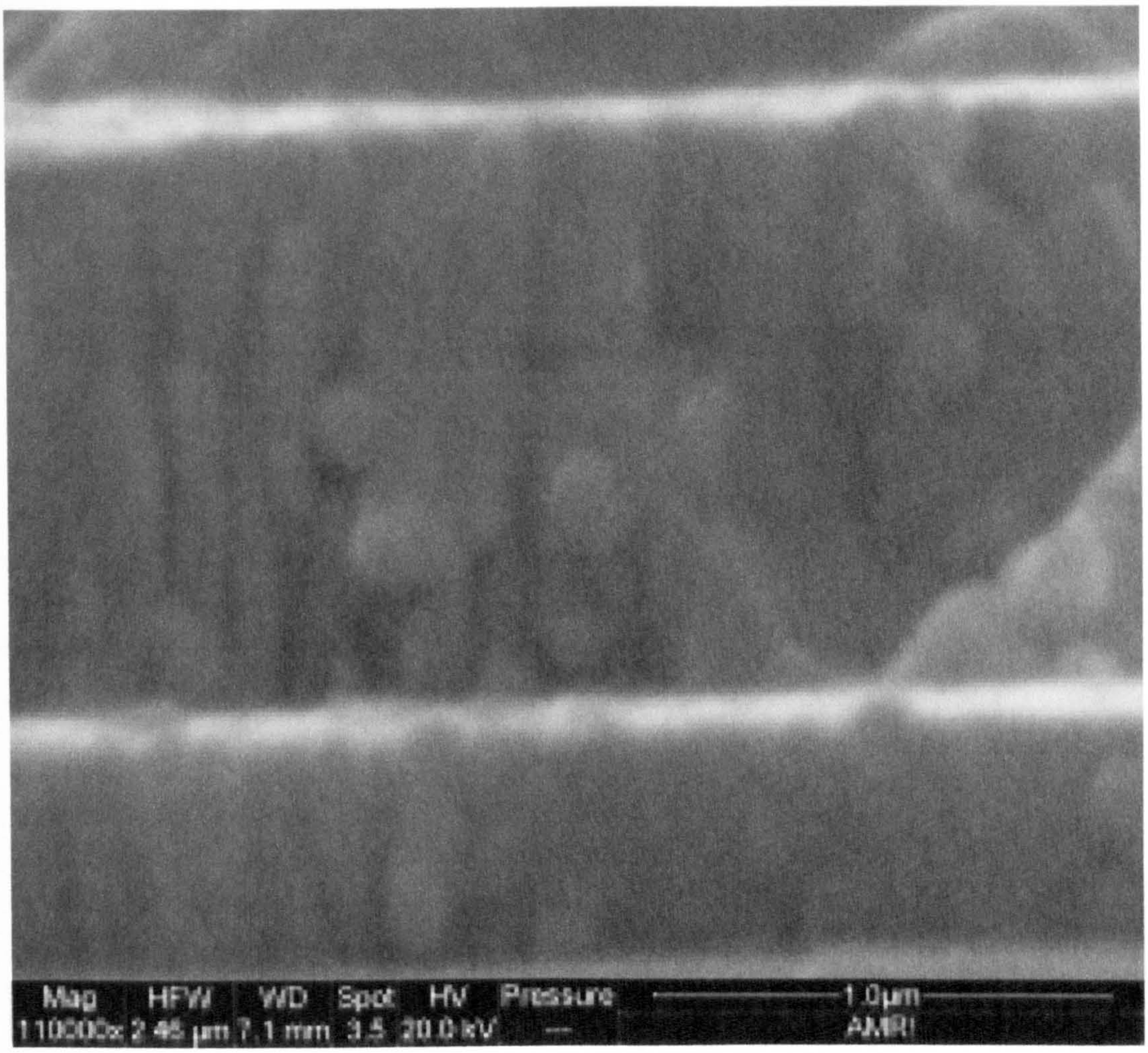

Figure 5.6. Edge-on SEM, showing a cross section through the Cu/In precursor layer. The top of the CuIn layer, the interface with the Mo back layer, and the substrate surface are visible. This shows the uniformity of thickness, and the dense structure, with few internal voids.

The RBS data on elemental composition is complemented by EDAX data, which gives the fractions of each element for a range of sputtering conditions (target power settings). The results show that a stoichiometric ratio can be achieved for a setting of approx. 39 W applied to the indium target. By applying power greater or less than this, n-type or p-type material respectively can be produced

The X-ray diffractogram shows peaks for $Cu_{11}In_9$, and an absence of peaks for elemental Cu or In. Thus, the metals have combined to form the alloy, with no metallic elements remaining. In combination with the RBS data, this shows both physical and chemical mixing of the elements. This was achieved without the need for post-deposition annealing, and thus obviates the time and energy budget, which would be incurred by this step. The absence of peaks for alloys of Mo and Cu, or Mo and In, shows that mixing has not occurred between the Mo and Cu/In layers, in agreement with the RBS data. Thus a well-defined junction between these two layers would appear to have formed.

The SEM images show similar uniformity, in terms of surface topography, and dense void-free structure. No indium liquid droplets were observed. These have previously been observed, due to separation of indium during annealing [3]. As annealing was not required for the Cu/In precursors produced in this work, these features did not form in this case.

In addition, the films have been found to have good adhesion to the substrate – a property of many materials deposited by sputtering [4, 5].

The uniformity of composition, over both area and depth, combined with good chemical mixing and good structural properties indicates that sputter deposition of Cu/In precursors could potentially be used as the first stage in fabrication of $CuInS_2$ films of large area (up to ~120 cm^2). (The $CuInS_2$ films actually produced

in this work were not of the same extent, but uniformity over the areas converted was assessed.) The results for these converted films are discussed in the next sections, for each of the sulphidisation processes explored in this work.

5.2 Conversion to copper indium disulphide using high pressure elemental sulphidisation

An important aspect of the evaluation of the $CuInS_2$ films is to assess the degree of incorporation of sulphur – both physically and chemically – into the precursor layers, and the evolution of this process with time. This latter factor can be assessed by comparing samples prepared under the same conditions for different periods of time.

Prior to commencing the experimental work, the spatial and temporal variations in temperature were measured. The temperature was measured (as a function of time) for the space between the inner and outer tubes, within the inner tube, and within the graphite box mounted centrally within the inner tube. The results are shown in Figure 5.7. The temperature 15 cm on either side of the mid-point was 7°C less than at the mid-point. These temperatures were also measured with argon flowing through the inner tube (in preparation for sulphur transport in an argon stream, as described in Section 5.3). In this case, the temperature downstream was similar to that at the mid-point, whereas that upstream was 15°C lower.

Temperatures used were in intervals of 50°C, from 300°C to 450°C. The time intervals, for which the substrates were at the selected temperature, ranged from 10 minutes up to 50 minutes, in 10 minute intervals.

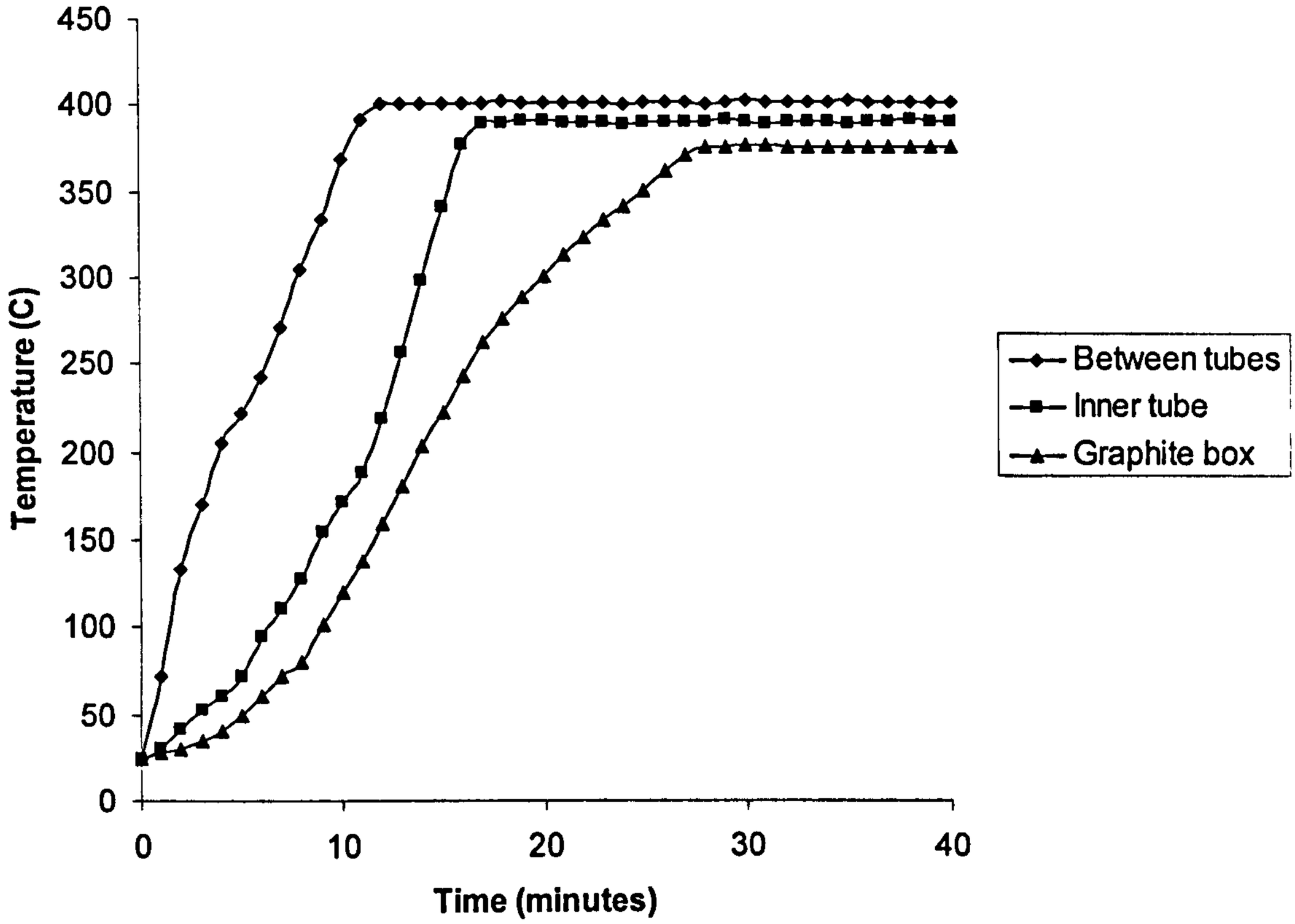

Figure 5.7 Temperature vs. time for a number of points in the tube furnace. (All points were at the axial mid-point.)

Other important factors are uniformity over the area of the film, and adhesion to the substrate. This includes adhesion of the $CuInS_2$ layer to the underlying Mo layer, and adhesion of the whole thin film structure to the glass substrate.

The elemental composition is shown in the EDAX data in Figure 5.8 and Table 5.3. The data show that the sulphur content reaches 50 % within 10 minutes, and subsequently rises to 60 %, after which it remains approximately constant. The Cu and In fractions decrease rapidly, as sulphur is incorporated. There is a preferential loss of indium, which becomes more pronounced for longer conversion times.

The data on elemental composition was complemented by analysis from XPS. This shows the surface composition of the material, which may differ from that of lower regions within the film – due to incomplete diffusion, re-evaporation, etc. The results are shown in Table 5.4 and in Figure 5.9.

The sulphur content reaches approx. 50 % within 10 minutes, and remains at this level for longer conversion times. This is approximately the stoichiometric value required for formation of $CuInS_2$. There is significant loss of indium, which occurs largely within the first 10 minutes, and continues slowly thereafter. The percentages of indium observed using XPS are slightly lower than the corresponding values obtained from EDAX.

The shifts of the peaks from the energy values for isolated atoms indicate the chemical combination(s) in which each element occurs. In the case of sulphur, S^{2-} is the dominant peak, and peaks for S^{-} and elemental sulphur are also observed. The spectrum for Cu consists of a large peak for Cu^{+} and a smaller one for Cu^{2+}. The major peak for In is In^{3+}.

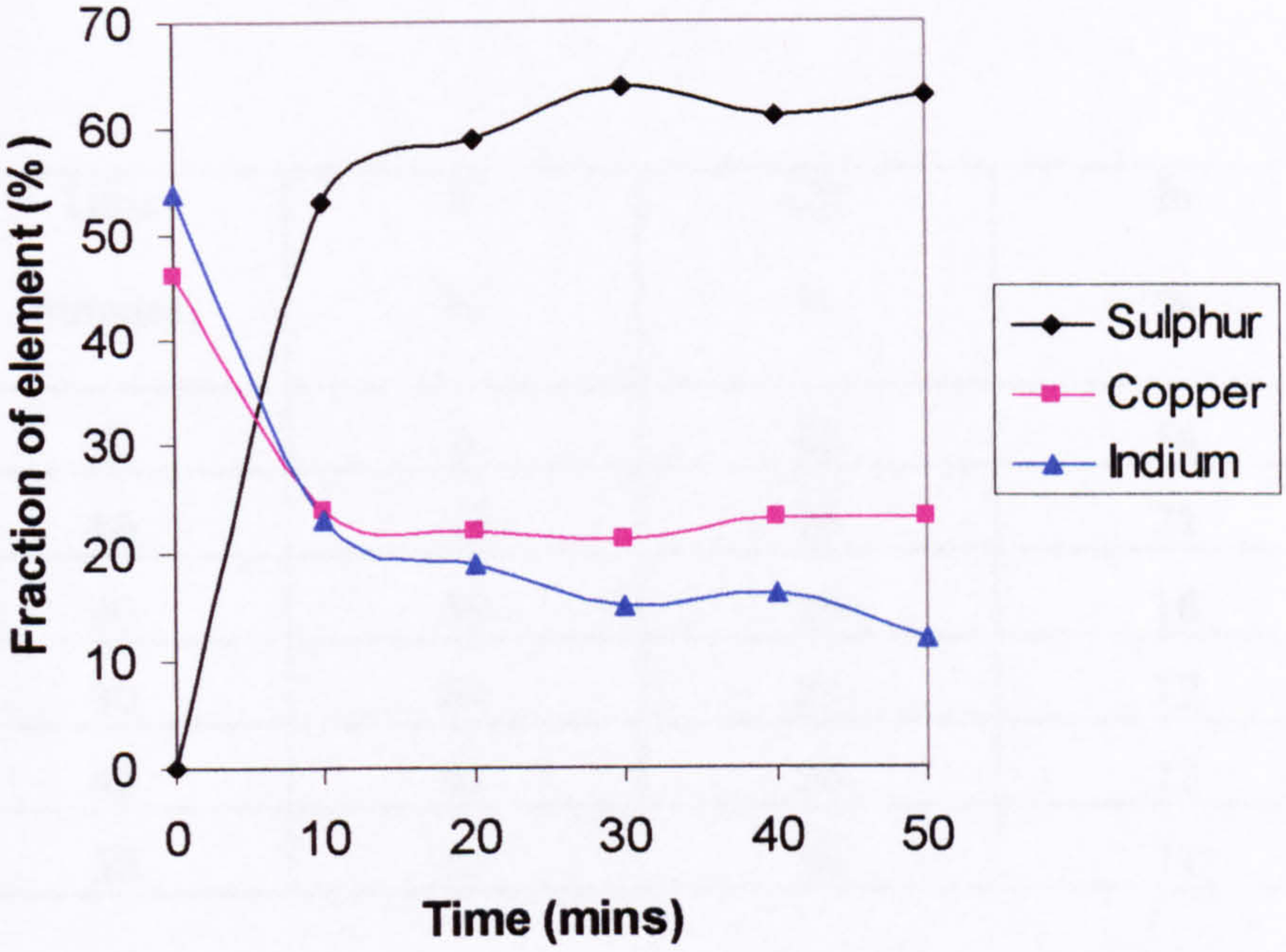

Figure 5.8. EDAX graph showing fractional elemental composition of converted films, for sulphidisation in a graphite box, at a temperature of 400°C.

Time (minutes)	S %	Cu %	In %
0	0	46	54
10	53	26	21
20	59	25	16
30	64	24	12
40	61	26	13
50	63	24	11

Table 5.3. EDAX data showing fractional elemental composition of converted films, for sulphidisation in a graphite box, at a temperature of 400°C.

Conversion Time	Cu	In	S
0	67	33	0
10	35.49	12.07	52.44
20	38.37	9.79	51.84
30	32.27	9.98	51.84
40	34.07	9.55	56.38

Table 5.4 Elemental composition of film surface, derived from XPS, for samples produced at 400°C. The sulphur content is approximately that required for $CuInS_2$. However, there is significant loss of indium.

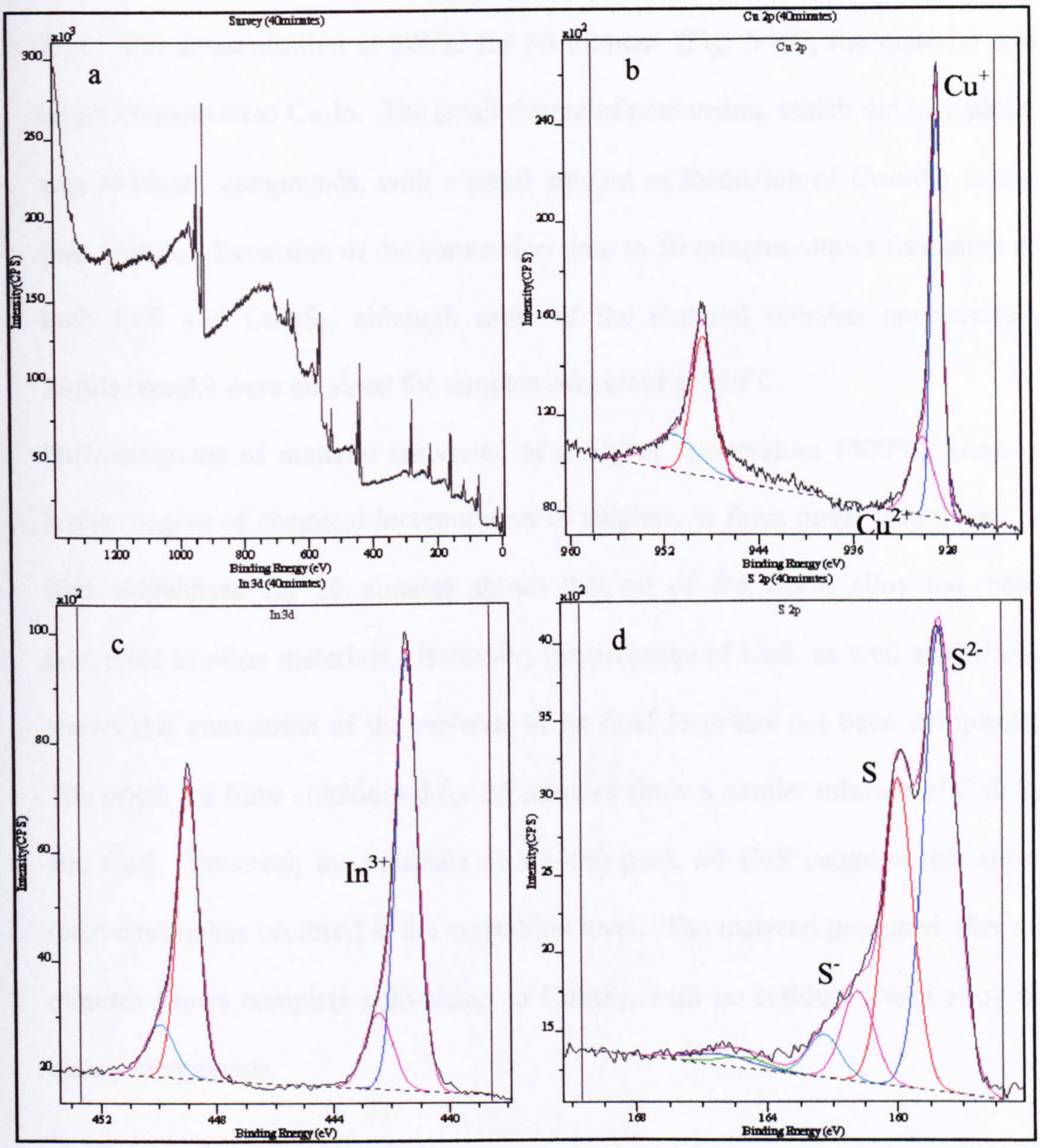

Figure 5.9 XPS scan for $CuInS_2$ film produced by conversion at 400°C for 40 minutes. Figure 5.8a shows the intensity across the whole energy range. Figures 5.8b, c and d show sections of this at higher resolution, focusing on the Cu (2p), In (3d) and S (2p) peaks respectively.

The degree of chemical incorporation of sulphur can be assessed using XRD. Diffractograms for a range of deposition conditions are shown in Figures 5.10 to 5.14. For sulphidisation at 300°C for 30 minutes (Fig. 5.10), the material was largely unconverted Cu_4In. The small degree of conversion, which did take place, was to binary compounds, with a small amount of formation of $CuIn_5S_8$, rather than $CuInS_2$. Extension of the conversion time to 50 minutes shows formation of both CuS and $CuInS_2$, although most of the material remains unconverted. Similar results were obtained for samples converted at 350°C.

Diffractograms of material converted at a higher temperature (400°C) show a higher degree of chemical incorporation of sulphur, to form metal sulphides. A film sulphidised for 30 minutes shows that all of the Cu/In alloy has been converted to other materials. However, the presence of CuS, as well as $CuInS_2$, shows that conversion of the material to its final form has not been completed. The graph for films sulphidised for 35 minutes show a similar mixture of $CuInS_2$ and CuS. However, the presence of a (006) peak for CuS suggests that some restructuring has occurred at the crystalline level. The material produced after 40 minutes shows complete conversion to $CuInS_2$, with no residual Cu/In alloy or binary compounds.

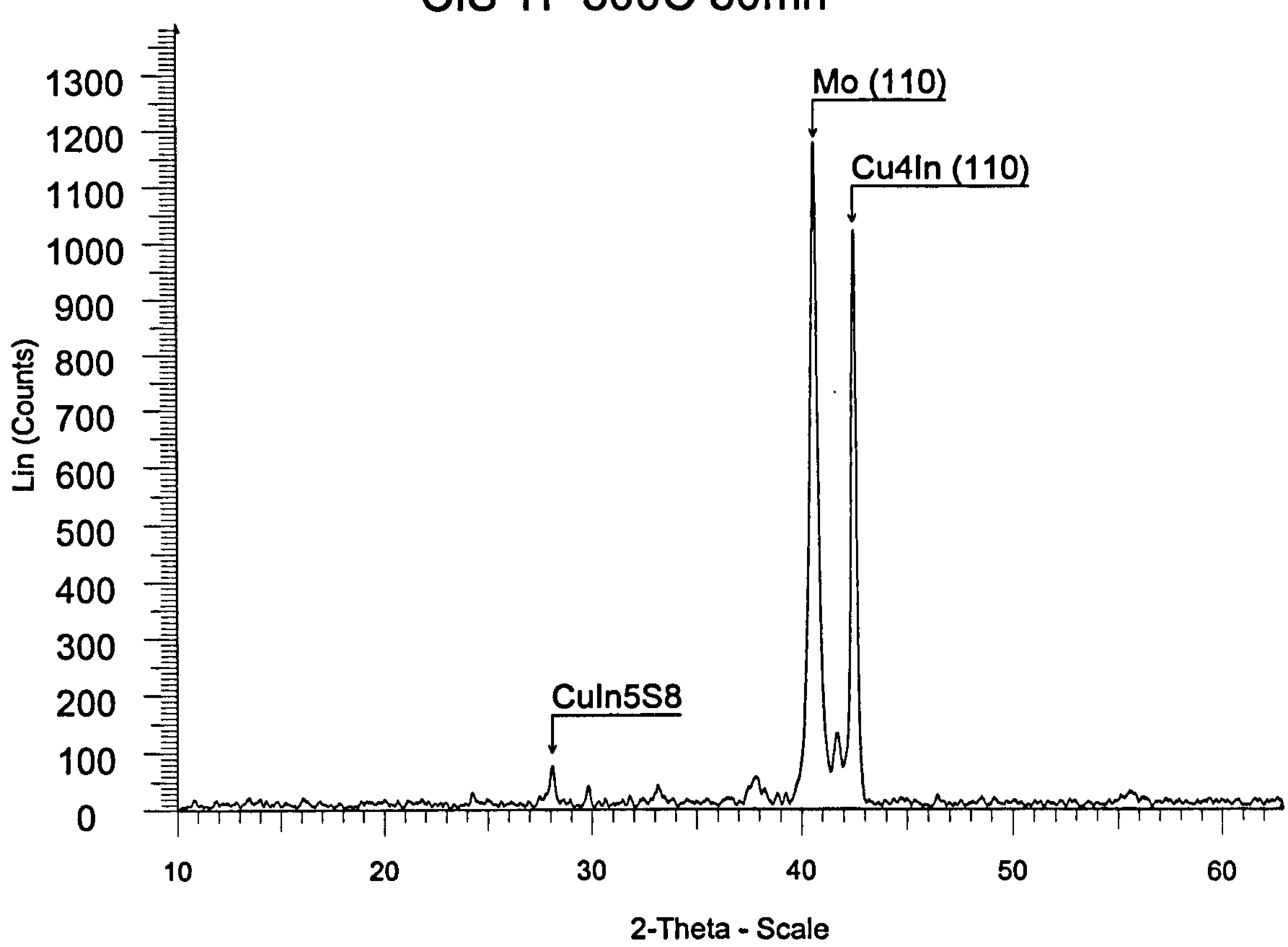

Figure 5.10. X-ray diffractogram of films sulphidised in a graphite box at 300°C for 30 minutes, showing largely unconverted material.

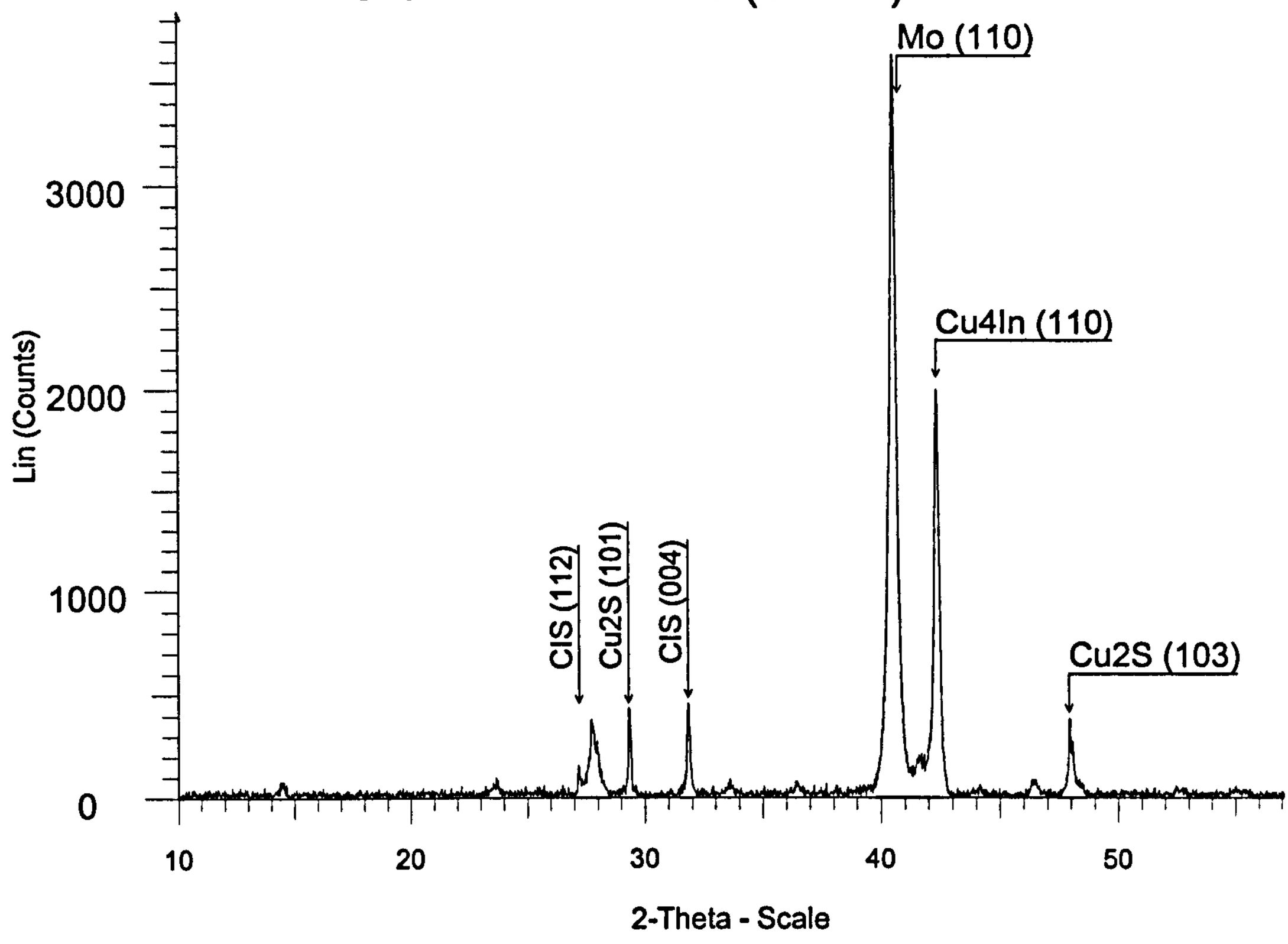

Figure 5.11. X-ray diffractogram of films sulphidised in a graphite box at 300°C for 50 minutes, showing some conversion to CuS and $CuInS_2$, and a remainder of largely unconverted material.

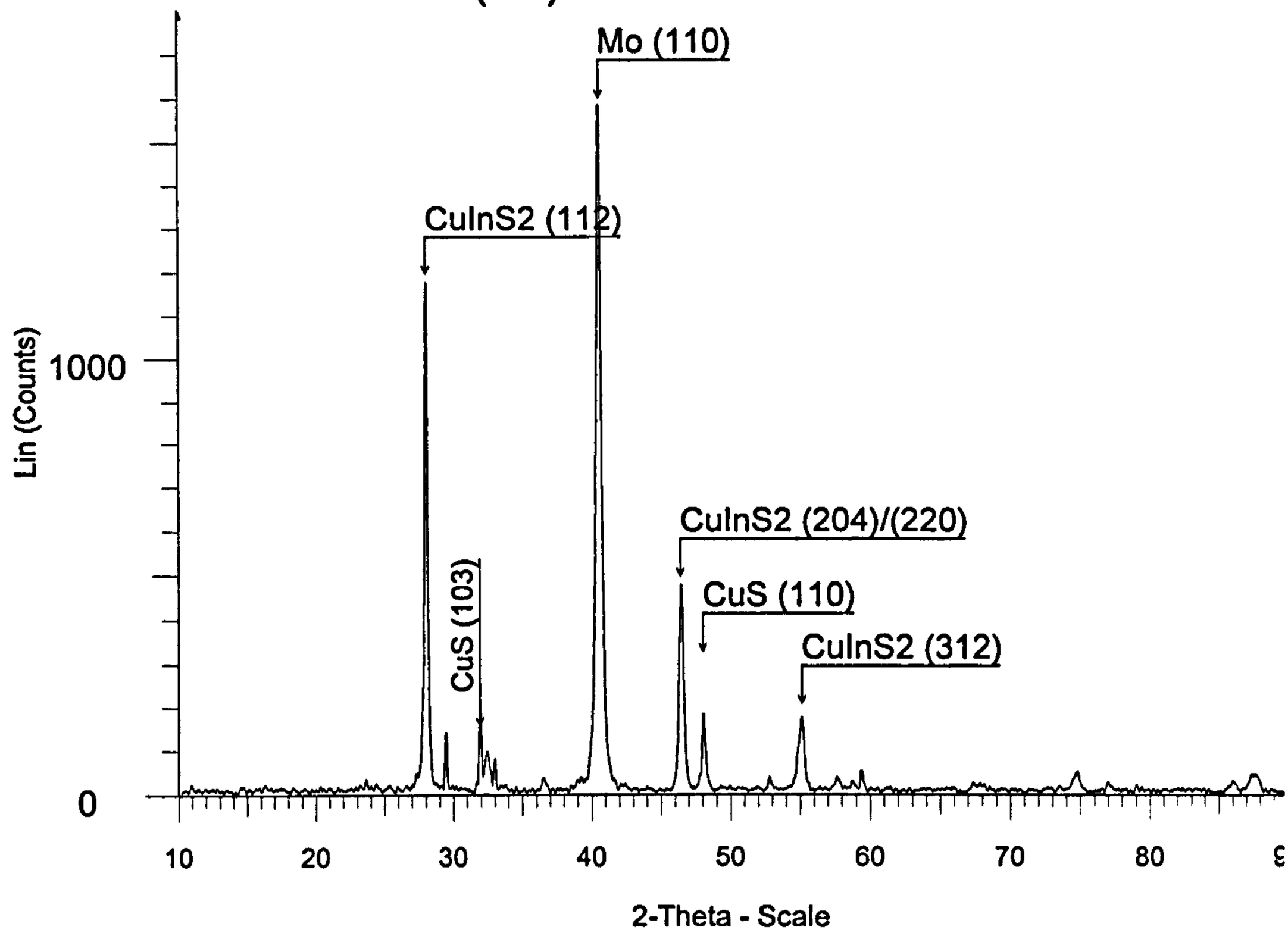

Figure 5.12. X-ray diffractogram of films sulphidised in a graphite box at 400°C for 30 minutes, showing conversion to CuS and $CuInS_2$, with no remaining unconverted material.

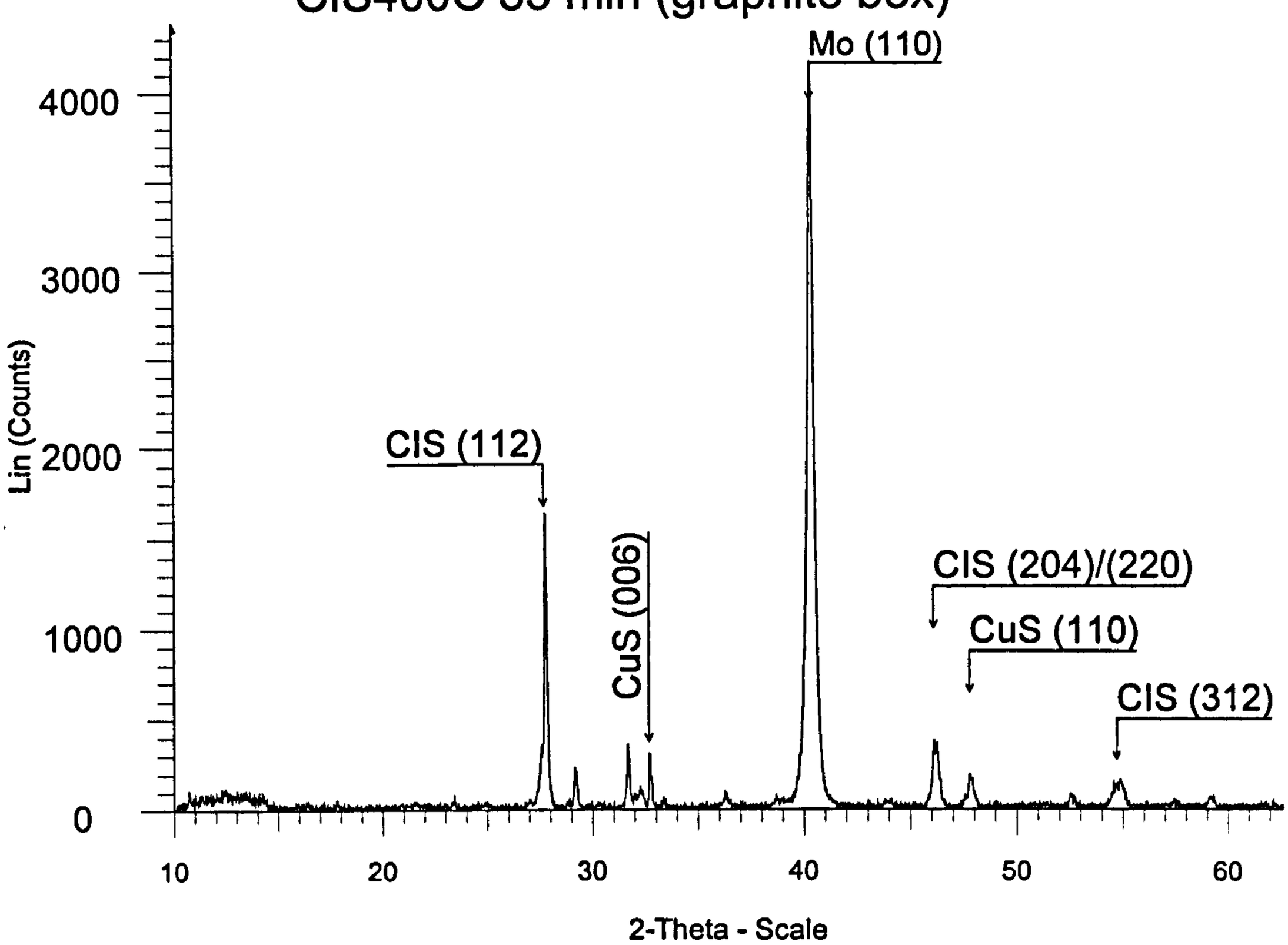

Figure 5.13. X-ray diffractogram of films sulphidised in a graphite box at 400°C for 35 minutes, showing the continued presence of partially converted material – CuS. The development of the (006) peak suggests some degree of crystalline restructuring.

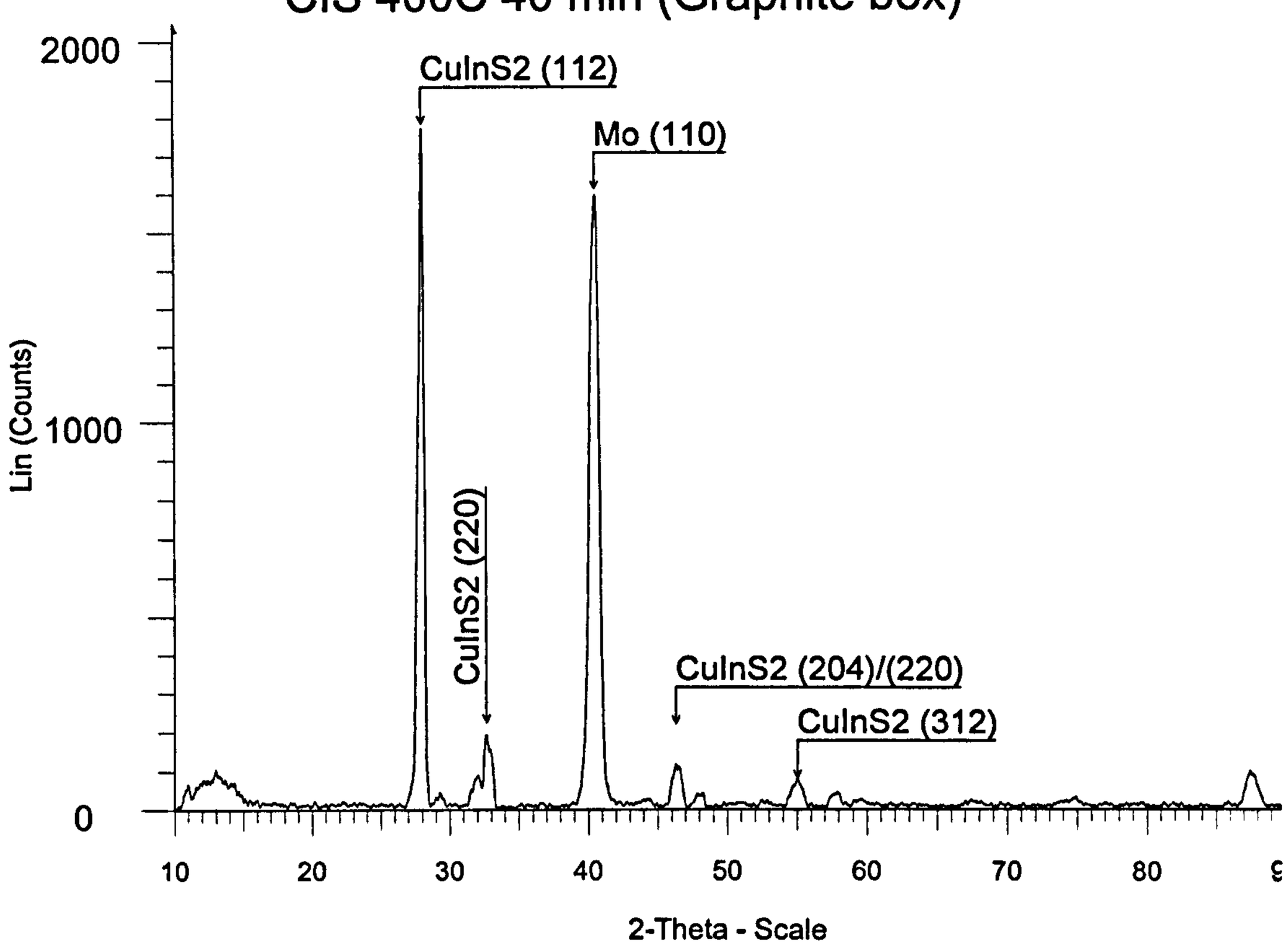

Figure 5.14. X-ray diffractogram of films sulphidised in a graphite box at 400°C for 40 minutes, showing complete conversion to $CuInS_2$.

Scanning electron microscopy shows irregular crystals, with typical dimensions of a few μm, in essentially random orientations, as shown in Figure 5.15. These crystals form a relatively dense structure. Although there are a number of inter-crystalline spaces, none of these appear to be large enough to constitute pinholes, which would provide short-circuit paths through the layer.

The optical spectroscopy measurements show a cut-off wavelength in the region 850 to 900 nm, as shown in Figure 5.16. The band gap is related to the cut-off wavelength by equation (4.9)

This gives a band gap in the range 1.38 to 1.46 eV. This is in agreement with the value usually given for $CuInS_2$. The transmittance at shorter wavelengths is negligible, indicating a high optical absorption coefficient.

From the spectroscopy measurements, a graph of $(\alpha hv)^2$ versus hv was derived, which gave a band gap of 1.42 eV, again in agreement with previously observed values. This is shown in Figure 5.17.

Visual inspection showed good uniformity, in terms of colour, texture, etc, over the area of the sample (up to 38 x 26 mm). Adhesion was good for films converted at 400°C. However, for conversion at higher temperatures (420 and 450°C), the layers were brittle, and had poor adhesion to the substrate. At higher temperatures - 500° - the soda-lime glass substrates tended to deform.

	Conversion time			
Conversion temperature	10 minutes	20 minutes	30 minutes	40 minutes
300°C	Little conversion or conversion to binaries only			
350°C	Little conversion or conversion to binaries only			
400°C	Mixed binary and ternary sulphides		Largely ternary sulphides with some binaries	
450°C	Layers converted to sulphides, but brittle			

Table 5.5 Conversion to binary and ternary sulphides for a range of conversion temperatures and times.

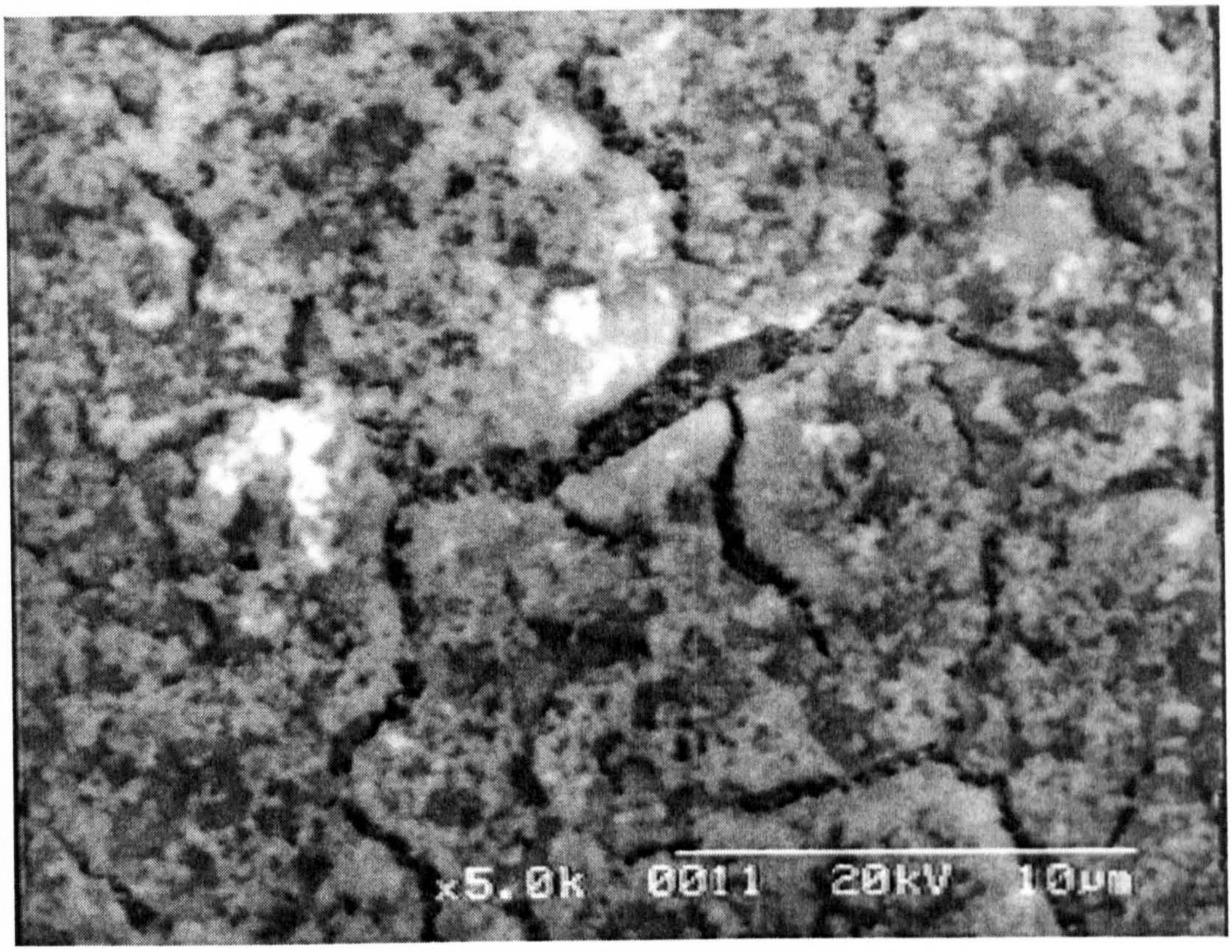

Figure 5.15. Scanning electron micrograph of $CuInS_2$ layer, showing a relatively dense structure.

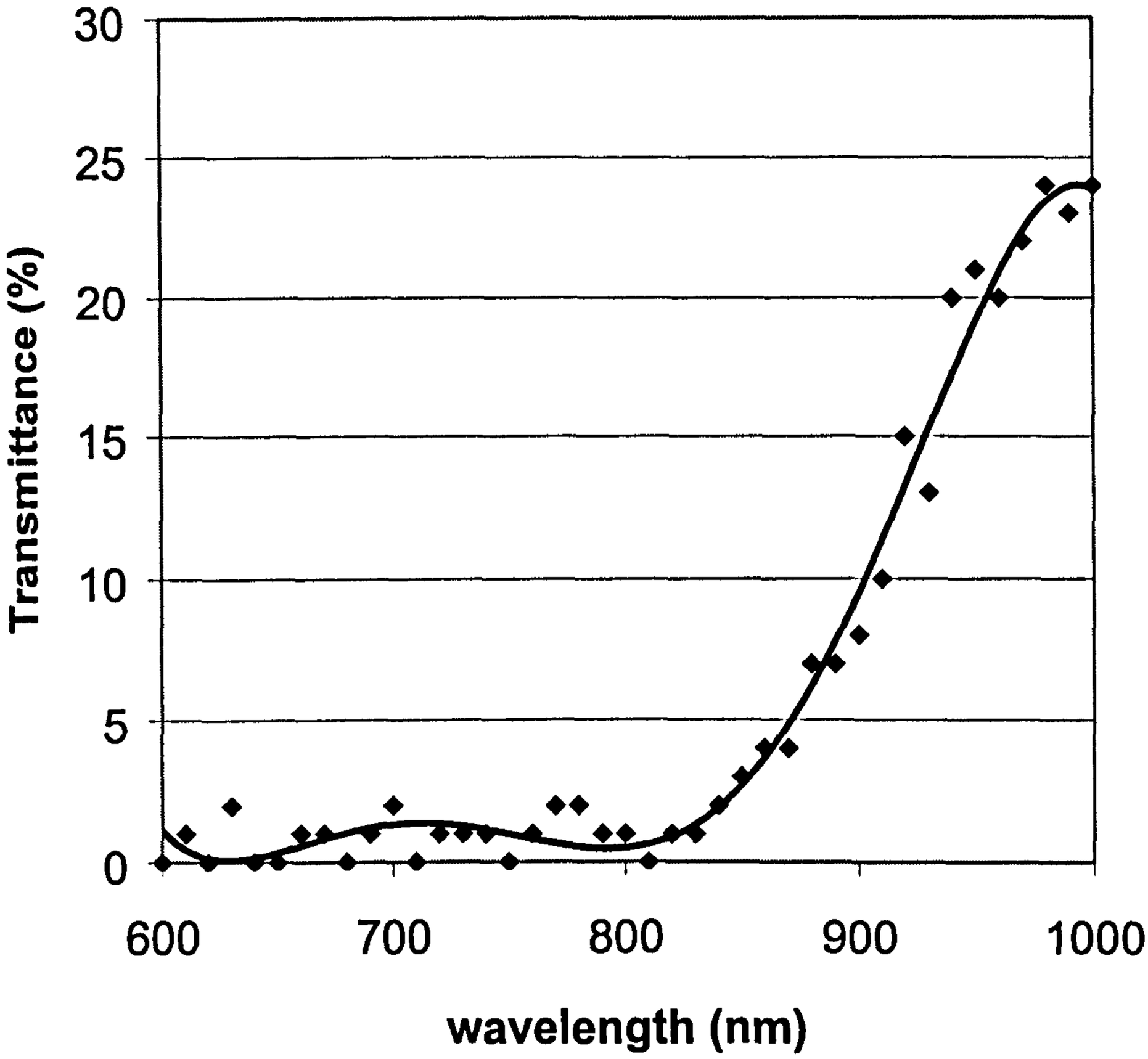

Figure 5.16 Transmittance vs wavelength for $CuInS_2$ produced by elemental sulphidisation, showing a cut off wavelength of 900 nm.

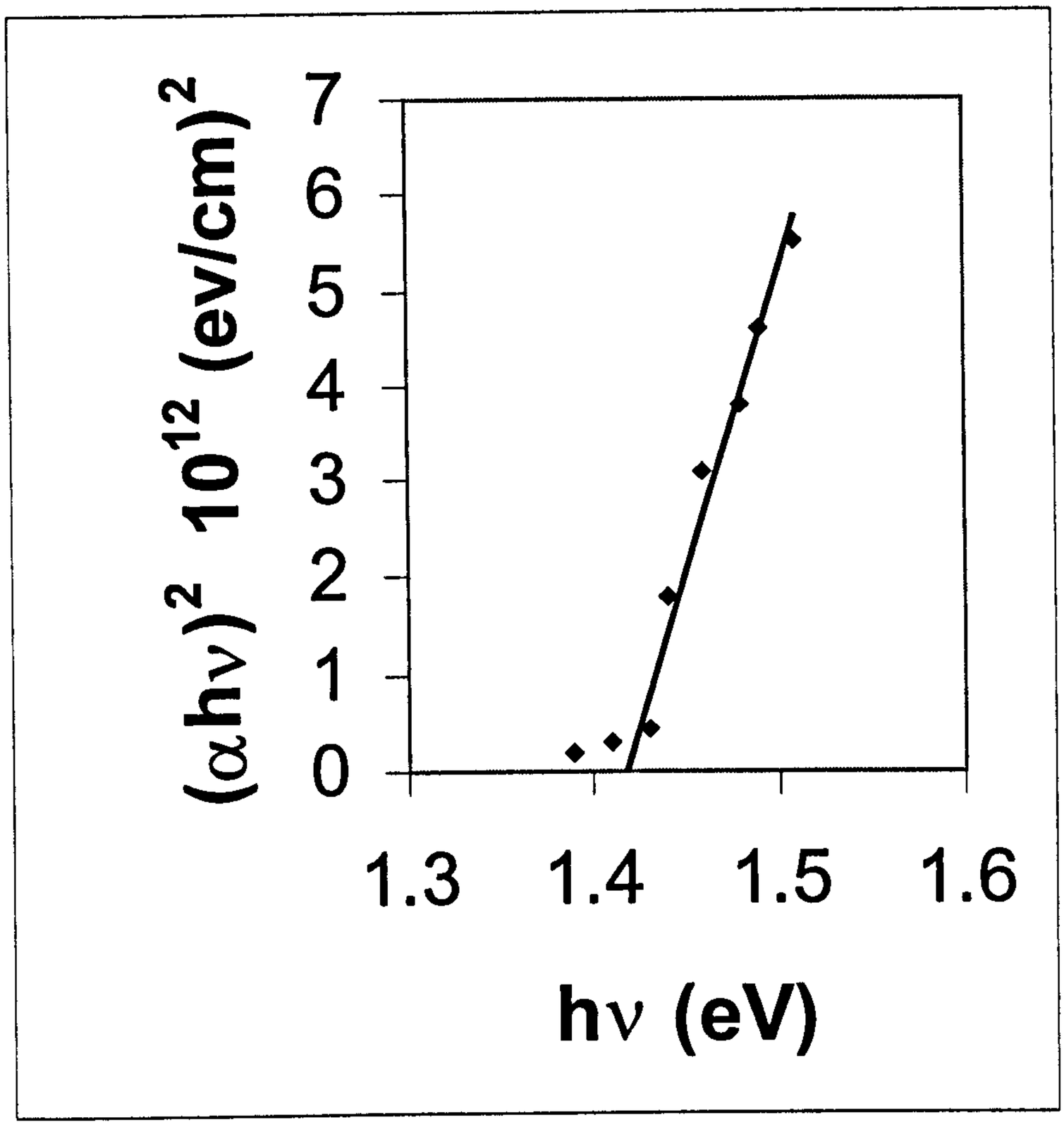

Figure 5.17. $(\alpha h\nu)^2$ versus $h\nu$ for $CuInS_2$ produced by elemental sulphidisation, showing a bang-gap energy of 1.42 eV

5.2.1 Discussion

The EDAX results show that sulphur incorporation reaches the stoichiometric value of 50 % within 10 minutes of reaching 400°C, and that the fractions of Cu and In remain approximately equal to each other after this time. The sulphur content increases somewhat above this value for longer conversion times. In addition, there is a preferential loss of indium for longer conversion times, which results in copper-rich material. This may be due to evaporation of indium from the films.

The XPS data showed similar trends in the evolution of the physical composition. However, the indium content was lower than that measured by EDAX. As XPS measures composition at the surface, whereas EDAX involves a degree of penetration into the material, this indicates that the indium content is lower at the surface than in the underlying layer. This is consistent with evaporation of indium during the conversion process, as this would occur most readily from the surface.

The shifts in the peaks observed in the XPS measurements give some indication of possible chemical combinations [6]. The S^{2-} oxidation state is consistent with $CuInS_2$, but is also consistent with Cu_2S and In_2S_3. The S^{-} state is consistent with a number of compounds, including CuS_2. Similarly, the Cu^{+} state and In^{3+} state are consistent with $CuInS_2$, and also with Cu_2S and In_2S_3. The Cu^{2+} state is consistent with CuS. These results suggest some degree of partial conversion, involving formation of other compounds in addition to $CuInS_2$.

The X-ray diffractograms indicate that a minimum temperature of 400°C is required for significant formation of sulphides, and that a period of 40 minutes at this temperature is required for full conversion to $CuInS_2$. Referring to the data produced by EDAX and XPS, it can be seen that heating for this time leads to a significant loss of indium, and hence production of non-stoichiometric material.

The SEM shows a dense crystalline structure with relatively narrow intergrain spaces. As such spaces tend to increase the rates of scattering and recombination, the electrical losses due to these effects should tend to be reduced. These narrow intergrain spaces are unlikely to penetrate the full depth of the film. Such spaces are referred to as pinholes, and act as short circuit paths between overlying and underlying layers in a complete photovoltaic device. This current path across the junction reduces the current available to the external circuit. The absence of observable pinholes would tend to reduce such losses.

The optical spectrophotometry measurements show a band gap of 1.38 to 1.46 eV, which is consistent with the generally quoted value [7]. This is in the optimum region for matching with the solar spectrum, and thus has the potential for forming high efficiency photovoltaic cells. The low optical transmittance at shorter wavelength indicates a high absorption coefficient for photons of energy higher than the band gap. Such photons would therefore be absorbed close to the top of the absorber layer, and hence close to the junction. This would reduce the distance, which photo-induced charge carriers would be required to travel before reaching the junction, and hence the recombination losses incurred in doing so.

The brittle nature, observed by visual inspection, of films produced by sulphidisation at temperatures higher than 400°C sets an upper limit to the conditions suitable for production of good films. Combined with the observations that sulphur incorporation is minimal for temperatures as low as 300°C, this indicates that a temperature of 400°C is appropriate.

In comparison with previous work, the lower temperature used (400°C vs. typically 500°C or higher) allows the use of soda-lime glass, rather than borosilicate glass. This has the potential for cost reduction, when applied at an industrial scale. The use of sulphur vapour, transferred by indirect transport (diffusion), avoids the limitations of line-of-sight transport, while avoiding the environmental problems of hydrogen sulphide.

5.3 Conversion to copper indium disulphide using elemental sulphur in argon carrier gas

The objectives of the measurements and analysis in this section of the work were essentially similar to those for the work on high pressure sulphidisation – assessment of physical and chemical incorporation of sulphur into the Cu/In precursors. Thus the same measurement techniques were used, and substantially the same analysis was performed. A series of sulphidisations was performed at each temperature, over a range from 200°C to 450°C in 50°C steps, and for times from 10 to 40 minutes in 10 minute steps.

The EDAX measurements (Fig. 5.18, Table 5.6) of films converted at 400°C show that physical incorporation of sulphur reached the required value of 50 % in approx. 25 minutes. The fractions of Cu and In decreased approximately in proportion until about 10 minutes. However, preferential loss of indium commenced after this time, and this was reduced to a little over half of the copper concentration by 40 minutes.

Rutherford back-scattering measurements, performed by collaborators at Cranfield University, provide additional data on elemental composition, including variation with depth through the film. The graph in figure 5.19 is based on data for a film sulphidised for 10 minutes at 400°C, and shows the partial incorporation of sulphur. The sulphur content is seen to be highest closest to the surface (highest back-scattered energy), which is consistent with diffusion into the layer from the surface. The fractions of Cu and In are approximately constant throughout the layer, with the In fraction being higher. The relatively high signal for indium is consistent with its initial high content (67 %) in the precursors.

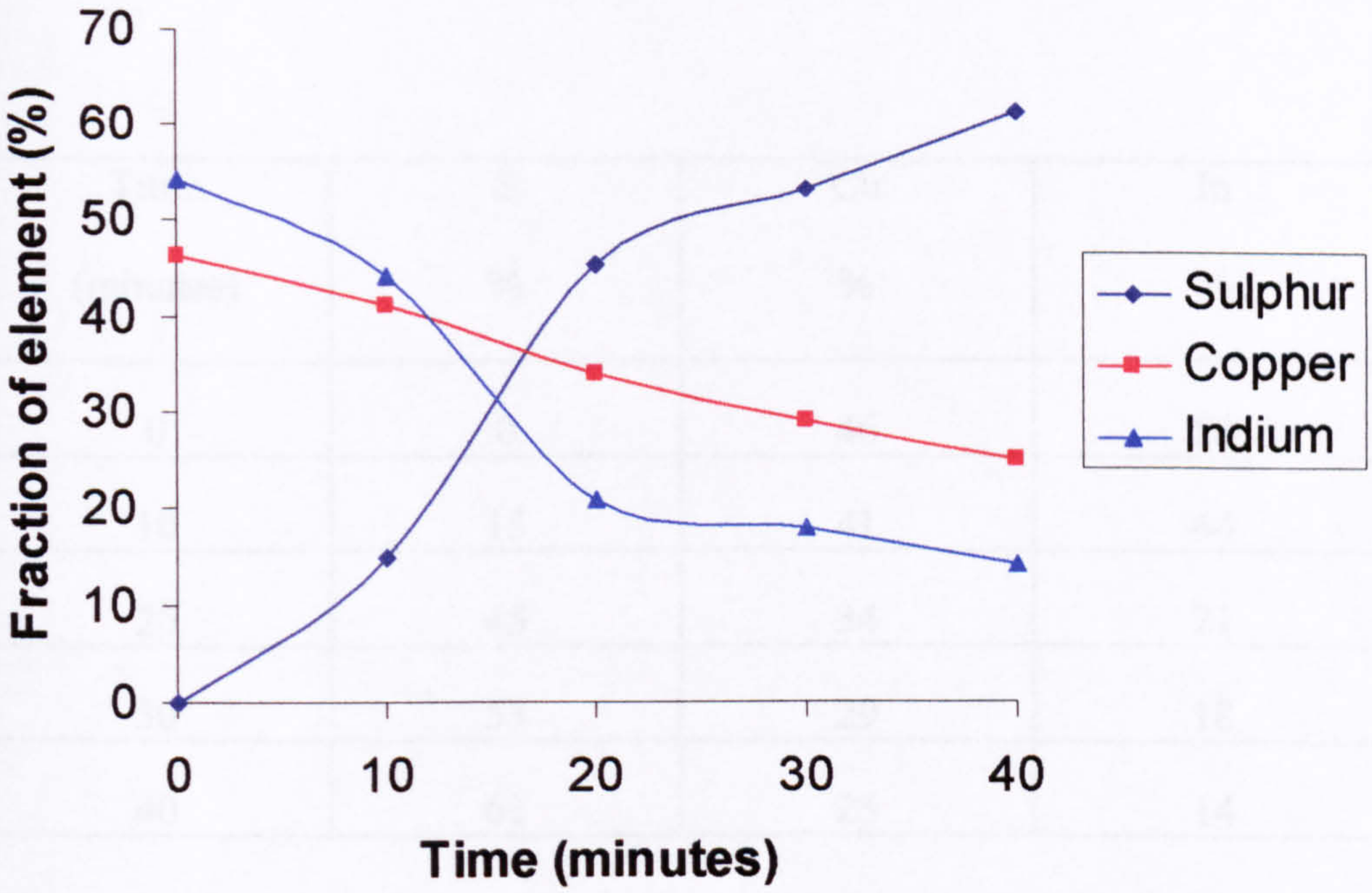

Figure 5.18. EDAX graph of films sulphidised at 400°C by elemental sulphur in an argon flow. The data show physical incorporation of sulphur occurring within 25 minutes, and preferential loss of indium becoming significant after 10 minutes.

Time (minutes)	S %	Cu %	In %
0	0	46	54
10	15	41	44
20	45	34	21
30	53	29	18
40	61	25	14

Table 5.6. EDAX data of films sulphidised at 400°C by elemental sulphur in an argon flow. The data show physical incorporation of sulphur occurring within 25 minutes, and preferential loss of indium becoming significant from 10 minutes onwards.

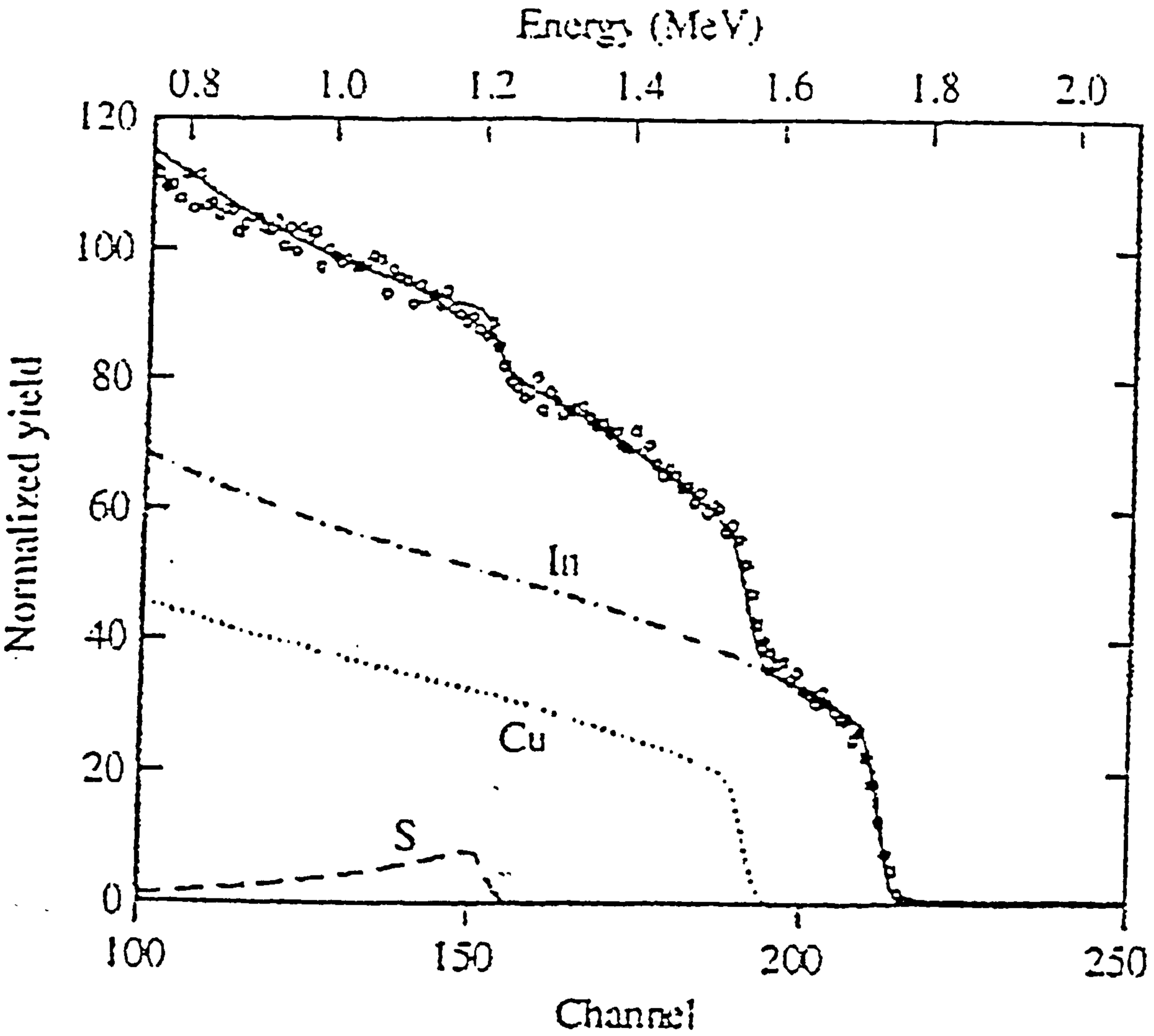

Figure 5.19. RBS graph of Cu/In precursor partially converted to $CuInS_2$. The graph shows a larger count close to the high-energy edge for sulphur, indicating a higher concentration of sulphur closer to the surface. This is consistent with diffusion from the surface. (Provided by Cranfield University.)

X-ray diffraction shows the development of the chemical incorporation of sulphur into the Cu/In precursors. For temperatures of 350°C or less, there is little conversion to sulphides, particularly complete conversion to $CuInS_2$. The results for material converted at 400°C are shown in Figures 5.20 to 5.23. After 10 minutes (Fig. 5.20), all of the precursor material has been converted to a number of sulphides, with no Cu/In alloy remaining. The binary compounds CuS and Cu_9S_5 have been identified, showing partial conversion. The material, which has been completely converted to ternary compounds, consists predominantly of $CuInS_2$, although there is a significant quantity of $CuIn_5S_8$.

After 20 minutes (Fig. 5.21), the quantity of binary compounds has been greatly reduced, with only a small peak for Cu_9S_5 remaining. The ternary compounds continue to be composed largely of $CuInS_2$, with some $CuIn_5S_8$. After 30 minutes (Fig. 5.22), all the material has been converted to ternary compounds. Most has been converted to $CuInS_2$, with very little being converted to $CuIn_5S_8$. For material sulphidised for 40 minutes, the diffractogram is essentially similar (Fig. 5.23), showing the same mixture of ternary compounds.

For all of the conversion times, the (112) peak is the most prominent, indicating oriented growth in this direction. There are no peaks observed for sulphides of Mo, or alloys of Mo with either Cu or In.

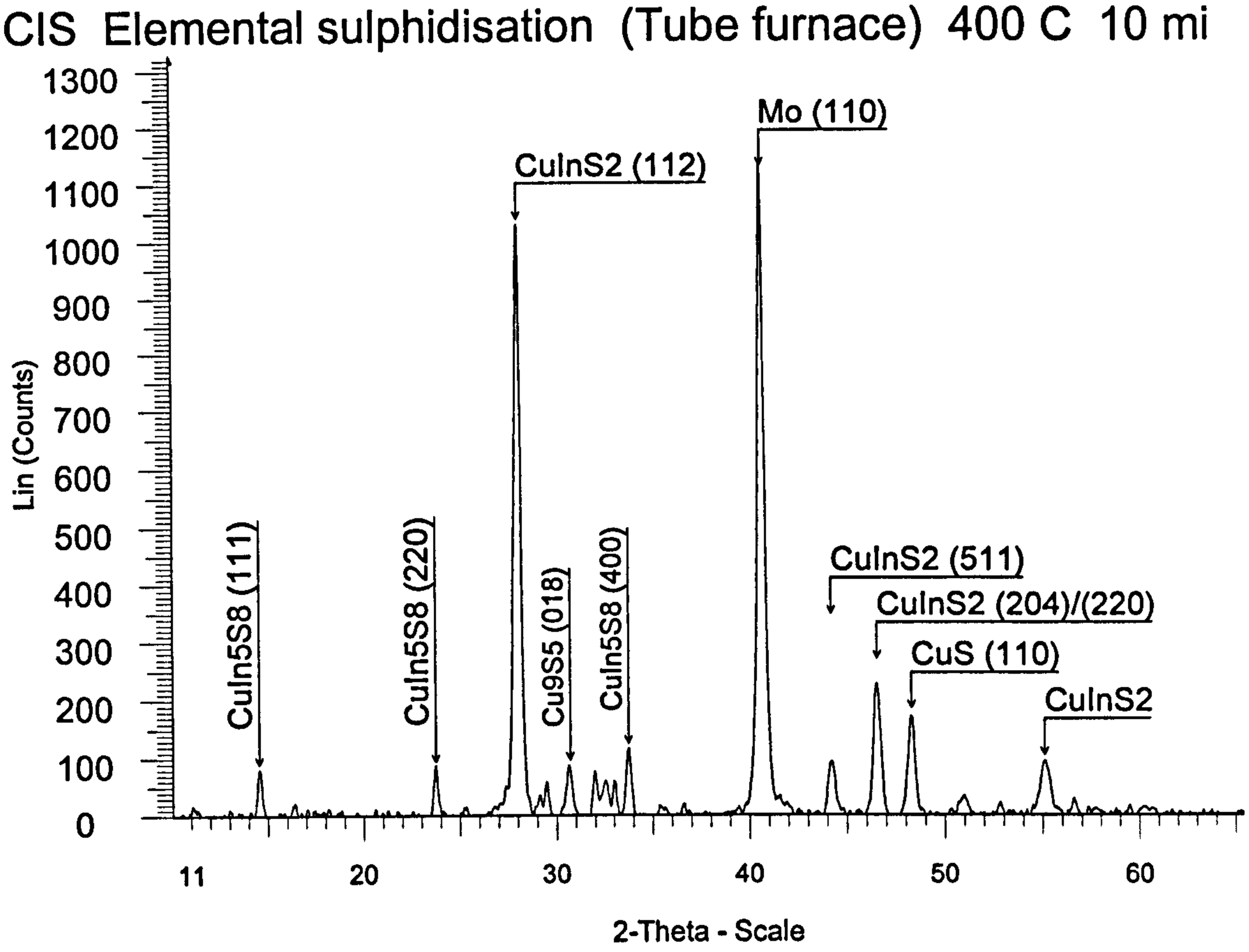

Figure 5.20. X-ray diffractogram of film sulphidised for 10 minutes at 400°C in flowing argon. Some of the material remains as partially converted binary compounds. Most of the ternary material is $CuInS_2$, with some $CuIn_5S_8$.

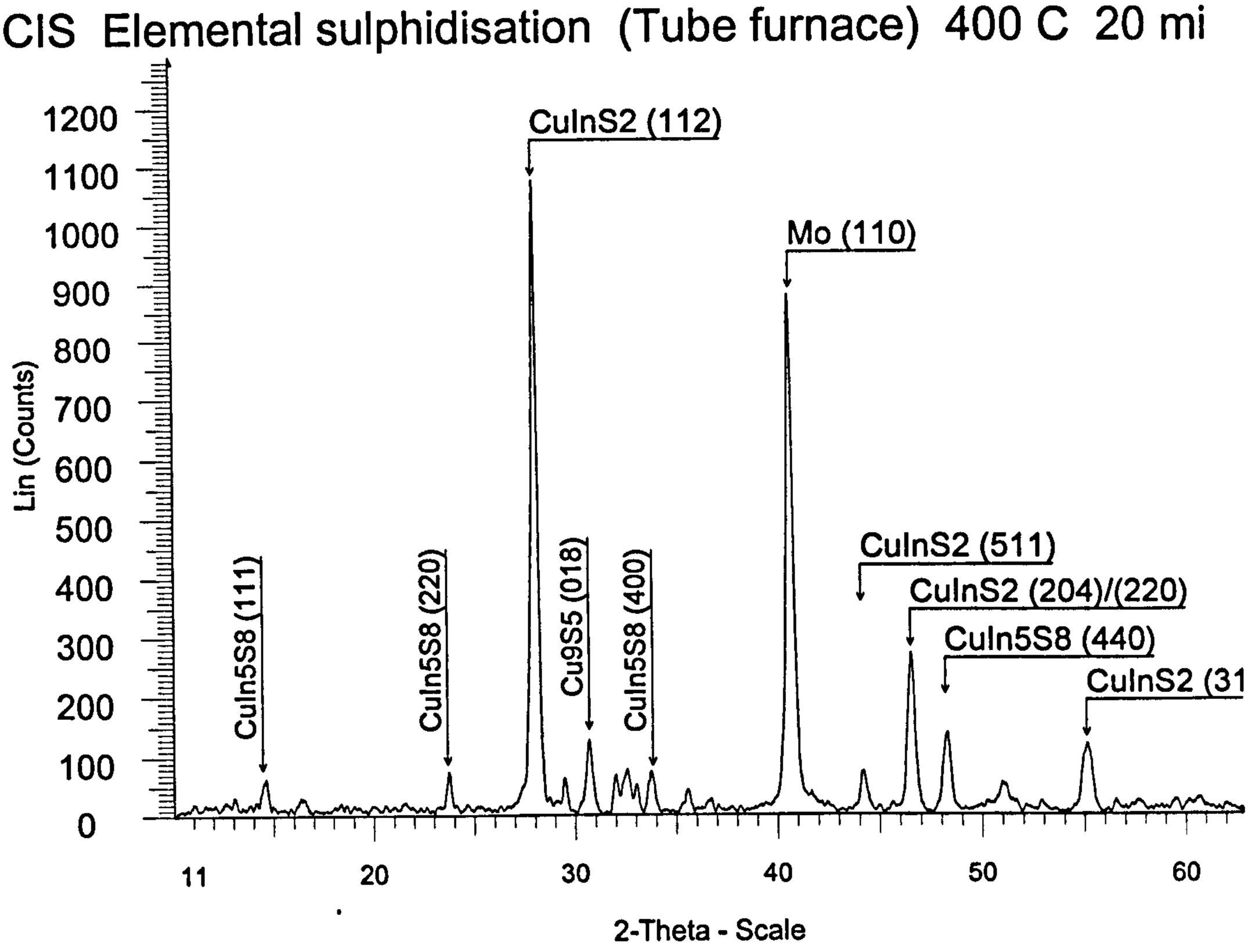

Figure 5.21. X-ray diffractogram of film sulphidised for 20 minutes at 400°C in flowing argon. Most of the partially converted binary compounds have undergone further change - either to Cu_9S_5 or to ternary compounds. Most of the ternary material remains $CuInS_2$, with some $CuIn_5S_8$.

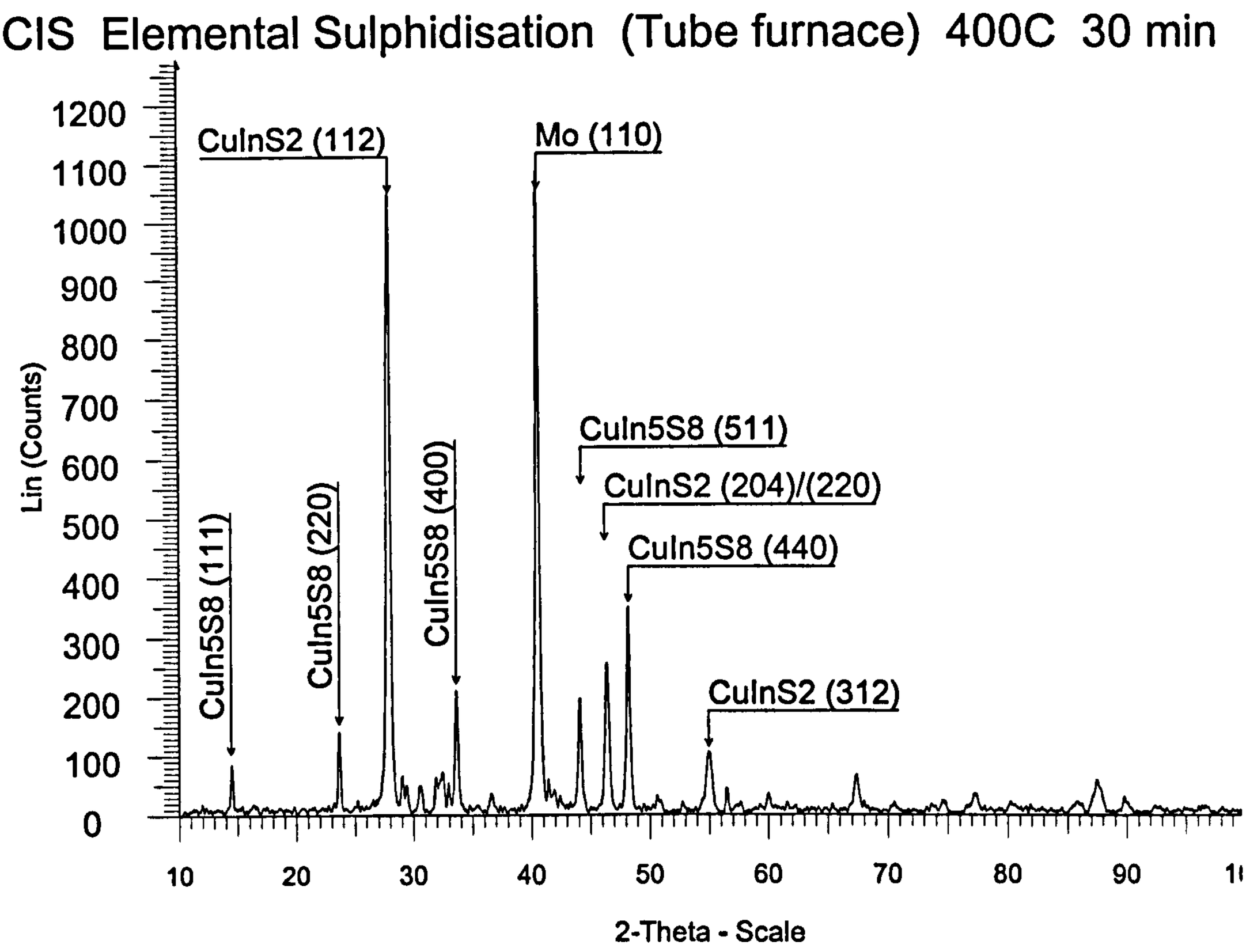

Figure 5.22. X-ray diffractogram of film sulphidised for 30 minutes at 400°C in flowing argon. All of the material has been converted to ternary compounds, most of it being $CuInS_2$, with some $CuIn_5S_8$.

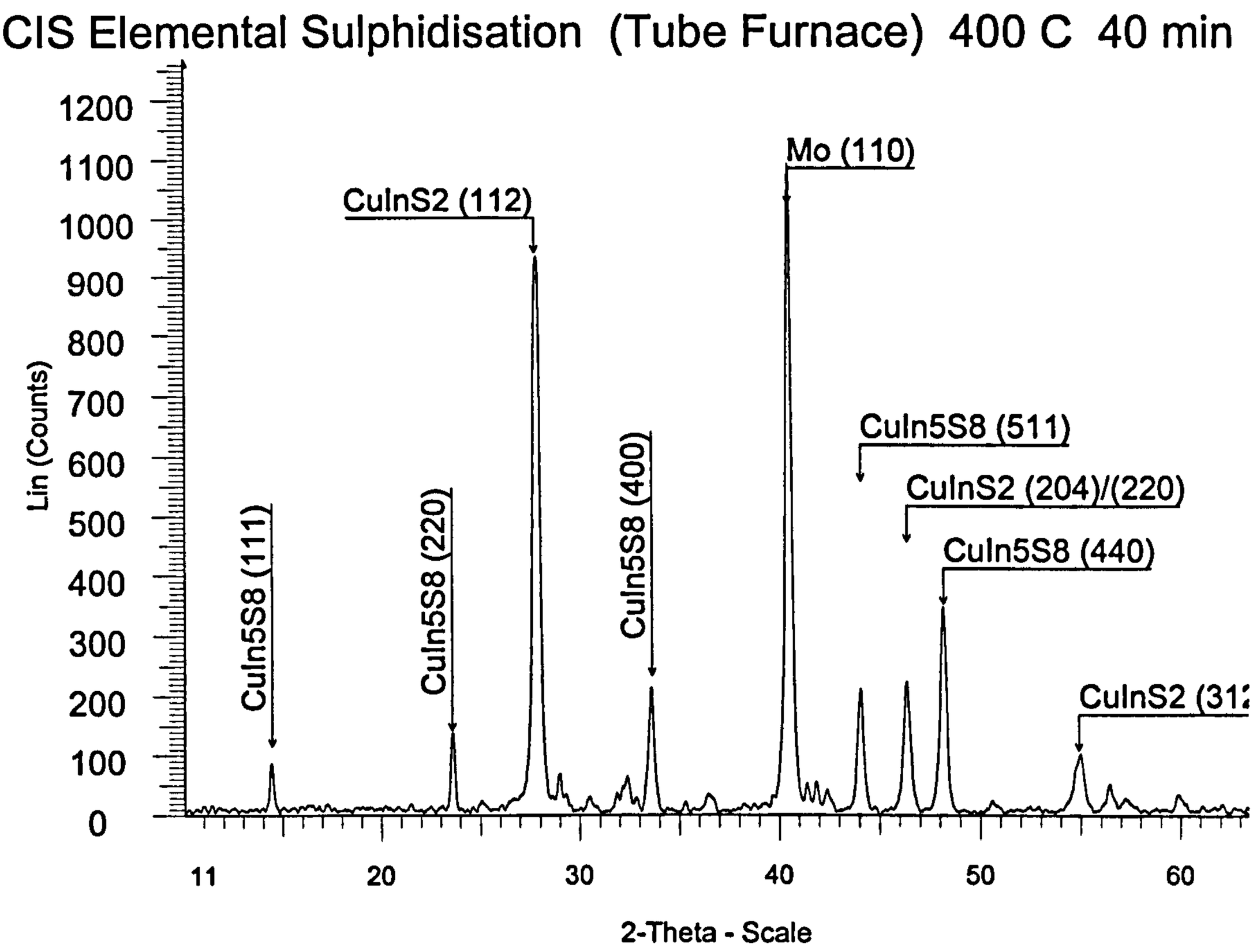

Figure 5.23. X-ray diffractogram of film sulphidised for 40 minutes at 400°C in flowing argon. All of the material has been converted to ternary compounds. There is no evident change in the presence of $CuIn_5S_8$.

5.3.1 Discussion

From the EDAX data, it is observed that the sulphur content reaches the level required for stoichiometric $CuInS_2$ after approx. 25 minutes. The fractions of Cu and In decrease in proportion over the first 10 minutes. After this time, there is a significant loss of indium, with the fraction of In being somewhat more than half that of Cu. (As EDAX measures only within a limited depth of the surface, it is possible that this loss occurs only near the surface.) The continued increase in the fractional sulphur composition may be due to loss of indium, rather than further incorporation of sulphur.

The RBS measurements were made on a film, which had been heated for 10 minutes at 400°C. The relatively high signal for indium, compared to copper, is consistent with its initial high content in the precursors, and the observations from EDAX, that preferential loss of indium did not become significant until after 10 minutes. The sulphur content decreases with distance into the film, which is consistent with diffusion from the surface. The quantity of sulphur is relatively low. This is in agreement with the observations from EDAX, that the sulphur content is only 15 % after 10 minutes at 400°C.

The X-ray diffractograms show the chemical incorporation of sulphur into the films, to form a range of sulphides. By comparing samples heated to the same temperature (400°C) for a range of times, it is possible to follow the formation of the compounds produced. The diffractogram for the sample heated for 10 minutes showed no remaining Cu/In alloys, indicating that all the precursor material had been converted to sulphides. The large peaks for the ternary compounds showed that most of the material had been fully converted - mostly to $CuInS_2$, with

smaller quantities of $CuIn_5S_8$. Some binary compounds were observed - CuS and Cu_9S_5, indicating that some of the material had only been partially converted.

The material converted for 20 minutes shows that CuS is no longer present - possibly due to conversion to ternary compounds, and that Cu_9S_5 remains at much the same level as for 10 minutes.

The diffractogram for 30 minutes shows no peaks for binary compounds, indicating that all the material has been converted to ternary compounds - $CuInS_2$ and $CuIn_5S_8$. The diffractogram for 40 minutes is essentially similar. This would suggest that these compounds are stable under the conditions present during conversion, and that further processing will not induce additional change, such as conversion of $CuIn_5S_8$ to $CuInS_2$.

For all of the diffractograms, covering the range 10 to 40 minutes at 400°C, no peaks were observed for sulphides of Mo, or for alloys of Mo with either Cu or In. This indicates that there has been no mixing between these layers and the substrate.

The lack of substantial conversion for temperatures of less than 350°C, and the brittleness of layers formed at higher temperatures suggests that 400°C is the optimum temperature. The minimum time for complete conversion is 30 minutes.

As for sulphidisation in the graphite box, the advantages, compared to previous work, are the lower substrate temperature, allowing the use of soda-lime glass, and the indirect transport of sulphur vapour, which avoids the limitations of line-of-sight transport, and the environmental hazards of hydrogen sulphide.

5.4 Conversion to copper indium disulphide by anodic sulphidisation

In this case, the properties of the films, which are to be assessed, are similar to those for the preceding sulphidisation techniques, and therefore the same analytical techniques are used. These include EDAX, XRD, and SEM. However, the deposition conditions are characterised by a different set of parameters, and the observed properties should be correlated with these parameters. Temperatures up to 70°C and current densities up to 60 mA cm^{-2} were used, these being applied for 20 to 100 seconds. However, a small number of conversions for longer times were also performed.

For the initial set of conversions, aqueous solutions were used. The X-ray diffractogram (Figure 5.24), taken for a sample converted using a current density of 60 mA cm^{-2} for 60s, showed peaks for $CuInS_2$, indicating that what conversion has occurred had developed completely to this material. However, it was found that the films produced were of low quality in two respects. Firstly, the adhesion to the substrate was low. Secondly, the films after conversion were highly non-uniform. This ranged from areas of completely unconverted Cu/In to areas where the film had electro-corroded all the way through to the glass substrate. Similar results were observed for a range of solution conditions, including concentration of alkali (NaOH or NH_4OH) and temperature.

Subsequent conversions used ethanediol as the solvent. For the first few of these, alkaline conditions (NaOH or NH_4OH) were used. There was a considerable improvement in uniformity over the aqueous solutions, with no corrosion observed through to the Mo back contact. However, although there was some improvement in adhesion, this remained problematic. Removal of the alkaline component improved adhesion further.

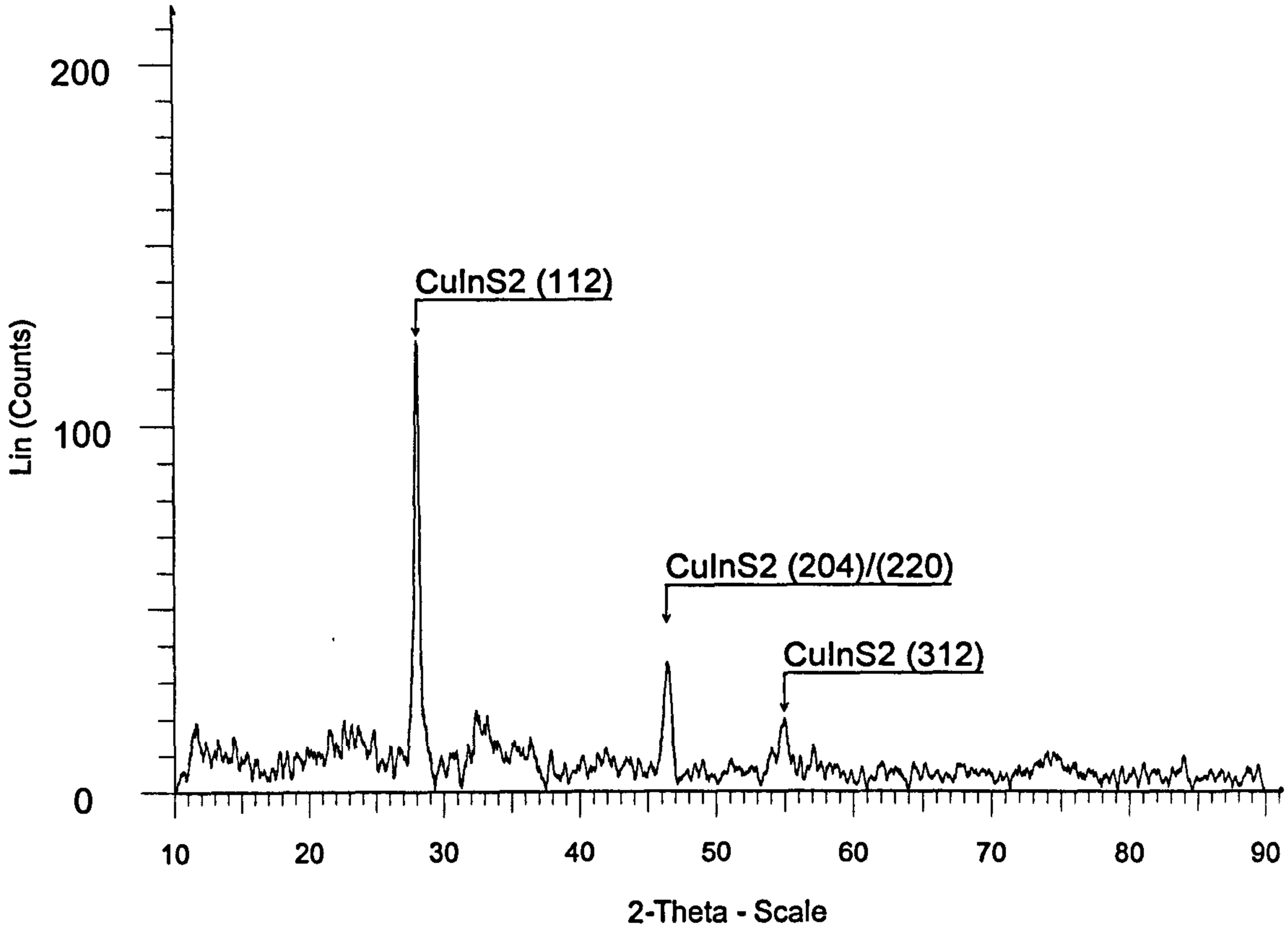

Figure 5.24. X-ray diffractogram of $CuInS_2$ produced by anodic conversion.

Current density = 60 mA cm^{-2}, time = 60 s.

Aqueous solution - 0.1 M Na_2S, 0.1 M NaOH.

Conditions used for aqueous solutions			
[NaOH]	0.1 - 0.5 M	Temperature	30 - 70°C
[NH_4OH]	0.1 - 0.5 M	Current density	20 - 60 mA cm^{-2}
[Na_2S]	0.1 M	Time	20 - 60 s
Conditions for initial conversion using ethanediol			
[NaOH]	0.1 - 0.5 M	Temperature	25 - 70°C
[NH_4OH]	0.1 - 0.5 M	Current density	20 - 60 mA cm^{-2}
[Na_2S]	0.1 M	Time	20 - 100 s
Conditions for subsequent conversion using ethanediol			
[Na_2S]	0.1 M	Current density	20 - 60 mA cm^{-2}
Temperature	40°C	Time	20 - 100 s

Table 5.7 Solution conditions, current density and time of application for anodic conversion.

A range of temperatures were used, from 25°C to 70°C. For temperatures above 40°C, adhesion was poor, while for lower temperatures, there was little conversion of Cu/In to $CuInS_2$. This temperature was used in all subsequent conversions.

Combining the above, the solution conditions were 0.1 M Na_2S in ethanediol (with no other components) and a temperature of 40°C.

The physical incorporation of sulphur into the films was assessed using EDAX. The results are shown in Figure 5.25. Over a range of current densities from 30 to 60 mA cm^{-2}, the sulphur content reaches the required 50 % after approx. 20 seconds, and saturates at 80 to 90 % after approx. 80 seconds.

The chemical incorporation of sulphur to form sulphides was evaluated using XRD. These were performed for pairs of films converted at the same current and time, with one film from each pair subsequently being annealed at 400°C for 30 minutes. The unannealed films all showed no peaks for $CuInS_2$, and large peaks of unconverted Cu/In. The diffractogram for a film converted using a current dnesity of 60 mA cm^{-2} for 80 seconds is shown in Figure 5.26. This suggests that the incorporation of sulphur is only physical, with no chemical conversion occurring.

Films annealed at 400°C for 30 minutes show some formation of $CuInS_2$. The development of this conversion with time can be seen by comparing diffractograms for the same current density (60 mA cm^{-2}) applied for different times. These are shown in Figures 5.27 to 5.30. After 20 seconds (Fig. 5.27), no peaks for $CuInS_2$ have developed. Peaks for $CuInS_2$ are visible for films, for which the current was applied for 60 seconds (Fig. 5.28). These continue to develop further for times of 80 and 100 seconds (Figs. 5.29 and 5.30). However, most of the Cu/In remains unconverted.

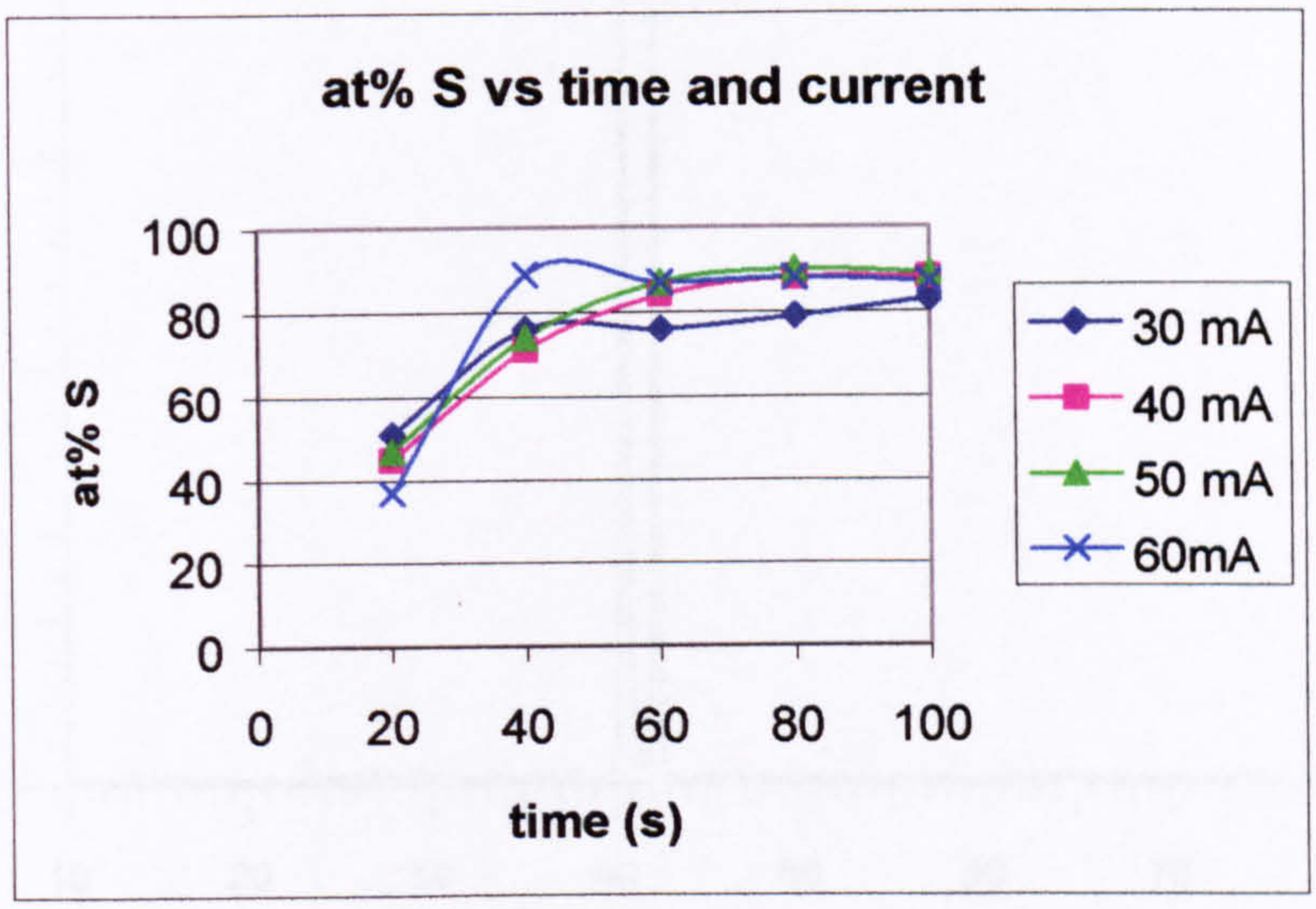

Figure 5.25. Sulphur content of converted films vs. time for a range of current densities.

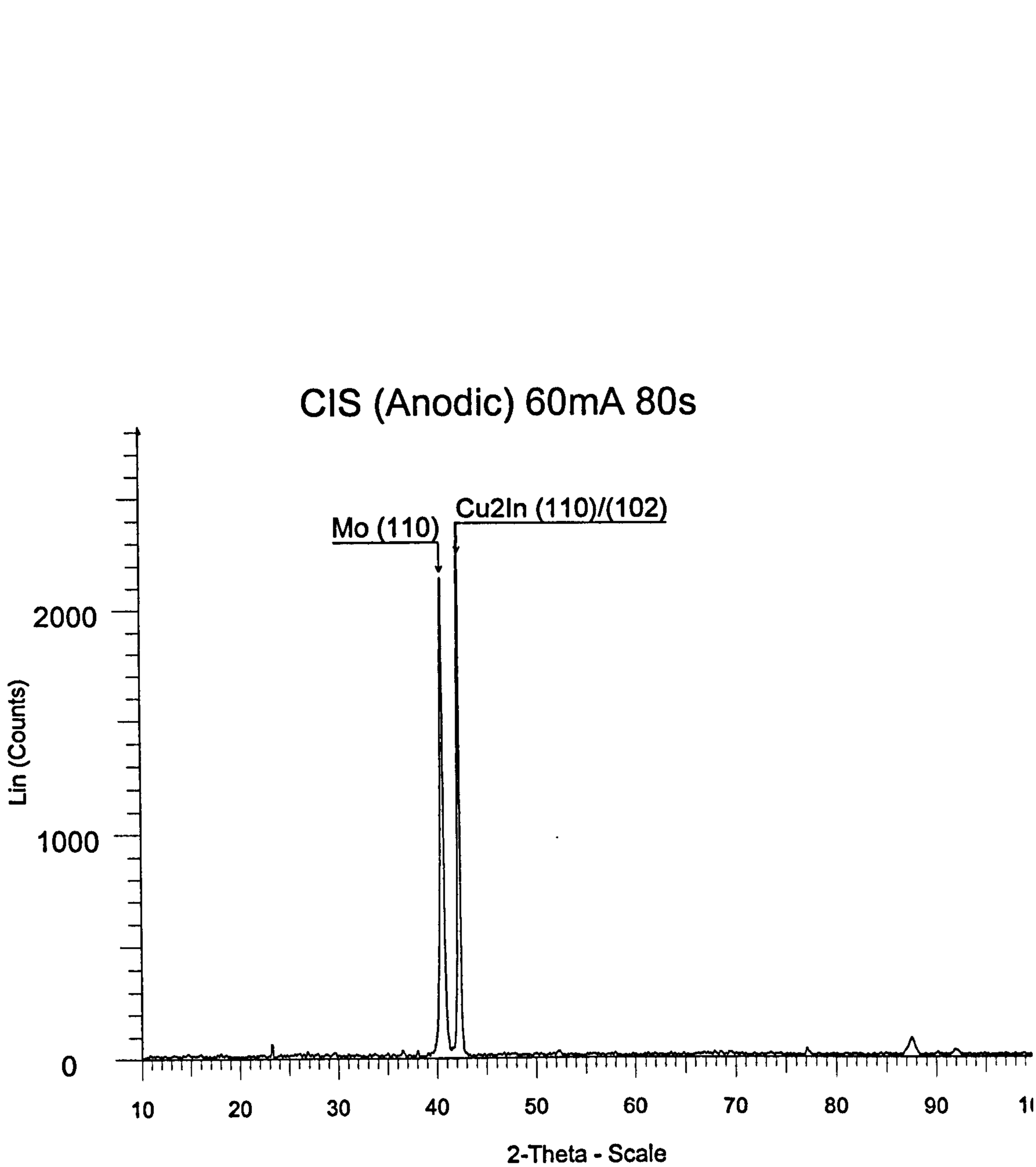

Figure 5.26. X-ray diffractogram of Cu/In film for current density of 60 mA cm^{-2} applied for 80 seconds. The Cu/In is unconverted. No $CuInS_2$ peaks are visible.

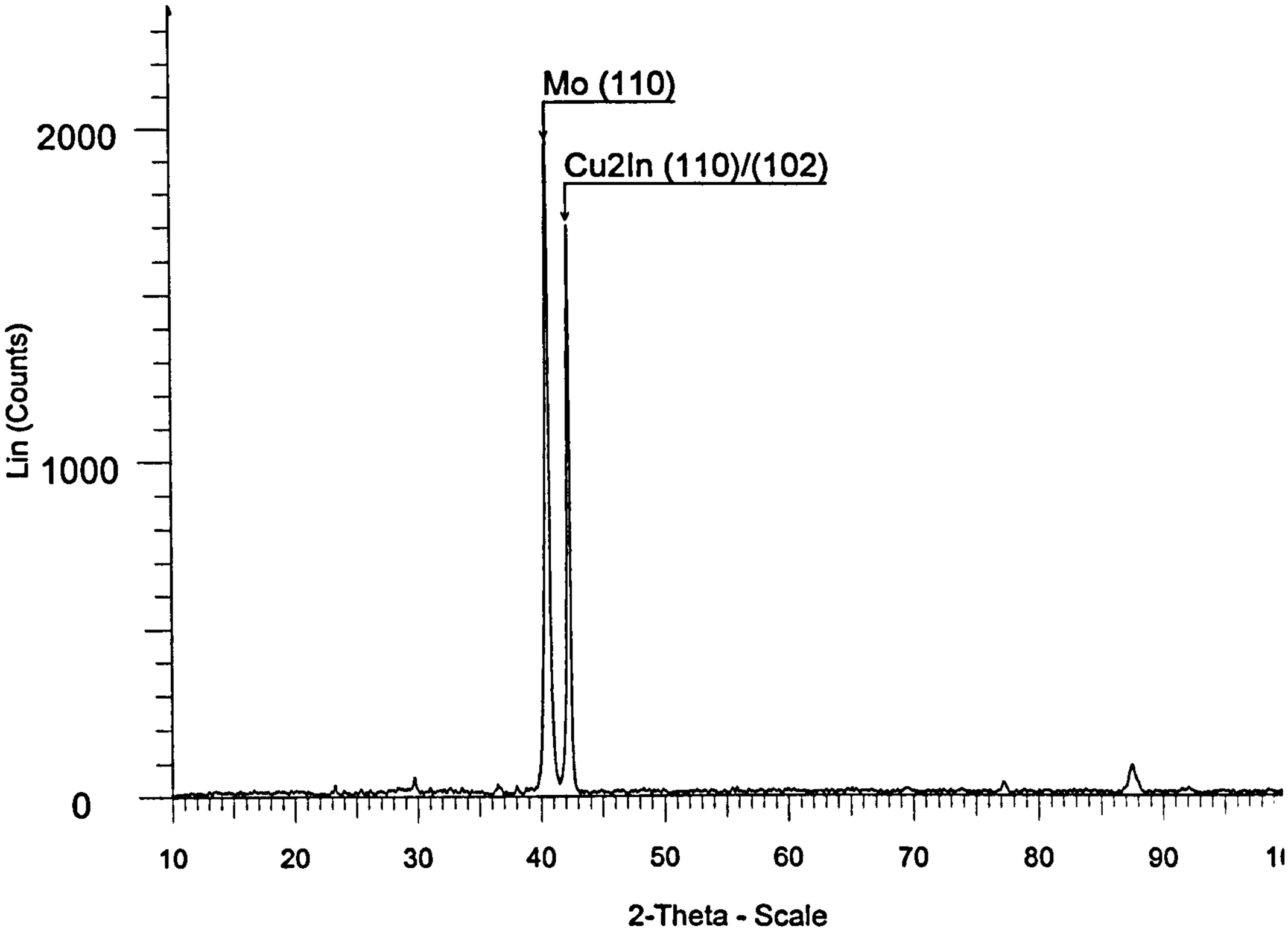

Figure 5.27. X-ray diffractogram of Cu/In film with a current density of 60 mA cm^{-2} applied for 20 seconds, and subsequent annealing at 400°C for 30 minutes. No $CuInS_2$ peaks have developed at this stage.

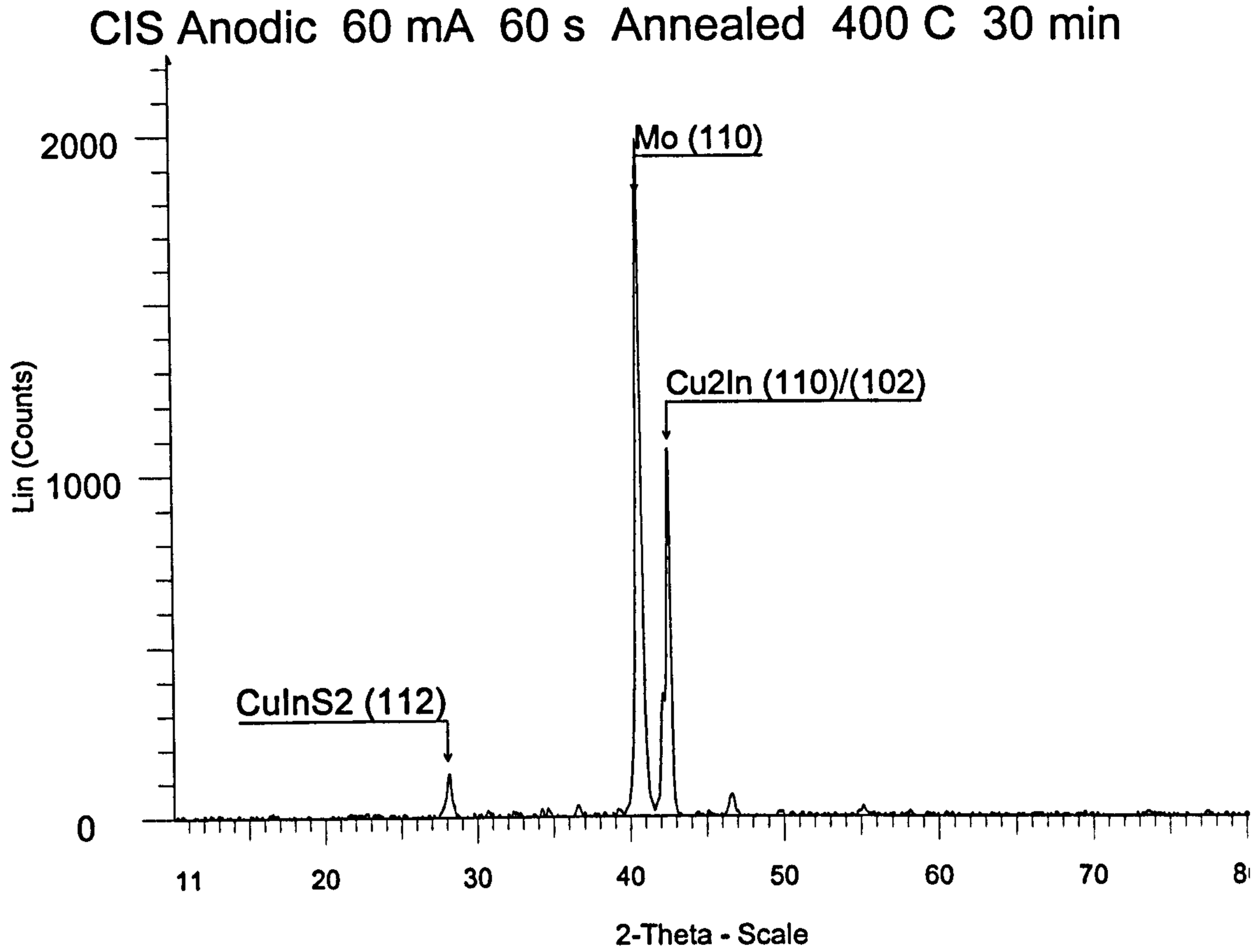

Figure 5.28. X-ray diffractogram of Cu/In film with a current density of 60 mA cm^{-2} applied for 60 seconds, and subsequent annealing at 400°C for 30 minutes. $CuInS_2$ peaks have started to develop.

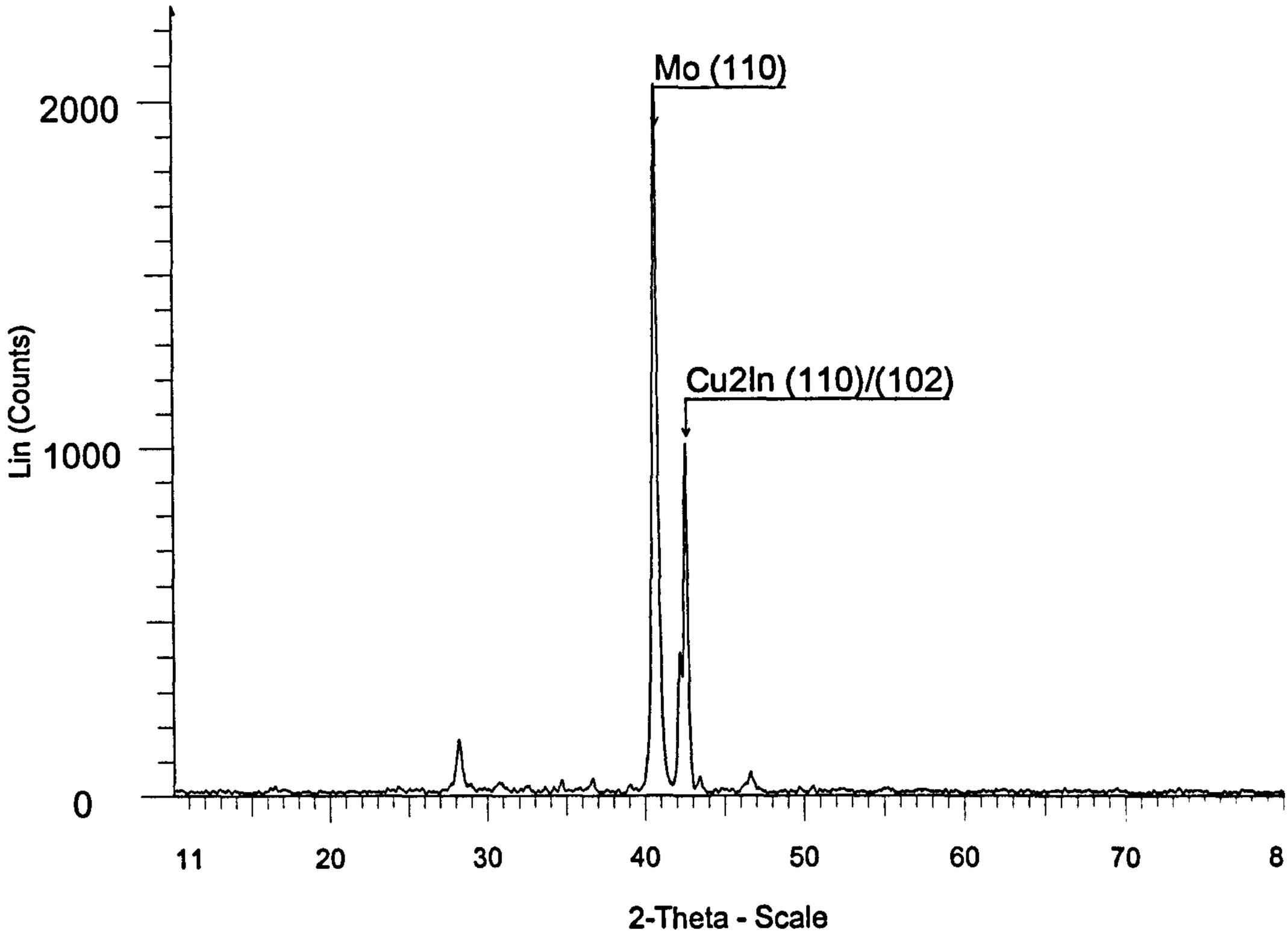

Figure 5.29. X-ray diffractogram of Cu/In film with a current density of 60 mA cm^{-2} applied for 80 seconds, and subsequent annealing at 400°C for 30 minutes. $CuInS_2$ peaks have continued to develop.

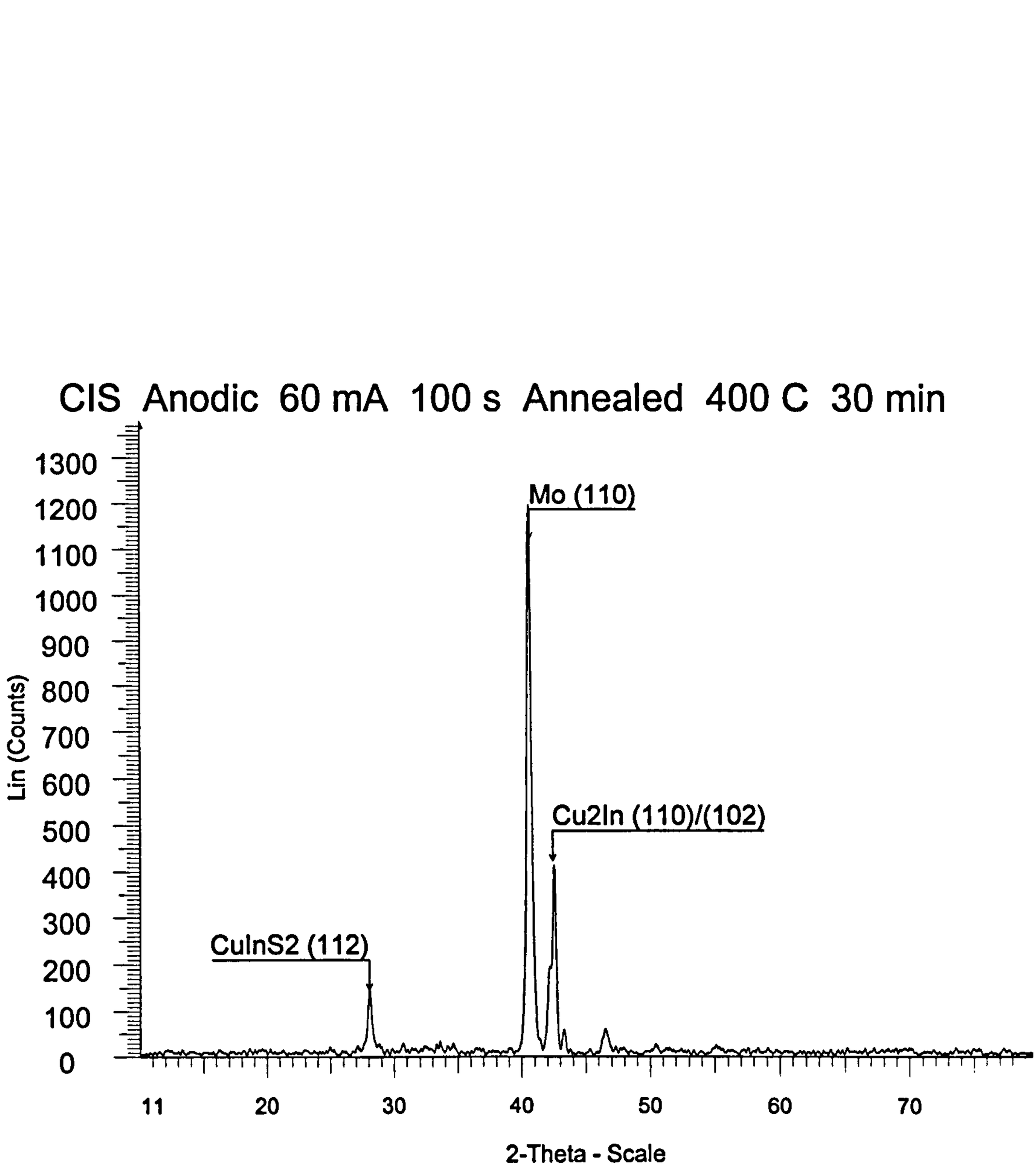

Figure 5.30. X-ray diffractogram of Cu/In film with a current density of 60 mA cm^{-2} applied for 100 seconds, and subsequent annealing at 400°C for 30 minutes.

$CuInS_2$ peaks have developed further. However, much of the Cu/In remains unconverted.

5.4.1 Discussion

The initial results, produced using an aqueous solution, resulted in good formation of $CuInS_2$, as indicated by the X-ray diffractogram (Fig. 5.24). However, the uniformity and adhesion of the films remained problematic, for a range of solution conditions and applied currents.

The results of anodic sulphidisation, using ethanediol as a solvent, show that, improved uniformity has been achieved, and that there has been some increase in adhesion to the substrate. However, there is a need for further improvement of this property.

As the fraction of sulphur in the film is considerably larger than the sum of the fractions of Cu and In, this suggests that most of the sulphur is incorporated physically, rather than chemically. Furthermore, as EDAX measures elemental composition in the surface and immediate sub-surface region only, the possibility exists that the excess sulphur observed in the region does not extend through the film. These results suggest the formation of a layer of elemental sulphur on the surface, which is consistent with visual observation.

The X-ray diffractograms show that, without subsequent annealing, none of the Cu/In alloy has been converted to sulphides, indicating that a post-conversion anneal is a necessary step in the process. For those films, which were annealed (400°C for 30 minutes), some conversion to $CuInS_2$ was observed. This was noted only for samples, for which the current was applied for periods of 60 s or longer. Even for the longest times (100 s), the peaks for $CuInS_2$ remained small. This indicates that chemical incorporation to form sulphides has only occurred to a minor extent, with most of the sulphur remaining in elemental form. However, the absence of binary compounds indicates that what conversion has occurred has proceeded all the way to the ternary compound.

5.5 Chemical bath deposition of zinc sulphide

In this work, tri-sodium citrate was used as a safer replacement for hydrazine hydrate. The results of analysis on the films were used to determine whether films of good quality (optical, electrical, etc) could be fabricated using this material.

Because chemical deposition depends on a large number of variable conditions – mostly concentrations of materials in solution – an important aspect of the analysis of results is to determine the range of these conditions under which deposition occurs.

The films were deposited either onto microscope slides (26 x 76 mm), or onto pieces (15 x 15 mm) of tin dioxide (SnO_2) coated glass. These were cleaned by immersion in detergent solution, rinsing in distilled water, degreasing in ethanol in an ultrasonic bath, followed by a further rinse in distilled water. The required quantity of NH_4OH was measured out from 2M stock solution, and made up to 800 ml with distilled water.

This solution was poured into a glass tank, and placed on a hotplate-stirrer. With the solution being stirred, tri-sodium citrate was added, followed by $ZnSO_4$. It was found that adding in this order improved the dissolution of the $ZnSO_4$. The solution was then heated and at the required temperature, $CS(NH_2)_2$ was added. The slides were mounted near-vertically on an acryllic rack - to minimise deposition of ZnS grains precipitated from solution - and were then immersed in the solution.

Chemical bath deposition was performed for a range of solution conditions. By varying one parameter between trials, and maintaining the other parameters constant, the limits of each parameter for successful deposition could be determined.

For the first series of depositions, the solution temperature was set at 70°C, and the concentrations of $ZnSO_4$, $CS(NH_2)_2$ and NH_4OH were 0.03 M, 0.05 M and 0.05 M respectively. A number of depositions were then performed with the concentration of tri-sodium citrate in each successive solution increasing in steps of 0.05 M from 0.05 M to 0.5 M. For a second series, the concentration of NH_4OH was increased to 0.1 M, and the concentration of tri-sodium citrate was increased from 0.05 M to 0.5 M, as before. The remaining concentrations and the temperature were as for the first series. This was repeated for a number of series, up to a concentration of NH_4OH of 0.25 M.

A further set of depositions was performed at 60, 70 and 80°C, to determine the range of usable temperatures. The concentrations of the materials in the solution, in each case, was – $ZnSO_4$: 0.03 M, $CS(NH_2)_2$: 0.05 M, NH_4OH: 0.15 M and tri-sodium citrate: 0.3 M.

The range of usable conditions was quantified by measuring the thickness of the films deposited as a function of each parameter. Under certain conditions, films were deposited, but they produced diffuse reflection, which reduced optical transmittance. As transmittance of radiation to the junction is a contributory factor to the conversion efficiency of photovoltaic cells, solution conditions which result in such diffuse reflection also define limits of the conditions for successful chemical bath deposition.

Other measurements included those which confirmed the identity of the material. In this work EDAX, XRD and optical spectrophotometry were used. The latter was also used to measure the transmittance across the spectrum, this being a contributing factor to the conversion efficiency of photovoltaic devices. The structural properties were assessed by SEM. For those films, for which aluminium compounds were added to the solution, measurements of resistance allowed the resistivity to be measured. The resistance of the film would form a component of the series resistance of a cell, and hence would tend to reduce conversion efficiency.

<table>
<tr><td colspan="2">Series 1</td><td colspan="2">Altered parameters</td></tr>
<tr><td colspan="2">Fixed parameters</td><td>[NH_4OH]</td><td>Tri-sodium citrate</td></tr>
<tr><td>[$ZnSO_4$]</td><td>0.3 M</td><td>0.05 M</td><td rowspan="6">0.05 - 0.5 M in steps of 0.1 M</td></tr>
<tr><td>[$CS(NH_2)_2$]</td><td>0.5 M</td><td>0.1 M</td></tr>
<tr><td>Temperature</td><td>70°C</td><td>0.15 M</td></tr>
<tr><td></td><td></td><td>0.2 M</td></tr>
<tr><td></td><td></td><td>0.25 M</td></tr>
<tr><td colspan="2">Series 2</td><td colspan="2">Altered parameter</td></tr>
<tr><td>[Tri-sodium citrate]</td><td>0.3 M</td><td rowspan="4">Temperature</td><td>60°C</td></tr>
<tr><td>[NH_4OH]</td><td>0.15 M</td><td>60°C</td></tr>
<tr><td>[$CS(NH_2)_2$]</td><td>0.05 M</td><td>80°C</td></tr>
<tr><td>[$ZnSO_4$]</td><td>0.03 M</td><td></td></tr>
</table>

Table 5.8 Solution parameters for chemical bath deposition of ZnS.

The variation of film thickness with concentrations of tri-sodium citrate and NH_4OH are shown in Figures 5.31 and 5.32. Figure 5.31 shows that film thickness increased rapidly for tri-sodium citrate concentrations between 0.2 M and 0.4 M, and increases more gradually beyond this. Film thickness was a maximum for $[NH_4OH] = 0.1$ M, and decreased for higher concentrations.

Visual inspection showed that, for concentrations of tri-sodium citrate higher than 0.4 M, and for concentrations of NH_4OH of 0.1 M or lower, the films had an observable degree of diffuse reflectivity. Films produced in the range 0.25 M < [tri-sodium citrate] < 0.4 M, and with $[NH_4OH] = 0.15$ M were observed to be highly transmissive, with no observable diffuse reflection. These conditions were used as the basis for further deposition and measurement.

Similarly, the variation in film thickness was measured with variation in temperature. As interference fringes were not observed from spectrophotometry, this method could not be used to determine thickness. Therefore, optical absorption in the wavelength range around the cut-off was used. The results are shown in Figures 5.33. The results show that deposition is minimal for temperatures of 65°C or lower, whereas it is substantially constant for temperatures of 70°C or higher. Based on this, a temperature of 70°C was used for subsequent depositions.

Energy dispersive X-ray analysis (EDAX) shows the presence of Zn and S, in the proportions 46% and 54% respectively. The excess of S is of the same order as the error in the measurement.

Attempts to produce X-ray diffractograms from films deposited by the normal process resulted in no discernible peaks. Therefore, the multiple deposition described in Chapter 4 was performed, in order to produce thicker films with larger grains. A longer scan was used, to produce a larger count in the reflected beam. The resultant diffractogram is shown in Figure 5.34, and shows a high level of background noise. Despite this noise, a number of peaks are discernible, and identify the material as zinc sulphide. However, the deposition conditions used to produce this film were substantially different from those normally used. The crystal phases present in this film are therefore not necessarily present in films produced under normal (single) deposition conditions.

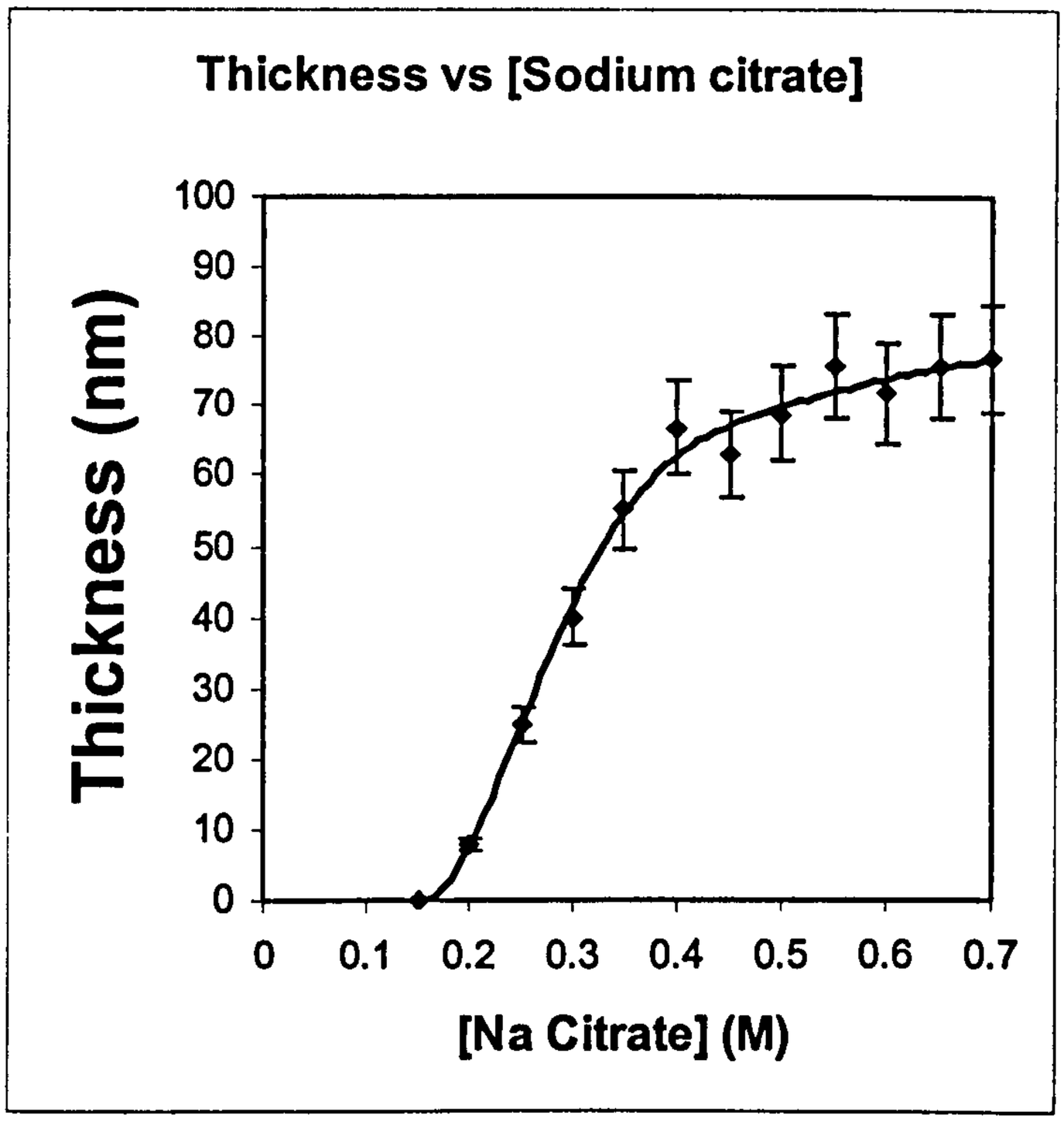

Figure 5.31. ZnS film thickness vs concentration of tri-sodium citrate.

$[ZnSO_4] = 0.03$ M

$[CS(NH_2)_2] = 0.05$ M

$[NH_4OH] = 0.15$ M

Temperature = 70°C

Time = 50 minutes

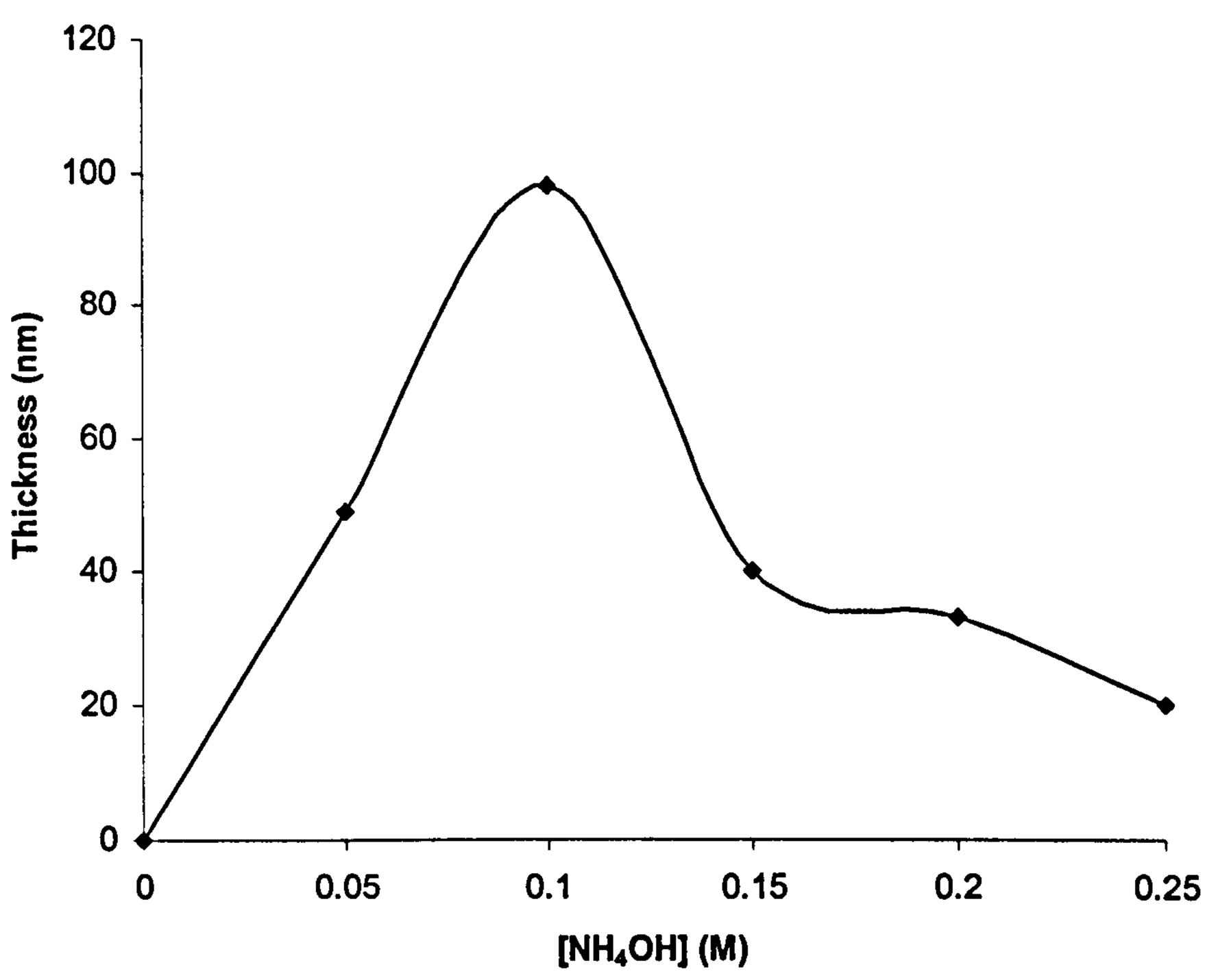

Figure 5.32. ZnS film thickness vs. concentration of NH_4OH.

$[ZnSO_4] = 0.03$ M

$[CS(NH_2)_2] = 0.05$ M

[tri-sodium citrate] = 0.3M

Temperature = 70°C

Time = 50 minutes

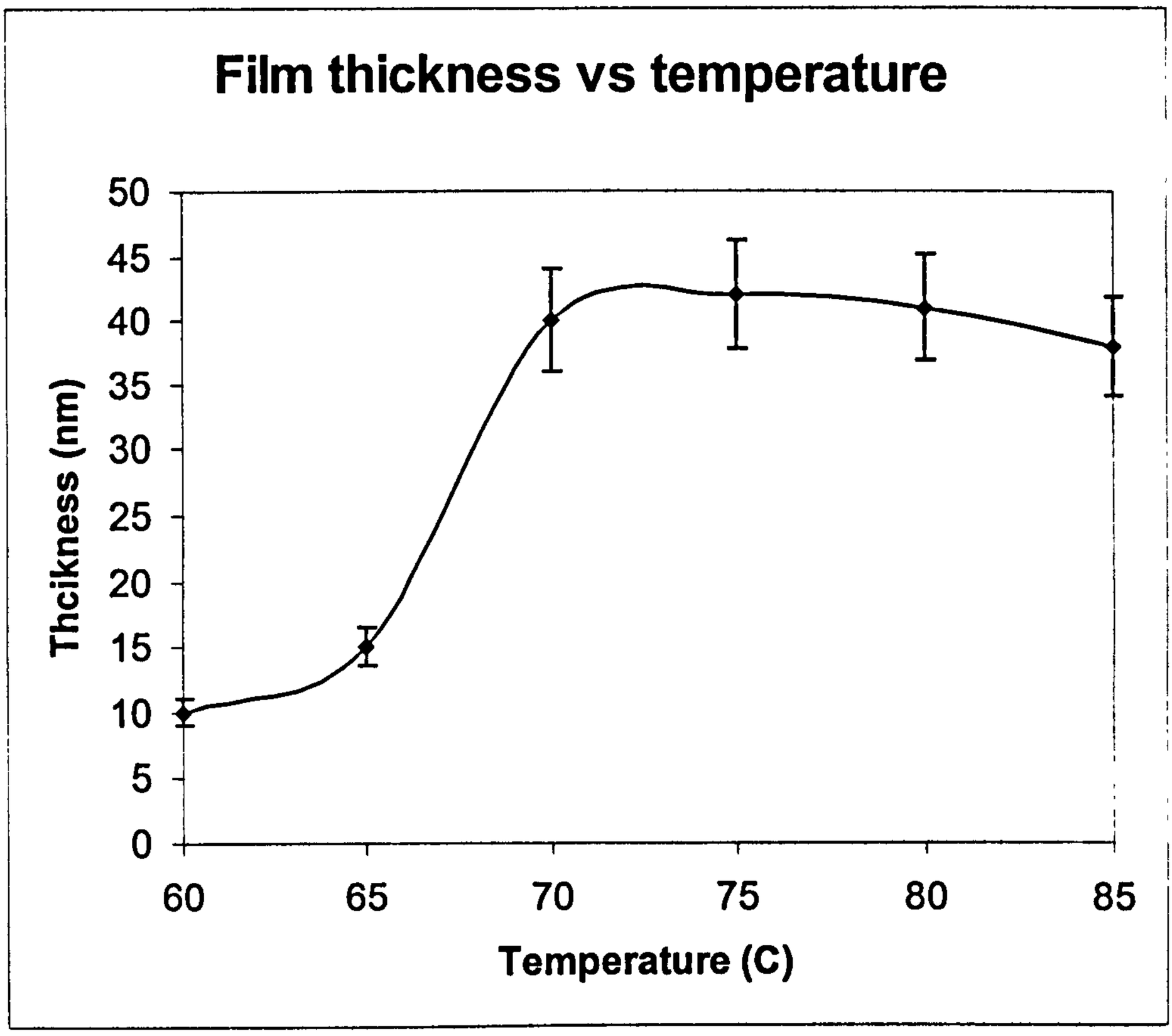

Figure 5.33. ZnS film thickness vs. temperature.

$[ZnSO_4] = 0.03$ M

$[CS(NH_2)_2] = 0.05$ M

$[NH_4OH] = 0.15$ M

[tri-sodium citrate] = 0.3M

Time = 50 minutes

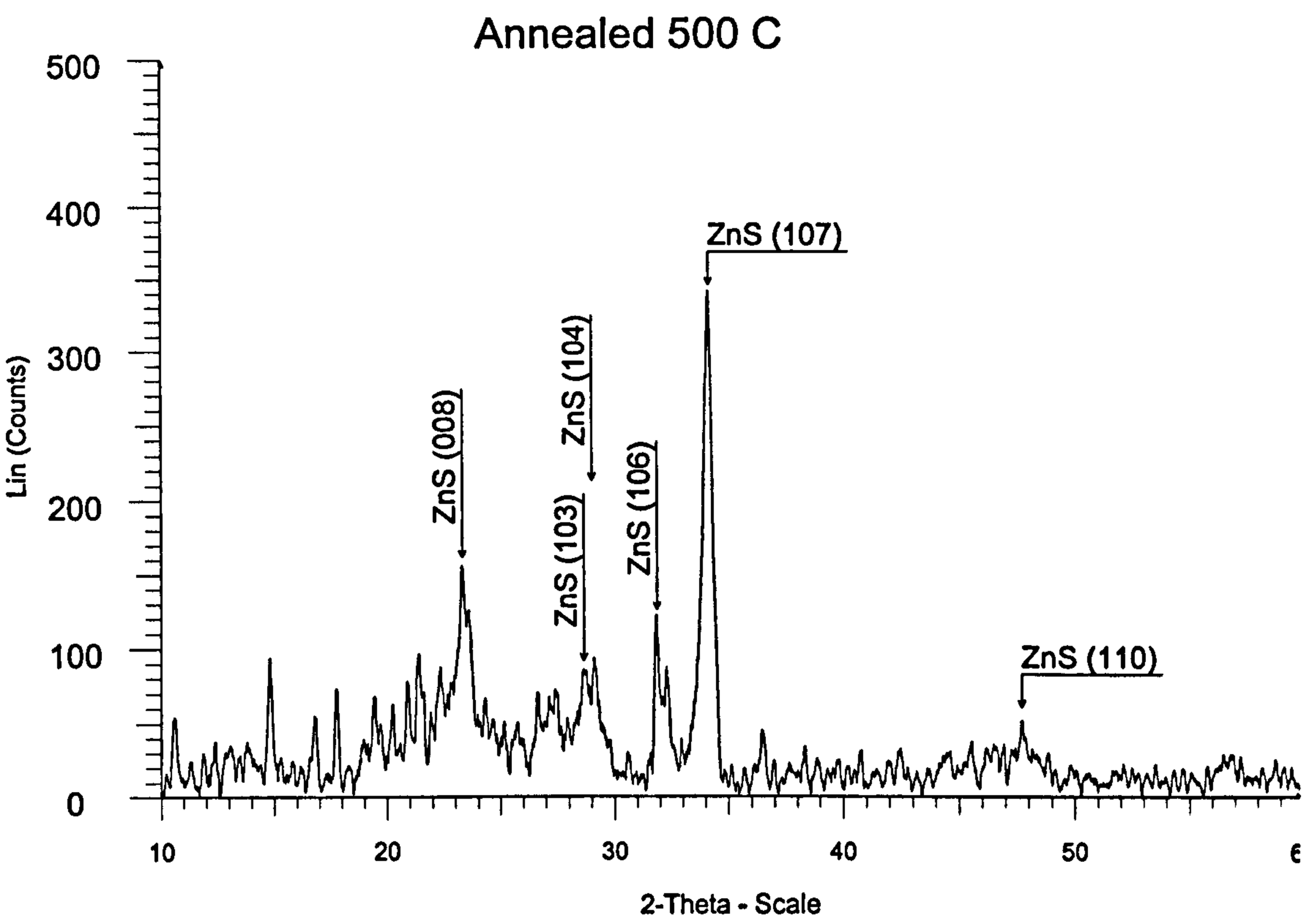

Figure 5.34. X-ray diffractogram of zinc sulphide produced by multiple deposition. The peaks confirm the identity of the material as ZnS, but may not be indicative of the crystal phases present in a normally produced film (single deposition).

Optical spectrophotometry showed a cut-off wavelength of 340 nm, as shown in Figure 5.35. From equation (4.9), the band gap energy can be calculated as 3.64 eV.

A more accurate value of the band-gap energy can be derived from the variation of absorption coefficient with photon energy. For a direct band-gap semiconductor, this variation is given by

$$\alpha \propto (h\nu - E_g)^{1/2}$$

Plotting a graph of $(\alpha h\nu)^2$ vs $h\nu$ results in a straight line which intercepts the $h\nu$ axis at E_g, thus allowing a value of this parameter to be determined . The results are shown in Fig. 5.36. The results give a value of 4.05 eV, which is somewhat higher than the value of 3.7 eV, observed for bulk ZnS.

For the optimum films (those with no diffuse reflection), the transmittance at wavelengths longer than the cut-off (340 nm), and extending into the near infra-red (1000 nm), are in the region of 90 %. For films, which did show diffuse reflection, the transmittance was somewhat lower, with 70 % being typical.

Scanning electron microscopy (Figure 5.37) shows a uniform layer of small crystals, forming an unbroken surface with smooth topography. (This complements the high uniformity observed by visual inspection.) No pinholes were observed. This suggests that very thin films (~ 50 nm) can be produced, resulting in high optical transmittance and low electrical resistance, without significant formation of pinholes. A few loosely attached crystals were observed on the surface. These crystals are due to homogeneous precipitation, and generally have low adhesion, and so can be easily removed, prior to the next step of device fabrication.

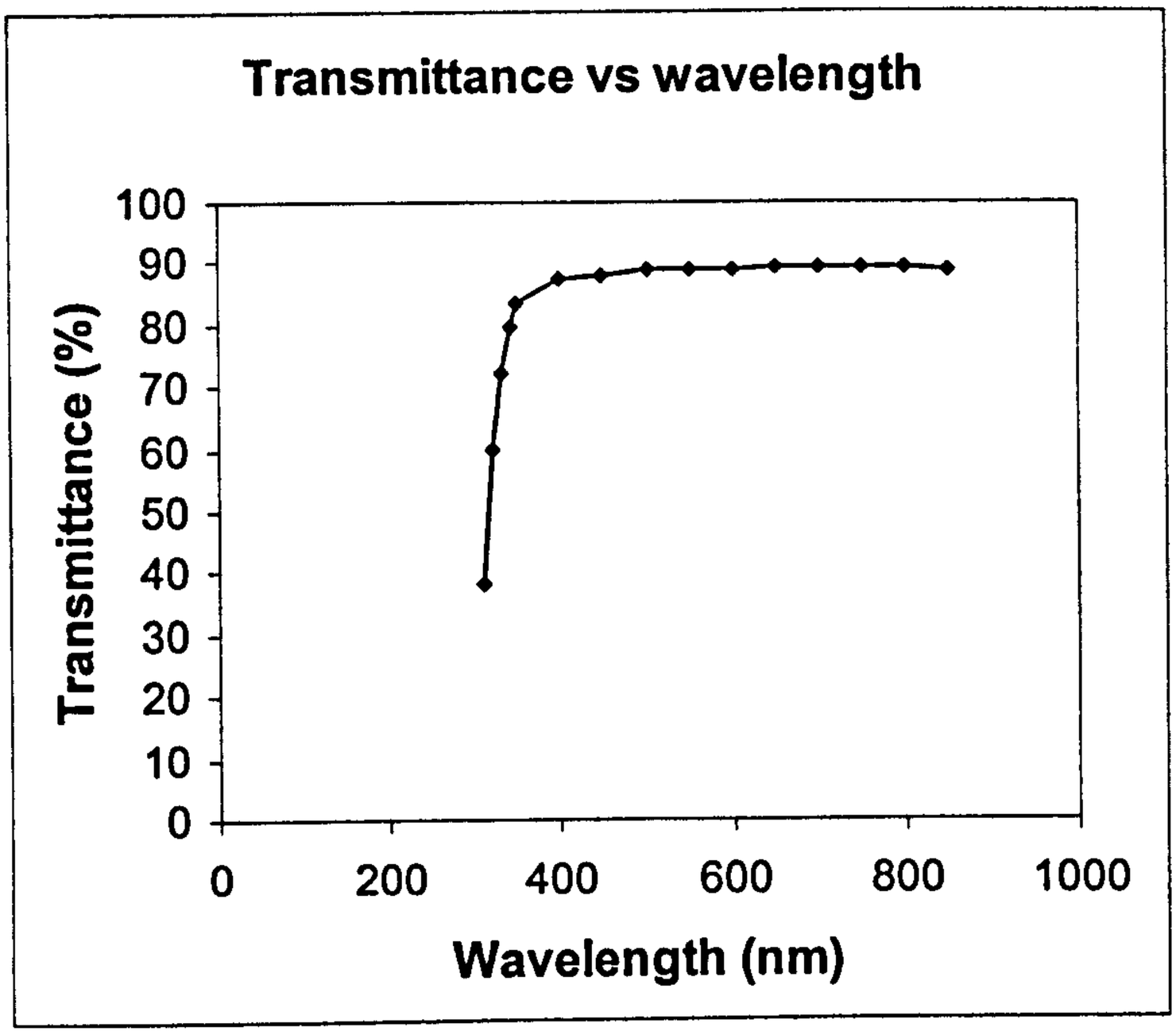

Figure 5.35. Spectral transmittance of a ZnS buffer layer.

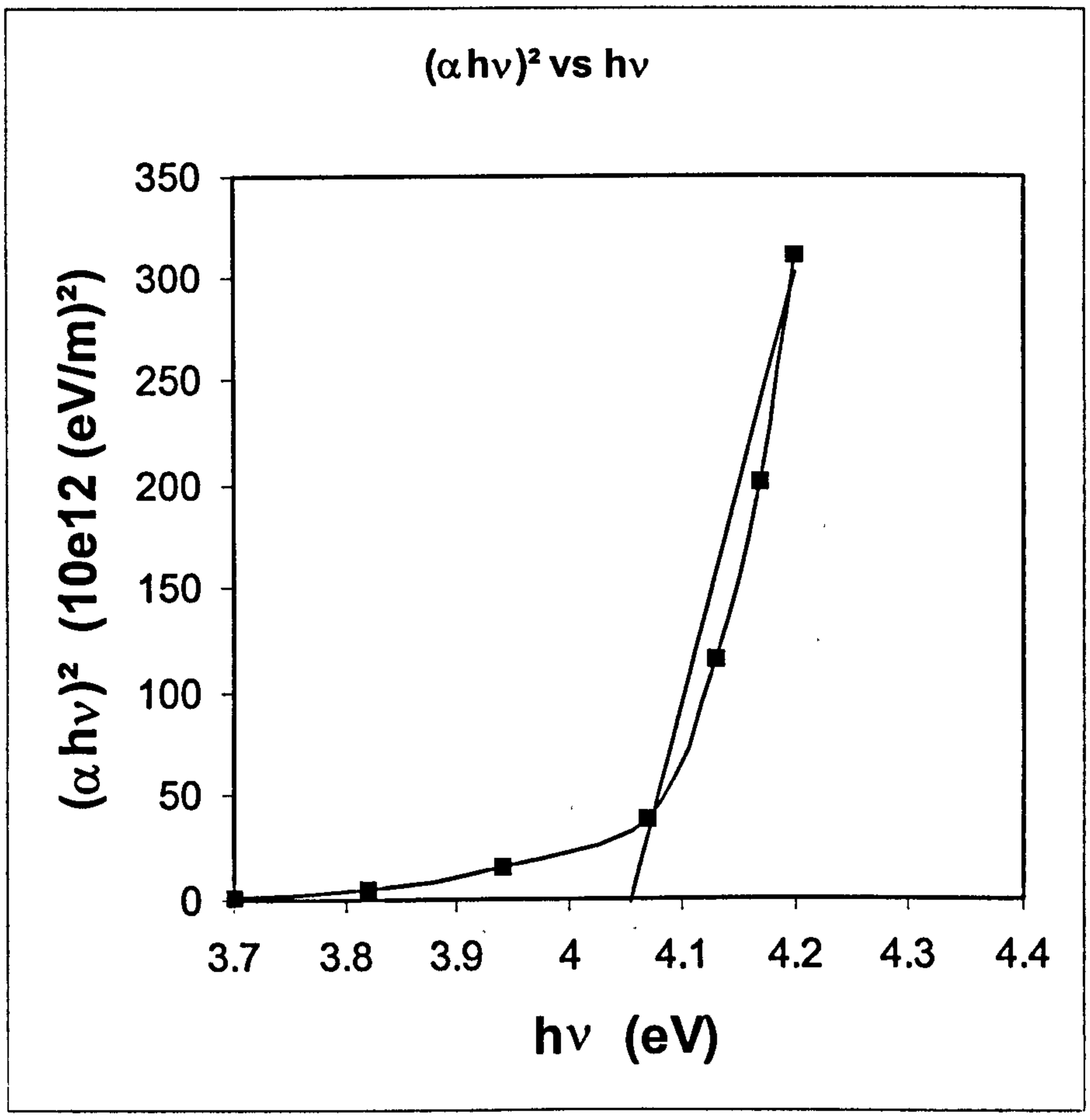

Figure 5.36. $(ahv)^2$ vs hv for chemically deposited ZnS.

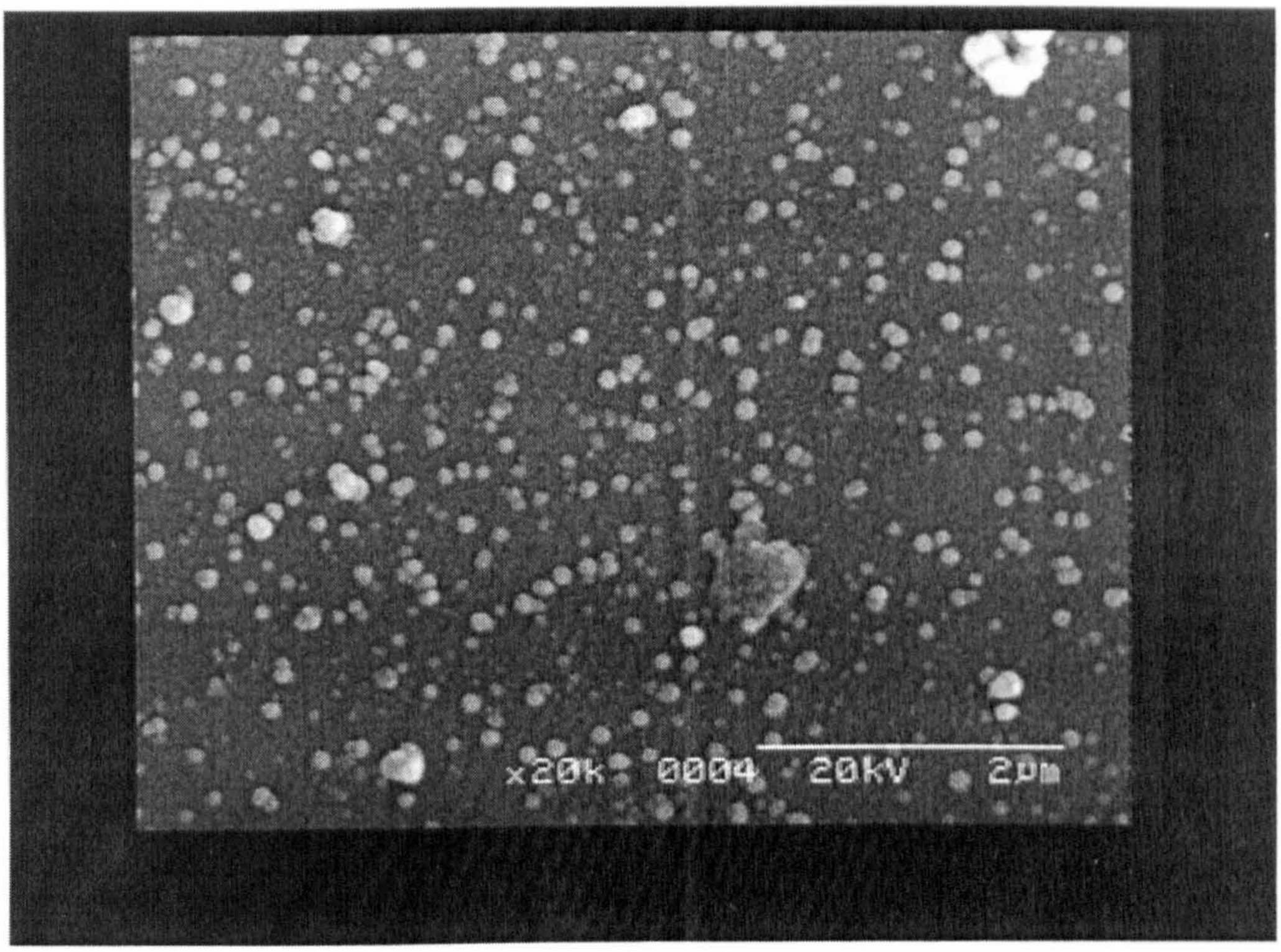

Figure 5.37. Scanning electron micrograph of chemically deposited zinc sulphide, showing uniform layer of small crystals, with overlying grains of homogeneously precipitated material.

Measurements of electrical resistivity were performed for films produced using solutions with different concentrations of $Al_2(SO_4)_3$, and for different temperatures during the subsequent annealing. For each level of doping, and for undoped samples used as a baseline, samples were annealed in vacuum for 20 minutes at temperatures of 100, 200, 300 and 400°C, and unannealed samples were used for comparison.

The results are shown in Figure 5.38. This shows that incorporation of aluminium reduces resistivity for films annealed at temperatures up to 300°C. At the highest annealing temperature – 400°C – the addition of aluminium to the solution has little effect, and the post-deposition annealing is the more important factor. The resistances, from which these resistivities were calculated, showed a minimum of approx. 1 Ω for a contact area of 1 cm diameter. (This was produced for 1 % aluminium in solution and an annealing temperature between 200 and 300°C.) The diameter gives an area transverse to the current of 0.78 cm^2, and hence a resistance of 0.78 Ω for a 1 cm^2 device. Measurements of optical transmittance showed that this was not measurably decreased by the presence of aluminium.

5.5.1 Discussion

In this section of the work, ZnS films were deposited by chemical bath deposition, using tri-sodium citrate as a complementary complexing agent. This replaced hydrazine hydrate, which had played an equivalent rôle in previous work [8, 9].

A range of conditions were identified over which ZnS films could be produced. In addition, the presence of diffuse reflection for films produced under certain conditions set further limits on the optimum conditions.

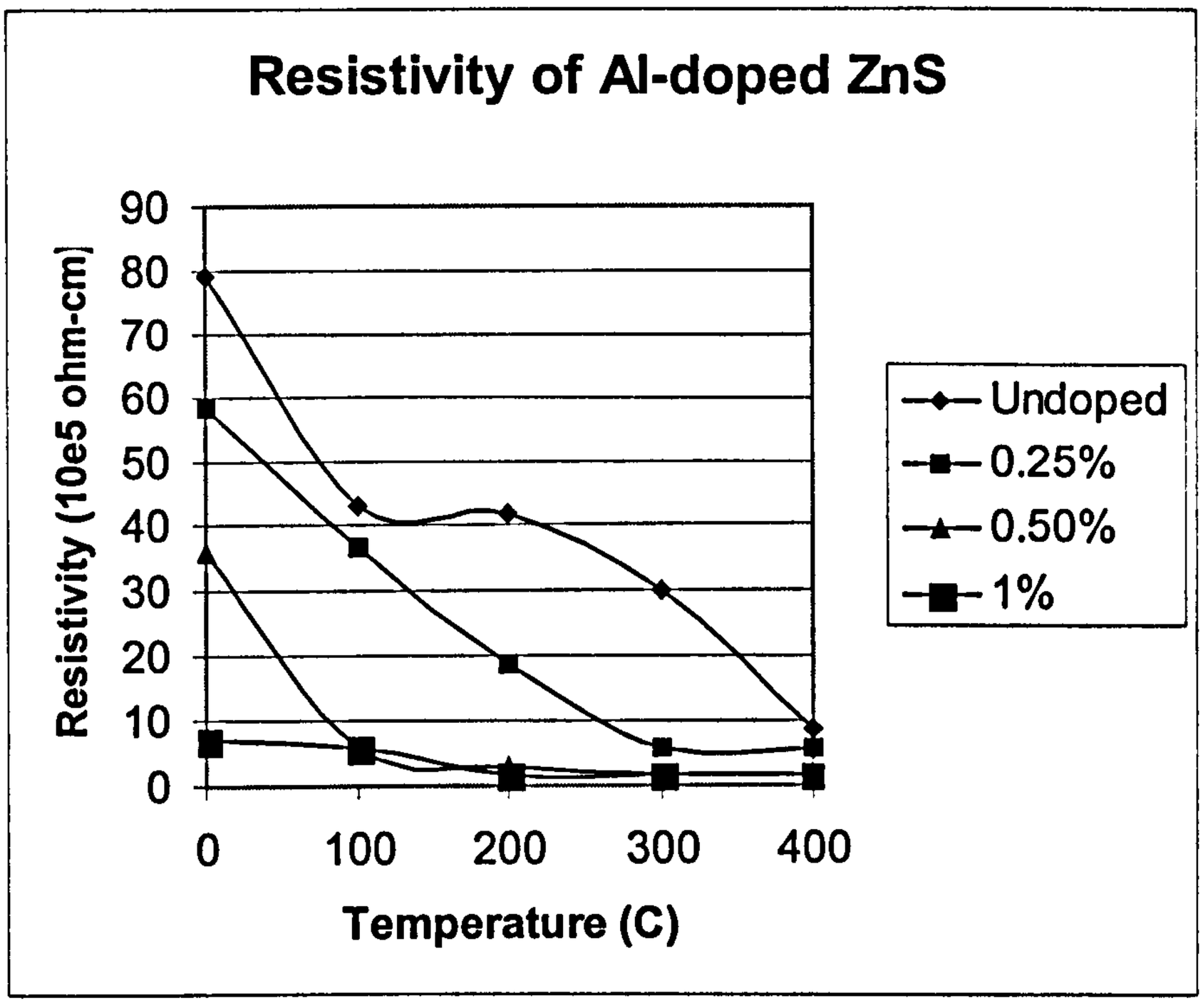

Figure 5.38. Electrical resistivity of films deposited using aluminium-containing solutions, with subsequent annealing.

These conditions are summarised below.

- Tri-sodium citrate — 0.25 to 0.4 M - upper limit set by diffuse reflection
- NH_4OH — 0.15 M - lower limit set by diffuse reflection
- $ZnSO_4$ — 0.03 M - limited by saturation in solution
- $CS(NH_2)_2$ — 0.05 M
- Temperature — 70°C

The films produced showed high transmittance (~ 90 %) over the wavelength range of the solar spectrum, which is comparable with that produced in previous work [8]. This would allow most of the solar radiation to reach the junction of a device fabricated using this material, thus leading to potentially high conversion efficiencies.

The films show good uniformity over both large and small scales, and good adhesion to the substrate. Electrical resistivity has been reduced, by a combination of aluminium incorporation and annealing, although annealing is the dominant factor at the highest temperatures (400°C). This may be attributable to the conversion of high-resistivity $Zn(OH)_2$ or Zn(OH,S) from the alkaline solution to ZnO or ZnS, which has a lower resistivity. Further reductions would be required, to reduce series resistance to values suitable for photovoltaic devices.

5.6 Overview of results and analysis of material fabrication

As a number of deposition techniques have been used, and their results analysed in this chapter, it is useful to note the major features, and make comparisons between the various methods.

The sputtered copper indium shows the required composition, with uniformity both with depth and across the area. The sputtering technique used in this work deposited a larger number of alternate layers than a number of previous methods, used for $CuInS_2$ and other chalcopyrite materials, based on either sputtering or thermal evaporation [10, 11, 12]. This resulted in thinner layers, which is conducive to improved mixing. Adhesion to the substrate/Mo layer is also good.

It is useful to compare the different methods of converting Cu/In to $CuInS_2$. Both of the methods involving evaporation of sulphur – graphite box and flowing argon – resulted in a high degree of conversion to the ternary compound, with some residual binary compounds. Uniformity and adhesion to the substrate were good in both cases, although somewhat better for the films produced using the graphite box. In comparison to previous methods of sulphidisation, involving either sulphur vapour or H_2S, it has been found that lower temperatures can be used - 400°C compared to typically 550°C [10, 11, 13, 14].

The anodic conversion to $CuInS_2$ produced more limited results. The degree of both physical and chemical incorporation of sulphur was relatively small. The uniformity improved over the series of experiments, as the solution was modified. There was some improvement in adhesion, although this was less than for the other conversion techniques.

Chemical bath deposition of zinc sulphide produced films with good uniformity and adhesion, with high optical transmittance. This was achieved using tri-sodium citrate as a safer alternative to hydrazine hydrate, which had previously been used as a complementary complexing agent [8, 9]. Addition of aluminium to the solution, combined with annealing, reduced the resistivity of the films.

5.7 Electrical measurements for devices fabricated at Sri Venkateswara University, India

The current-voltage characteristics are shown, for two variations of the device configuration, in Figures 5.39 and 5.40. Under illumination, the short circuit current density was 11 mA cm^{-2}. This is somewhat lower than values of 30 to 40 mA cm^{-2} obtained for a range of chalcopyrite-based devices [15, 16, 17]. However, further optimisation may improve on these preliminary results.

The open circuit voltage was approx. 420 mV, which is typical for this type of device. The graphs indicate a fill factor of the order of 0.4, leading to moderate efficiencies. As for the current, further optimisation may lead to improved results. This is considered further in the next chapter, on conclusions and future work.

From Figure 5.40, the gradient of the curve at zero current is -1/10 mA/mV. This gives a series resistance of 10 Ω. This is considerably higher than the recommended resistance for a 1 cm^2 device. The resultant fill factor is less than 0.5, which would significantly reduce the efficiency of the device. Mechanisms which may contribute to this series resistance are - recombination and scattering in the polycrystalline copper indium disulphide, similar losses in the interfaces between the constituent layers ($CuInS_2$/ZnS and ZnS/ZnO), and resistance to lateral conduction in the ZnO layer.

The gradient of the curve at zero volts is too small to be measured, suggesting a very high shunt resistance. This would thus have a lower effect on resistance. As the mechanisms leading to series resistance include pinholes and diffusion of conductive material along grain boundaries, the high shunt resistance suggests that these processes are not significant in the devices produced.

Applying a best-fit curve to the dark characteristics in Figure 5.39 gives an ideality factor - η - of two. This suggests that recombination in the depletion region is the dominant current generating mechanism. This is consistent with the high level of recombination, indicated by the series resistance. The higher ideality factor (compared to a value of 1, for a device in which diffusion is the dominant current generating mechanism) results in a less steep slope in the positive voltage region of the current-voltage characteristic. This reduces the fill factor, and thus reduces this component of cell efficiency.

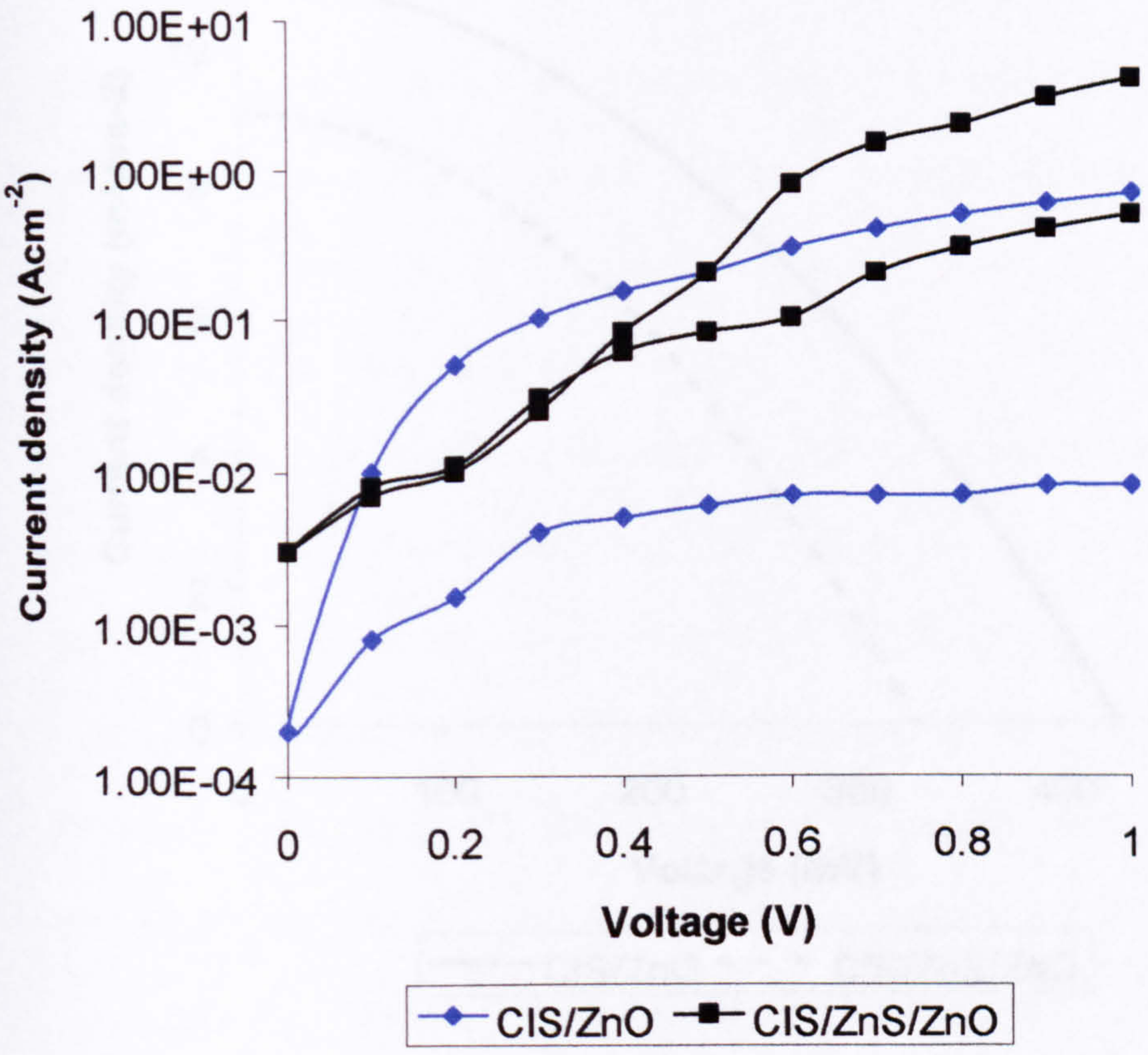

Figure 5.39. Current-voltage characteristics of unilluminated devices.

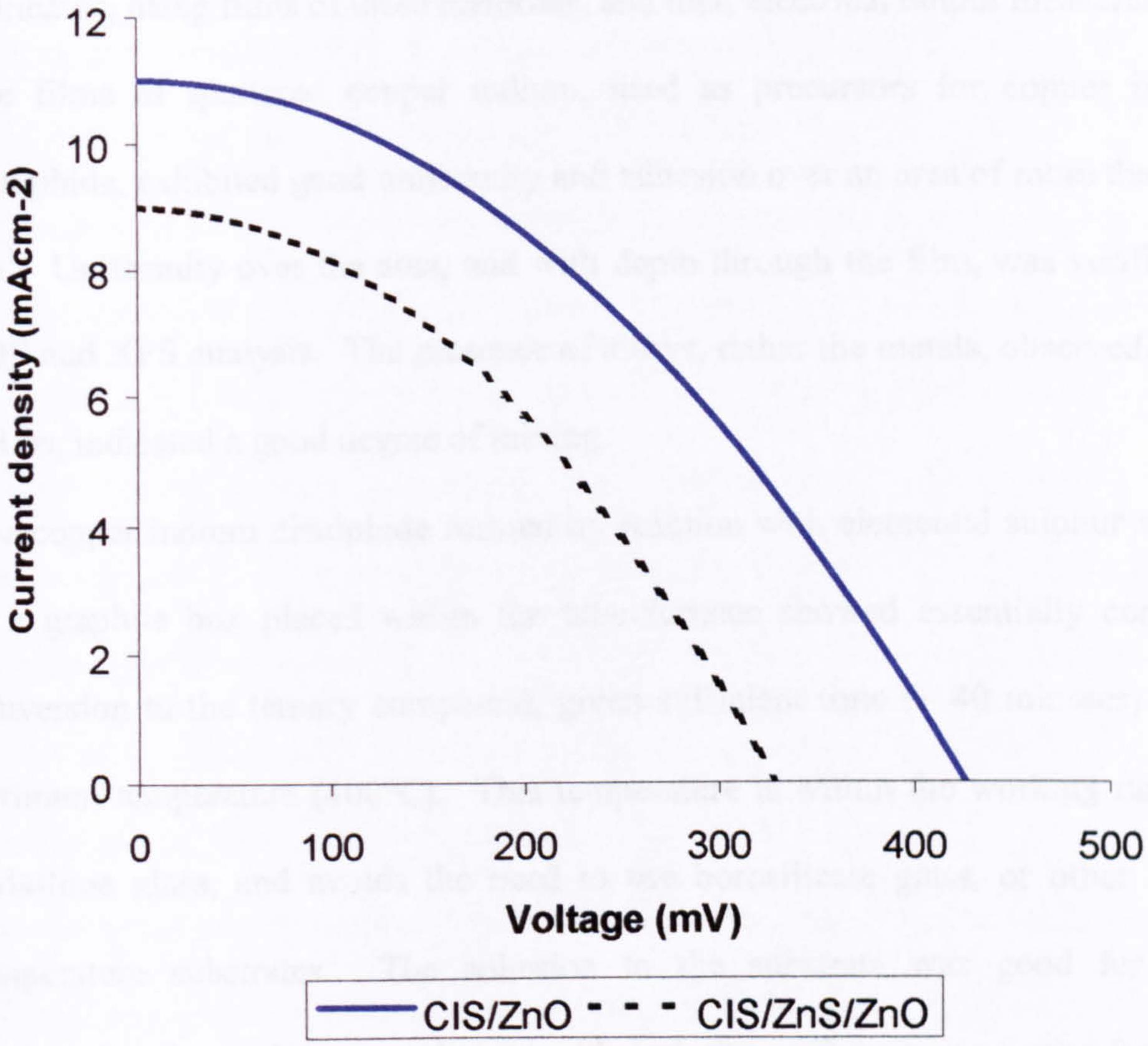

Figure 5.40. Current-voltage characteristics of devices under illumination.

6 Conclusions

In this work, deposition processes were investigated for the production of zinc sulphide and copper indium disulphide films, and their properties were evaluated, with a focus on how these relate to solar cell performance. Solar cells were then fabricated, using films of these materials, and their electrical output measured.

The films of sputtered copper indium, used as precursors for copper indium disulphide, exhibited good uniformity and adhesion over an area of more than 100 cm^2. Uniformity over the area, and with depth through the film, was verified by RBS and XPS analysis. The presence of alloys, rather the metals, observed in the XRDs, indicated a good degree of mixing.

The copper indium disulphide formed by reaction with elemental sulphur vapour in a graphite box placed within the tube furnace showed essentially complete conversion to the ternary compound, given sufficient time (~ 40 minutes) at the optimum temperature (400°C). This temperature is within the working range of soda-lime glass, and avoids the need to use borosilicate glass, or other higher temperature substrates. The adhesion to the substrate was good for films produced under optimum conditions, although the uniformity was poor for some samples. For those films exhibiting good uniformity, this extended over the area of the substrate (~ 20 cm x 20 cm). There was a preferential loss of indium for films heated for longer periods.

Similar results were obtained for films sulphidised using flowing argon as a carrier gas. The optimum conditions were the same as for those films sulphidised in a graphite box - 400°C for 40 minutes. Complete conversion to the ternary compound was observed for these conditions. Adhesion to the substrate was good, although the films were less uniform than those produced using a graphite box.

With the exception of this variable uniformity, the structural and compositional properties of the films produced by this method were good. This may indicate suitability for use in solar cells.

For copper indium disulphide produced by anodic conversion, the results showed partial success. For films converted using aqueous solutions, the XRDs showed a high degree of conversion to copper indium disulphide. However, the films exhibited poor adhesion and were highly non-uniform.

The films produced using ethanediol as the solvent showed a significant improvement in uniformity, and some improvement in adhesion, for those produced at a lower solution temperature. The results of EDAX showed excess sulphur on the surface, while the XRD showed unconverted copper indium, indicating insufficient penetration of sulphur into the films. The work done so far indicates that this process has not met all the requirements for thin films for use in solar cells. However, further investigation, involving a different range of conditions, may yield different results.

Zinc sulphide has been developed in recent years as an alternative to cadmium sulphide, in order to reduce environmental effects and to improve efficiency. Chemical bath deposition has been developed as a method, which has the potential to reduce production costs. However, the use of hydrazine hydrate in the production process has offset the benefits of eliminating cadmium. In this work, zinc sulphide films have been successfully deposited, with the hydrazine hydrate replaced by tri-sodium citrate. This has removed the primary environmental hazard from the process.

The properties of zinc sulphide which are relevant to device performance are optical transmittance and electrical resistivity. The high band gap energy results

in a short cut-off wavelength. For the polycrystalline material deposited by chemical bath deposition, the cut-off wavelength was less than 330 nm. Transmittance at longer wavelengths was close to 90 %. This would allow transmission of most of the AM1.5 solar spectrum to the junction.

The electrical resistivity of zinc sulphide is high. However, this was reduced by a combination of annealing and incorporation of aluminium. The latter was achieved by adding aluminium sulphate to the chemical bath solution. The best results, obtained for aluminium doping and an annealing temperature of 200°C or higher, correspond to a resistance of approximately 1 Ω for a 1 cm^2 device. Although this is an improvement on the undoped material, it is slightly higher than is generally recommended for production devices.

The adhesion of the films to the substrate was good. Observations by visual inspection and SEM showed the films were uniform over a wide range of scales. These properties should allow chemically deposited zinc sulphide to form good interfaces with other materials, potentially leading to high-quality devices.

Experiments on devices measured the current-voltage characteristics. These showed the almost unidirectional current flow expected of a diode. Measurements made on illuminated devices showed open circuit voltages, which are comparable with those produced previously for similar devices. The short circuit current was somewhat lower than for similar devices. Thus the conversion efficiency was also lower. However, these preliminary results indicate that some photovoltaic activity has occurred, and that devices produced using the methods developed in this work have the potential to operate as solar cells.

6.1 Future work

For each of the materials and processes developed in this work, a number of properties were measured. Some of the properties observed were sufficiently good for use in photovoltaic devices. Other properties showed the need for further improvement.

In order to produce copper indium disulphide films over a larger area, the uniformity will need to be improved. This will involve, among other things, providing uniform temperatures over a sufficiently large volume. In this work, the size of the graphite box was constrained by the diameter of the quartz tube used in the tube furnace. This in turn constrained the size of sample, which could be sulphidised in the box. Future work would include an alternative heating system, which would allow the use of a larger box, and hence larger substrates.

The use of flowing argon was adopted, in order to provide a transport medium, which could transfer sulphur vapour over longer distances, and so would not be limited be the line of sight, as in most thermal evaporation techniques. Successful application of this technique would require improvements in uniformity. It would also require a gas flow configuration that circulates argon over all of the substrates within the furnace, and thus delivers the sulphur over the same area.

Further development of anodic conversion would need to address the issues of non-uniformity and poor adhesion, as well as a low level of conversion to copper indium disulphide. The use of specialist power supplies, and additional components in the solution may produce some improvement.

The substitution of tri-sodium citrate for hydrazine hydrate removed the main health and environmental hazard from the chemical bath deposition of zinc sulphide. However, the process still involves the use of thiourea, which presents

some degree of hazard. Further research may be able to identify a safer substitute, for use as a source of sulphur. A related area is the potential for re-cycling of the waste material from the deposition process.

The optical transmittance of the films produced was high, so that there is little scope for further improvement. Although the electrical resistance was reduced by doping with aluminium, it was still too high for use in efficient solar cells. More work will be required to reduce the resistance further, to the point where the films can usefully be incorporated into solar cells.

The open circuit voltages observed for the photovoltaic devices completed and analysed at Sri Venkateswara University were comparable with the results for similar devices produced elsewhere. However, the short circuit currents were substantially lower. This suggests that current loss mechanisms are significant factors in the reduced efficiency, and that future work should identify the specific mechanisms, and should modify the fabrication processes to reduce the effects of such mechanisms.

A number of deposition and analysis facilities have recently become available at Northumbria University. These allow the development of research in a range of directions. The new multi-function deposition facility includes sputtering and thermal evaporation systems. These include an increased number of targets and sources respectively. Thus sputtering could be extended from CuIn to Cu(In,Ga) alloys. Thermal evaporation could include selenium, as well as sulphur, to be incorporated. This would allow the full range of chalcopyrite materials - $Cu(In,Ga)Se_2$, $CuIn(S,Se)_2$, etc - to be fabricated. The facility also has the ability to deposit Al-doped ZnO, which would allow the TCO layer to be fabricated at Northumbria University, rather than at another research centre. Thus the entire

photovoltaic device could be fabricated at Northumbria, possibly in one machine, and without breaking vacuum.

Given the potential for fabrication of complete devices, the interfaces between adjacent layers become significant. This includes a range of surface treatments, such as etching of the $CuInS_2$ absorber layer to achieve the correct composition, prior to deposition of the buffer layer.

The new SEM/EDAX facility at the Advanced Materials Research Institute (AMRI) has improved accuracy in compositional analysis. This would allow much better evaluation of the stoichiometry of deposited compounds and alloys. The X-ray photo-electron spectroscopy (XPS) system became available in August 2004 (also at AMRI), and it was possible to include some analysis from this system in the later stages of this work. Subsequent work could make further use of this facility. This would include analysis of the variation in composition with depth, which would be useful for graded films, and to evaluate the extent of mixing between layers in devices. Secondary ion mass spectrometry (now available at both NPAC and AMRI) would also allow the composition to be measured as a function of depth, complementing the capabilities of XPS.

The capability of producing complete devices at Northumbria increases the scope for measurement of device characteristics. This includes current-voltage characteristics, both in darkness and under a range of standard illumination conditions. From this, it should be possible to derive measurements of energy conversion efficiency.

A range of techniques, including capacitance-voltage measurements and spectral photocapacitance can be used to investigate the properties of the p-n junction - traps, crystal defects, impurities, etc - and thus identify potential mechanisms for

reducing efficiency. The results of such analysis can then be used to modify the deposition processes. By repeating this process of modification of the fabrication process, followed by analysis, it should be possible to significantly improve the performance of the devices produced.

References: Chapter 1

[1] K.J.H. Phillips, Guide to the Sun, Cambridge University Press (1995)

[2] S. Sze, Semiconductors Devices, Physics and Technology, Wiley (1995)

[3] L. Partain, Solar Cells and Their Applications, Wiley (1995)

[4] E.S. Cassedy, P.Z. Grossman, Introduction to Energy, Cambridge (1998)

[5] R. Bube, Photovoltaic Materials, Imperial College Press (1998)

[6] H.S. Ullal, National Renewable Energy Laboratory, Polycrystalline Thin Film Technologies: Progress and Technical Issues (2004)

[6] National Renewable Energy Laboratory (2004)

[7] National Renewable Energy Laboratory, Proc. European MRS Meeting (2004) Strasbourg, France; in press

[8] M. Ch. Lux-Steiner, A. Ennaoui, Ch. -H. Fischer, A. Jäger-Waldau, J. Klaer, R. Klenk, R. Könenkamp, Th. Matthes, R. Scheer, S. Siebentritt, A. Weidinger, Thin Solid Films 361-362 (2000) 533

[9] H.W. Lewerenz, Sol. Energy Mater. Sol. Energy Mater. Sol. Cells 83 (2004) 395

[6] J Doña, J. Herrero, J. Electrochem. Soc. 141 1 (1994) 205

[7] C.D. Lokhande, P.S. Patil, H. Tributsch, A. Ennaoui, Sol. Energy Mater. Sol. Cells 55 (1998) 323

[8] S. Bandyopahyaya, S. Chaudhuri, A.K. Pal, Sol. Energy Mater. Sol. Cells 60 (2000) 323

[9] P.K. Nair, M.T.S. Nair, V.M. García, O.L. Arenas, Y. Peña, A. Castillo, I.T. Ayala, O. Gomezdaza, A Sánchez, J. Campos, H. Hu, R. Suárez, M.E.Rincón, Sol. Energy Mater. Sol. Cells 52 (1998) 313

[10] O. Savadogo, Sol. Energy Mater. Sol. Cells 52 (1998) 361

References: Chapter 2

[1] K.J.H. Phillips, Guide to the Sun, Cambridge University Press, 1995

[2] K.R. Lang, The Sun from Space, Springer-Verlag, 2000

[3] G.N. Tiwari, Solar Energy, Alpha Science, 2002

[4] L. Partain, Solar Cells and Their Applications, Wiley, (1995)

[5] S.M. Sze, Semiconductors, Physics and Technology, Wiley, 1985

[6] S.M. Sze, Physics of Semiconductor Devices, Wiley, 1981

[7] E.S. Yang, Fundamentals of Semiconductor Devices, McGraw-Hill, 1978

[8] C.T. Sah, Fundamentals of Solid State Electronics, World Scientific, 1991

[9] P. Roblin, H. Rohdin, High-speed Heterojunction Devices, Cambridge University Press, 2002

[10] R.H. Bube, Photovoltaic Materials, Imperial College Press (1998)

[11] R.L. Anderson, Solid State Electron., Vol. 5 (1962) 431

[12] S.S. Pearlman, D.L. Feucht, Solid State Electron., Vol. 7 (1964) 63

[13] R.H. Rediker, S.Stopek, J.H.R. Ward, Solid State Electron., Vol. 7 (1964) 911

[14] A.R. Riben, D.L. Feucht, Solid State Electron., Vol. 9 (1966) 1055

[15] J.P. Donnelly, A.G. Milnes, Proc. I.E.E. 113, (1966) 1468

[16] D. Buie, M. J. McCann, K. J. Weber, C. J. Dey, Sol. Energy Mater. Sol. Cells 81 (2004) 13

[17] D. J. Aiken, Sol. Energy Mater. Sol. Cells 64 (2000) 393

[18] L. Castañer, S. Silvestre, J. Carter, D. Parton, P. Ashburn, Sol. Energy Mater. Sol. Cells 53 (1998) 115

[19] A. Kress, O. Breitenstein, S. Glunz, P. Fath, G. Willeke, E. Bucher, Sol. Energy Mater. Sol. Cells 65 (2001) 555

[20] D. König, G. Ebest, Sol. Energy Mater. Sol. Cells 75 (2003) 381

[21] M. F. Stuckings, A. W. Blakers, Sol. Energy Mater. Sol. Cells 59 (1999) 381

[22] I. Latimer, J. Hawkes, Lasers: Theory and Practice, Prentice Hall, 1995

[23] H.S. Rauschenbach, Solar Cell Array Design Handbook, Van Nostrand Reinhold, 1980

[24] T. Nakada, M. Mizutani, Y. Hagiwara, A. Kunioka, Sol. Energy Mater. Sol. Cells 67 (2001)

[25] A. Kassis, M. Saad, Sol. Energy Mater. Sol. Cells 80 (2003) 491

[26] W. Shockley, H. J. Queisser, Applied Physics 32, p. 510-519, 1961

[27] M. A. Green, K. Emery, D. L. King, S. Igari, W. Warta, Progress in Photovoltaics: Research and Applications, 11, p. 347–352, 2003

[28] M. A. Martínez, J. Herrero, M. T. Gutiérrez, Sol. Energy Mater. Sol. Cells 45 (1997) 75

[29] H. Hirasawa, M. Yoshida, S. Nakamura, Y. Suzuki, S. Okada and K. Kondo, Sol. Energy Mater. Sol. Cells 67 (2001) 231

[30] B. Sang, K. Kushiya, D. Okumura, O. Yamase, Sol. Energy Mater. Sol. Cells 67 (2001) 237

[31] A. Maldonado, R. Asomoza, J. Cañetas-Ortega, E. P. Zironi, R. Hernández, R. Patiño, O. Solorza-Feria, Sol. Energy Mater. Sol. Cells 57 (1999) 331

[32] M. Saad, A. Kassis, Sol. Energy Mater. Sol. Cells 79 (2003) 507

[33] S. Lalitha , R. Sathyamoorthy , S. Senthilarasu , A. Subbarayan, K. Natarajan, Sol. Energy Mater. Sol. Cells 82 (2004) 187

[34] X. Mathew, G. W. Thompson, V. P. Singh, J. C. McClure, S. Velumani, N. R. Mathews, P. J. Sebastian, Sol. Energy Mater. Sol. Cells 76 (2004) 293

[35] F. H. Karg, Sol. Energy Mater. Sol. Cells 66 (2001) 645

[36] R. W. Birkmire, Sol. Energy Mater. Sol. Cells 65 (2001) 17

[37] S. Martirosyan, Sol. Energy Mater. Sol. Cells 70 (2001) 115

[38] Y. Nagoya, B. Sang, Y. Fujiwara, K. Kushiya, O. Yamase, Sol. Energy Mater. Sol. Cells 75 (2003) 163

[39] M. Saad, A. Kassis, Sol. Energy Mater. Sol. Cells 79 (2003) 507

[40] M. Igalson, C. Platzer-Björkman, Sol. Energy Mater. Sol. Cells 84 (2004) 93

[41] A. Ennaoui, S. Siebentritt, M. Ch. Lux-Steiner, W. Riedl, F. Karg, Sol. Energy Mater. Sol. Cells 67 (2001) 31

[42] M. Bodegård, K. Granath, L. Stolt, A. Rockett, Sol. Energy Mater. Sol. Cells 58 (1999) 199

[43] T. Wada, Sol. Energy Mater. Sol. Cells 49 (1997) 249

[44] J. R. Sites, Sol. Energy Mater. Sol. Cells 75 (2003) 243

[45] J. R. Sites, J. E. Granata, J. F. Hiltner, Sol. Energy Mater. Sol. Cells 75 (2003) 43

[46] T. Nakada, T. Kume, A. Kunioka, Sol. Energy Mater. Sol. Cells 50 (1998) 97

[47] J. K. Rath, Sol. Energy Mater. Sol. Cells 76 (2003) 431

[48] Y. Tawada, H. Yamagishi, K. Yamamoto, Sol. Energy Mater. Sol. Cells 78 (2003) 647

[49] A. K. Turner, J. M. Woodcock, M. E. Özsan, D. W. Cunningham, D. R. Johnson, R. J. Marshall, N. B. Mason, S. Oktik, M. H. Patterson, S. J. Ransome *et al.* Sol. Energy Mater. Sol. Cells 35 (1994) 263

[50] H. J. Lewerenz, Sol. Energy Mater. Sol. Cells 83 (2004) 395

[51] M. Powalla, B. Dimmler, Sol. Energy Mater. Sol. Cells 75 (2003) 27

[52] J. Kessler, J. Wennerberg, M. Bodegård, L. Stolt, Sol. Energy Mater. Sol. Cells 75 (2003) 35

[53] H.S. Ullal, National Renewable Energy Laboratory, Polycrystalline Thin Film Technologies: Progress and Technical Issues (2004)

[54] National Renewable Energy Laboratory (2004)

[55] National Renewable Energy Laboratory, Proc. European MRS Meeting (2004) Strasbourg, France; in press

[56] Thin film processes, J. L. Vossen, W. Kern, Academic Press (1991)

[57] L.I. Maissel, R. Glang, Handbook of Thin Film Technology, McGraw-Hill

[58] A. M. Hermann, C. Gonzalez, P. A. Ramakrishnan, D. Balzar, N. Popa, P. Rice, C. H. Marshall, J. N. Hilfiker, T. Tiwald, P. J. Sebastian, Sol. Energy Mater. Sol. Cells 70 (2001) 345

References: Chapter 3

[1] Richard Bube, Photovoltaic materials. Imperial College Press (1998)

[2] K. Ramanathan, R. Noufi, J. Granata, J. Webb, J. Keane, Sol. Energy Mater. Sol. Cells 55 (1998) 15

[3] G. Gordillo, M. Grizalez, L.C. Hernandez, Sol. Energy Mater. Sol. Cells 51 (1998) 327

[4] T. Nakada, H. Ohbo, M Fukuda, A. Kuniado, Sol. Energy Mater. Sol. Cells 55 (1998) 15

[5] A. Gupta, S. Isomura, Sol. Energy Mater. Sol. Cells 53 (1998) 385

[6] T. Nakada, T. Kume, A Kunioka, Sol. Energy Mater. Sol. Cells 50 (1998) 97

[7] N. Kavcar, Sol. Energy Mater. Sol. Cells 52 (1998) 183

[8] S.C. Park, S.H. Kwon, J.S. Song, B.T. Ahn, Sol. Energy Mater. Sol. Cells 50 (1998) 43

[9] S.D. Kim, H. J. Kim, K.H. Yoon, J Song, Sol. Energy Mater. Sol. Cells 62 (2000) 357

[10] F.O. Adurodija, S.K. Kim, S.D. Kim, J.S. Song, K.H. Yong, B.T. Ahn, Sol. Energy Mater. Sol. Cells 55 (1998) 225

[11] J.H. Schön, O. Schenker, L.L. Kulyuk, K. Freimelt, E. Bucher, Sol. Energy Mater. Sol. Cells 51 (1998) 371

[12] R. Ahuja, S. Auluck, O. Eriksson, J.M. Wills, B. Johansson, Sol. Energy Mater. Sol. Cells 53 (1998) 357

[13] T. Ohashi, K. Inakoshi, Y. Hashimoto, K. Ito, Sol. Energy Mater. Sol. Cells 50 (1998) 37

[14] L.I. Maissel, R. Glang, Handbook of Thin Film Technology, McGraw-Hill (1970)

[15] S. Niki, I. Kim, P.J. Fons, H. Shibata, A. Yamada, H. Oyanagi, T. Kurafuji, S. Chichibu, H. Nakanishi, Sol. Energy Mater. Sol. Cells 49 (1997) 319

[16] S.A. Al Kuhaimi, Sol. Energy Mater. Sol. Cells 52 (1998) 69

[17] K. Yoshino, T. Shimuzu, A. Fukuyama, K. Maeda, P.J. Fons, A. Yamada, S. Niki, T. Ikari, Sol. Energy Mater. Sol. Cells 50 (1998) 127

[18] F.O. Adurodija, M.J. Carter, R. Hill Sol. Energy Mater. Sol. Cells 37 (1995) 203

[19] R.R. Gay, Sol. Energy Mater. Sol. Cells 47 (1997) 19

[20] A.V. Mudryi, I.V. Bodnar, V.F. Gremenok, I.A. Victorov, A.I. Patuk, I.A. Shakin, Sol. Energy Mater. Sol. Cells 53 (1998) 247

[21] Y. Ohtake, T. Okamoto, A Yamada, M. Konagai, K. Saito, Sol. Energy Mater. Sol. Cells 49 (1997) 269

[22] L. Kronik, B. Mishori, E. Fefer, Y. Shapira, W. Riedl, Sol. Energy Mater. Sol. Cells 51 (1998) 21

[23] K.T. Ramakrishna Reddy, R.B.V. Chalapathy, M.A. Slifkin, A.W. Weiss, R.W. Miles, Thin Solid Films 387 (2001) 205

[24] R. Herberholz, V. Nadenau, U. Rühle, C. Köble, H.W. Schock, B. Dimmler, Sol. Energy Mater. Sol. Cells 49 (1997) 227

[25] Y. Ohtake, T. Okamoto, A Yamada, M. Konagai, K. Saito, Sol. Energy Mater. Sol. Cells 49 (1997) 269

[26] M.A. Contreras, H. Wiesner, J. Tuttle, K. Ramanathan, R. Noufi, Sol. Energy Mater. Sol. Cells 49 (1997) 239

[27] N.G. Dhere, S.R. Ghongadi, M.B. Pandit, A.A. Kadam, A.H. Jahagirdar, V. S. Gade, Proc. 29th IEEE Photo. Spec. Conf. 2002

[28] T. Nakada, H. Ohbo, T. Watanabe, H. Nazakawa, M. Matsui, A. Kunioka, Sol. Energy Mater. Sol. Cells 49 (1997) 285

[29] F. Itoh, O. Saitoh, M. Kita, H. Nagamori, H. Oike, Sol. Energy Mater. Sol. Cells 50 (1998) 119

[30] K. Kushiya, M. Tachiyuki, T. Kase, I. Sugiyama, Y. Nagoya, D. Okumura, M. Sato, O. Yamase, H. Takeshita, Sol. Energy Mater. Sol. Cells 49 (1997) 119

[31] T. Tanaka, N. Tanahashi, T. Yamaguchi, A Yoshida, Sol. Energy Mater Sol. Cells 50 (1998) 13

[32] M. Topič, F. Smole, J. Furlan, Sol. Energy Mater. Sol. Cells 49 (1997) 311

[33] R.N. Bhattacharya, W. Batchelor, K. Ramanathan, M.A. Contreras, T. Moriarty, Sol. Energy Mater. Sol. Cells 63 (2000) 367

[34] M.E. Calixto, R.N. Bhattacharya, P.J. Sebastian, A.M. Fernandez, S.A. Gamboa, R.N. Noufi, Sol. Cells 55 (1998) 23

[35] N.G. Dhere, K.W. Lynn, Sol. Energy Mater. Sol. Cells 41/42 (1996) 271

[36] F.O. Adurodija, J. Song, I.O. Asia, K.H. Yoon, Sol. Cells 58 (1999) 287

[37] S. Nakamura, A. Yamamoto, Sol. Cells 49 (1997) 415

[38] S. Nakamura, A. Yamamoto, Sol. Cells 75 (2003) 81

[39] S. Marsillac, M.C. Zouaghi, J.C. Bernède, T.B. Nasrallah, S. Belgacem, Sol. Energy Mater. Sol. Cells 76 (2003) 125

[40] S. Bandyopadhaya, S. Chauduri, A.K. Pal, Sol. Energy Mater. Sol. Cells 60 (2000) 323

[41] R.W. Miles, K.T. Ramakrishna Reddy, I. Forbes, J. Crystal Growth 198/199 (1999) 316

[42] J.R.Sites, J.E. Granata, J.F. Hiltner, Sol. Energy Mater. Sol. Cells 55 (1998) 43

[43] T. Wada, Sol. Energy Mater. Sol. Cells 49 (1997) 249

[44] K. Kondo, S. Nakamura, H. Sano, H. Hirasawa, K. Sato, Sol. Energy Mater. Sol. Cells 49 (1997) 327

[45] G-C. Park, H-D. Chung, C-D. Kim, H-R. Park, W-J. Jeong, J-U. Kim, H-B. Gu, K-S. Lee, Sol. Energy Mater. Sol. Cells 49 (1997) 365

[46] R.H. Mauch, J. Hedström, D. Lincot, M. Ruckh, J. Kessler, R. Klinger, L. Stolt, J. Vedel, H.W. Schock, Proc IEEE Photovoltaics Conference 1991

[47] A. Tiburcio-Silver, A. Sanchez-Juarez, A. Avila-Garcia, Sol. Energy Mater. Sol. Cells 55 (1998) 3

[48] J. Ma, F. Ji, H-L. Ma, S-Y. Li, Sol. Energy Mater. Sol. Cells 60 (2000) 341

[49] A.E. Jiménez-González, J.A. Soto Urueta, Sol. Energy Mater. Sol. Cells 52 (1998) 345

[50] P.K. Nair, M.T.S. Nair, V.M. García, O.L. Arenas, Y. Peña, A. Castillo, I.T. Ayala, O. Gomezdaza, A. Sánchez, J. Campos, H. Hu, R. Suárez, M.E. Rincón, Sol. Energy Mater. Sol. Cells 52 (1998) 313

[51] J.M. Doña, J. Herrero, J. Electrochem. Soc. 141 1 (1994) 205

[52] C.D. Lokhande, P.S. Patil, H. Tributsch, A. Ennaoui, Sol. Energy Mater. Sol. Cells 55 (1998) 379

[53] D. Johnston, M.H. Carletto, K.T.R. Reddy, I. Forbes, R.W. Miles, Thin Solid Films, 403-404 (2002) 102-106

[54] P.K. Vidyadharan Pillai, K.P. Vijayakumar, Sol. Energy Mater. Sol. Cells 51 (1998) 47

References: Chapter 4

[1] N. Chauvez. MSc Project Report. Northumbria University 2000

[2] Thin film processes, J. L. Vossen, W. Kern, Academic Press (1991)

[3] L.I. Maissel, R. Glang, Handbook of Thin Film Technology, McGraw-Hill (1970)

[4] K.T. Ramakrishna Reddy, I. Forbes, R.W. Miles. Applied Surface Science 6555 (2000) 1-5

[5] C. Paris. MSc Project Report. Northumbria University 2002

[6] S. Bandyopadhyaya, S. Chaudhuri, A. K. Pal, Sol. Energy Mater. Sol. Cells 60 (2000) 323

[7] M. Abaab, M. Kanzari, B. Rezig, M. Brunel, Sol. Energy Mater. Sol. Cells 59 (1999) 299

[8] T. Watanabe, M. Matsui, K. Mori, Sol. Energy Mater. Sol. Cells 35 (1994) 239

[9] D. Johnston, I. Forbes, K.T. Ramakrishna Reddy, R.W. Miles, Rapid Anodic Processes for Producing Chalcopyrite Compounds, UK Patent GB 3 270 282 Published 26/06/2002

[10] J.M. Doña, J. Herrero, J. Electrochem. Soc. 141 1 (1994) 205

[11] C.D. Lokhande, P.S. Patil, H. Tributsch, A. Ennaoui, Sol. Energy Mater. Sol. Cells 55 (1998) 379

[12] P.K. Nair, M.T.S. Nair, V.M. García, O.L. Arenas, Y. Peña, A.Castillo, I.T. Ayala, O. Gomezdaza, A. Sánchez, J. Campos, H.Hu, R. Suárez, M.E.Rincón, Sol. Energy Mater. Sol. Cells 52 (1998) 313

[13] O. Savadogo. Sol. Energy Mater. Sol. Cells 52 (1998) 361

[14] F.G. Smith, J.H. Thompson, Optics, Wiley (1982)

[15] J.-H. Lee, B.-W. Yeo, B.-O. Park, Thin Solid Films, 457 2, (2004) 333

[16] S.M. Sze, Physics of Semiconductor Devices, Wiley Inter-Science (1981)

[17] R.H. Bube, Photovoltaic materials, Imperial College Press (1998)

[18] E.F. Kaelble, Handbook of X-rays, McGraw-Hill (1967)

[19] T.J.M. Boyd, J.J. Sanderson, The Physics of Plasmas, Cambridge (2003)

[20] W.-X. Ni, J. Birch, Y. S. Tang, K. B. Joelsson, C. Sotomayor-Torres, Å. Kvick, G. V. Hansson, Thin Solid Films, 294 1-2, (1997) 300

[21] D.L. Kay, Techniques for Electron Microscopy, Blackwell Scientific Publications, Oxford (1967)

[22] A. Zouaoui, M. Lachab, M. L. Hidalgo, A. Chaffa, C. Llinarès, N. Kesri Thin Solid Films, 339, 1-2, (1999) 10

[23] J. C. Bernède, L. Assmann, Vacuum, 59 4, (2000) 885

[24] J.C. Russ, Fundamentals of Energy Dispersive X-ray Analysis, Butterworths (1971)

[25] W.K. Chu, J.W. Mayer, M.A. Nicolet, Backscattering Spectrometry, Academic Press (1973)

[26] T.A. Carlson, Photoelectron and Auger Spectroscopy, Plenum Press (1973)

[27] D. Briggs, M.P. Seah, Practial surface analysis volume 1 (1990): Auger and X-ray photoelectron spectroscopy. John Wiley and Sons (1976)

[28] S. Oswald, S. Baunack Thin Solid Films, 425, 1-2, (2003), 9

[29] L.J. van der Pauw, Philips Technical Review, Vol. 20, No. 8 (1958/9)

[30] L. Partain, Solar Cells and Their Applications, Wiley (1995)

References: Chapter 5

[1] N. Chauvez. MSc Project 2000

[2] I. Forbes, K.T. Ramakrishna Reddy, D. Johnston, R.W. Miles, D.W. Lane, K.D. Rodgers, A. Chapman, J. Mater. Sci: Materials in Electronic 14 (2003) 567-571

[3] R.W. Miles, K.T. Ramakrishna Reddy, I. Forbes, J. Crystal Growth 198/199 (1999) 316-320

[4] L.I. Maissel, R. Glang, Handbook of Thin Film Technology, McGraw-Hill (1970)

[5] J.L. Vossen, W. Kern, Thin Film Processing, Academic Press (1991)

[6] T.A. Carlson, Photoelectron and Auger Spectroscopy, Plenum Press (1973)

[7] R.H. Bube, Photovoltaic materials, Imperial College Press (1998)

[8] J.M. Doña, J. Herrero, J. Electrochem. Soc. 141 1 (1994) 205

[9] C.D. Lokhande, P.S. Patil, H. Tributsch, A. Ennaoui, Sol. Energy Mater. Sol. Cells 55 (1998) 379

[10] T. Nakada, H. Ohbo, M. Fukuda, A. Kunioka, Sol. Energy Mater. Sol. Cells 49 (1997) 261

[11] N. Kavcar, Sol. Energy Mater. Sol. Cells 52 (1998) 183

[12] F. Itoh, O. Saitoh, M. Kita, H. Nagamori, H. Oike, Sol. Energy Mater. Sol. Cells 50 (1998) 119

[13] S. Bandyopadhyaya, S. Chaudhuri, A.K. Pal, Sol. Energy Mater. Sol. Cells 60 (2000) 323

[14] T. Ohashi, K. Inakoshi, Y. Hashimoto, K. Ito, Sol. Energy Mater. Sol. Cells 50 (1998) 37

[15] T. Nakada, H. Ohbo, T. Watanabe, H. Nakazawa, M. Matsui, A. Kunioka, Sol. Energy Mater. Sol. Cells 49 (1998) 285

[16] Y. Ohtake, T. Okamoto, A. Yamada, M. Konagai, K. Saito, Sol. Energy Mater. Sol. Cells 49 (1997) 269

[17] T. Nakada, T. Kume, A. Kunioka, Sol. Energy Mater. Sol.Cells 50 (1998) 97